Informatics Control Measurement
in Economy and Environment Protection

2/2022

Informatyka Automatyka Pomiary

w gospodarce i ochronie środowiska

www.e-IAPGOS.pl

ISSN 2083-0157

Kwartalnik Naukowo-Techniczny

fot. Michał Stopel

XXXII Zjazd Dziekanów Wydziałów Elektrycznych, Elektroniki, Telekomunikacji, Automatyki i Robotyki, Cybernetyki, Mechatroniki oraz Informatyki
19-21 maja 2022 r., Politechnika Bydgoska

XXXII Congress of Deans of the Faculties of Electrical, Electronics, Telecommunications, Automatics, Robotics, Cybernetics, Mechatronics and Computer Science

The XXXII Congress of Deans of the Faculties of Electrical, Electronics, Telecommunications, Automatics, Robotics, Cybernetics, Mechatronics and Computer Science took place in Bydgoszcz between 19-21 May 2022. The congress is a cyclical undertaking, the individual editions of which were organized in various universities in Poland. The first congress was held in Silesian University of Technology in Gliwice in 1991. The Deans met for the second time in Bydgoszcz in 2003.

Dean's Reunions is a long and glorious tradition continued in many academic environments. This year, the organizer of the Congress was the Faculty of Telecommunications, Computer Science and Electrical Engineering of the Bydgoszcz University of Science and Technology named after Jan and Jędrzej Śniadecki. It is the youngest in the noble group of polytechnic schools in our country, although with 70 years of tradition. It was established 7 months ago as a result of changing the name of the UTP University of Sciences and Technology named after Jan and Jędrzej Śniadecki in Bydgoszcz. It was an undoubted honor for this young University to host such honorable guests representing renowned universities from all over the country. For years, the conventions have been a place for exchanging experiences and sharing the so-called good practices between the Authorities of individual departments. The Congress allows new members of our community to establish invaluable direct contacts. During the speeches invited guests raised the most bothersome issues in the field of science, education, organization and cooperation with the economic environment. The event was supported by L.K. Control from Bydgoszcz. Nearly 90 participants took part in the congress. During the 3 days of the congress there were 8 invited speeches. The participants had the opportunity to take part in a trip around Bydgoszcz, during which they visited the most important attractions of the city.

The next Congress of Deans will take place in the Military University of Technology in Warsaw.

foto: arch. PBS

2/2022

kwiecień – czerwiec

Wydanie pod redakcją naukową
prof. dr hab. inż. Waldemara Wójcika

INFORMATYKA AUTOMATYKA POMIARY
W GOSPODARCE i OCHRONIE ŚRODOWISKA
Informatics Control Measurement in Economy and Environment Protection

p-ISSN 2083-0157, e-ISSN 2391-6761, www.e-iapgos.pl

PRINTING HOUSE – DRUKARNIA

Soft Vision Mariusz Rajski
https://www.printone.pl

nakład: 100 egzemplarzy

OTHER INFORMATION – INNE INFORMACJE

Czasopismo jest indeksowane w bazach:

DOAJ	doaj.org
BazTech	baztech.icm.edu.pl
IC Journals Master List	www.journals.indexcopernicus.com
Google Scholar	scholar.google.pl
POL-index	pbn.nauka.gov.pl
Sherpa RoMEO	www.sherpa.ac.uk
OAJI	oaji.net
SCOPUS	www.scopus.com

Czasopismo *Informatyka, Automatyka, Pomiary w Gospodarce i Ochronie Środowiska* zostało objęte finansowaniem przez Ministerstwo Nauki i Szkolnictwa Wyższego w ramach programu *Wsparcie dla czasopism naukowych* w latach 2019-2020.

Czasopismo znajduje się w wykazie czasopism naukowych opublikowanym w Komunikacie Ministra Edukacji i Nauki z dnia 1 grudnia 2021 r., Unikatowy Identyfikator Czasopisma: 200167 – z przypisaną liczbą punktów przyznawanych za publikację artykułu równą 20.

Zasady publikowania artykułów, przygotowania tekstów, zasady etyczne, procedura recenzowania, wykazy recenzentów oraz pełne teksty artykułów dostępne są na stronie internetowej czasopisma:

www.e-iapgos.pl

W celu zwiększenia oddziaływania czasopisma w środowisku naukowym redakcja zaleca:

- w artykułach publikowanych w IAPGOS cytować artykuły z renomowanych czasopism międzynarodowych (szczególnie indeksowanych w bazach Web of Science oraz Scopus) używając oficjalnych skrótów nazw czasopism,
- w artykułach publikowanych w innych czasopismach (zwłaszcza indeksowanych w bazach Web of Science oraz Scopus) cytować prace publikowane w IAPGOS – zwłaszcza posługując się numerami DOI, np.:
  Kluszczyński K. *Modelowanie – umiejętność czy sztuka?* Informatyka, Automatyka, Pomiary w Gospodarce i Ochronie Środowiska – IAPGOS, 1/2016, 4–15, https://doi.org/10.5604/20830157.1193833.

CONTENTS – SPIS TREŚCI

http://doi.org/10.35784/iapgos.2901 *received: 16.03.2022 | revised: 01.06.2022 | accepted: 15.06.2022 | available online: 30.06.2022*

CKRIPT: A NEW SCRIPTING LANGUAGE FOR WEB APPLICATIONS

Wiktor Kania, Radosław Wajman
Lodz University of Technology, Institute of Applied Computer Science, Lodz, Poland

Abstract. *The project aimed to develop and implement an efficient web server in the C++ programming language. A highly concurrent network server was achieved using system calls such as polls and a limited number of threads. The server has built-in support for a new scripting language called Ckript. It is an original project that exposes most of the server's functionality and is the primary way of developing back-end web applications. Ckript is an interpreted language with a strong typing system, garbage collection, semi-manual memory management, first-class functions, explicit variable references, support for certain object-oriented patterns and many others. In the article the syntax of the language but also the environment architecture has been explained. Finally, the testing procedure has been described with the results' presentation and discussion at each step.*

Keywords: HTTP server, scripting language, interpreter, parser, garbage collector, C++

CKRIPT: NOWY JĘZYK SKRYPTOWY APLIKACJI INTERNETOWYCH

Streszczenie. *Celem projektu było opracowanie oraz implementacja wydajnego serwera przy użyciu języka C++. Zastosowanie wywołań systemowych oraz ograniczonej liczby wątków pozwoliło zbudować wysoko współbieżny serwer. Posiada on wbudowane wsparcie dla nowego języka skryptowego Ckript. Jest to projekt autorski, który udostępnia większość funkcjonalności serwera i jest głównym środkiem budowania aplikacji back-endowych. Ckript to język interpretowany z systemem silnego typowania, mechanizmem porządkowania pamięci, półautomatycznym zarządzaniem pamięcią, wbudowanymi funkcjami, referencjami do zmiennych, obsługą pewnych wzorców zorientowanych obiektowo i wiele innych. W artykule wyjaśniono składnię języka, ale także architekturę środowiska. Na koniec opisana została procedura testowania wraz z prezentacją wyników i dyskusją na każdym etapie.*

Słowa kluczowe: serwer HTTP, język skryptowy, interpreter, parser, garbage collector, C++

Introduction

PHP was one of the first programming languages for building dynamic web applications, even though it has a mixed reputation. However, it is still one of the favourite programming languages due to its simplicity and approach to solving challenges associated with building web applications. When run on a web server such as Apache or nginx, PHP shares many similarities with the project.

This work aimed to build a highly efficient HTTP server written in C/C++ called Mish. To achieve this, research on parallel and concurrent programming techniques was done to find optimal ways to handle a few thousand connections at a time. Ckript is a general-purpose scripting language developed to integrate it with the server's architecture and make it more suitable for back-end development. Ckript has been inspired by other programming languages such as C, JavaScript, and Go. It is an interpreted language with a strong typing system, garbage collection, semi-manual memory management, first-class functions, explicit variable references, and support for certain object-oriented patterns. What makes Ckript different from most other programming languages is its support for high-level and low-level programming and integrated type system while remaining a dynamically interpreted language. Most scripting languages abstract away things like memory management and variable references. Ckript allows the programmer to choose whether to allocate data on a stack or the heap. The programmer can also use explicit references to other variables making it possible to choose between passing by value and passing by reference. This is usually only possible in low-level programming languages such as C/C++, most high-level languages pass all compound type (arrays, objects) variables by reference and primitive types (integers, Booleans) by value. Manual memory allocation is also exclusive to lower-level languages.

The integrated type system and strong typing allows writing more error-free and readable code. Usually, only compiled languages use static typing, scripting languages often opt instead for dynamic typing with the possibility of installing extensions to enable type annotations (Typescript, Ruby RBS).

A series of benchmarks was run with the implemented HTTP server to compare the server's capabilities to existing and widely used solutions. The whole project was written in C/C++ in the C++17 standard. C++ was chosen due to its high performance, extensive standard library, and access to some low-level network functionality.

1. Ckript syntax characteristics

1.1. Variables type system

Ckript is strongly and statically typed. Each variable needs to have a type assigned before the program can run. There is no type inference, and a variable's type cannot change during runtime. Since Ckript is an interpreted language, type checking is done at the program's execution time. Even though the language is strongly typed, some features are implemented to simplify a developer's life, such as implicit casts, e.g., when adding an integer to a float. Ckript defines 7 built-in types:

- **int** – a 64-bit signed integer value,
- **double** – a double-precision floating-point value,
- **str** – a string of characters used to represent human-readable text,
- **bool** – a boolean (false or true) value,
- **func** – a first-class function,
- **arr** – a dynamic array capable of holding multiple different values of the same type,
- **obj** – an instance of a class containing methods and fields.

There's also the *ref* keyword which can be coupled with any of the type mentioned above to indicate a reference to a type e.g., *ref int*.

Additionally, each variable declaration requires an assignment. There are no default or null values. This makes the whole language null-safe and less error-prone. Early versions of Ckript allowed provoking null pointer errors through invalid use of manual memory management e.g., by accessing a dynamically allocated variable after deallocating it. Situations like this are not possible after adding garbage collection and removing the ability to deallocate variables manually.

1.2. Functions

All functions in Ckript are first-class functions meaning that they are treated like any other variable. Functions can be passed as arguments to other functions, returned by other functions, stored in variables or data structures such as objects and arrays. There is support for anonymous functions (also known as lambdas in languages like Python or C++) and immediately-invoked function expressions making Ckript a very flexible language. Since functions can be stored in variables, a decision was made not to implement named functions.

Ckript functions must respect the language's type system, which means that all function expressions must define types for their parameters and return values. A function declaration and invocation might look like this:

```
1  func fib = function(int n) int {
2    if (n <= 1) return n;
3    return fib(n - 1) + fib(n - 2);
4  };
5
6  println("fib(10) =", fib(10));
```

Fig. 1. Ckript functions

This expression declares a function that accepts one parameter of name n and type int and returns a value of type int.

```
1  int six = (function(int a, int b) int {
2    return a * b;
3  })(2, 3);
4
5  println(six);
```

Fig. 2. An immediately-invoked function

This is an example of an immediately-invoked function expression. The function is executed right after declaration without storing it in a variable, instead the result of the function is stored.

```
1  func runTenTimes = function(func f) void {
2    int i = 0;
3    for (; i < 10; i += 1) {
4      f();
5    }
6  };
7
8  func greet = function(void) void {
9    println('Hello');
10 };
11
12 runTenTimes(greet);
```

Fig. 3. The usage of a first-class function

Fig. 3 presents an example of a function being passed to another function by argument. The above code should display the message "Hello" ten times on separate lines.

1.3. Variable scope

The scope of a variable is the part of a program where the variable's name can be used to access it. In Ckript, all variables are local to the function they were declared in by default and can be only accessed in that function. While there is no way to make a variable visible outside the function, there is a way to make a function capture outside variables by adding the > operator. See the function expression in line 3:

```
1  double PI = 3.1415;
2
3  func f = function>(void) void {
4    println(PI);
5  };
6
7  f();
```

Fig. 4. Capturing variables

Even though the language makes this possible, the preferred way of passing values between functions is by arguments or return values as it minimizes the number of possible human-errors, hence why functions don't capture outside variables by default.

An exception to the rule are the function variables. When a function is assigned to a variable, its name is pushed onto its own stack to allow recursion. Ckript allows for variable shadowing.

There is no block scope in Ckript i.e., variables declared in statements like if, while, or for are still local to the function they were declared in.

1.4. Classes and objects

Ckript allows defining classes and instantiating objects. Ckript objects are very similar to structures from C – they are composite data types that allow a programmer to hold several variables under the same name. These variables can be of any type.

Even though Ckript functions are first-class functions and are treated like any other variable, there is a way to treat a function as a method. When an object is allocated on the heap and one of its fields is of *func* type, the reference to that object is bound to the function. The virtual machine creates a new variable of type *ref obj* and named ***this*** and pushes it onto the function's stack, allowing it to reference the object it is assigned to.

```
1  class Person(
2    str name,
3    int age,
4    func greet
5  );
6
7  alloc obj Wiktor = Person('Wiktor', 23, function(void) void {
8    println(this.name, 'is', this.age, 'years old');
9  });
10
11 Wiktor.greet();
```

Fig. 5. The usage of Ckript classes

Line 8 references the object allocated on line 7 by using ***this*** keyword. If the variable Wiktor was not allocated with the **alloc** keyword, the program would throw an error on line 11 saying that 'this' is not defined.

Class declarations are treated like variable declarations. Classes are allocated on the current function's stack and are local to it. There are no complex object constructors, instead a programmer is encouraged to write their own functions that can act as constructors. This pattern is commonly found in languages such as C and Go.

```
1  alloc func newUser = function(str nickname, str email) ref obj {
2    class User(
3      str nickname,
4      str email,
5      bool verified
6    );
7    alloc obj user = User(nickname, email, false);
8    return user;
9  };
10
11 ref obj bob = newUser('bob', 'bob@email.com');
12 println(bob);
```

Fig. 6. Constructor's example in Ckript

1.5. Standard library and other properties

Ckript includes a small standard library for most common programming tasks such as file I/O, math operations, string manipulation, and type conversions. The full list may be found in the README.md file on the Ckript GitHub repository. Follow the repository's URL in the chapter 5.

There are also several mathematical functions such as sin, sinh, cos, cosh, tan, tanh, sqrt, log, log10, exp, floor, ceil, round, pow, and abs.

Ckript strings can be concatenated by using the + operator. One of the convenient features of the language is the ability to format strings.

```
1  str tag = "<@1>@2</@1>";
2  str div = tag('div', 123);
3  println(div);
```

Fig. 7. Strings concatenation and formatting

Line 1 declares a string variable. Line 2 executes the string like a function and passes two arguments. The corresponding arguments will replace the placeholders @n. Finally, execution of line 3 will print " 123 ". Since this method allows

any type of arguments to be passed, it is more than a mere shorthand for writing functions for string formatting. Functions need to specify the type of their arguments, so the same functionality wouldn't be possible without major code duplication.

Ckript allows creating arrays of any built-in type, including arrays and objects (see Fig. 8). Arrays in Ckript are strongly typed, meaning that each array can hold values of one type, and it's not possible to mix different types together. To create an array in Ckript, the array keyword must be used. Optionally, initial elements inside the parentheses can be defined. At the end of an array declaration there must be the type of its elements defined explicitly.

It is possible to check the size of an array with the size function, iterate over it, and print each individual element. To append or prepend a new element to an array, it simply needs to be added to it. To remove an element from an array, the index of the element can be subtracted from the array.

```
arr numbers = array(1, 2, 3) int;
println("numbers:", numbers);

int i = 0;
for (; i < size(numbers); i += 1) {
  println("numbers[@1] = @2"(i, numbers[i]));
}
```

```
Ckript console
numbers: array<int>(1, 2, 3)
numbers[0] = 1
numbers[1] = 2
numbers[2] = 3
```

Fig. 8. The usage of arrays (left) and its output (right)

2. The environment architecture

2.1. Memory allocation

Most high-level scripting languages do not give the choice of whether to allocate a variable on the stack or heap. In Ckript, all variables are allocated on function stacks by default. However, the ***alloc*** keyword instructs the interpreter to allocate the variable on the heap. What's the difference? There are multiple stacks (one for each function), but only one global heap. Whenever a function finishes execution, its stack is destroyed, and all the variables allocated on it are popped. When a variable is allocated on the heap, it remains there as long as some part of the program has at least one reference to it. It means, it may still be reachable. Variables without references are eventually garbage collected.

Using references also avoids the problem of unnecessary data duplication when passing variables to functions – by default, all variables are passed by copy. Passing by reference is especially useful when dealing with bigger objects or arrays.

```
1  func passByCopy = function(int a) void {
2    a += 5;
3  };
4
5  func passByReference = function(ref int a) void {
6    a += 5;
7  };
8
9  int foo = 3;
10 alloc int bar = 3;
11
12 passByCopy(foo);
13 passByReference(bar);
14 println(foo, bar);
```

Fig. 9. The usage of references in Ckript

Both *passByCopy* and *passByReference* increment the argument *a* by 5, but *passByReference* uses the *ref* keyword on line 5 to indicate that it accepts a reference to an int. Line 12 will copy foo, and the value of foo will remain the same after the function execution. Line 13 will copy the reference to bar, and the value of bar will change. Line 14 will output "3 8".

2.2. Bump allocator

Ckript implements a bump allocator on top of C++'s standard allocator. A bump allocator is simple in design – it can only grow and never shrink. It maintains a list of free chunks (a free list). Whenever a chunk is freed, it is placed on the free list and marked as "free" on the heap as in free to use, but not deallocated. Whenever a new chunk is requested, a chunk from the top of the free list is returned. If there are no free chunks, the allocator allocates a new chunk and expands the heap. This approach enables very fast allocation and free operations, but never allows the heap to shrink during the program's execution time. Since the Ckript programming language is intended for developing back-end scripts that shouldn't take more than a couple of hundred milliseconds, this trade-off bears more positives than negatives. The implementation of such allocator is straightforward and much less error prone.

2.3. Garbage collector

The garbage collector (GC) in Ckript is based on the mark-and-sweep algorithm [2]. The idea behind it is very simple – during the mark phase, it goes through all the variables on stacks and marks them as reachable. The sweep phase goes through all the variables on the heap and deallocates all the variables that are not marked as reachable. If a variable is not reachable in any of the program stacks, it will never be reachable, and it can be safely deleted from the heap. The GC in Ckript uses the previously described bump allocator interface to free variables, so they're not deleted, making it faster. This matters because it is a stop-the-world garbage collector, which means that once it runs, the whole program execution halts until garbage collection is finished. Ckript's garbage collector has threshold before looking for data to free. At first, it waits for at least five chunks to be allocated on the heap before it runs and then adjusts this threshold dynamically depending on how many chunks there are.

2.4. Lexer

Before the source code can be executed, it needs to be transformed into a more computer-friendly format [2]. The Ckript interpreter uses a linear sequence of specialized components to achieve that, namely the lexer, parser, and evaluator. The lexer performs lexical analysis (also known as tokenization). It is the process of transforming source code, which is a string of characters, into a series of tokens. Source code often contains information that is not very useful to a computer, such as whitespace and comments, and many of the keywords are unnecessarily verbose.

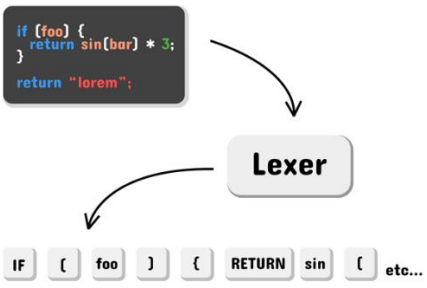

Fig. 10. The outline of the lexer's workflow

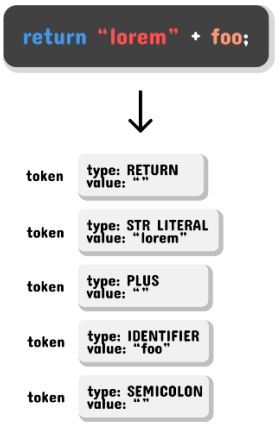

Fig. 11. The conversion of the source code to tokens

A single token is a bit more complex. It holds information about its type, a value, and some metadata such as the source file and line to help build meaningful error messages. Tokens of type **`FUNCTION`**, **`RETURN`**, **`TRUE`**, **`FALSE`** etc. are self-contained and don't need to store more information since they're used to describe language keywords. The enum type defining the type of a token is implemented as an integer value in the C++ language making tokens lightweight to use and store. Tokens such as **`STRING_LITERAL`**, **`DECIMAL`**, or **`IDENTIFIER`** need to store additional information about the contents of the token. That's where the value field comes in. See in Fig. 11 a string literal such as `"lorem"` in the example would be transformed to a token of type **`STRING_LITERAL`** and value `"lorem"`.

The Ckript lexer iterates through source code character by character and groups them. A group of characters that means something is called a lexeme. When a new lexeme is found, it is transformed into a token. A set of rules that determines how a language groups characters into lexemes is called a lexical grammar. The Ckript grammar is very similar to that of the C programming language.

2.5. Parser

The parser is responsible for syntax analysis. It takes a series of tokens as input and transforms them into an Abstract Syntax Tree (AST). An AST is a tree structure that consists of nodes. Each node can have child's nodes. An AST does not contain information such as braces, semicolons, or parentheses. The structure of an AST is designed in a way to represent these implicitly.

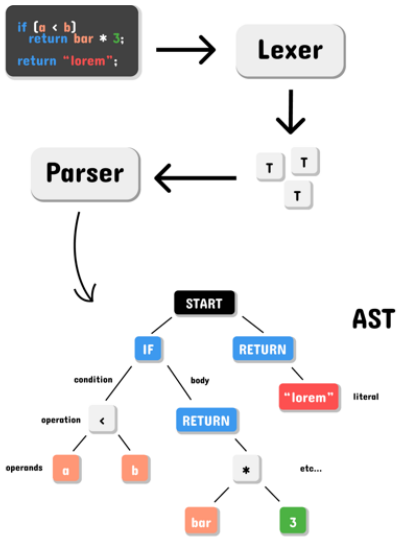

Fig. 12. The outline of the parser's workflow

The Ckript parser distinguishes three types of nodes:

- Declaration – a piece of code that introduces a new variable or class i.e., int number = 5;
- Expression – a piece of code that evaluates to a value e.g., a mathematical operation i.e., sin(5)*a;
- Statement – any executable piece of code. That includes expressions and declarations.

In Ckript, all nodes are some kind of statement nodes. Ckript defines a program as a set of statements, that's why treating everything as a statement makes it easier to execute code.

Fig. 13. The grammar of a declaration statement

Every **declaration statement** must start with a type, followed by an identifier, followed by an equal sign, followed by an expression, and end with a semicolon.

Every **expression statement** must start with an expression and end with a semicolon.

Every **compound statement** (a statement that can contain multiple other statements) must start with a left brace {, then contain one or more statements, and end with a right brace }.

Every **while statement** must start with the `"while"` keyword, followed by a left parenthesis, followed by an expression, followed by a right parenthesis, and end with a statement.

Expressions are also a complicated concept in Ckript since a lot of code can fall under that category, and most expressions are made up from other expressions.

Fig. 14. An example of a binary expression

Binary expressions are made up from two expressions separated by a binary operator (such as `"+"`, `"-"` etc.). The binary expressions can also contain compound expressions on either of the sides, such as in the following example (Fig. 15) where the right-hand side of the binary expression is another binary expression.

Fig. 15. Compound binary expression

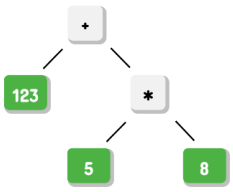

Fig. 16. The tree representation of an expression

Parsing mathematical expressions introduces two new problems to solve – operator precedence and associativity. Ckript's operator precedence was heavily inspired by the C++ operator precedence [3]. If there was no precedence, an excessive number of parentheses would be required to write valid mathematical expressions. Thanks to operator precedence, the parser knows that, for example, multiplication should be evaluated before addition. An expression like 123+5*8; should be parsed to an AST node like this in Fig. 16:

By traversing the tree recursively from left to right and evaluating it, the correct result will be calculated.

To parse an expression to a tree, the *Shunting Yard Algorithm* [5] can be used. Ckript uses a slightly modified version of the algorithm that parses tokens to *Reverse Polish Notation* [1] (RPN). For example, the expression `"1 + 2 * 3 + 4"` will be converted to `"1 2 3 * + 4 +"` which can be later reduced to the actual value with an RPN calculator.

2.6. Evaluator & Virtual Machine

The evaluator is the place where the actual program execution happens. It takes an AST as input, traverses it, and executes each statement node. Another important part of the evaluator is the expression evaluator which takes an RPN stack and evaluates it to a value. There are also functions responsible for declaring variables, classes, executing built-in and user-defined functions, instantiating objects etc. The evaluator is closely tied to the virtual machine.

The virtual machine (VM) is the place where all the data is stored during program execution. The VM contains the global

heap, the stack trace, output buffers, references to all the evaluators using the VM, and the reference to the client that made the HTTP request that invoked the script. Usually, there are multiple evaluators (one for each executed function), but only one VM. Each evaluator instance holds the reference to the same VM so that all functions can access the exact same data, and the VM keeps track of all the active evaluators to enable garbage collection (since function stacks are stored in their respective evaluators). The VM also defines all the built-in (standard library) functions available globally during program execution, such as **`echo()`**, **`abort()`** etc.

For example, whenever an evaluator defines a new variable on the heap, it needs to use the associated VM to store the variable's value.

The Value class models all available data types, such as integers, strings, arrays etc. A value can be either stored in a Variable object or a Chunk object on the heap, depending on whether it was allocated on the heap or a stack. Values that live on stacks are returned as variables that hold the actual values. Values allocated on the heap are returned as variables with a heap reference value, which basically acts as a pointer to the location of the Chunk object on the heap that holds the actual value.

The Heap class holds an array of Chunk objects, it also has a Cache instance that holds references to unused Chunks.

The NativeFunction class in an abstract class defines a standard library function. Other classes can implement their own ***execute*** methods – see Fig. 17. The standard library is a map of key-value pairs where the keys are the names of the functions, and the values are NativeFunction pointers - each having its own implementation.

```
297  class NativeEcho : public NativeFunction {
298    public:
299      Value execute(std::vector<Value> &args, std::int64_t line, CVM &VM) {
300        if (args.size() == 0) {
301          VM.throw_runtime_error("echo() expects at least one argument", line);
302        }
303        std::size_t i = 0;
304        const std::size_t end_index = args.size() - 1;
305        for (auto &arg : args) {
306          VM.output_buffer += VM.stringify(arg);
307          if (i != end_index) VM.output_buffer += " ";
308          i++;
309        }
310        return {Utils::VOID};
311      }
312  };
```

Fig. 17. C++ source code of the echo function implementation

For example, the echo function accepts at least one argument and saves the string representation of all of them to the output buffer (which is later rendered to the client) and returns void.

The CVM (Ckript Virtual Machine) class is the heart of the whole VM. It is closely tied to the Heap object, contains garbage collection utility methods, keeps track of stack traces, and can throw all kinds of errors.

3. Tests and results

To test the performance of the HTTP server, **Siege** [4] utility program was used. The tests compared Ckript scripts running on the server with similar PHP scripts running on an Apache server.

The machine used for testing was running on an Intel Core 10th Gen i5-10210U Processor with 4 cores, 8 threads, clocking 1.60 GHz at base frequency and 4.20 GHz at max frequency. The machine had 16GB DDR3 RAM. The tests were run on Ubuntu 20.04 on WSL2 on Windows 10.

All the tests used the same Siege settings – there were no delays between requests, there were 200 concurrent users simulated at the same time, and the tests were repeated 200 times, meaning that each test ran 40000 times. The command used to invoke the tests looked like this:

siege -r200 -c200 -b <URL>

The following test cases were performed.

Hello world test

hello.php

```
1  <?php
2    echo 'Hello world';
3  ?>
4
```

hello.ck

```
1  <&
2    echo('Hello world');
3  &>
4
```

The first test ran a script that only returned the "Hello world" string back to the client. It tested the speed of parsing simple HTTP requests and constructing HTTP responses.

	Elapsed time	Transaction rate	Throughput
Mish server	4.97 secs	8048.29 trans/sec	0.08 MB/sec
Apache server	3.59 secs	11142.06 trans/sec	0.12 MB/sec

Simple HTML page test

The second test requested an HTML page from the server. The page used for testing was the Apache2 Ubuntu Default Page. The results are as follows:

	Elapsed time	Transaction rate	Throughput
Mish server	10.75 secs	7441.86 trans/sec	50.56 MB/sec
Apache server	9.95 secs	8040.20 trans/sec	24.83 MB/sec

One might notice an oddity here - even though the elapsed time and transaction rates are comparable, the Mish server doubled the throughput. It is due to caching mechanisms that the Apache server is using, some page resources were not transferred multiple times (such as images).

Fibonacci sequence test

The last test ran a script that generated and displayed first ten Fibonacci numbers recursively (see Fig. 18). This method is known for being a CPU-intensive task.

	Elapsed time	Transaction rate	Throughput
Mish server	49.88 secs	801.92 trans/sec	0.11 MB/sec
Apache server	4.11 secs	9732.36 trans/sec	0.78 MB/sec

The speed of parsing HTTP requests and serving HTTP responses is comparable between the two tested servers, with the Apache server performing a bit better.

fib.php

```
1  <?php
2    function fib($n) {
3      if ($n ⩽ 1) return $n;
4      return fib($n - 1) + fib($n - 2);
5    }
6
7    for ($i = 1; $i ⩽ 10; $i++) {
8      echo "fib(" . $i . ") = " . fib($i) . "<br>";
9    }
0  ?>
```

fib.ck

```
1  <&
2    func fib = function(int n) int {
3      if (n ⩽ 1) return n;
4      return fib(n - 1) + fib(n - 2);
5    };
6
7    int i = 1;
8    for (; i ⩽ 10; i += 1) {
9      echo("fib(" + i + ") = " + fib(i) + "<br>");
10   }
11 &>
```

Fig. 18.Recursive Fibonacci function in PHP (top) and Ckript (bottom)

It is noticeable that Ckript is a rather slow programming language and was a bottleneck in the Fibonacci test, it performed about ten times slower than PHP. This is because Ckript uses a tree-walk interpreter, while PHP has been a just-in-time compiled language since version 8.

4. Summary

The server at its current state is fully capable of powering small and medium-sized web projects. It's fast enough to handle the traffic of a semi-popular website, and the scripting language allows for developing most common back-end tasks. Ckript enables web developers to build complex page templates when combined with HTML code. Most other programming languages require external templating engines or front-end libraries to achieve that. Most popular front-end frameworks such as React, Vue, or Angular rely on client-side rendering, which is not great for a site's SEO. There are libraries (such as Nuxt or Next) that work on top of these frameworks to solve this problem. Ckript coupled with the web server makes server-side rendering possible without having to install any additional software. It is possible to define business logic directly in the presentation layer or make reusable components by creating template strings and then interpolating them later. These components can be exported to external files and then included in the presentation layer if needed.

There are a few ways that could improve the usability of the server, such as implementing user sessions which would streamline developing authentication and authorization systems. Right now, this can be achieved by sending tokens to the server with each request, but most web servers available today offer tools that handle cookies and sessions under the hood. Database drivers could be added to enable integration with databases such as MySQL, PostreSQL, or MongoDB and allow for easier persistent data storage. Although Ckript offers file I/O capabilities, these can prove to be hard to work with if there's structured data to be stored. The scripting language could be made faster by optimizing the interpreter or writing an ahead-of-time or a just-in-time compiler for it. Ckript is not a blazing fast language due to its tree-walk interpreter. Traversing an AST is rather slow since its nodes are all over the place in memory, which leads to cache misses. A way to speed it up would be writing a compiler targeting bytecode. Bytecode can be represented as an array that can be processed linearly, reducing the number of cache misses and so-called pointer chasing. This would also require writing an entirely new virtual machine, since the existing one can only work with ASTs but would speed things up significantly.

5. Additional resources

Language repository with documentation: https://github.com/Roller23/ckript-lang

HTTP server repository with language fork and documentation for the server only: https://github.com/Roller23/Mish

Online interpreter for language. It uses WebAssembly (C ++ compilation to WASM) to run the interpreter in the browser: https://ckript.netlify.app/ and the repository for the online interpreter: https://github.com/Roller23/ckript-online.

Ckript implementation in Javascript in the Node.js environment. This version is being developed in parallel with the C ++ version. It has some improvements such as access to network functions or a simplified type system for numbers: https://github.com/Roller23/ckript-js.

Acknowledgments

The authors want to thank Dr Piotr Duch (ORCID ID 0000-0003-0656-1215) and Dr Tomasz Jaworski (ORCID ID 0000-0001-8600-3760) for their inspiration, support and fruitful advice.

This work was financed by the Lodz University of Technology, Faculty of Electrical, Electronic, Computer and Control Engineering as a part of statutory activity no. 501/2-24-1-2

References

[1] Hamblin C. L.: Translation to and from Polish Notation. Comput. J. 5, 1962, 210–213. [http://doi.org/10.1093/COMJNL/5.3.210].
[2] Nystrom R.: Crafting Interpreters. Genever Benning, 2021.
[3] C++ Operator Precedence – cppreference.com, (n.d.). https://en.cppreference.com/w/cpp/language/operator_precedence (18.02.2022).
[4] Siege: HTTP/HTTPS stress tester – Linux man page, (n.d.). https://linux.die.net/man/1/siege (18.02.2022).
[5] The Shunting Yard Algorithm, (n.d.). http://mathcenter.oxford.emory.edu/site/cs171/shuntingYardAlgorithm/ (18.02.2022).

Eng. Wiktor Kania
e-mail: victorkaniaweb@gmail.com

Wiktor Kania is a graduate of Lodz University of Technology. His interests lie in modern web development, network programming, operating systems, and computer architecture.

http://orcid.org/0000-0002-0128-2762

DSc. Ph.D. Eng. Radosław Wajman, prof. TUL
e-mail: radoslaw.wajman@p.lodz.pl

Radosław Wajman is a professor at the Institute of Applied Computer Science at the Lodz University of Technology. In his work, he deals with the issues in the field of electrical capacitance tomography, fuzzy inference, software engineering, two-phase gas-liquid flow recognition, image reconstruction, and recognition.

http://orcid.org/0000-0002-6372-5960

http://doi.org/10.35784/iapgos.2963 *received: 12.05.2022 | revised: 13.06.2022 | accepted: 15.06.2022 | available online: 30.06.2022*

MULTICLASS SKIN LESSIONS CLASSIFICATION BASED ON DEEP NEURAL NETWORKS

Magdalena Michalska-Ciekańska
Lublin University of Technology, Department of Electronics and Information Technology, Lublin, Poland

Abstract. *Skin diseases diagnosed with dermatoscopy are becoming more and more common. The use of computerized diagnostic systems becomes extremely effective. Non-invasive methods of diagnostics, such as deep neural networks, are an increasingly common tool studied by scientists. The article presents an overview of selected main issues related to the multi-class classification process: the stage of database selection, initial image processing, selection of the learning data set, classification tools, network training stage and obtaining final results. The described actions were implemented using available deep neural networks. The article pay attention to the final results of available models, such as effectiveness, specificity, classification accuracy for different numbers of classes and available data sets.*

Keywords: dermatoscopic images, multiclass classification, skin lesions, deep neural networks

WIELOKLASOWA KLASYFIKACJA ZNAMION SKÓRNYCH W OPARCIU O GŁĘBOKIE SIECI NEURONOWE

Streszczenie. *Choroby skóry diagnozowane za pomocą dermatoskopii są coraz powszechniejsze. Wykorzystanie skomputeryzowanych systemów diagnostyki staje się niezwykle skuteczne. Nieinwazyjne metody diagnostyki, jakimi są głębokie sieci neuronowe są coraz powszechniejszym narzędziem badanym przez naukowców. W artykule przedstawiono przegląd wybranych głównych zagadnień związanych w procesem klasyfikacji wieloklasowej: etap wyboru bazy danych, wstępnego przetwarzania obrazów, doboru zestawu danych uczących, narzędzi klasyfikacji, etapu trenowania sieci i otrzymania wyników końcowych. Opisane działania zostały zaimplementowane za pomocą dostępnych głębokich sieci neuronowych. W artykule zwrócono uwagę na wyniki końcowe dostępnych modeli, takich jak skuteczność, specyficzność, dokładność klasyfikacji dla różnej ilości klas i dostępnych zestawów danych.*

Słowa kluczowe: obrazy dermatoskopowe, wieloklasowa klasyfikacja, zmiany skórne, głębokie sieci neuronowe

Introduction

Skin cancers are often diagnosed dangerous skin diseases, including: squamous cell carcinoma, malignat melanoma, basal cell carcinoma and many others. Malignat melanoma is definitely the cancer with the highest growth dynamics, although it ranks 14th in terms of the number of cancer cases in Poland. In 2016, over 3,600 new cases and over 1,300 deaths were recorded in Poland [49]. However, the most commonly diagnosed benign birthmarks are: nevus, pigmented benign keratosis and seborrheic keratosis. The problem of diagnosing skin cancers is difficult, because it is often ignored by patients who come to the dermatologist too late to consult a skin lesion. Patients come to the doctor already with an advanced condition requiring specialized oncological treatment.

Dermatoscopy is a non-invasive imaging technique that allows you to make many, high-resolution images of skin birthmarks. Diagnostics based on images is currently very effective due to the use of algorithms based on artificial intelligence [7, 21, 24, 26]. The skin nevus diagnosed by the algorithm to confirm the diagnosis should be examined by a doctor. If the doctor's diagnosis is confirmed with the diagnosis of the diagnostic tool, the patient should undergo a histopathological examination.

Over the past decade, methods of automatic diagnosis of skin birthmarks from dermatoscopic images have gained great popularity [8, 23]. We owe the emergence of automatic methods to the machine learning development, the aim of which is to build a system capable of automatic improvement and acquisition of new skills based on the information provided. Widely used in non-invasive diagnostics of skin diseases find deep convolutional neural networks DCNN [10, 22, 31]. Deep learning has made it possible to diagnose many diseases through the use of a segmentation and classification process. Statistics indicate the greatest interest in the use of artificial neural networks in the process of segmentation. Increasingly, DCNN is used for this purpose to segment the region of interest, network training to classify dermatoscopic images [11, 48, 50].

Nowadays, it is the diagnostic methods based on these structures that develop the fastest. The most commonly implemented classification in earlier years was the binary classification [5, 16, 27]. The input data was divided into two classes, malignant melanoma versus no-melanoma or begin nevi. As the complexity of algorithms developed, deep neural networks developed, and more computational capabilities appeared in the classification of more classes. Currently developed models allow the classification of 5, 6 and even 7 different skin diseases [28, 29]. The use of more dermatoscopic images and more complex models of convolutional networks allowed to achieve great success in the diagnostic process [25, 43, 44]. Even papers are being created comparing the diagnostic capabilities of neural networks and dermatologists [13].

1. Database and preprocessing

Many works have been created using many generally available dermatoscopic databases. These databases contain images of skin lesions previously well diagnosed by doctors, making them a reliable basis for training the training of created neural network models. The most extensive and largest database is the ISIC database [20], which contains more than 20,000 dermatoscopic images of previously diagnosed skin lesions. MED-NODE database [30] contains 100 images of melanoma and 70 skin nevi. Among them should be mentioned the most famous: PH2 [34], PAD-UFES-20 [32], DERMOFIT [9]. Figure 1 shows examples of dermatoscopic images of six skin diseases from the most well-known and largest of the databases.

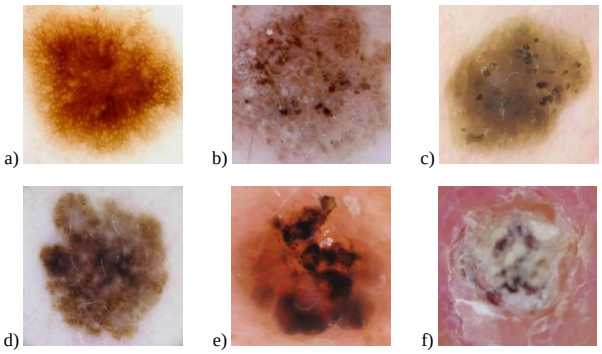

Fig. 1. Sample images of each class in ISIC: a) Nevus, b) Pigmented benign keratosis, c) Seborrheic keratosis, d) Malignant melanoma, e) Basal cell carcinoma, f) Squamous cell carcinoma [20]

Images of skin lesions taken from the database are subjected to a preliminary preparation process. In order to give images to the segmentation process, they should be well prepared. Images often contain artifacts such as medical tags, a scale applied to the skin, dark hair, air bubbles, blood vessels and skin lines. Automatic tools have been developed to remove artifacts from dermatoscopic images: edge filters, DullRazar. Artifacts in the images interfere with the process of identifying the skin lesion.

The next stage is to prepare an appropriate database of training and test images for a given class. Images previously diagnosed correctly by doctors based on a biopsy. Before the segmentation stage, areas of interest (ROI) are designated, which includes the skin lesion. Computer image analysis is used to monitor the boundaries of skin lesions. Currently, a number of automatic edge segmentation algorithms, active contours, K-medium, Otsu, fuzzy c-averages, "center split", "split and merge" and adaptive thresholding are used.

2. Training networks

Deep neural networks consist of multiple layers, each identifying more complex elements of the input image. For the created network, the input image of the skin lesion can be classified as an element of one of the defined classes. Deep neural networks consist of multiple layers, each identifying more complex elements of the input image. A convolutional network is a complex structure, which has the number of layers ranges from several dozen to several hundred. The subsequent steps that take place in each (parameterized by weights) layers transform the input data set into the output set.

Many neural network models have been created for image processing, including MobileNet [17], MobileNetV2 [40], DenseNet [18], NASNet, Xception, VGG16, VGG19, ResNet, InceptionV3, InceptionResNetV2 and many others. These models are very often used by researchers. The obtained samples are divided into three sets: training, validation and test. The created models are implent and the learning process takes place. Figure 2 shows a simplified diagram of the example architecture of the created DenseNet-201 network model, which was used in [43] to classify dermatoscopic images. It was created on the basis of the Keras library [33], which is used in transfer learning. In the network diagram there are blocks that contain fine-tuned layers (red), the non-modified (blue). The last of them are marked in purple the dense layers. Model has hidden layers and the ReLU function. Softmax is an activation function. DenseNet uses layer-to-layer connections, each previous layer is connected to the incoming layer. Also dense blocks, feature maps of all recent layers are combined with subsequent layers.

The entire network learning process is accompanied by skilful diagnostics of the model based on the created learning and validation curves. Based on the course of learning and validation charts, it is possible to determine whether there is undertraining, overtraining or matching in a given model. Depending on the implemented model, the training process gives a different effect. The assessment of the effectiveness of the model is made on the basis of the accuracy and loss value in relation to the number of epochs made through the network on the charts. Figure 3 shows evolution of accuracy and loss of the training and validation processes in [43]. After the process of training the network, the chart presented below should be obtained, the interpretation of these curves informs about the effect of the training method or about the selection of appropriate training data. The best results during training are achieved when the accuracy value tends closest to 1. After the process of training the network, the chart presented below should be obtained, the interpretation of these curves informs about the effect of the training method or about the selection of appropriate training data. It is important that the network is well trained, not overtrained, and that the data is matched to the model created.

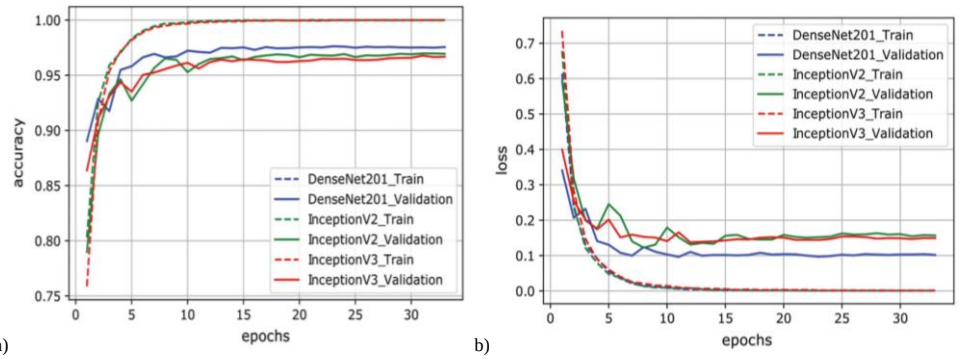

a) b)

Fig. 3. Evolution of a) accuracy and b) loss of the training and validation [43]

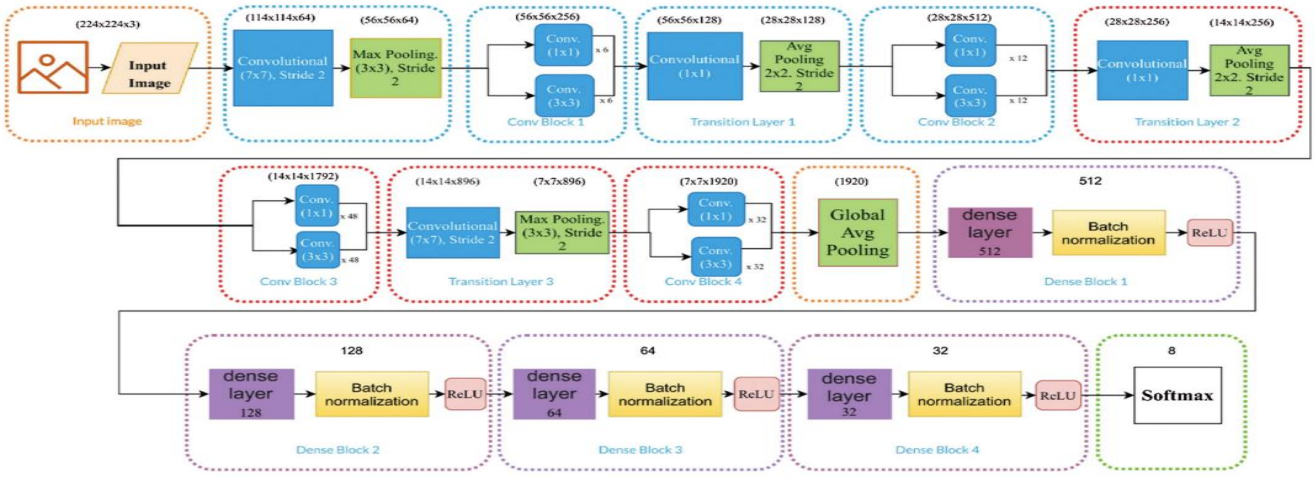

Fig. 2. DenseNet-201 model optimization [43]

The process of learning very large networks can be extremely time-consuming. An element that has a huge impact on the speed of learning is the appropriate the optimizer selection The optimizer is one of the essential elements of network models [1, 37]. Its task is to determine the course of network training. The loss function (which is a value minimized in the training process), it acts as a measure of the success of the task performed. Its task is to compare the results of network predictions with target labels. Based on them, he calculates the value of the loss. The optimizer uses them when modifying network weights, modifies networks based on the loss function. In [15] experiments were carried out to compare the results of the optimizers used and the linear rate (LR). Figure 4 shows the result for training and validation accuracy. Choosing the right LR value is not an easy task, which is why their values were analyzed. Adadelta, Adam, different LR scheduler schemes, Cyclical Learning Rates (CyLR) were studied. The most commonly used optimizers are momentum optimization, Nesterov algorithm, AdaGrad, RMSProp, Adam algorithm.

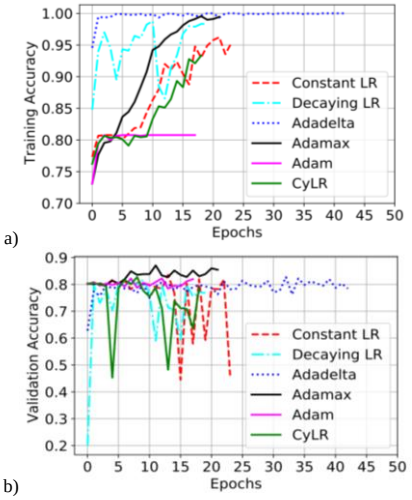

Fig. 4. The results for used optimizers and learning rate for: a) training accuracy, b) validation accuracy [15]

3. Lesions classification process

The emergence of new models of deep neural networks has increased interest in automated diagnostic processes for many diseases. Also the object of interest became the skin and skin birthmarks on it. Work on multi-class classification began to 3 classes, then expanding algorithms and increasing the computational capabilities of the created classification by 3, 5, 7 [7] and even 10 different classes. Classification can be based on a set of data divided into several classes. Deep neural networks allow you to diagnose even several skin diseases at the same time It all depends on how many samples we have. Extensive systems use images of different birthmarks, each of the diseases is marked as a class. The review of the multiclass classification was carried out in many works [2, 4, 21, 36, 38, 47]. Table 1 presents a list of works that achieved a high ACC score for the classification of skin birthmarks based on CNN. Many tools were used in the works, e.g. Generative Adversarial Network, fine-grained classification, augmenting labeled images, Combining Global–Local model. Combining them with a well-chosen network model and a representative database allowed to obtain high AUC values.

Over the years, scientists have focused on developing an algorithm to classify as many skin diseases as possible. [26] diagnosed 3 disease classes (SK, melanoma, and nevus) based on a database containing (training set) 2,000 and (test set) 150 images. The classification results are 76% sensitivity, 85% specificity and AUC 0.87. Of course, using as many images as possible also gives you more success. This was proven in [29] using more than 11,000 biopsyverified images to classify five (AK, intraepithelial carci-noma, benign keratosis, melanocytic nevi, and melanoma) and achieving a score of AUC = 0.96.

Table 1. Results for the segmentation and classification CNN's models in 2020 [38]

Study	Used model	Main details	Accuracy
[35]	ResNet50 GANs	data augmentation technique based on Generative Adversarial Network (GAN) ISIC 2018	95.2%
[45]	DC-MobileNetV1 DC-DenseNet121	Lightweight recognition model, discriminates features guided by fine-grained classification ISBI 2016	96%
[39]	MobileNet, VGG16 Custom model	classification augmenting labeled images, extracting features PH2	97.25%
[46]	LBP Resnet-50 DenseNet-121	Global–Local model, tailor-made features and deep Conv-features ISIC-2017	84.8 % for MM 91.3 % for SK
[3]	Inception-ResNet-v2	binary classification (benign and melanoma cases), integrated deep learning-based CAD system ISIC 2016	81.79%

Table 2. Results for the best algorithms in [42] for seven classes

Disease categories	Sensitivity	Specificity	Negative predictive value	Positive predictive value
Actinic keratoses and Bowen's disease	90.7%	98.5%	99.7%	62.9%
Basal cell carcinoma	88.4%	98.4%	99.2%	78.5%
Benign keratinocytic lesions	83.8%	98.3%	97.2%	89.3%
Dermatofibroma	81.8%	99.3%	99.5%	78.3%
Melanoma	81.9%	96.2%	97.6%	73.6%
Melanocytic nevus	91.6%	94.2%	88.3%	96.0%
Vascular lesions	89.2%	99.5%	99.7%	82.5%

The [7] MobileNet model was used based on multiple dermatosp images, and they were classified into seven selected classes, and the highest AUC score was over 0.95. Comparing the effects of different network models is one of the main activities of researchers. Classification also into 7 classes (actinic keratoses and Bowen's disease, basal cell carcinoma, benign keratinocytic lesions, dermatofibroma; melanoma; melanocytic nevi, vascular lesions were made in [32]. The paper compared the results of 139 models that were designed by 77 different teams. Table 2 shows the best results achieved for three algorithms when classifying seven different skin diseases diagnosed on images of skin lesions. The paper [42] analyzed the effectiveness of not only deep network models, but also doctors. An analysis was made for thirty selected dermatoscopic images, much better diagnostic results were achieved by selected neural networks than average human reader or even expert readers. The right number of diagnosed dermatoscopic images allows you to evaluate as many as 8 different classes [43].

In [14], the largest number of classes was diagnosed – 10disease (ne-vus, angio-ma/angiokeratoma, seborrheic keratosis, dermatofi-broma, solar lentigo, actinic keratoses, Bowen's disease, mela-noma, basal cell carcinoma and squamous cell carcinoma) based on imaging data from multiple databases. The degree of malignancy of lesions from begin to more malignat diseases was also estimated. The highest scores achieved were 95.0% sensitivity and 80.4% specificity for benign versus malignant. The process of network learning primarily takes place in the hidden network layer. Here, first of all, linear and nonlinear dependencies are sought. There can be multiple hidden layers. The more hidden layers a network has, the deeper dependencies it can find.

4. Testing networks

An appropriate dataset is also prepared for the network testing process. To assess the performance of classifiers, measures of the quality of the classifications carried out are used [12]. Performance metrics are used to assess effectiveness, one of which is the confusion matrix, where prediction results for individual classes are given. Figure 5 shows the confusion matrix it is characterized by the number of cases diagnosed as positive

and negative cases based on the real and predicted class. In the case considered in figure 5, the classification included seven classes with the highest probability of being diagnosed correctly with melanoma (class MEL).

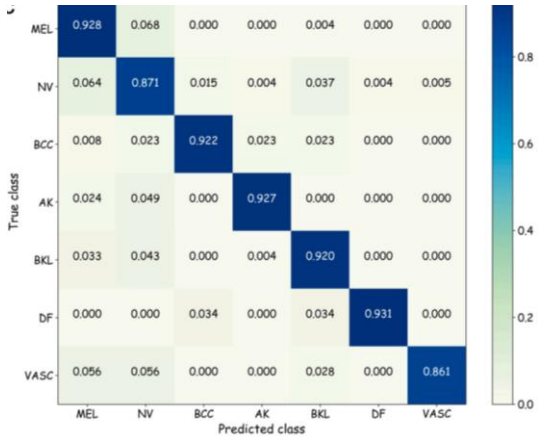

Fig. 5. Confusion matrices on seven skin lesion classes in ISIC-18 [19]

The ROC (Receiver Operating Characteristic Curve) shown in figure 6 is built by sensitivity and specificity values. It is used to compare the effectiveness of different types of classifiers. The area under the curve describes the effectiveness of the classifier, which can take values in the range of 0-1. The closer the curve is to the left right corner of the chart, the larger the field below the graph and the higher the classifier's performance. The ROC curves shown in Figure 6 are an example from the results of the studies presented in [19]. They confirm the high efficiency of the model for the DF class (area = 0.997). For the remaining classes, the area under the ROC curve is smaller and varies in the range of 0.984÷0.996. The lowest area under the curve has an NV class of 0.978.

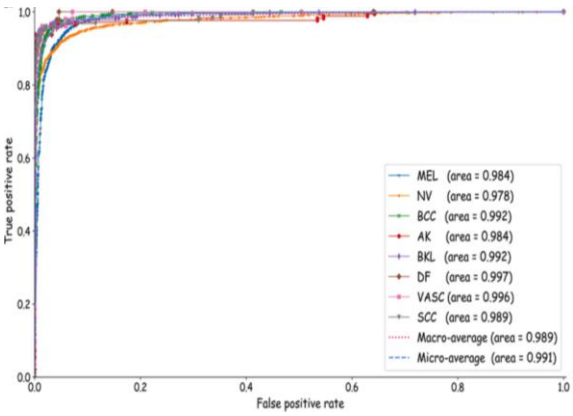

Fig. 6. ROC curves on the test sets foreight skin lesion classes in ISIC-19 MEL – Melanoma, NV – Melanocytic nervi, BCC – Basal cell Carcinoma, AK – Actinic Keratoses, BKL – Benign Keratosis, DF – Dermatofibrom, VASC – Vascular skin lesions, SCC – Squamous cell carcinoma [19]

A very important parameter is sensitivity (True Positive Rate, TPR) is defined as the ratio of true positive (TP) results to the sum of true positive (TP) and false negative (FN). Sensitivity of 100% means that all changes of character for the state of the disease have been recognized. Table 3 provides a list of selected works in which the most frequently mentioned parameters determined during network testing are determined. Among them are: precision, specificity, accuracy, F1 score, AUROC of proposed DCNN models. [6, 19] compiles a comparison of selected available works carried out in recent years. Examples of values obtained in [3, 7, 19, 24, 37, 41] are shown in table 3.

Increasing the number of classes also affects the F1-score value, as shown in figure 7. F1-score achieved a higher score for 2 classes than for 3. The highest score was achieved by the Inception-ResNet-v2 model with an F1-score of 83% for 2 classes. A larger number of classes is associated with more images, which significantly complicate the operation of the network model. For seven classes, the ResNet-50 network achieved the highest score than for 2 classes.

Table 3. Results of comparative methods [19]

Study	Precision	Sensivity	Specificity	Accuracy	F1 score	AUROC
[37]	91.3%	89.9%	92.2%	89.9%	90.0%	0.890
[7]	89.0%	83.0%	-	83.2%	83.0%	-
[41]	-	-	92%	85.3%	-	-
[24]	-	87.3%	82.2%	87.7%	-	0.914
[19]	90.5%	88.8%	95.7%	88.8%	89.1%	0.989
[3]		81.8%	71.4%	81.79%	82.6%	

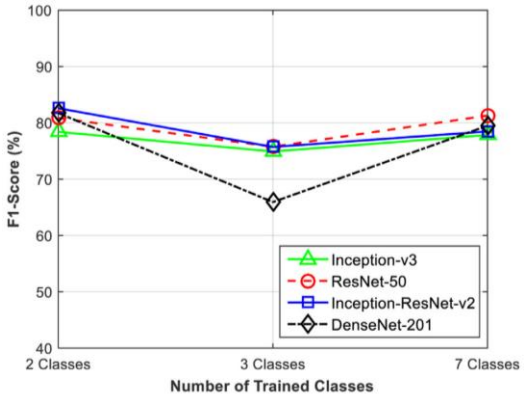

Fig. 7. F1-score values for training classes on different classification [3]

5. Discussion and conclusions

The examples of research listed in the article give a cross-section of the networks used for multi-class classification. They turned out to be the best solutions to the diagnostic tasks set – the classification of skin lesions. The classification concerned images of skin lesions, regardless of the form of the data set and the set of features. Of course, the teaching and test data for each of the works differ. Differences may result from the different number of sets and classes or the set of characteristic features itself. Where there are many available networks, types and methods of classification, it is important to compare the results obtained for a wider spectrum of available methods. The use of more methods in research allows you to be sure that the right choice of method has been made. The obtained results allowed to select the most effective sets of features for the construction of classification models.

Analysis of the results of network training allows you to assess the impact of the abundance of the set and selected dermatoscopic images. The use of a larger data set resulted in high accuracy for these networks. The size of the data set has a significant impact on the accuracy of traditional and deep learning models. The analysis of the results of network testing on smaller data sets presented allows us to conclude that the high results obtained during training were possible thanks to the use of models that were previously trained on a large data set (transfer learning). When testing databases, most often researchers use models VGG16, VGG19, ResNet50, DenseNet201. They also achieve high results during training.

Models built with the use of color images offer the highest classification efficiency, color images have the highest informational load capacity. The data corresponding to images of skin lesions are complex and difficult to classify. The included notes and observations can be helpful in solving other binary and multiclass classification tasks as well. With the continuous development of available models of deep networks and available methods of classification, more and more work will be created on this topic. The resulting research will contribute in the future to increasing the diagnostic effectiveness of skin diseases.

References

[1] Aburaed N., Panthakkan A., Al-Saad M., Amin S. A., Mansoor W.: Deep convolutional neural network (DCNN) for skin cancer classification. Proceedings of the 2020 27th IEEE International Conference on Electronics, Circuits and Systems (ICECS), 2020, 1–4.

[2] Adegun A., Viriri S.: Deep learning techniques for skin lesion analysis and melanoma cancer detection: a survey of state of the art. Artif Intell Rev 54, 2021, 811–841.

[3] Al-masni M. A., Kim D., Kim T.: Multiple skin lesions diagnostics via integrated deep convolutional networks for segmentation and classification. Computer methods and programs in biomedicine 190, 2020, 105351.

[4] Barata C., Celebi M., Marques J.: A survey of feature extraction in dermoscopy image analysis of skin cancer. IEEE Journal of Biomedical and Health Informatics 23(3), 2019, 1096–1109.

[5] Brinker T. J., Hekler A., Enk A. H., Klode J., Hauschild A., Berking C.: Deep learning outperformed 136 of 157 dermatologists in a head-to-head der moscopic melanoma image classification task. Eur J Cancer 113, 2019, 47–54.

[6] Cassidy B., Kendrick C., Brodzicki A., Jaworek-Korjakowska J., Yap M.: Analysis of the ISIC image datasets: usage, benchmarks and recommendations. Medical Image Analysis 75, 2022, 102305 [http://doi.org/10.1016/j.media.2021.102305].

[7] Chaturvedi S. S., Gupta K., Prasad P. S.: Skin Lesion Analyser: An Efficient Seven-Way Multi-class Skin Cancer Classification Using MobileNet. Advances in Intelligent Systems and Computing 1141, Springer, Singapore, 2020 [http://doi.org/10.1007/978-981-15-3383-9_15].

[8] Codella N. C. F., Nguyen B., Pankanti S., Gutman D., Helba B., Halpern A., Smith J. R.: Deep learning ensembles for melanoma recognition in dermoscopy images. IBM Journal of Research and Development 61(4/5), 173, 2017.

[9] Dermofit Image Library https://licensing.edinburghinnovations.ed.ac.uk/i/software/dermofit-imagelibrary.html?item=dermofit-image-library (04.01.2021).

[10] Ge Y., Li B., Zhao Y., Guan E., Yan W.: Melanoma segmentation and classification in clinical images using deep learning. ICMLC 2018: Proceedings of the 2018 10th International Conference on Machine Learning and Computing, 2018, 252–256.

[11] Ge Z., Demyanov S., Chakravorty R., Bowling A., Garnavi R.: Skin disease recognition using deep saliency features and multimodal learning of dermoscopy and clinical images. Descoteaux M., Maier-Hein L., Franz A., Jannin P., Collins D. L., Duchesne S. (eds.), Springer, Cham LNCS 10435, 2017, 250–258.

[12] Gessert N., Sentker T., Madesta F. et al.: Skin lesion classification using CNNs with patch-based attention and diagnosis-guided loss weighting. IEEE Trans. Biomed. Eng. 67, 2019, 495–503 [http://doi.org/10.1109/TBME.2019.2915839].

[13] Haenssle H. A., Fink C., Schneiderbauer R., Toberer F., Buhl T., Blum A.: Man against machine: diagnostic performance of a deep learning convolutional neural network for dermoscopic melanoma recognition in comparison to 58 dermatologists. Ann Oncol 29, 2018, 1836–1342.

[14] Haenssle H. A., Fink C., Toberer F. et al.: Man against machine reloaded: performance of a market-approved convolutional neural network in classifying a broad spectrum of skin lesions in comparison with 96 dermato-logists working under less artificial conditions. Ann Oncol 31, 2020, 137–143.

[15] Hasan M. M., Elahi M., Alam M. A.: DermoExpert: Skin lesion classification using a hybrid convolutional neural network through segmentation, transfer learning, and augmentation. medRxiv, 2021. [http://doi.org/10.1101/2021.02.02.21251038].

[16] Hekler A., Utikal J. S., Enk A. H., Solass W., Schmitt M., Klode J.: Deep learning outperformed 11 pathologists in the classification of histopathological melanoma images. Eur J Cancer 118, 2019, 91–96.

[17] Howard A. G., Zhu M., Chen B., Kalenichenko D., Wang W., Weyand T., Andreetto M. Hartwig A.: MobileNets: Efficient convolutional neural networks for mobile vision applications. Computer Science, Computer Vision and Pattern Recognitionar, Xiv:1704.04861v1 [http://doi.org/10.48550/arXiv.1704.04861].

[18] Huang G., Liu Z., Maaten L., Weinberger K.: Densely Connected Convolutional Networks. Computer Vision and Pattern Recognition arXiv:1608.06993v5. [http://doi.org/10.48550/arXiv.1608.06993].

[19] Iqbal I., Younus M., Walayat K., Ullah Kakar M., Ma J.: Automated multi-class classification of skin lesions through deep convolutional neural network with dermoscopic images. Computerized Medical Imaging and Graphics 88, 2021, 101843 [http://doi.org/10.1016/j.compmedimag.2020.101843].

[20] ISIC Archive https://www.isic-archive.com/#!/topWithHeader/onlyHeaderTop/gallery (23.03.2022).

[21] Kareem O. S., Abdulazee A. M., Zeebaree D. Q.: Skin lesions classification using deep learning techniques: Review. Asian Journal of Research in Computer Science 9(1), 2021, AJRCOS.68652, 1–22.

[22] Lopez A. R., Giro-i-Nieto X., Burdick J., Marques O.: Skin lesion classification from dermatoscopic images using deep learning techniques. Conference Paper 2017 [http://doi.org/JO.23J6/P.20l7.852-053].

[23] Maglogiannis I., Doukas C. N.: Overview of advanced computer vision systems for skin lesions characterization. IEEE transactions on information technology in biomedicine 13(5), 2009, 721–733.

[24] Mahbod A., Schaefe G., Ellinger, I., Ecker R., Pitiot A., Wang C.: Fusing fine tuned deep features for skin lesion classification. Comput. Med. Imaging Graph. 71, 2019, 19–29 [http://doi.org/10.1016/j.compmedimag.2018.10.007].

[25] Majumder S., Ahsan Ullah M.: Feature extraction from dermoscopy images for an effective diagnosis of melanoma skin cancer. 10th International Conference on Electrical and Computer Engineering Bangladesh, 2018, 185–188.

[26] Marchetti M. A., Liopyris K., Dusza S. W. et al.: Computer algorithms show potential for improving dermatologists' accuracy to diagnose cutaneous melanoma: results of the international skin imaging collaboration 2017. J Am Acad Dermatol 82, 2020, 622–627.

[27] Marchetti M. A., Codella N. C., Dusza S. W. et al.: Results of the 2016 international skin imaging collaboration international symposium on biomedical imaging challenge: comparison of the accuracy of computer algorithms to dermatologists for the diagnosis of melanoma from dermoscopic images. J Am Acad Dermatol 78, 2018, 270–277.

[28] Marchetti M. A., Liopyris K., Dusza S. W., Codella N. C. F., Gutman D. A., Helba B.: Computer algorithms show potential for improving dermatologists' accuracy to diagnose cutaneous melanoma: results of the international skin imaging collaboration 2017. J Am Acad Dermatol 82, 2020, 622–627.

[29] Maron R. C., Weichenthal M., Utikal J. S., Hekler A., Berking C., Hauschild A.: Systematic outperformance of 112 dermatologists in multiclass skin cancer image classification by convolutional neural networks. Eur J Cancer 119, 2019, 57–65.

[30] MED-NODE Dataset http://www.cs.rug.nl/~imaging/databases/melanoma_naevi/ (23.03.2022).

[31] Nida N., Irtaza A., Javed A., Yousaf M., Mahmood M.: Melanoma lesion detection and segmentation using deep region based convolutional neural network and fuzzy C-means clustering. International Journal of Medical Informatics 124, 2019, 37–48.

[32] PAD-UFES-20 Dataset https://data.mendeley.com/datasets/zr7vgbcyr2/1 (23.03.2022)

[33] Panja A., Jackson J. Ch., Quadir Md. A.: An approach to skin cancer detection using keras and tensorflow. Journal of Physics: Conference Series 1911, 2021, 012032 [http://doi.org/10.1088/1742-6596/1911/1/012032].

[34] PH2 Dataset, https://www.fc.up.pt/addi/ph2%20database.html (23.03.2022).

[35] Qin Z., Liu Z., Zhu P., Xue Y.: A GAN-based image synthesis method for skin lesion classification. Computer Methods and Programs in Biomedicine, 2020, 105568.

[36] Raza R., Zulfiqar F., Tariq S., Anwar G. B., Sargano A. B., Habib Z.: Melanoma classification from dermoscopy images using ensemble of convolutional neural networks. Mathematics 10(1), 2022, 26.

[37] Rebouças Filho P. P., Peixoto S. A., Medeiros da Nobrega R. V., Hemanth D. J., Medeiros A. G., Sangaiah A. K., de Albuquerque V. H. C.: Automatic histologically-closer classification of skin lesions. Comput. Med. Imaging Graph. 68, 2018, 40–54 [http://doi.org/10.1016/j.compmedimag.2018.05.004].

[38] Saeed J., Zeebaree S.: Skin lesion classification based on deep convolutional neural networks architectures. JASTT 2(01), 2021, 41–51.

[39] Salian A. C., Vaze S., Singh P., Shaikh G. N., Chapaneri S., Dayaswal D.: Skin lesion classification using deep learning architectures. 2020 3rd International Conference on Communication System, Computing and IT Applications (CSCITA) IEEE, 2020, 168–173.

[40] Sandler M., Howard A., Zhu M., Zhmoginov A., Chen L. C.: MobileNetV2: Inverted Residuals and Linear Bottlenecks. The IEEE Conference on Computer Vision and Pattern Recognition (CVPR), 2018, 4510–4520.

[41] Srinivasu P. N., SivaSai J. G., Ijaz M. F., Bhoi A. K., Kim W., Kang J. J: Classification of skin disease using deep learning neural networks with MobileNet V2 and LSTM. Sensors 21, 2852, 2021.

[42] Tschandl P., Codella N., Akay B. N. et al.: Comparison of the accuracy of human readers versus machine-learning algorithms for pigmented skin lesion classification: an open, webbased, international, diagnostic study. Lancet Oncol 2019b(20), 2019, 938-947.

[43] Villa-Pulgarin J., Ruales-Torres A., Arias-Garzón D. et al.: Optimized Convolutional Neural Network Models for Skin Lesion Classification. Computers, Materials & Continua Tech Science Press, CMC 70(2), 2022, 2131–2148.

[44] Wang Y., Cai J., Louie D., Wang J., Lee T.: Incorporating clinical knowledge with constrained classifier chain into a multimodal deep network for melanoma detection. Computers in Biology and Medicine 137, 2021, 104812.

[45] Wei L., Ding K., Hu H.: Automatic Skin Cancer Detection in Dermoscopy Images based on Ensemble Lightweight Deep Learning Network. IEEE Access 8, 2020, 99633–99647.

[46] Xiao F., Wu Q. Visual saliency based global–local feature representation for skin cancer classification. IET Image Processing 14(10), 2020, 2140–2148.

[47] Young A. T., Xiong M., Pfau J., Keiser M. J, Wei M. L.: Artificial intelligence in dermatology: A Primer. Journal of Investigative Dermatology 140, 2020, 1504–1512.

[48] Yu L., Chen H., Dou Q., Qin J., Heng P. A.: Automated melanoma recognition in dermoscopy images via very deep residual networks. IEEE Trans. Med. Imaging 36(4), 2017, 994–1004.

[49] Zakład Epidemiologii i Prewencji Nowotworów Centrum Onkologii – Instytut w Warszawie. Krajowy Rejestr Nowotworów (KRN) http://onkologia.org.pl/ (02.08.2019).

[50] Zhang J., Xie Y., Wu Q., Xia Y.: Skin lesion classification in dermoscopy images using synergic deep learning. Springer Nature Switzerland. LNCS 11071, 2018, 12–20.

M.Sc. Magdalena Michalska-Ciekańska
e-mail: magdalena.michalska@pollub.edu.pl

Ph.D. student at Department of Electronics and Information Technology, Lublin University of Technology. Recent graduate Warsaw University of Technology The Faculty Electronics and Information Technology. Her research interests include medical image processing, optoelectronics, spectrophotometry.

http://orcid.org/0000-0002-0874-3285

http://doi.org/10.35784/iapgos.2947 *received: 08.05.2022 | revised: 08.06.2022 | accepted: 15.06.2022 | available online: 30.06.2022*

THE SYNTHESIS OF MATHEMATICAL MODELS OF NONLINEAR DYNAMIC SYSTEMS USING VOLTERRA INTEGRAL EQUATION

Borys I. Mokin[1], Vitalii B. Mokin[1], Oleksandr B. Mokin[1], Orken Mamyrbaev[2], Saule Smailova[3]
[1]Vinnytsia National Technical University, Faculty of Intelligent Information Technologies and Automation, Vinnytsia, Ukraine, [2]Al Farabi Kazakh National University, Institute of Information and Computer Technologies, Almaty, Kazakhstan, [3]D. Serikbayev East Kazakhstan Technical University, Ust-Kamenogorsk, Kazakhstan

Abstract. *The problem of creating mathematical models of nonlinear dynamical systems does not have an unambiguous solution and requires the creation of a separate synthesis method for each such object. To develop a method for synthesizing mathematical models of an extensive class of nonlinear dynamical systems with polynomial nonlinearities. The work uses a method based on the solution of the Volterra integral equation in the ideology set forth in Van Trees H.L., according to which the structure of a nonlinear dynamical object present47s a series connection of the linear part, characterizing the inertial properties of the system, and the nonlinear element, given by static characteristic. The difference of the suggested version of the method from the classical one, proposed in the works of Van Trees H.L., is an expansion of their input and output signals into Fourier series and a representation of the inertial part of these systems by their Bode plots, connected into one structure with input and output signals and non-linearity by Volterra integral equation. The algorithm of the proposed method is disclosed by the example of solving the problem of identifying a nonlinear dynamical system which impulse response of the inertial part satisfies the separability requirement, the order of the polynomial nonlinearity is three, and the model of the input signal has the form of a sinusoid "raised" over the time axis on a priori given constant level. A computational experiment was carried out on the example of nonlinear dynamical systems with the third order of the nonlinear characteristic and the first and second orders of the model of the inertial part of these systems with the specified algorithms of their parametric identification. The suggested method allows to synthesis the mathematical model of a nonlinear dynamical system with the polynomial static characteristic to the case when the input signal has an arbitrary number of harmonics, and the model of the inertial part and the nonlinear polynomial function have an arbitrary order.*

Keywords: nonlinear dynamical system, mathematical model, polynomial nonlinearity function, Bode plot, Fourier series, Volterra integral equation

SYNTEZA MATEMATYCZNYCH MODELI NIELINIOWYCH UKŁADÓW DYNAMICZNYCH Z WYKORZYSTANIEM RÓWNANIA CAŁKOWEGO VOLTERRY

Streszczenie. *Problem tworzenia modeli matematycznych nieliniowych układów dynamicznych nie ma jednoznacznego rozwiązania i wymaga stworzenia odrębnej metody syntezy dla każdego takiego obiektu. Celem pracy jest opracowanie metody syntezy modeli matematycznych rozległej klasy nieliniowych układów dynamicznych o wielomianowej nieliniowości. W pracy zastosowano metodę opartą na rozwiązaniu całkowego równania Volterry w ideologii przedstawionej przez Van Trees H.L., zgodnie z którą struktura nieliniowego obiektu dynamicznego przedstawia szeregowe połączenie części liniowej, charakteryzującej własności inercyjne układu, oraz elementu nieliniowego, zadanego charakterystyką statyczną. Różnica proponowanej wersji metody od klasycznej, zaproponowanej w pracach Van Treesa H.L., polega na rozwinięciu sygnałów wejściowych i wyjściowych w szeregi Fouriera oraz przedstawieniu części inercyjnej tych układów za pomocą ich charakterystyk Bodego, połączonych w jedną strukturę z sygnałami wejściowymi i wyjściowymi oraz nieliniowością za pomocą całkowego równania Volterry. Algorytm proponowanej metody ujawniono na przykładzie rozwiązania problemu identyfikacji nieliniowego układu dynamicznego, którego odpowiedź impulsowa części inercyjnej spełnia warunek rozdzielności, rząd nieliniowości wielomianowej jest trzeci, a model sygnału wejściowego ma postać sinusoidy "uniesionej" nad osią czasu na zadanym z góry stałym poziomie. Przeprowadzono eksperyment obliczeniowy na przykładzie nieliniowych układów dynamicznych o trzecim rzędzie charakterystyki nieliniowej oraz pierwszego i drugiego rzędu modelu części inercyjnej tych układów z zadanymi algorytmami ich identyfikacji parametrycznej. Zaproponowana metoda pozwala na syntezę modelu matematycznego nieliniowego układu dynamicznego o wielomianowej charakterystyce statycznej dla przypadku, gdy sygnał wejściowy ma dowolną liczbę harmonicznych, a model części inercyjnej i nieliniowa funkcja wielomianowa mają dowolny rząd.*

Słowa kluczowe: nieliniowy układ dynamiczny, model matematyczny, wielomianowa funkcja nieliniowości, charakterystyki Bodego, szereg Fouriera, równanie całkowe Volterry

Introduction

The purpose of this paper is the synthesis of a wide class of mathematical models of nonlinear dynamic systems with polynomial nonlinearities. And the movement toward this purpose we start with the observation that the problem of constructing mathematical models of nonlinear dynamic systems does not have a unique solution and requires to create a separate synthetic procedure for each object. The majority of these methods, are presented in a review papers [6, 16, 17], which states that the most efficient methods, based on various options for solving Volterra integral equation ideology laid down in the [18], following which, the nonlinear dynamic object structure shall be formed as a serial connection of the line part that characterizes the inertial properties of the system, and nonlinear section, set by nonlinear static characteristic.

One of the authors started to research the possibilities for practical application of the ideas suggested in [18] at the beginning of the 80-th of the last century, suggesting in the work [9] a recovery method for the input signals of the measuring systems with non-linear polynomial function of conversion with the presentation of these systems by frequency characteristics of inertial part as well as using the integral Volterra equation for their binding into one mathematical structure. The modified algorithm of this method was suggested in [8] for the simultaneous solution of the problem of input signals recovery in nonlinear dynamical systems, as well as the problem of synthesis of mathematical models of these systems.

With the decomposition into the Fourier series of the output signal of nonlinear dynamic systems and its presentation by the Fourier series with the unknown coefficients of its input signal, which are stipulated for by the computational algorithm of the suggested method, there appear the complex combinatorial relationships of the Fourier coefficients with the discrete values of the frequency characteristics of inertial part of these systems. The work [12] suggests an algorithm for automatic determination of combinatorial relationships that made this method available for synthesis of mathematical models of signals and systems for practical application.

But despite the automated search for combinatorial links, the suggested algorithm was too complicated and did not find a wide application. This encouraged the authors to find the simplified options for the method, one of which was suggested in [11], a distinctive characteristics of which is the fact that it uses only the first harmonica of the whole Fourier series, which present the input signal of nonlinear dynamic system, and to receive the frequency characteristics of the inertial part of this nonlinear system it uses a special algorithm for processing a segment of the system response to an input signal, described by a stepped unit function.

The work, presented below, we suggest a modified version of the method for synthesis of mathematical models of nonlinear dynamic systems suggested in the [11], the implementation of which does not require an additional experiment on determining the frequency characteristics of inertial nonlinear dynamic system, neither it needs the use of a special algorithm for processing

the response of the system to the input signal in the form of a single stepped function.

1. Formulation of the problem

The withdrawal of the design ratio for method of synthesis of mathematical models of nonlinear dynamic systems as the initial conditions of the method, as well as in [8, 9, 11], there had been taken first the condition set in the [18], stating that the nonlinear dynamic system under consideration may be presented as a serial connection of the two structural units, as shown in Fig. 1, where one of the links characterizes the inertial properties and is described by impulse response g(t), and the second, the inertia-free one characterizes the nonlinear properties, connecting its input with the output Z of an ordered polynomial:

$$Z = f_k(y) = \nu_1 y + \nu_2 y^2 + \cdots + \nu_k y^k \tag{1}$$

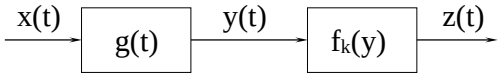

Fig. 1. Block diagram of a nonlinear dynamical system

This precondition, as shown even in the same work [18], allow to bind an input signal $x(t)$ of the system with the output $z(t)$ Volterra integral equation

$$z(t) = \sum_{i=1}^{k} \nu_i \cdot \int_{-\infty}^{\infty} \cdots \int_{-\infty}^{i} x(t-\tau_1)\ldots x(t-\tau_i) \times g(\tau_1,\ldots,\tau_i)\, d\tau_1 \ldots d\tau_i \tag{2}$$

The other initial precondition is the possibility for presenting signals $x(t)$, $z(t)$ by the truncated Fourier series –

$$x(t) = \sum_{n=-N}^{N} c_n \cdot e^{jn\omega_1 t} \tag{3}$$

$$z(t) = \sum_{n=-M}^{M} q_n \cdot e^{jn\omega_1 t} \tag{4}$$

where

$$\omega_1 = \frac{2\pi}{T} \tag{5}$$

is the frequency of the first harmonica, T is its period, and

$$c_n = \frac{1}{T}\int_0^T x(t)\cdot e^{-jn\omega_1 t}\, dt \tag{6}$$

$$q_n = \frac{1}{T}\int_0^T z(t)\cdot e^{-jn\omega_1 t}\, dt \tag{7}$$

are the Fourier coefficients of function $x(t)$ and $z(t)$.

As a result, we obtain algorithms for the synthesis of functions $g(t)$, $f_k(t)$.

As we have already noted, the problem of constructing mathematical models of nonlinear dynamic systems does not have an unambiguous solution and requires the creation of a separate synthesis method for each such object. The majority of these methods, are presented in a review papers [6, 16, 17], which states that the most efficient methods, based on various options for solving Volterra integral equation ideology laid down in the [17], following which, the nonlinear dynamic object structure shall be formed as a serial connection of the line part that characterizes the inertial properties of the system, and nonlinear section, set by nonlinear static characteristic.

Primarily we must mention those methods, described in the works of [1, 2].

And the works to be mentioned after the publications of [6, 16, 17], are those issued by [3–5], in which the mathematical models of nonlinear dynamic systems are given in the form of transfer functions, algebraically structured in skew polynomials, as well as the works of [13–15], in which mathematical models of nonlinear dynamic systems set by transfer functions with coefficients which depend on the frequency and amplitude of the input periodic signals, shall be really reduced to the class of cybernetic models since their identification is carried out by iterative numerical methods in powerful software environment MATLAB.

2. Theoretical research

To receive the calculated ratios, suitable for qualitative analysis, we specify the number of members N of the series (3) and the value of the polynomial index k (1).

Let $N = 1$, a $k = 3$, i.e., let

$$x(t) = \sum_{n=-1}^{1} c_n \cdot e^{jn\omega_1 t} \tag{8}$$

$$Z = f_3(y) = \nu_1 y + \nu_2 y^2 + \nu_3 y^3 \tag{9}$$

Substituting expressions (8) and (9) in the integral equation (2), we receive:

$$\begin{aligned} z(t) = {} & \nu_1 \cdot \int_{-\infty}^{\infty} \sum_{n=-1}^{1} c_n \cdot e^{jn\omega_1 (t-\tau_1)} \cdot g(\tau_1)\, d\tau_1 + \\ & + \nu_2 \cdot \int_{-\infty}^{\infty}\int_{-\infty}^{\infty} \sum_{n=-1}^{1} c_n \cdot e^{jn\omega_1 (t-\tau_1)} \times \\ & \times \sum_{n=-1}^{1} c_n \cdot e^{jn\omega_1 (t-\tau_2)} \times g(\tau_1,\tau_2)\, d\tau_1\, d\tau_2 + \\ & + \nu_3 \cdot \int_{-\infty}^{\infty}\int_{-\infty}^{\infty}\int_{-\infty}^{\infty} \sum_{n=-1}^{1} c_n \cdot e^{jn\omega_1 (t-\tau_1)} \times \\ & \times \sum_{n=-1}^{1} c_n \cdot e^{jn\omega_1 (t-\tau_2)} \times \sum_{n=-1}^{1} c_n \cdot e^{jn\omega_1 (t-\tau_3)} \times \\ & \times g(\tau_1,\tau_2,\tau_3)\, d\tau_1\, d\tau_2\, d\tau_3 \end{aligned} \tag{10}$$

Let the impulse response $g(t)$, which, as is generally accepted, presents the response of the type

$$g(t) = \begin{cases} g(t) \text{ at } t \ge 0 \\ 0 \quad \text{at } t < 0 \end{cases} \tag{11}$$

of this dynamic system to the input signal as a Dirac delta function where

$$\delta(t) = \begin{cases} \infty \text{ at } t = 0 \\ 0 \text{ at } t \ne 0 \end{cases} \quad \int_{-\infty}^{\infty} \delta(t)dt = 1 \tag{12}$$

is separable, that is, let the condition come true for it

$$g(\tau_1,\tau_1,\ldots,\tau_k) = g(\tau_1)\cdot g(\tau_2)\cdots g(\tau_k) \tag{13}$$

For this case the equation (10) takes the form of

$$\begin{aligned} z(t) = {} & \nu_1 \cdot \sum_{n=-1}^{1} c_n \cdot e^{jn\omega_1 t} \int_{-\infty}^{\infty} g(\tau_1)\cdot e^{-jn\omega_1 \tau_1}\, d\tau_1 + \\ & + \nu_2 \cdot \left(\sum_{n=-1}^{1} c_n \cdot e^{jn\omega_1 t} \int_{-\infty}^{\infty} g(\tau_1)\cdot e^{-jn\omega_1 \tau_1}\, d\tau_1 \right) \times \\ & \times \left(\sum_{n=-1}^{1} c_n \cdot e^{jn\omega_1 t} \int_{-\infty}^{\infty} g(\tau_2)\cdot e^{-jn\omega_1 \tau_2}\, d\tau_2 \right) + \\ & + \nu_3 \cdot \left(\sum_{n=-1}^{1} c_n \cdot e^{jn\omega_1 t} \int_{-\infty}^{\infty} g(\tau_1)\cdot e^{-jn\omega_1 \tau_1}\, d\tau_1 \right) \times \\ & \times \left(\sum_{n=-1}^{1} c_n \cdot e^{jn\omega_1 t} \int_{-\infty}^{\infty} g(\tau_2)\cdot e^{-jn\omega_1 \tau_2}\, d\tau_2 \right) \times \\ & \times \left(\sum_{n=-1}^{1} c_n \cdot e^{jn\omega_1 t} \int_{-\infty}^{\infty} g(\tau_3)\cdot e^{-jn\omega_1 \tau_3}\, d\tau_3 \right) \end{aligned} \tag{14}$$

Please note that the integrals in equation (14) are the values of Bode magnitude and Bode phase plots (Bode plot) $W(j\omega)$ at the points $\omega = n\omega_1$, since, as is well known, the Bode plot $W(j\omega)$ is a Fourier transformation of impulse response $g(t)$, that is

$$W(j\omega)=\int_{-\infty}^{\infty} g(t)\cdot e^{-j\omega t}\,dt=\int_{0}^{\infty} g(t)e^{-j\omega t}dt \qquad (15)$$

In view of the above, the equation (14) may be rewritten as

$$\begin{aligned} z(t)=&\varphi_{-3}(\nu_3,c_{-1},W(-j\omega_1))\cdot e^{-j3\omega_1 t}+\\ &+\varphi_{-2}(\nu_3,\nu_2,c_{-1},c_0,W(-j\omega_1),W(0))\times e^{-j2\omega_1 t}+\\ &+\varphi_{-1}(\nu_3,\nu_2,\nu_1,c_{-1},c_0,c_1,W(-j\omega_1),W(0),W(j\omega_1))\times\\ &\times e^{-j\omega_1 t}+\\ &+\varphi_0(\nu_3,\nu_2,\nu_1,c_{-1},c_0,c_1,W(-j\omega_1),W(0),W(j\omega_1))+\\ &\varphi_1(\nu_1,\nu_2,\nu_3,c_{-1},c_0,c_1,W(-j\omega_1),W(0),W(j\omega_1))\times e^{j\omega_1 t}+\\ &+\varphi_2(\nu_2,\nu_3,c_0,c_1,W(0),W(j\omega_1))\cdot e^{j2\omega_1 t}+\\ &+\varphi_3(\nu_3,c_1,W(j\omega_1))\cdot e^{j3\omega_1 t} \end{aligned} \qquad (16)$$

The expression (16) shows that the signal $z(t)$, except for the first harmonica and constant component, stipulated for by the set in the form of a truncated series (8) signal $x(t)$, also contains the second and the third harmonics stipulated for by nonlinearity (9).

Therefore, with the realization of the output signal $z(t)$ on the interval T, we set it by the truncated Fourier series, which includes a constant component and the first three harmonics, i.e.

$$\begin{aligned} z(t)=&q_{-3}\cdot e^{-j3\omega_1 t}+q_{-2}\cdot e^{-j2\omega_1 t}+\\ &+q_{-1}\cdot e^{-j\omega_1 t}+q_0+q_1\cdot e^{j\omega_1 t}+\\ &+q_2\cdot e^{j2\omega_1 t}+q_3\cdot e^{j3\omega_1 t} \end{aligned} \qquad (17)$$

where q_n, $n=(-3,-2,-1,\ 0,\ 1,\ 2,\ 3)$ are the Fourier coefficients that shall be calculated by the formula (7).

Substituting the truncated series (17) in equation (16) instead of $z(t)$, will have an identity that is executed if and only if the coefficients of the same harmonics in the left and right parts of equations (16) considering (17) are the same, that is, when

$$\begin{cases} \varphi_{-3}(\nu_3,c_{-1},W(-j\omega_1))=q_{-3}\\ \varphi_{-2}(\nu_3,\nu_2,c_{-1},c_0,W(-j\omega_1),W(0))=q_{-2}\\ \varphi_{-1}(\nu_3,\nu_2,\nu_1,c_{-1},c_0,c_1,W(-j\omega_1),W(0),W(j\omega_1))=q_{-1}\\ \varphi_0(\nu_3,\nu_2,\nu_1,c_{-1},c_0,c_1,W(-j\omega_1),W(0),W(j\omega_1))=q_0\\ \varphi_1(\nu_1,\nu_2,\nu_3,c_{-1},c_0,c_1,W(-j\omega_1),W(0),W(j\omega_1))=q_1\\ \varphi_2(\nu_2,\nu_3,c_0,c_1,W(0),W(j\omega_1))=q_2\\ \varphi_3(\nu_3,c_1,W(j\omega_1))=q_3 \end{cases} \qquad (18)$$

Specifying the function $\varphi_{-3}(\cdot)$, $\varphi_{-2}(\cdot)$, $\varphi_{-1}(\cdot)$ $\varphi_0(\cdot)$, $\varphi_1(\cdot)$, $\varphi_2(\cdot)$, $\varphi_3(\cdot)$ by performing all algebraic operations on the right part of the expression (16), instead of the indefinite system of equations (18) we obtain the system of equations

$$\begin{cases} \nu_3\cdot c_{-1}^3\cdot W^3(-j\omega_1)=q_{-3}\\ \nu_2\cdot c_{-1}^2\cdot W^2(-j\omega_1)+3\cdot\nu_3\cdot c_{-1}^2\cdot c_0\times\\ \times W^2(-j\omega_1)\cdot W(0)=q_{-2}\\ \nu_1\cdot c_{-1}\cdot W(-j\omega_1)+2\cdot\nu_2\cdot c_{-1}\cdot c_0\times\\ \times W(-j\omega_1)\cdot W(0)+3\cdot\nu_3\cdot c_{-1}^2\cdot c_1\times\\ \times W^2(-j\omega_1)\cdot W(j\omega_1)+\\ +3\cdot\nu_3\cdot c_{-1}\cdot c_0^2\cdot W(-j\omega_1)\times W^2(0)=q_{-1}\\ \nu_1\cdot c_0\cdot W(0)+2\cdot\nu_2\cdot c_{-1}\cdot c_1\times\\ \times W(-j\omega_1)\cdot W(j\omega_1)+\nu_2\cdot c_0^2\times\\ \times W^2(0)+6\cdot\nu_3\cdot c_{-1}\cdot c_0\times\\ \times c_1\cdot W(-j\omega_1)\cdot W(0)\cdot W(j\omega_1)+\\ +\nu_3\cdot c_0^3\cdot W^3(0)=q_0\\ \nu_1\cdot c_1\cdot W(j\omega_1)+2\cdot\nu_2\cdot c_0\cdot c_1\times\\ \times W(0)\cdot W(j\omega_1)+3\cdot\nu_3\cdot c_{-1}\times\\ \times c_1^2\cdot W(-j\omega_1)\cdot W^2(j\omega_1)+\\ +3\cdot\nu_3\cdot c_0^2\cdot c_1\cdot W^2(0)\cdot W(j\omega_1)=q_1\\ \nu_2\cdot c_1^2\cdot W^2(j\omega_1)+3\cdot\nu_3\cdot c_0\times\\ \times c_1^2\cdot W(0)\cdot W^2(j\omega_1)=q_2\\ \nu_3\cdot c_1^3\cdot W^3(j\omega_1)=q_3 \end{cases} \qquad (19)$$

which may be used for making specific calculations as for the problem with identification of nonlinear characteristics $f_k(y)$ of the dynamic system, and for the problem of parameters identification of Bode plot $W(j\omega)$ its inertial component, the solution of which require the algorithms, which are to be built below.

We built an algorithm for solving the problem of identification of nonlinear dynamic system, the inertial impulse response $g(t)$ of which satisfies the condition of separability (13), the order polynomial nonlinearity $f_k(y)$ equals three, i.e., $k = 3$, and a model of the input signal $x(t)$ looks like a sinusoids with a frequency ω_1, "lifted" over the axis of time by a permanent component, c_0, i.e., has the form of (20). We generalize the results for the case when the nonlinearity has a random order, i.e., is approximated by a polynomial function (1), and the input signal contains a random number of harmonic components, i.e. is approximated by a cut-off Fourier series (3).

From the expressions (1)-(3), (10), (13), (14) for the above formulated conditions we will have

$$z(t)=\sum_{i=1}^{k}\nu_i\left(\sum_{n=-N}^{N}c_n W(jn\omega_1)e^{n\omega_1 t}\right)^i \qquad (20)$$

It is easy to see that from the expression (20), setting $k = 3$, $N = 1$, we get the expression (16), which in turn during decomposition in cut Fourier series (17), we obtain the system of equations (19). In the case of random order of polynomial inequality, which equals k, this system will have $2k+1$ equations (as for the number of coefficients of Fourier truncated series, in which the output signal $z(t)$ will be decomposed to receive the harmonic identity with the right-hand side of equation (20)).

But if the expressions (20) are fair then there appears a question: "Is it possible to transform them in a way that they remain equitable on condition that the impulse response of dynamic system contains multiple exponential components which number, as we know from the theory of linear differential equations equals the order of differential equation, which describes the process in this dynamic system?"

Further, based on our work [10], we show that the answer to this question is positive.

Let the impulse response of the inertial part of nonlinear dynamical system can be represented as

$$g(t) = g_1(t) + g_2(t) \tag{21}$$

where both components are exhibitors that differ only by the index of power and coefficients, by which these exponentials are multiplied.

Substituting expression (21) in the expression (2), we get

$$\begin{aligned} z(t) &= \sum_{i=1}^{k} \nu_i \int_{-\infty}^{\infty} \bullet\bullet^{i} \bullet\bullet \int_{-\infty}^{\infty} x(t-\tau_1)...x(t-\tau_i) \times \\ &\times [g_1(\tau_1,...,\tau_i) + g_2(\tau_1,...,\tau_i)] d\tau_1...d\tau_i = \\ &= \sum_{i=1}^{k} \nu_i [\int_{-\infty}^{\infty} \bullet\bullet^{i} \bullet\bullet \int_{-\infty}^{\infty} x(t-\tau_1)...x(t-\tau_i) \times \\ &\times g_1(\tau_1,...,\tau_i) d\tau_1...d\tau_i + \\ &+ \int_{-\infty}^{\infty} \bullet\bullet^{i} \bullet\bullet \int_{-\infty}^{\infty} x(t-\tau_1)...x(t-\tau_i) \times \\ &\times g_2(\tau_1,...,\tau_i) d\tau_1...d\tau_i] \end{aligned} \tag{22}$$

Assuming that each component of the expression (28) holds the identity (13) – and if each component is exponential, then this identity, as we have mentioned above is always performed – and according to the execution of the property (11) for each component, we can present the expression (29) in the form of

$$\begin{aligned} z(t) &= \sum_{i=1}^{k} \nu_i [\left(\int_{0}^{\infty} x(t-\tau) g_1(\tau) d\tau \right)^{i} + \\ &+ \left(\int_{0}^{\infty} x(t-\tau) g_2(\tau) d\tau \right)^{i}] \end{aligned} \tag{23}$$

In turn, the expression (30) using a ratio (3), (13), (15) is easily reduced to the form

$$\begin{aligned} z(t) &= \sum_{i=1}^{k} \nu_i [\left(\sum_{n=-N}^{N} c_n W_1(jn\omega_1) e^{n\omega_1 t} \right)^{i} + \\ &+ \left(\sum_{n=-N}^{N} c_n W_2(jn\omega_1) e^{n\omega_1 t} \right)^{i}] \end{aligned} \tag{24}$$

where

$$\begin{cases} W_1(jn\omega_1) = W_1(s)\Big|_{s=jn\omega_1} \\ W_2(jn\omega_2) = W_2(s)\Big|_{s=jn\omega_2} \end{cases} \tag{25}$$

$$\begin{cases} W_1(s) = \int_{0}^{\infty} g_1(t) e^{-st} dt \\ W_2(s) = \int_{0}^{\infty} g_2(t) e^{-st} dt \end{cases} \tag{26}$$

Summarizing the expression (21) up to M components, i.e., presenting the impulse response of the inertial part of nonlinear dynamical system of the M-th order as

$$g(t) = \sum_{m=1}^{M} g_m(t) \tag{27}$$

on condition that each component of the expression (34) the property (11) is fair, we can easily come to the generalized expression

$$z(t) = \sum_{i=1}^{k} \nu_i [\sum_{m=1}^{M} \left(\sum_{n=-N}^{N} c_n W_m(jn\omega_1) e^{n\omega_1 t} \right)^{i}] \tag{28}$$

where

$$W_m(jn\omega_1) = W_m(s)\Big|_{s=jn\omega_1}, \ m = 1,2,...,M$$

$$W_m(s) = \int_{0}^{\infty} g_m(t) e^{-st} dt \tag{29}$$

We start this extension with the appeal to expression (21), in which on the right side there is the sum of two exponents.

As we know from the theory of linear differential equations, in this case the differential equation systems will have the 2nd order and depending on whether its characteristic polynomial roots be of negative numbers or complex-conjugate pair of numbers with negative real parts, the processes in this system will be aperiodic of the 2nd order (curves 2 in Fig. 2) or oscillatory (curve 3 in Fig. 2). Our work [7] shows that the differential equations of 2nd order describe a wide class of real dynamic systems; it also presents the received conditions which describe the way to determine that.

In order to be able to match the level of complexity of the system of equations, we obtain as a result of solving the problem, formulated in the title, with the equations that we have received for nonlinear dynamical system with inertial part of the 1st order, i.e., the system of equations (19), also ask, as in the problem input $x(t)$ in the form (8), and the output signal Z after nonlinearities in the form (9).

3. Experimental research

To build an algorithm for the identification of mathematical model of nonlinear dynamic system, we set its input signal $x(t)$ as sinusoid with a frequency ω_1, "lifted" over the time axis by a constant component c_0, i.e., in the form

$$\begin{aligned} x(t) &= c_0 + A\sin\omega_1 t = c_0 + A\frac{e^{j\omega_1 t} - e^{-j\omega_1 t}}{2j} = \\ &= \frac{A}{2j} e^{j\omega_1 t} + c_0 + \frac{A}{-2j} e^{-j\omega_1 t} = c_1 e^{j\omega_1} + c_0 + c_{-1} e^{-j\omega_1 t} \end{aligned} \tag{30}$$

and nonlinearity we set by a polynomial function (9).

It is known that

$$W(j\omega) = W_1(s)\Big|_{s=j\omega} = \frac{K_1}{1 + j\omega T_1} \tag{31}$$

Substituting an expression (25) in equation (19), we obtain the system of equations

$$\begin{cases} \nu_3 c_{-1}^3 \left(\frac{K_1}{1 - j\omega_1 T_1} \right)^3 = q_{-3} \\ \nu_2 c_{-1}^2 \left(\frac{K_1}{1 - j\omega_1 T_1} \right)^2 + 3\nu_3 c_{-1}^2 c_0 \left(\frac{K_1}{1 - j\omega_1 T_1} \right)^2 K_1 = q_{-2} \\ \nu_1 c_{-1} \left(\frac{K_1}{1 - j\omega_1 T_1} \right) + 2\nu_2 c_{-1} c_0 \left(\frac{K_1}{1 - j\omega_1 T_1} \right) K_1 + \\ +3\nu_3 c_{-1}^2 c_1 \left(\frac{K_1}{1 - j\omega_1 T_1} \right)^2 \left(\frac{K_1}{1 + j\omega_1 T_1} \right) + \\ +3\nu_3 c_{-1} c_0^2 \left(\frac{K_1}{1 - j\omega_1 T_1} \right) K_1^2 = q_{-1} \\ \nu_1 c_0 K_1 + 2\nu_2 c_{-1} c_1 \left(\frac{K_1}{1 - j\omega_1 T_1} \right) \left(\frac{K_1}{1 + j\omega_1 T_1} \right) + \nu_2 c_0^2 K_1^2 + \\ +6\nu_3 c_{-1} c_0 c_1 \left(\frac{K_1}{1 - j\omega_1 T_1} \right) K_1 \left(\frac{K_1}{1 + j\omega_1 T_1} \right) + \nu_3 c_0^3 K_1^3 = q_0 \\ \nu_1 c_1 \left(\frac{K_1}{1 + j\omega_1 T_1} \right) + 2\nu_2 c_0 c_1 K_1 \left(\frac{K_1}{1 + j\omega_1 T_1} \right) + \\ +3\nu_3 c_{-1} c_1^2 \left(\frac{K_1}{1 - j\omega_1 T_1} \right) \left(\frac{K_1}{1 + j\omega_1 T_1} \right)^2 + \\ +3\nu_3 c_0^2 c_1 K_1^2 \left(\frac{K_1}{1 + j\omega_1 T_1} \right) = q_1 \\ \nu_2 c_1^2 \left(\frac{K_1}{1 + j\omega_1 T_1} \right)^2 + 3\nu_3 c_0 c_1^2 K_1 \left(\frac{K_1}{1 + j\omega_1 T_1} \right)^2 = q_2 \\ \nu_3 c_1^3 \left(\frac{K_1}{1 + j\omega_1 T_1} \right)^3 = q_3 \end{cases} \tag{32}$$

So, there are only 5 indeterminates and there are 7 equations in the system (32). To determine these 5 indeterminates, it is sufficient to take any 5 equations from the system (26) and create a system of five equations with five indeterminates, solving which by using a standard soft MATLAB allows to obtain the numerical values of all parameters of nonlinear dynamical system, and the two equations from the system (26) which will remain not used, may serve as criteria of the correctness for solving the problem of identification.

4. Conclusions

There had been developed a method for synthesis of mathematical models of nonlinear dynamic systems with non-linear characteristics in the kind of polynomials and models of the inertial part in the form of Bode plot, based on the algorithm of transferred of multiple Volterra integrals, set in the time domain, to one-fold integrals, for the solution of which there shall be used the Bode plot of the inertial part of these systems.

There had been done the generalization of the suggested class of the mathematical models into the nonlinear dynamical system with a random order of both, their nonlinear characteristics and the characteristics of their inertial properties.

On the example of nonlinear dynamic systems with the third-order of nonlinear characteristics and the 1st and 2nd orders of the inertial part of these systems, there had been specified an algorithm for their parametric identification.

References

[1] Chua L. O., Ng C-Y.: Frequency domain analysis of nonlinear systems: general theory. Electronic Circuits and Systems 3(2), 1979, 165–185.

[2] Chua L. O., Ng C-Y.: Frequency domain analysis of nonlinear systems: formulation of transfer functions. Electronic Circuits and Systems 3(4), 1979, 257–269.

[3] Halas M., Huba M., Kotta Ü.: An overview of transfer function formalism for nonlinear systems. Journal of Cybernetics and Informatics 8(3), 2009, 28–35.

[4] Halas M.: An algebraic framework generalizing the concept of transfer functions to nonlinear systems. Automatica 44(2), 2008, 1181–1190 [http://doi.org/10.1016/j.automatica.2007.09.008].

[5] Halas M., Kotta Ü.: A transfer function approach to the realization problem of nonlinear systems. International Journal of Control 85(1), 2012, 320–331 [http://doi.org/10.1080/00207179.2011.651748].

[6] Kerschen G., Worden K., Vakakis A. F. et al.: Past, present and future of nonlinear system identification in structural dynamics. Mechanical Systems and Signal Processing 20(3), 2006, 505–592 [http://doi.org/10.1016/j.ymssp.2005.04.008].

[7] Mokin A. B., Mokin V. B., Mokin B. I. et al.: Determining the Conditions and Designing the Methods for Description of Processes in Complex Dynamic Objects by Equivalent Models not Higher than the Third-Order. Journal of Automation and Information Sciences 48(3), 2016, 83–97 [http://doi.org/10.1615/JAutomatInfScien.v48.i3.90].

[8] Mokin B. I., Mokin O. B.: The Fourier Integral Method in the Problems of Identification and Input Signal Renewal of Nonlinear Dynamical Systems. Visnyk of Vinnytsia Polytechnical Institute 3, 2000, 107–112.

[9] Mokin B. I.: Vossstanovleniye vkhodnykh signalov snelineynymi kharakteristikami preobrazovaniya. Metody teorii identifikatsii v zadachakh izmeritel'noy tekhniki i metrologii: III Vsesoyuznyy simpozium. 1982, 207–209.

[10] Mokin O. B., Mokin B. I., Khomiuk Ya. V.: Conditions of Equivalentiation of Nonlinear Dynamic Systems with Power Nonlinearities in the Frequency Domain. Visnyk of Vinnytsia Polytechnical Institute 5, 2016, 40–44.

[11] Mokin O. B., Mokin B. I.: Modeling and optimization of movement of multi-mass electric vehicles with difficult terrain surfaces. Vinnytsia National Technical University, Vinnytsia 2013.

[12] Mokin O. B., Mokin B. I.: Renewal of input signals of nonlinear Measuring converters by Fourier-integral method. International Measurement Confederation (IMEKO): XVII World Congress of the (Metrology in the 3rd Millennium), Dubrovnik 2003, 468–471.

[13] Nassirharand A., Mousavi Firdeh S.R.: Design of nonlinear controllers using describing functions with application to servomechanism. Asian Journal of Control 11(3), 2009, 446–450.

[14] Nassirharand A., Mousavi Firdeh S.R.: Design of nonlinear lead and/or lag compensators. International Journal of Control, Automation and Systems 6(3), 2008, 394–400.

[15] Nassirharand A., Teh S.H.: Describing function-based identification of nonlinear transfer functions for nonlinear systems from experimental/simulation data. Int. J. Modelling, Identification and Control 25(2), 2016, 93–101 [http://doi.org/10.1504/IJMIC.2016.075270].

[16] Pavlenko V. Speranskyy V.: Polyharmonic test signals application for identification of nonlinear dynamical systems based on volterra model. International Conference on Information and Telecommunication Technologies and Radio Electronics (UkrMiCo), 2017, 1–5 [http://doi.org/10.1109/UkrMiCo.2017.8095372].

[17] Rijlaarsdam D., Nuij P., Schoukens J., Steinbuch M.: A comparative overview of frequency domain methods for nonlinear systems. Mechatronics 42, 2017, 11–24 [http://doi.org/10.1016/j.mechatronics.2016.12.008].

[18] Van Trees H. L.: Synthesis of Optimum Non-Linear Control Systems. Massachusetts Inst. of Technology, Cambridge 1962.

Prof. Borys Mokin
e-mail: borys.mokin@gmail.com

Doctor of Technical Sciences, professor, Professor of the Department of System Analysis and Information Technologies of Vinnytsia National Technical University. Author of over 700 publications, including 28 monographs, 25 textbooks, 80 patents for inventions, more than 500 scientific articles in professional journals, 15 of which are in the scientometric databases Scopus and Web of Science.

http://orcid.org/0000-0002-5906-6122

Prof. Vitalii Mokin
e-mail: vbmokin@gmail.com

Doctor of Technical Sciences, professor, Head of the Department of System Analysis and Information Technologies of Vinnytsia National Technical University. Author of more than 400 publications, including 14 monographs, 25 textbooks, 49 copyright certificates and patents for inventions and more than 150 scientific articles in professional journals, 15 of which are in scientometric databases Scopus and Web of Science.

http://orcid.org/0000-0003-1946-0202

Prof. Oleksandr Mokin
e-mail: abmokin@gmail.com

Doctor of Technical Sciences, professor, Professor of the Department of System Analysis and Information Technologies of Vinnytsia National Technical University. Author of more than 150 publications, including 4 monographs, 8 textbooks, 21 copyright certificates and patents for inventions and more than 120 scientific articles in professional journals, 8 of which are in scientometric databases Scopus and Web of Science.
http://orcid.org/0000-0002-9277-3312

Ph.D. Orken Mamyrbayev
e-mail: morkenj@mail.ru

Deputy Deputy General Director in science and head of the Laboratory of computer engineering of intelligent systems at the Institute of Information and Computational Technologies of the Kazakh National Technical University named after K. I. Satbayev and associate professor in 2019 at the Institute of Information and Computational Technologies. Main research field: machine learning, deep learning, and speech technologies.

http://orcid.org/0000-0001-8318-3794

Ph.D. Saule Smailova
e-mail: Saule_Smailova@mail.ru

Sa Smailova is currently a lecturer at the Department of Information Technology. She is a co-author over 60 papers in journals, book chapters, and conference proceedings. Member of Expert Group in the Computer Science specialization of IQAA. Her professional interests are teaching, artificial intelligence, software engineering, data processing.

http://orcid.org/0000-0002-8411-3584

http://doi.org/10.35784/iapgos.2931 *received: 29.04.2022 | revised: 10.06.2022 | accepted: 15.06.2022 | available online: 30.06.2022*

THE SPECTRUM LENGTH METHOD IN QUANTITATIVE INTERPRETATION OF SELECTED OPTICAL SPECTRA

Martyna Wawrzyk
Lublin University of Technology, Doctoral School, Lublin, Poland

Abstract. *Different algorithms are used for the quantitative interpretation of optical spectra. Regression methods e.g CLS (Classical Least Squares) or PLS (Partial Least Squares) are often used in typical problems of laboratory spectroscopy. The spectra analysis is generally a multi-step process, in which, depending on the spectra type, modification of individual regression methods or special dedicated methods are applied. For example, contour length method or spectra length algorithm are used in this purpose. The basic version of the algorithm is very simple in terms of mathematics. It has been proposed for the analysis of spectra in the OP-FTIR open path spectroscopy, where there are significant fluctuations in the spectrum baseline. The spectrum length is a parameter closely related to the content of the analyzed gas component. Independently of spectral length algorithm, a method has been developed in which difference length of two spectra (measured and reference) is used to compare the spectra. The minimum length of the spectral difference is an indicator of their best fitting. The article presents two ways of using the spectrum length: as a direct and indirect parameter indicating the measured quantity on the basis of the spectrum. There were performed the spectrum length algorithm as a digital differentiating filter with a specific frequency response. There were also analyzed more advanced differentiating filter and the possibility of frequency spectrum filter design used in an analysis of optical spectral signal. There were performed the analysis of the spectrum length method in the case of the synthetic calibration involving the use of model spectra from simulations realized by HITRAN database. There were analyzed numerically the problem of the Instrument Line Shape influence on the synthetic spectra and results of the determining the content of components by the minimizing the difference of spectral length.*

Keywords: OP-FTIR, optical spectra, quantitative analysis, digital differentiating filter

METODA DŁUGOŚCI WIDMA W ILOŚCIOWEJ INTERPRETACJI WYBRANYCH WIDM OPTYCZNYCH

Streszczenie *Do ilościowej interpretacji widm optycznych wykorzystuje się wiele różnych algorytmów. W typowych zagadnieniach spektroskopii laboratoryjnej wykorzystuje się m. in. metody regresji CLS, PCR PLS. Interpretacja widm to często proces wieloetapowy, w którym w zależności od rodzaju widm wykorzystuje się modyfikację poszczególnych metod regresji lub też stosuje się specjalne metody dedykowane. Jedną z takich metod jest algorytm długości konturu lub też długości widma. Jego podstawowa wersja jest bardzo prosta pod względem matematycznym. Została zaproponowana do analizy widm ze spektroskopii otwartej ścieżki OP-FTIR, dla której występują znaczące fluktuacje linii bazowej widma. Długość widma jest parametrem, który jest odwzorowany bezpośrednio na zawartość danego składnika gazowego. Niezależnie od algorytmu długości widma powstała metoda, w której długość różnicy dwóch widm (mierzonego i odniesienia) służy do porównania widm. Minimalna długość różnicy widm jest wskaźnikiem ich najlepszego dopasowania. W pracy porównane zostaną obydwa sposoby wykorzystania długości widma: jako parametru bezpośrednio lub pośrednio wskazującego wielkość poszukiwaną na podstawie widma. Przeanalizowany zostanie algorytm długości widma jako cyfrowy filtr różniczkujący posiadający określoną charakterystykę częstotliwościową. Przeanalizowane zostanie zagadnienie wykorzystania bardziej zaawansowanego filtru różniczkującego oraz możliwość uwzględnienia w wyborze i projektowaniu filtra widma częstotliwościowego optycznego sygnału spektralnego. Kolejno poruszanym zagadnieniem będzie analiza metody długości widma w przypadku tzw. kalibracji syntetycznej polegającej na wykorzystaniu jako widm wzorcowych widm pochodzących z symulacji wykorzystujących bazę danych Hitran. Przeanalizowany numerycznie zostanie problem wpływu kształtu odpowiedzi instrumentu pomiarowego na syntetyczne widma i wyniki wyznaczania zawartości składników metodą minimalizacji długości różnicy widm.*

Słowa kluczowe: OP-FTIR, widma optyczne, ilościowa analiza, cyfrowe filtry różniczkujące

Introduction

Optical data can be measured in different ways. The optical spectra measurement can be processed in laboratory or *in situ*. Some kinds of industry require to conduct measurements from a distance of atmospheric gases or gas products of chemical reaction e.g outlet gases from as a product of combustion of biogas [4]. In the context of sustainable urban design, measurements of atmospheric gas, in particular greenhouse gases are crucial [8]. The open path Fourier Transform Infrared Spectroscopy (OP-FTIR) is a method using in situ measurements. The main advantages of this method are: non-invasive measurements, possibility of simultaneous measurement of many components (the entire spectral range of the spectrum is determined in one measurement act), simple measuring system, quick process of conducting measurements and no necessity of preparing samples for analysis [12]. Additionally, OP-FTIR spectrometer enables measurements in difficult weather condition, where there may be high temperature and high dust level [13].

Due to unstable measuring conditions, e.g. non-constant temperature, frequent changes of the reference spectrum, interference from water vapor and carbon dioxide, the data from OP-FTIR spectrometer is not suitable for direct qualitative or quantitative analysis. The second major problem in the context of optical spectral preprocessing is background spectra measurements. In order to calculate the content of the spectrum component, there is a need a knowledge of a sample single-beam spectrum and background spectrum without spectrum of the analyzed compound [11]. Background spectrum measurement is very complicated or even not possible to conduct (e.g the atmospheric gas measurements). For these reasons obtained measurement spectrum require implementation of advanced spectrum processing techniques.

1. Quantitative analysis in OP-FTIR

The conducting of a spectra quantitative analysis is mainly aimed at construction a mathematical model on the basis of which it will be possible to determine the content of a selected substance in the spectrum. The construction of such a calibration model allows to avoid additional costs and save time as a result of carrying out subsequent measurements. In this regard, various methods of regression analysis are used, e.g. regression of principal components PCR (Principal Component Regression), partial least squares regression PLS (Partial Least Square Regression) and multiple linear regression MLR (Multi-linear Regression) [7, 14].

Due to the characteristics of the OP-FTIR spectrometer measurement data, in some cases it is not possible to perform a direct calibration. It caused the development an alternative methods as a quantitative analysis of optical spectra. For reference spectrum measurements issue, there were developed quantitative methods for measuring analyte concentrations, for instance spectral subtraction method of gas phase FTIR [10] and a single beam titration method [16]. It was developed the spectrum length method applied in gas concentration analysis [1] and was successfully implemented in the context of quantitative analysis of spectra measured by TFBG (Tilted fiber Bragg grating) [6].

As concerns the spectrum analysis with any parameters, spectral features modelling with mathematical methods are applied. For this purpose, simulation spectra are most often used, available e.g in the HITRAN database [9]. The influence of temperature on OP-FTIR spectra quantitative analysis is very significant and complicates conducting an appropriate model calibration [5]. For high temperature measurements there is a need to use a dedicated HITEMP database [15].

2. Materials and experimental methods

2.1. Data description

The analysis was performed on the basis of synthetic data and measured data. The simulation spectra have been modelled in accordance with HITRAN database [9] and there were conducted modelling of carbon (II) oxide spectra (CO) for different concentrations (2.5%, 5%, 10%, 20%, 25%, 33% and 50%). The analysis of calibration spectra was conduct using the calibration spectra of CO [2] and methan (CH_4) [3]. The calibration for two gases CO and CH4 was also performed for different concentration. The conditions for the gases calibration were as follows: path length was 10 cm, the spectra were collected at 4 cm^{-1} resolution [2, 3]. The concentrations for CO gas was as below: 2.5%, 5%, 10%, 20%, 25%, 33% and 50% [2] and for CH_4 gas: 2%, 5%, 7%, 10%, 20%, 30%, 40%, 50%, 60%, 70% [3].

2.2. Methods applied

The algorithm which was applied in this experimental has been developed in MATLAB.

In order perform the quantitative analysis of spectra for different concentrations there were applied a spectrum length method (SLM) , which was based on a very simple idea. The main goal of this method is compute the spectrum length by summing up the differences between two adjacent points of analyzed spectrum [1].

The length of absorbance spectrum, which contains N points can be obtained by formula below:

$$L = \sum_{i=0}^{N-1} |A_{i+1} - A_i| \quad (1)$$

where A is the absorbance of spectrum [1]. The difference between two points of spectrum can be received by subtracting absorbance values from two adjacent points. However, digital differentiating filters may be used as a spectrum length algorithm. In this paper, there were designed several digital differentiating filters depending on the frequency spectrum of optical spectral signal.

2.3. Digital differentiating filter designing

Before the designing of digital differentiating filters, there were computed the frequency spectrum of selected optical spectra by using FFT (Fast Fourier Transform), which computes the DFT (Discrete Fourier Transform). This procedure was conducted with the aim to define the frequency ranges with useful information and the others ranges with unwanted signal e.g. signal noise.

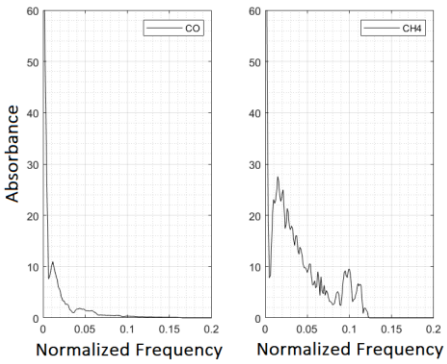

Fig. 1. Frequency spectrum of CH4 spectra and CO spectra

Based on received frequency spectrum of two gases (Fig. 1), the frequency ranges necessary for the design of differential filters were obtained. In the case of the CH_4 spectra, there were observed the useful information in the range 0-0.2 frequency and for the CO spectra is the range 0-0.1 frequency. For this reason, it was important to design differentiating filters, which will attenuate signal out of defined ranges with information.

With the aim to conduct optimal signal filtration, there were used built-in functions in MATLAB. Three types of filters were selected. Firstly, the Savizty-Golay filter was applied, where there were selected seventh filter order. With using the function *firpm* the Parks-McClellan FIR differential filter was designed. It was selected the 30th order of filter. The Least-square linear-phase FIR filter with 15th filter order was designed based on the *firls* function. Fig. 2 presents the frequency response of designed filters.

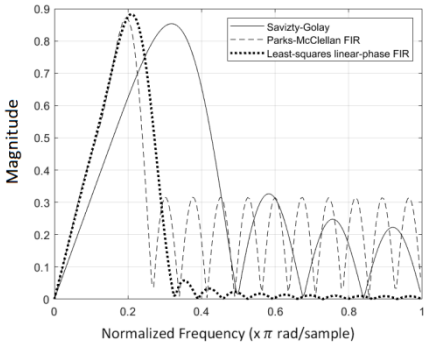

Fig. 2. Frequency response of selected digital filters

In the next step of spectrum processing, there were used constructed digital filters in order to compute the differential of the gas spectra as a SLM procedure. The spectra differentiation was performed on the preprocessing data (e.g. selection of wavenumber ranges with characteristic peaks of analyzed gas). In the final processing step, the contour spectra length was calculated. As an example there were presented the differential of spectra of 50% concentration CO obtained by Savizty-Golay filter.

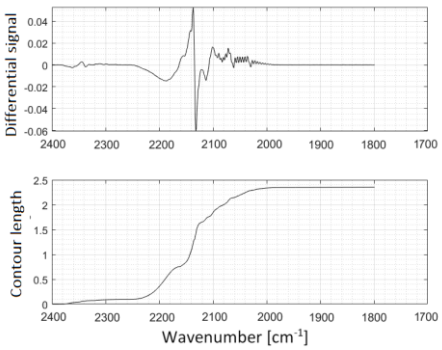

Fig.3. The differential signal and contour length for CO spectra

To perform the SLM procedure, there were selected three types of digital differential filters to demonstrate the difference between them. The two calibration spectra (CO and CH_4) was processed by using the same types of digital differential filters.

2.4. SLM procedure with synthetic spectra

On the base of HITRAN database, there were calculated synthetic spectra using by line-by line method. The CO synthetic spectra was selected with different concentrations (as the same in the case of calibration spectra). It was computed the proper Instrument Line Shape (ILS) function with measurement resolution 4 cm^{-1}. The data loading and processing also was supported by MATLAB. In the next step, it was added to synthetic spectra the modeled errors representing the signal noise

and inappropriate ILS distortion. This process was performed to demonstrate the SLM procedure as a parameter to evaluate of modeling synthetic spectra.

Additionally, there were designed the Difference Length Spectrum (DLS) parameter to evaluate the ILS function adjustment. The algorithm of DLS parameter was based on calculation of difference between analyzed contour length (CL_a) and ideal contour length (CL_i) with correct parameters. The algorithm of DLS parameter was based on formulas below:

$$DLS(w) = CL_a - CL_i \quad (2)$$

DLS parameter was described as a function of wavenumber (w). In the next step, there were calculated a derivative of $DLS(w)$ and *NDLS* (Normalized Difference Length Spectrum):

$$NDLS(w) = \frac{|DLS'(w)|}{\max(|DLS'(w)|)} \quad (3)$$

The optimal synthetic calibration result is obtained by the minimum of *NDLS*.

3. Results

In this section there were presented the results of SLM procedure in the case of concentrations analysis of calibration spectra and of evaluation correct synthetic spectra modeling.

3.1. Calibration spectra

There were processed three types of digital differential filters in SLM procedure. As the results there were obtained charts presents the contour length spectra as an analysis of gas concentrations of CO and CH_4. Fig. 4 and Fig. 5 presents the implementation results of SLM procedure to determine gas concentrations for CO and CH_4 spectra.

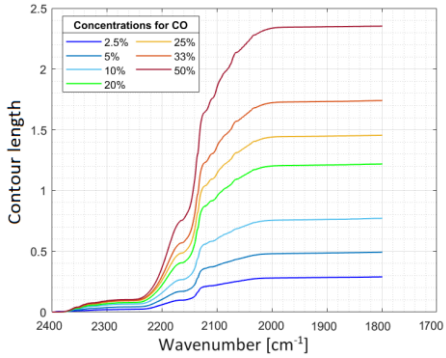

Fig. 4. SLM procedure with Savizty-Golay filter. CO calibration spectra

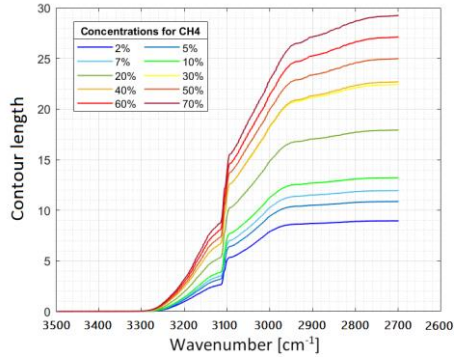

Fig. 5. SLM procedure with Least-square linear-phase FIR filter. CH_4 calibration spectra

The received contour length results could be used to support interpretation of gas content in the case of input spectra data with fluctuating baselines. There is possibility to distinguish the concentrations values of analyzed gases.

In order to compare three filters applied, there were obtained max values of contour length method for each gases. The Fig. 6 and Fig. 7 shows the differences between DDF applied.

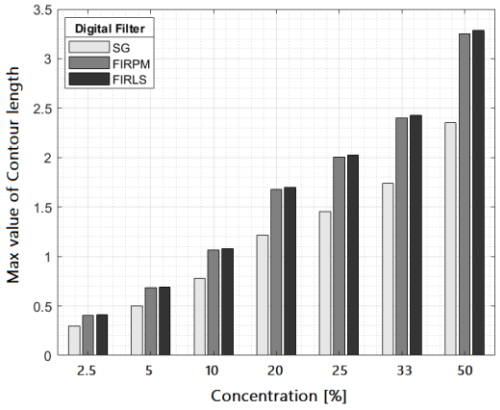

Fig. 6. The differences between three types of DDF. CO Calibration spectra

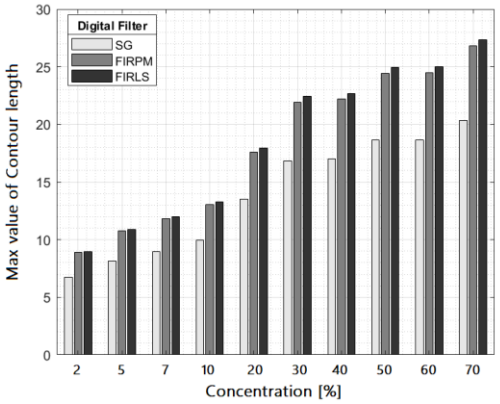

Fig. 7. The differences between three types of DDF. CH_4 Calibration spectra

Based on the obtained results of three types of DDF, there were observed the lowest value of contour length in the case of CO spectra and CH_4 spectra. Additionally, the highest values were presented by the same DDF least square linear phase FIR in both cases of spectra.

3.2. Synthetic spectra

SLM procedure was used in processing of modelling synthetic spectra as parameter to determine the simulation spectra quality. In the first case, there were modelled signal noise and added to analyzed synthetic spectra to illustrate the SLM sensitivity to added noise.

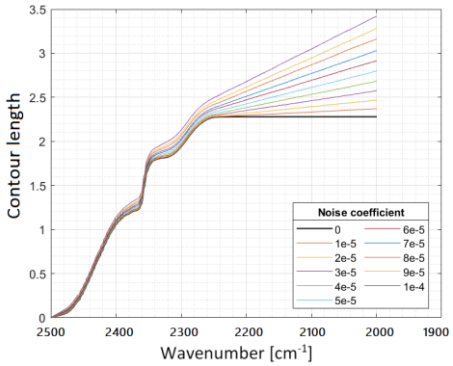

Fig. 8. Influence of adding signal noise to SLM results

Fig. 8 presents the significant influence of signal noise with small coefficient. The SLM procedure has a high sensitivity to noise signal.

In the second case, there were considered the influence of spectrometer measurement resolution to ILS function, which is selected during simulation synthetic spectra in order to modelled influence of measuring instrument.

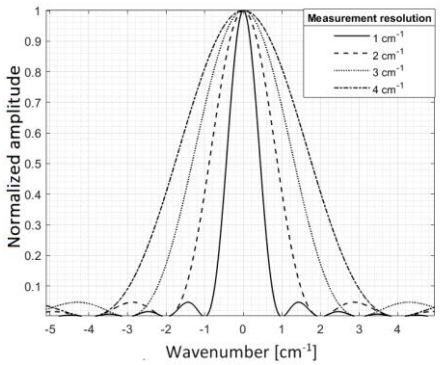

Fig. 9. Measurement resolution influence on ILS function

The Fig. 10 describes the impact of inappropriate ILS function on SLM results. The contour length spectra obtained by selected measurements resolution presents significant differences, which are caused by selection small measurement resolution range. Therefore, there is a need to make property selection of ILS function to calculate correctly simulation synthetic spectra.

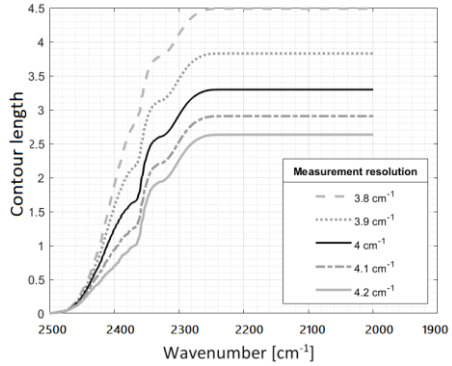

Fig. 10. Measurement resolution influence on SLM results

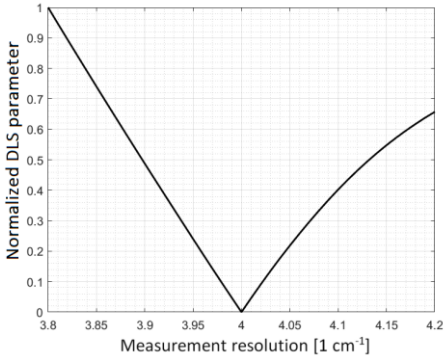

Fig. 11. NDLS parameter results

The *NDLS* parameter was designed to support the correct selection of measurement resolution (Fig. 11). The lowest value of *NDLS* parameter indicate the best adjustment of ILS functions. To demonstrate the NLDS operation, the 4 cm^{-1} measurement value was taken as a reference value.

4. Summary

The spectrum length method as a quantitative analysis method of optical spectra meets the assumptions. There were processed the gas concentrations analysis by using different digital filters. The method is fast and very simple to implement. Regard to possibility of many filters selection, the SLM procedure could be matched to several kinds of input data. It worth to point out, that due to the reduction of computational complexity, the DDF with the lowest filter order are desirable. On the other hand, the processing SLM with synthetic spectra demonstrated inadequacies of this method in the case of spectra with signal noise or inappropriate ILS function. For this reason, further research will be focus on development SLM procedure, which will be not sensitivity to noise signal and imperfect ILS model.

Acknowledgments

This work was supported by **Szkoła Doktorska-Grant-Martyna Wawrzyk**.

References

[1] Bak J.: Retrieving CO concentrations from FT-IR spectra with nonmodeled interferences and fluctuating baselines using PCR model parameters. Applied Spectroscopy 55(5), 2001, 591–597.
[2] Bochentyn B., Błaszczak P.: Carbon (II) oxide (CO) calibration set of FTIR spectra [Data set]. Gdańsk University of Technology. 2021 [http://doi.org/10.34808/nnej-je87].
[3] Bochentyn B., Błaszczak P.: Methane (CH4) calibration set of FTIR spectra [Data set]. Gdańsk University of Technology. 2021 [http://doi.org/10.34808/4vzx-0y14].
[4] Chlipała M., Błaszczak P., Wang S. F., Jasiński P., Bochentyn B.: In situ study of a composition of outlet gases from biogas fuelled Solid Oxide Fuel Cell performed by the Fourier Transform Infrared Spectroscopy. International Journal of Hydrogen Energy 44(26), 2019, 13864–13874.
[5] Cięszczyk S.: A local model and calibration set ensemble strategy for open-path FTIR gas measurement with varying temperature. Metrology and Measurement Systems 20(3), 2013, 513–524.
[6] Cięszczyk S., Harasim D., Kisała P.: A novel simple TFBG spectrum demodulation method for RI quantification. IEEE Photonics Technology Letters 29(24), 2017, 2264–2267.
[7] Gautam R., Vanga S., Ariese F., Umapathy S.: Review of multidimensional data processing approaches for Raman and infrared spectroscopy. EPJ Techniques and Instrumentation 2(1), 2015, 1–38.
[8] Griffith D. W., Pöhler D., Schmitt S., Hammer S., Vardag S. N., Platt U.: Long open-path measurements of greenhouse gases in air using near-infrared Fourier transform spectroscopy. Atmospheric Measurement Techniques 11(3), 2018, 1549–1563.
[9] Hill C., Gordon I. E., Kochanov R. V., Barrett L., Wilzewski J. S., Rothman L. S.: HITRANonline: An online interface and the flexible representation of spectroscopic data in the HITRAN database. Journal of Quantitative Spectroscopy and Radiative Transfer 177, 2016, 4–14.
[10] Kozlov D., Besov A.: Method of spectral subtraction of gas-phase Fourier transform infrared (FT-IR) spectra by minimizing the spectrum length. Applied Spectroscopy 65(8), 2011, 918–923.
[11] Lin C. H., Grant R. H., Heber A. J., Johnston C. T.: Application of open-path Fourier transform infrared spectroscopy (OP-FTIR) to measure greenhouse gas concentrations from agricultural fields. Atmospheric Measurement Techniques 12(6), 2019, 3403–3415.
[12] Mroczka J. (red.): Problemy metrologii elektronicznej i fotonicznej. Oficyna Wydawnicza Politechniki Wroclawskiej, Wrocław 2008.
[13] Oppenheimer C., Kyle P. R.: Probing the magma plumbing of Erebus volcano, Antarctica, by open-path FTIR spectroscopy of gas emissions. Journal of Volcanology and Geothermal Research 177(3), 2008, 743–754.
[14] Roggo Y., Chalus P., Maurer L., Lema-Martinez C., Edmond A., Jent N.: A review of near infrared spectroscopy and chemometrics in pharmaceutical technologies. Journal of Pharmaceutical and Biomedicalanalysis 44(3), 2007, 683–700.
[15] Rothman L. S., Gordon I. E., Barber R. J. et al.: HITEMP, the high-temperature molecular spectroscopic database. Journal of Quantitative Spectroscopy and Radiative Transfer 111(15), 2010, 2139–2150.
[16] Sung L. Y., Lu C. J.: A single-beam titration method for the quantification of open-path Fourier transform infrared spectroscopy. Journal of Quantitative Spectroscopy and Radiative Transfer 145, 2014, 43–49.

M.Sc. Eng. Martyna Wawrzyk
e-mail: m.wawrzyk@pollub.pl

Ph.D. student, M.Sc. Eng. of Biomedical Engineering at Lublin University of Technology in the Faculty of Electrical Engineering and Computer Science. The author several articles about biomedical signal processing, data analysis, data classification and spectrum analysis. Her current research interests include algorithms applied in pre-processing of data, for example filtering data or baseline correction. Additionally, her other scientific interests involve analysis spectrum of optical data and open path FT-IR spectroscopy.

http://orcid.org/0000-0002-0380-0949

http://doi.org/10.35784/iapgos.2982 *received: 30.05.2022 | revised: 06.06.2022 | accepted: 09.06.2022 | available online: 30.06.2022*

DEVELOPMENT OF AUTOMATION OF WASTE SORTING AS AN INTEGRAL PART OF ENVIRONMENTAL PROTECTION

Nataliia Stelmakh, Oleg Belman
National Technical University of Ukraine "Igor Sikorsky Kyiv Polytechnic Institute", Instrument production department, Kyiv, Ukraine

Abstract. *The paper regards the urgency of creating small - sized systems for automated local sorting of household waste for modern residential complexes based on visual spectrometry. For this purpose, algorithms for system operation were developed and the procedure for designing a functional control scheme for the sorting process with the construction of the necessary contours of automated control was presented.*

Keywords: plastic waste sorting, automated sorting system, sorting system control board, algorithm, functional diagram

ROZWÓJ AUTOMATYZACJI SORTOWANIA ODPADÓW JAKO INTEGRALNA CZĘŚĆ OCHRONY ŚRODOWISKA

Streszczenie. *Artykuł dotyczy pilną potrzebę stworzenia małogabarytowych systemów zautomatyzowanego lokalnego sortowania odpadów komunalnych dla nowoczesnych zespołów mieszkaniowych w oparciu o spektrometrię wizualną. W tym celu opracowano algorytmy pracy systemu oraz przedstawiono procedurę projektowania schematu funkcjonalnego sterowania procesem sortowania wraz z budową niezbędnych obwodów automatycznego sterowania. Przeprowadzono również analizę zastosowania modelu do oceny niezawodności zautomatyzowanego systemu sortowania odpadów.*

Słowa kluczowe: sortowanie odpadów z tworzyw sztucznych, zautomatyzowany system sortowania, tablica sterownicza systemu sortowania, algorytm, diagram funkcjonalny

Introduction

Household waste is the result of human life, the morphological composition of which determines the features of the collection, sorting and subsequent scheme of preparation and processing of waste. Therefore, one of the important characteristics of consumer waste is its morphological composition, which represents the ratio of individual components: packaging, textiles, metal, plastic, construction waste and other types of mixed state. Reliable information on the amount and composition of municipal waste generated in the settlements will ensure effective planning and management, including collection, transportation, disposal, use and safe disposal.

Solid waste is generated from two sources: residential buildings; institutions and enterprises of public purpose (catering, educational, entertainment, hotels, kindergartens, etc.). The composition of solid waste is influenced by factors such as climate zone, the degree of improvement of housing (the presence of garbage, gas, water, sewerage, heating, heating), surface area, type of fuel for local heating, catering, trade culture and, no less important, lifestyle and well-being of the population [2].

Morphologically, solid waste is divided into components: paper, cardboard (waste paper); food waste; tree; metal (black and non-ferrous); textile; bones; glass; skin; rubber; stones; polymeric materials; others.

Separate sorting has recently been increasingly introduced into society, but this decision at this stage of implementation only partially reduces the "flow" of solid waste and does not help in the fight against the elimination of huge landfills. We should not expect that separate sorting will make our cities and air cleaner, this requires a comprehensive approach. There are not many methods of dealing with household waste, and they can be divided into passive and active.

Thus, the issue of collection and further processing of household waste becomes one of the competitive advantages of existing modern and residential complexes under construction [1].

1. Development of algorithms for the operation of small-sized automated sorting system for household waste

Today, many designs of automated sorting systems for household waste are known and they have their disadvantages and advantages. In this paper we consider the development of a small sorting system based on visual spectrometry. After analyzing the existing designs of automated sorting systems, their advantages and disadvantages were proposed the following principle of construction of the sorting system. To avoid unwanted objects on the sorting line, the first step is to grind the material into pieces of adjustable size in the shredder, shafts with carbide plates grind any material. Solid household waste is not a completely dry material, so a special hydrophobic coating must be applied to prevent corrosion and adhesion to the surface in contact with the waste.

The next stage of sorting is sterilization, drying and separation of biological substance from the material. To do this, the crushed waste enters the autoclave, where under the action of high pressure and temperature, moisture evaporates. Paper and leftover food are separated by mixing. After sterilization, the material is dry and disinfected. Next is the process of separating ferrous and nonferrous metals. The next step is to pass through a vibrating screen that separates dust and fine particles, which is relatively clean compost because the temperature in the autoclave does not exceed the decay temperature of the plastics. Macro-lines of the material after the vibrating screen are divided into films and flat materials, as well as three-dimensional shapes, their separation is necessary because the films can interfere with the recognition of smaller particles covering them. A ballistic separator is used to separate the shape. The final stage is the sorting of plastics by type, sorting glass by color. Glass and other materials are in a special vibrating hopper.

Due to the specifics of the selected sorting scheme, there is a problem related to the balance of performance in the system, which in case of violation of the sequence of modules can significantly affect the quality of sorting. The main indicator of ensuring balance in the system is the constant accumulation of solid waste at intermediate stages of sorting. It is important to understand that achieving 100% performance on all modules of the system is almost impossible, and the total bandwidth will be equal to the bandwidth of the "weak spot" of the system, ie the module with the lowest performance. In the proposed small-scale system of sorting household waste "bottleneck" is the sterilization module, according to the functional scheme, it is at the beginning and thus sets the rate of sorting to avoid the accumulation of solid waste at intermediate levels of the sorting system (Fig. 1) [4].

The most time-consuming in the full sorting cycle is the procedure of sterilization of the material, to save energy of other modules of the system during downtime, a special procedure was developed to put them in standby mode. The following notations of functional modules of the solid waste sorting system were proposed in the paper: 1 module – shredder; 2 module – autoclave; 3 module – magnetic conveyor (Fig. 2); 4 module – magnetic rotor; 5 module – vibrating screen; module 6 – ballistic separator (Fig. 3); 7 module – optical sorting module; and: bunker 1 – designed for rapid unloading of the autoclave, and uniform supply

of material; bunker 2 – designed for storage of plastic and uniform supply of material; bunker 3 – designed for storage of glass and uniform supply of material; conveyor 1 – conveyor for current separation of metals with built-in magnetic rotor; conveyor 2 – conveyor for transporting plastic material to the optical sorting module; conveyor 3 – conveyor for transporting glass material to the optical sorting module (Fig. 4).

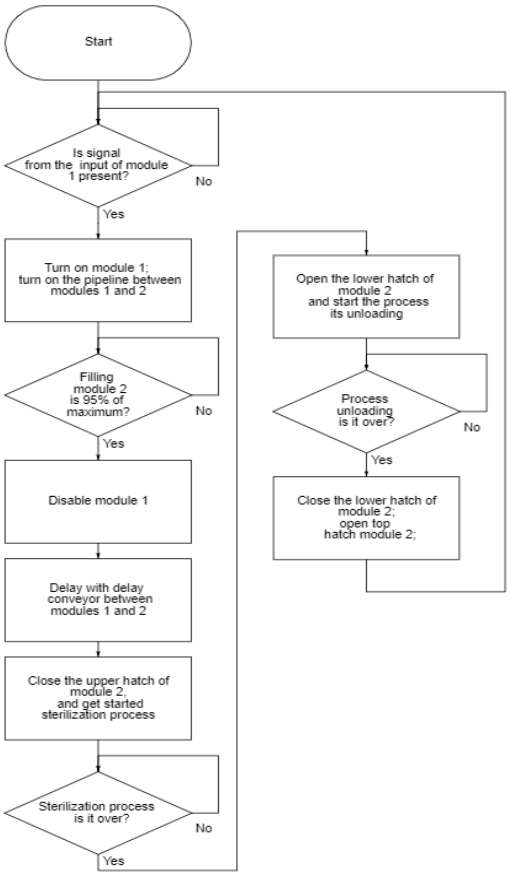

Fig. 1. Algorithm of grinding and sterilization procedure

The sorting system operates according to the following algorithm: Household waste enters the shredder (module 1), where the motion sensor signals the inclusion of a shredder and a conveyor that transports material to the autoclave chamber (module 2). After the autoclave is filled to 95% with the volume sensor, a signal is sent to turn off the shredder (module 1), and the delayed conveyor is switched off, the autoclave (module 2) is closed and the sterilization process begins. After the sterilization process is completed, the conveyor for unloading the autoclave (module 2) is switched on. During unloading, the presence of material inside is monitored in order to start grinding (module 1) of the new batch of material, which will ensure continuous, efficient operation of modules 1 and 2.

Sterilized material from the autoclave (module 2) enters the hopper 1. Then turn on sequentially: feed from the hopper 1, the conveyor for the current separation of metals (conveyor 1), magnetic conveyor (module 3), magnetic rotor (module 4). The trigger for disabling these modules is the absence of material in the hopper 1, and the absence of a signal from the motion sensor after the magnetic rotor (module 3).

After receiving a signal from the motion sensor located behind the magnetic rotor (module 4), the conveyor-conveyor, vibrating screen (module 5), ballistic separator (module 6), conveyor for transporting materials after sorting and conveyor 2 and 3 for optical sorting are switched on, hoppers 2 and 3 supply of sorted materials for optical sorting, optical sorting module (module 7).

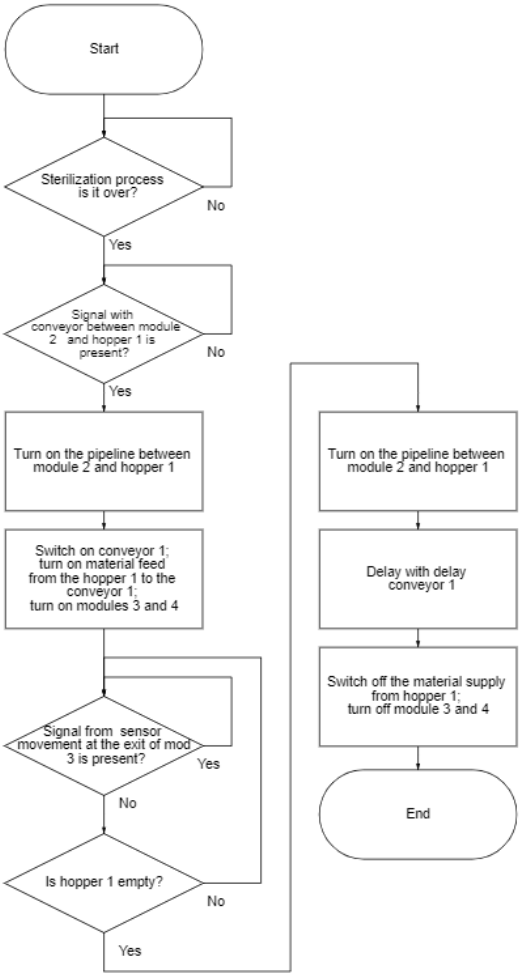

Fig. 2. Algorithm of metal separation procedure

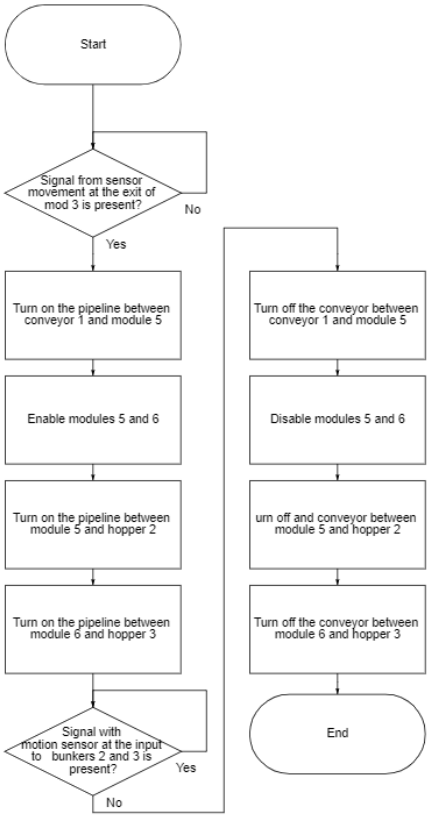

Fig. 3. Algorithm of the procedure of sorting by physical inhomogeneity

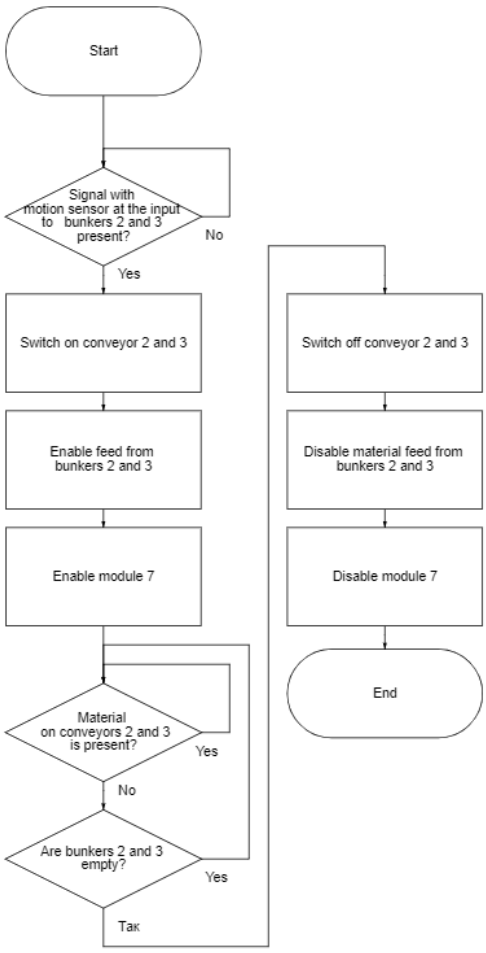

Fig. 4. Algorithm of optical sorting procedure

At the input and output of the vibrating screen (module 5) and the ballistic separator (module 6) the presence of material is detected by a motion sensor, the absence of a signal is a trigger to disable these modules and associated conveyors. The operation of the optical sorting module is controlled by sensors for the presence of material in hoppers 2 and 3, as well as optical control of the presence of material in the recognition area. For the correct operation of all modules, each shutdown of the functional elements of the sorting system solid waste is carried out with a delay. The functional diagram of the system also shows the main parameters of the modules, which will be displayed on the control monitor during operation, and can also be adjusted automatically or manually [5].

2. Development of a functional diagram of a small-sized automated system for sorting household waste

Consider the functional diagram of a small system of sorting household waste. In order to facilitate the presentation of information, the functional diagram was divided into several contours [3].

Contour of grinding and sterilization. At the discrete signal from the controller (pos. 1-1), the shredder (module 1) is switched on and enters standby mode. Analog motion sensor (pos. 1-2) monitors the presence of material at the inlet to the shredder, when solid waste enters the area of the motion sensor (pos. 1-2), the conveyor and shredder go from standby mode to operating mode. The shredder shaft speed is monitored by an analog speed sensor (pos. 1-3) and controlled by a discrete controller (pos. 1-4). Similar sensors (pos. 2-2, 2-3) were used to control the conveyor speed. Filling the autoclave (module 2) is measured by an analog acoustic level sensor (pos. 3-6), after filling the autoclave by 95%, a discrete signal is given to turn off the shredder (pos. 1-1), as well as turning off the conveyor with a delay -1). After the conveyor stops working, the autoclave closes and the sterilization process begins. The pressure in the autoclave chamber is controlled by means of an analog pressure sensor (pos. 3-2). In combination with the temperature sensor (pos. 3-3) the autoclave maintains a constant temperature. The speed of mixing of household waste is controlled by the analog speed sensor (pos. 3-5), and regulation by the discrete controller (pos. 3-6). After sterilization and unloading of the autoclave is completed, the autoclave level sensor (pos. 3-6) sends an electrical signal to the autoclave controller (pos. 3-1) and the shredder controller (pos. 1-1), which puts them in standby mode (Fig. 5) [4].

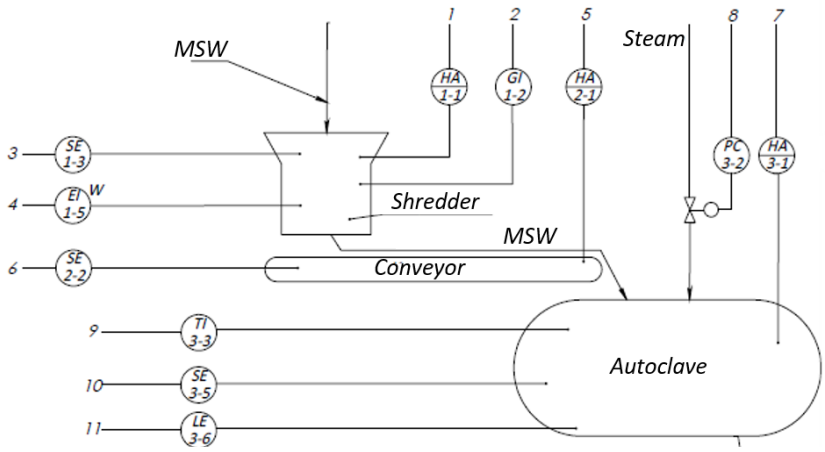

Fig. 5a. Contour of grinding and sterilization

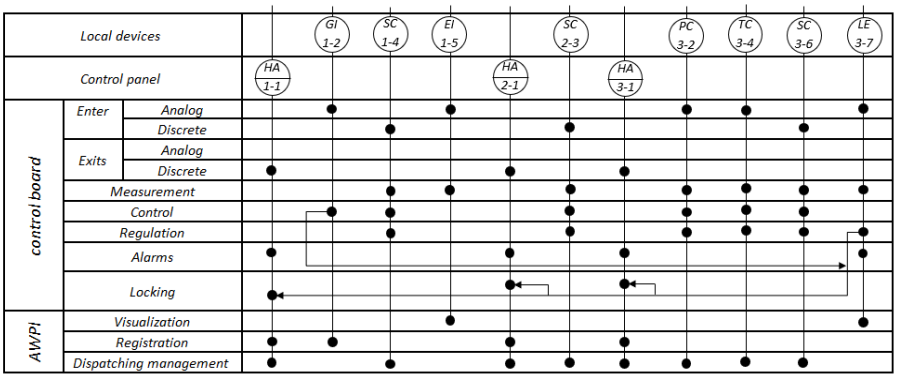

Fig. 5b. Contour of grinding and sterilization

Metal separation contour. The level sensor (pos. 3-6) sends a switch-on signal to the conveyor controller (pos. 4-1). To control the speed of the conveyor used sensors (pos. 4-4,4-5), similar to those described above. Analog motion sensor (pos. 4-4) monitors the presence of material on the conveyor belt, if any, sends a signal to: controller (pos. 5-1) of the hopper of the dispenser (hopper 1), controller (pos. 6-1) of the modified conveyor (conveyor 1) with magnetic rotor (module 4) and controller (pos. 7-1) of the magnetic conveyor (module 3) (Fig. 6).

The control of the feed rate from the dispenser hopper is carried out by an analog speed sensor (pos. 5-3), and control by a discrete controller (pos. 5-4). The speeds of the modified conveyor (pos. 6-2, 6-3), the magnetic rotor (pos. 6-4, 6-5) and the magnetic conveyor (pos. 7-2, 7-3) are controlled similarly. The signal to turn off the modules of the metal separation contour is formed from the logical multiplication of signals from the motion sensor (pos. 4-4) at the inlet to the hopper of the dispenser, and the signal of no material on the modified conveyor coming from the sensor (pos. 6-6).

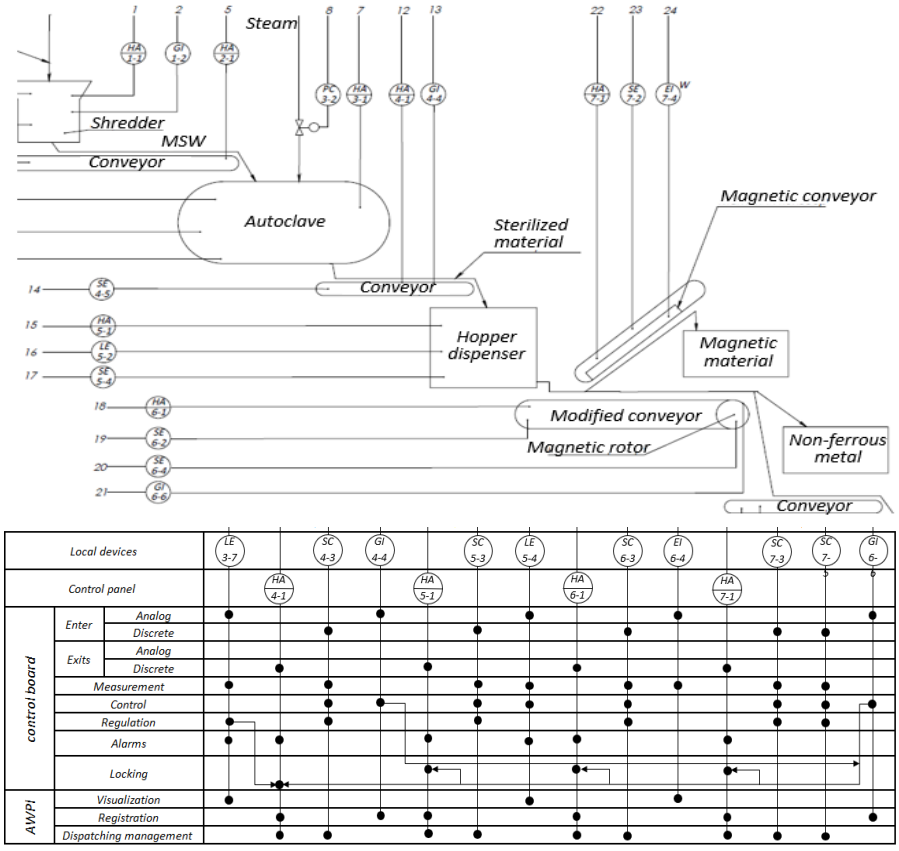

Fig. 6. Metal separation contour

Sorting contour according to the physical heterogeneity of the material. The motion sensor on the modified conveyor (pos. 6-6) sends the activation signal to the controllers of the modules of the sorting contour according to the physical heterogeneity of the material: conveyor controller (pos. 8-1), vibrating screen controller (module 5) (pos. 9-1), controller ballistic separator (module 6) (pos. 10-1) and controllers of plastic selection conveyors (pos. 11-1) and glass (pos. 12-1) (Fig. 7).

To control the speed of the conveyors in this contour of sorting modules by physical inhomogeneity of the material used sensors: (pos. 8-2, 8-3) for the conveyor before the vibrating screen, (pos. 11-2, 11-3) for the plastic selection conveyor and the selection conveyor glass (pos. 12-2, 12-3). Regulation and control of physical parameters of the vibrating screen and ballistic separator is carried out by controlling the speed of electric motors. Accordingly, for the vibrating screen this function is performed by sensors (pos. 9-2, 9-3), and for the ballistic separator sensors (pos. 10-2, 10-3) Motion sensors on the plastic selection conveyor (pos. 11-4) and motion sensors on the glass selection conveyor (pos. 12-4) are responsible for the transfer of modules and conveyors included in the physical inhomogeneity sorting contour. If there is no material on the conveyors, the operation of the modules will be stopped.

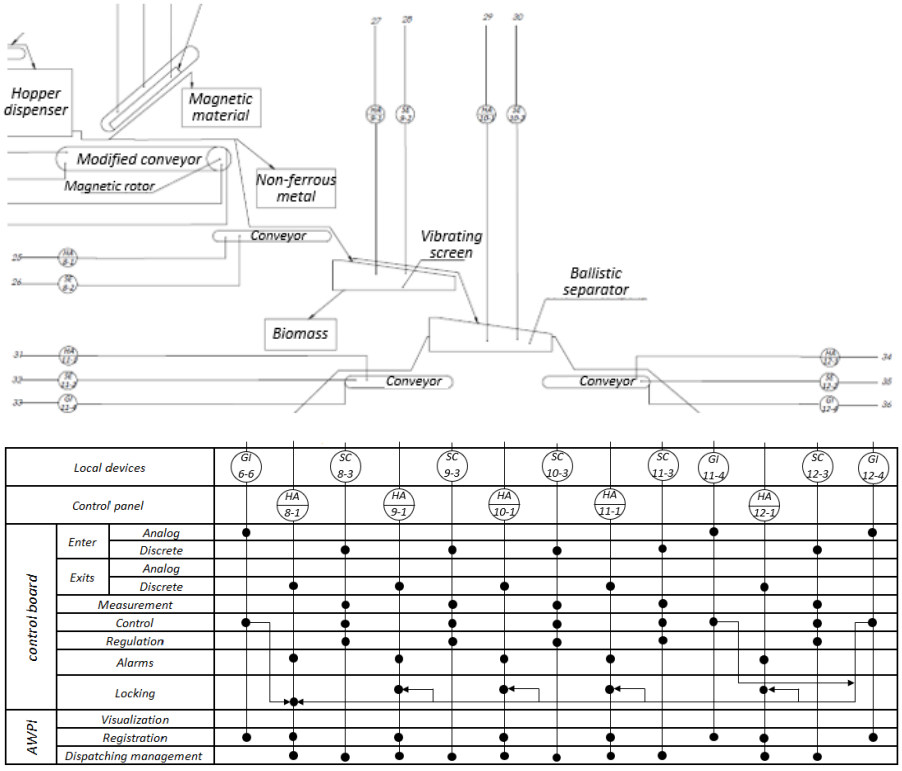

Fig. 7. Sorting contour according to the physical heterogeneity of the material

Optical separation contour. After passing the material through the motion sensors (pos. 11-4 and pos. 12-4) on the conveyors, on the controllers of the optical separation contour modules, an on signal is given: plastic supply from the plastic hopper (hopper 2) is switched on (controller pos. 13-1); the supply of glass from the hopper for glass material (hopper 3) (controller pos. 14-1) is switched on; as well as the plastic transportation conveyor (conveyor 2) (controller pos. 15-1) and the glass transportation conveyor (conveyor 3) (controller pos. 16-1); optical sorting module (module 7) (controller pos. 17-1) (Fig. 8).

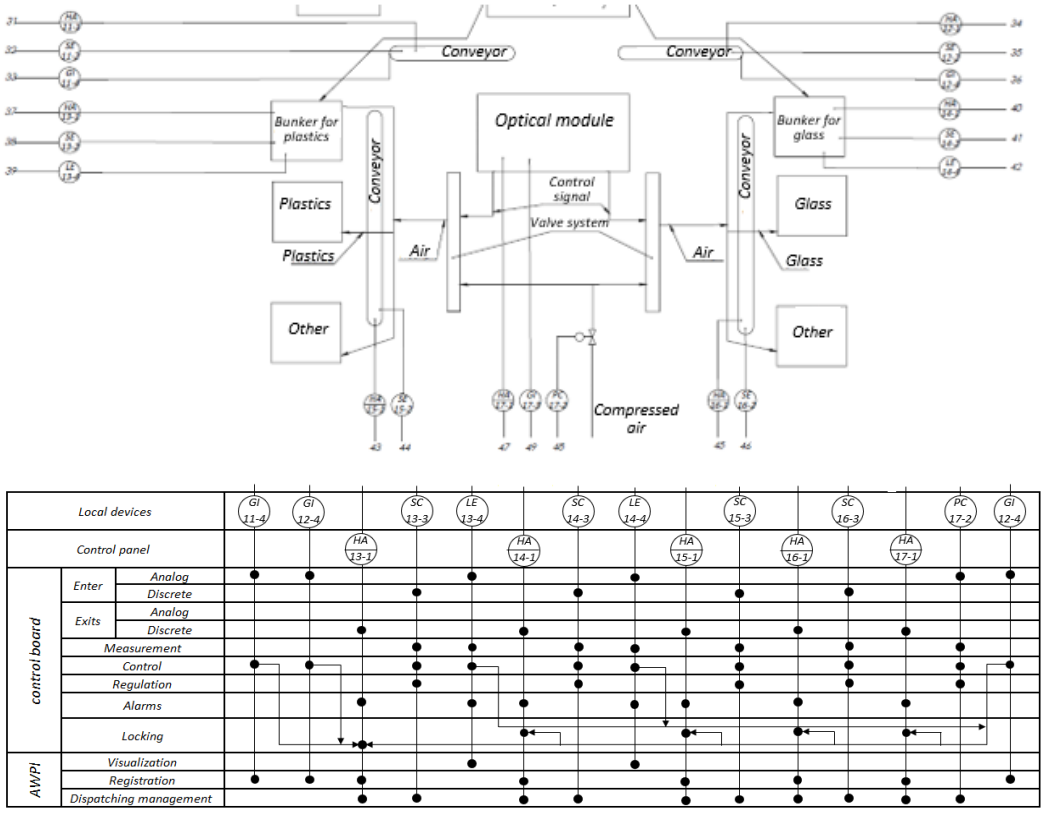

Fig. 8. Optical separation contour

Control of conveyor speeds in this contour is carried out by means of the corresponding sensors: for the conveyor of transportation of plastics (sensors pos. 11-2, 11-3), for the conveyor of transportation of glass (sensors pos. 12-2, 12-3). Also in the optical module there is a pressure control (pressure gauge pos. 17-2) of compressed air for sorting valves. The signal about the absence of material in the hoppers of glass and plastic with level sensors (pos. 13-4 for the hopper with plastic and pos. 14-4 for the hopper with glass), in combination with the signal about the absence of material on the conveyors, form a command to switch to expectations for all components of the optical separation contour.

3. Summary

Algorithms and a functional diagram of a small-sized solid waste sorting system have been developed. The absence of increased requirements for the positioning accuracy of the system modules makes it possible not to use highly qualified workers during installation work. Automation and high quality components of the sorting system provides high reliability and durability. In addition, the technological design of the modules allows you to quickly replace worn parts, which improves the efficiency and performance of the system as a whole. Under normal use, the small sorting system is able to work around the clock, and the quality of the sorted material does not decrease over time. In the perspective of further research, it is advisable to improve the hardware part of the management in order to increase the efficiency of the sorting system.

References

[1] Belman O. I., Stelmakh N. V.: Automated waste sorting system based on visual spectrometry. New directions in the development of instrumentation: Proceedings of the 13th International Scientific and Technical Conference of Young Scientists and Students. BNTU, Minsk 2020, 4.
[2] Gundupalli S. P., Hait S., Thakur A.: A review on automated sorting of source-separated municipal solid waste for recycling. Waste Manag. 60, 2017, 56–74. [http://doi.org/10.1016/j.wasman.2016.09.015].
[3] Mastenko I. V., Stelmakh N. V.: Generative design of a frame type construction. KPI Science News 2, 2021, 81–89 [http://doi.org/10.20535/kpisn.2021.2.236954].
[4] da Silva D. J., Wiebeck H.: Current options for characterizing, sorting, and recycling polymeric waste. Prog. Rubber Plast. Recycl. Technol. 36, 2020, 284–303 [http://doi.org/10.1177/1477760620918603].
[5] Stelmakh N., Sapon S., Belman O.: Automated plastic waste sorting module. Technical Sciences and Technologies 1(23), 2021, 37–44.

Ph.D. Nataliia Stelmakh
e-mail: n.stelmakh@kpi.ua

Associate professor in Department of Device Production at the Faculty of Instrumentation Engineering, National Technical University of Ukraine „Kyiv Polytechnic Institute". Author and co-author of more than 50 scientific papers, 10 patents for utility models. Research interests: automation and computer-integrated technologies, assembly of devices and preparation of production.

http://orcid.org/0000-0003-1876-2794

M.Sc. Oleg Belman
e-mail: o_belman@ukr.net

Master of Automation and Computer Integrated Technologies, design engineer at the Progresstech Ukraine. Author of 5 scientific papers. Research interests: automation and computer-integrated technologies, green technology, design and engineering

http://orcid.org/0000-0003-4636-2587

http://doi.org/10.35784/iapgos.2918 *received: 10.04.2022 | revised: 04.06.2022 | accepted: 15.06.2022 | available online: 30.06.2022*

METHOD FOR EVALUATION QUALITY PARAMETERS OF TELECOMMUNICATIONS SERVICES

Valentyn Zablotskyi, Yosyp Selepyna, Viktor Lyshuk, Natalia Yakymchuk, Anatolii Tkachuk
Lutsk National Technical University, Faculty of Computer and Information Technologies, Department of Electronics and Telecommunications, Lutsk, Ukraine

Abstract. *Currently, cellular networks have become widespread, the operators of which simultaneously use the infrastructure of the second generation GSM networks, DCS to build third generation W-CDMA networks that provide broadband multiple access with code division. At the same time, the problem of providing high-speed Internet connections is exacerbated due to the growing volume of data of diverse types transmitted over the Internet. When testing the entire network coverage area, the total number of voice calls increases, so a method of long-term measurement of bit rate of information transmission via wireless communication channels is proposed, which does not increase the service information in the network. Mathematical modeling of Internet traffic consumption using the proposed measurement method is performed and entropy estimates of information channel bandwidth are given.*

Keywords: communication channel, mobile network, subscriber, internet connection, bit rate

SPOSÓB OCENY PARAMETRÓW JAKOŚCI USŁUG TELEKOMUNIKACYJNYCH

Streszczenie. *Obecnie upowszechniły się sieci komórkowe, których operatorzy jednocześnie wykorzystują infrastrukturę sieci drugiej generacji GSM, DCS do budowy sieci W-CDMA trzeciej generacji, które zapewniają szerokopasmowy wielokrotny dostęp z podziałem kodowym. Jednocześnie problem zapewniania szybkich łączy internetowych jest nasilany przez rosnącą ilość danych różnego typu przesyłanych przez Internet. Przy testowaniu całego obszaru pokrycia sieci wzrasta sumaryczna liczba połączeń głosowych, dlatego proponuje się metodę długoterminowego pomiaru przepływności transmisji informacji kanałami komunikacji bezprzewodowej, która nie zwiększa informacji o usłudze w sieci. Przeprowadzane jest matematyczne modelowanie zużycia ruchu internetowego przy użyciu proponowanej metody pomiaru i podane są entropijne estymacje przepustowości kanału informacyjnego.*

Słowa kluczowe: kanał komunikacji, sieć komórkowa, abonent, połączenie internetowe, przepływność

Introduction

Currently, cellular networks have become widespread, the operators of which use the infrastructure of the second generation network GSM, DCS to build third generation networks W-CDMA, providing broadband multiple access with code division. At the same time, both types of networks work simultaneously, complementing each other. The second-generation networks are mostly voice calls, and the third-generation networks are mostly traffic. To ensure a high level of communication networks service quality, operators have to constantly test existing systems. Hardware and software systems from manufacturers such as Ericsson, ASCOM, Rohde & Schwartz are used to test the networks. These complexes are able to perform measurements in both 2G and 3G networks [2].

A significant disadvantage of such complexes is the mandatory presence of qualified operators at the control panel of the measuring complex. The exception is the TEMS Automatic complex, which collects data from the subscriber terminal without the user's knowledge, and there are restrictions. For example, when testing an active connection, funds from the subscriber's account will be spent. Also, for testing a certain sector, it is necessary that the subscriber is in this sector.

1. Literature review

One of the important parameters that affect the quality of communication is the bit rate of the Internet connection. The problem of providing high-speed Internet connections is exacerbated by the growing amount of data transmitted over the Internet. Wireless networks are now very actively used for watching movies in streaming mode, as well as for visiting social networks, where information pages are heavily overloaded with graphic information. For comfortable work on the Internet at the moment speeds of 1.5...2 Mbit/s are necessary. In light of the above, the requirements for the quality of the data channel, as well as the stability of technical and operational characteristics of cellular networks are increasing [7].

An important task is to monitor the speed of the Internet connection, which is currently used to ensure various Internet resources, such as the speed test provided by nPerf or SpeedTest.net. These services allow you to quickly determine the speed of the Internet connection but have a number of significant limitations, such as a limited number of requests per day, the inability to test the speed of the Internet connection without user participation (Automated testing), the inability to arbitrarily change the test size package. In this regard, there is a need to develop a test system that is independent of any external services [10].

Currently, telecommunications are developing rapidly. One of the most important areas of development is cellular communication. In recent decades, there has been a sharp jump in increasing the capacity of the designed communication networks. For example, the second generation GSM system – Global System for Mobile Communications with add-on packet data GPRS (General Packet Radio Services), and then Enhanced Data rates for GSM Evolution) has a maximum bandwidth of 474 kbps in packet switching mode (8 slots × 59.2 kbit on the coding scheme MCS-9). Further development of cellular communication has led to the emergence of third-generation communication systems UMTS (Universal Mobile Telecommunications System – Universal Mobile Telecommunications System). UMTS, using the development of WCDMA (English Wideband Code Division Multiple Access – broadband multiple access with code division), allows you to maintain the data rate at a theoretical level up to 21 Mbps. when using HSPA + (High-Speed Packet Access – high-speed packet data) in multi-channel mode [1, 5].

Currently, the highest speeds are considered to be 384 kbps for mobile stations of R99 technology and 7.2 Mbps for HSDPA stations (High-Speed Downlink Packet Access) in data mode. from the base station to the mobile terminal. Data transfer speeds in third-generation networks are hundreds of times faster than data rates in second-generation networks. As a result, you can comfortably browse the Web, stream movies, and listen to multimedia resources.

However, the second-generation GSM network currently has a much larger coverage area than the third-generation W-CDMA network. In addition, second-generation subscriber terminals are characterized by the low cost of manufacture and ease of maintenance. In this regard, there is a double situation where two generations of cellular communication coexist and operate simultaneously: the existing GSM network is used for voice information, and the third generation W-CDMA network is used mainly for data transmission (Internet traffic). The third generation of cellular communication systems has much higher bandwidth then the radio channel and therefore has a much higher

data rate. Therefore, the third generation of WCDMA communication is used mainly for broadband Internet access, as well as for video calls and streaming movies. These systems can operate simultaneously without interfering with each other, as they have different frequency ranges [3, 11].

2. Researches methodology

To assess the quality of services to the end-user, a large number of parameters of data transmission are studied, but the level of consumer satisfaction with the received service, regardless of the data transmission technology used, is based on the following parameters:

- criterion "availability of communication", which meets such a quality indicator as to the share of successful calls from the total number of calls when establishing a connection with a subscriber of both mobile and fixed networks. The share of successful calls is estimated from measurements of the number of successful and unsuccessful calls created by network subscribers in the direction of network subscribers and fixed-line subscribers.

$$P_y = \frac{Q}{N} \quad (1)$$

N – the total number of control calls for all measurement sessions,

Q – the total number of successful control calls for all measurement sessions.

- the criterion of "continuity of communication", which meets such a quality indicator as to the proportion of calls that ended in disconnection at the initiative of the subscriber. The share of calls with scheduled disconnection is estimated from measurements of the number of successful calls and calls with premature disconnection.

$$P_n = \frac{R}{N} \quad (2)$$

R – the total number of control calls that ended in disconnection of the established connection at the initiative of the subscriber.

- the criterion "quality of broadcasting", which meets such an indicator of quality as the share of calls that meet the standards for the quality of broadcasting. The share of calls that meet the standards for the quality of speech transmission is estimated from measurements of the number of calls with satisfactory and unsatisfactory quality of speech transmission.

$$R_y = \frac{N_{np}}{N} \quad (3)$$

N_{np} – the total number of control calls that meet the standards for the quality of broadcast transmission, for all measurement sessions.

Thus, to determine these quality indicators in any part of the network it is necessary to make a large number of voice calls. When testing the entire network coverage area, the total number of voice calls will be very large, which increases the load on the network [1, 4].

Another parameter to which high requirements are placed is the speed of data transfer when a subscriber uses the Internet. For comfortable work on the Internet at the moment speeds of 1.5...2 Mbit/s are enough. The inability of the cellular operator to provide such speeds leads to the fact that subscribers move to competitors who provide higher quality services. In light of the above, the requirements for the quality of the data transmission channel of cellular networks, as well as the stability of the characteristics of the claimed services.

To ensure high-quality services, it is necessary to conduct regular testing and monitoring. Monitoring requires highly qualified specialists as well as specialized measuring systems.

To measure the bit rate, a measurement technique is proposed, which determines the actions of the operator in the measurement process, as well as during the primary processing of the results.

Method of long-term measurement of the bit rate of information transmission via wireless communication channels [5, 12].

The method contains the following items:

1) Select the measurement location.
2) Install the test (testing) tool in the selected location.
3) Carry out daily monitoring of the speed of the Internet connection in an active way, by exchanging data between the server and the test (testing) tool. When performing daily monitoring, it is necessary to register the signal power level and the signal-to-noise ratio brought to the input.
4) Calculate the value of the daily change in bit-rate based on the data obtained about the signal power level and the signal-to-noise ratio brought to the input.
5) Find the maximum value of the bit rate measured by the active method.
6) Find the maximum value of the bit rate.
7) Carry out daily monitoring of the bit rate of the Internet connection in a passive way, by recording the data obtained on the signal power levels and the signal-to-noise ratio brought to the input, at the required time.
8) Calculate the value of the bit rate of the Internet connection.
9) Output information for analysis in text or graphical form.

3. Results

When using the described method according to the above method, there is a significant saving of radio network resources. Consider the cost of traffic for round-the-clock monitoring of bit rate during the week, using the active and passive methods. In Fig. 1 presents the results of mathematical modeling of Internet traffic consumption in MathCAD.

From the graphs presented in fig. 1, it is seen that the total cost of Internet traffic increases when using the standard method, and when using the proposed method remains constant. This is due to the fact that when using the method described above, the flow of traffic occurs only when determining the correction factor on the first day of measurements. Further measurement of the bit rate of the Internet connection takes place without active data exchange, so traffic costs do not increase.

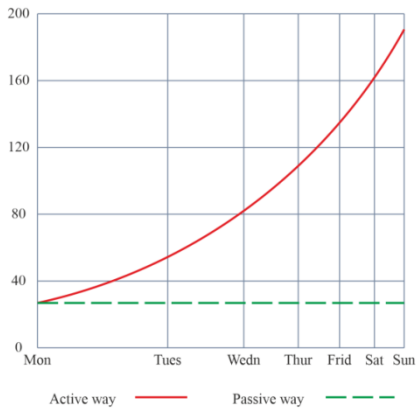

Fig. 1. The results of mathematical modeling of Internet traffic consumption using the known and proposed measurement method

However, during the monitoring, it is necessary to take into account that recently the volumes of traffic transmission (speech, video, data) are starting to significantly exceed the volumes of transmitted voice messages. The statistical characteristics of such heterogeneous traffic can no longer be described using standard distributions. Non-parametric methods should be used to assess the quality parameters of such networks, for example, using information-entropy measures of these distributions.

To quantify the information used logarithmic measure (Hartley measure):

$$I = log a \cdot N \quad (4)$$

I – the amount of information obtained from one count;

N – the number of possible different measurement results by this measuring instrument;

a – a number that determines the unit of information; when $a = 2$ unit of information is called a bit.

1 bit of information is contained in one bit of the binary number. Indeed, one digit can take one of two values: 0 and 1, ie $N = 2$. Then $I = \log 2 + 2 = 1$ bit.

Hartley's formula is valid only when each of the N messages appears with equal probability. The fact is that the information is only a message, not previously known to the recipient of this message. The amount of information in a reliable (in a pre-known message) is zero.

In the general case, the amount of information contained in one message depends on the probability of this message:

$$I_i = log_2\left(\frac{1}{p_i}\right) \quad (5)$$

p_i – the probability of the *i*-th message.

From the above formula it is clear that the less likely the message is received, the more information it carries. If the law of distribution of values of the measured parameter (in the range of change of this parameter) is NOT equally possible, the results obtained in the process of measurements will carry a different amount of information.

For information estimation of the system "researched object-measuring instrument" the concept of entropy is introduced in the information theory. Entropy is the average amount of information per message [9].

To obtain a formula for determining entropy, consider a source of information that can issue N independent discrete messages with probability $p_1, p_2, \ldots, p_i, \ldots, p_N$. Consider a long sequence of m messages ($m >> N$). According to probability theory, each *i*-th message will appear in this order $m \cdot pi$.

Given that each *i*-th message carries information:

$$I_{1i} = \log_2 \frac{1}{p_i} = -\log_{p_i} \quad (6)$$

all received messages will give information:

$$I_{mi} = -m \cdot p_i \cdot \log_2 p_i \quad (7)$$

General information from all m messages will be:

$$I_m = -m \cdot \sum p_i \cdot \log_2 p_i \quad (8)$$

The average amount of information per message, ie the entropy of the source, will be:

$$H = \frac{I_m}{m} = -\sum p_i \cdot \log_2 p_i \quad (9)$$

This formula is called Shannon's formula.

It is easy to see that for all equally possible messages ($p_1 = p_2 = \ldots = p_N$) this formula will turn into a Hartley formula:

$$H = log_2 \cdot N \quad (10)$$

The physical quantity controlled in the process of measurement is, as a rule, a continuous random process characterized by the law of probability distribution $F(X)$ or probability density $\varphi(X)$.

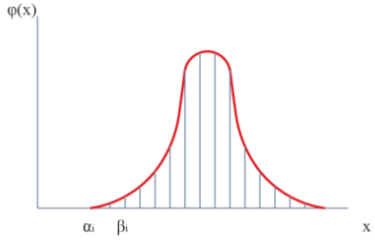

Fig. 2. Distribution of the measured value

To estimate the entropy of the system "signal source – controlled parameter – measuring instrument" it is necessary to take into account the resolution of the device Δx. In this case, the system can be considered as discrete with the interval of a division of the measuring range $X_{max} - X_{min}$ into discrete segments equal to Δx. Denoting by αi and βi the boundaries of the *i*-th partition section (Fig. 2), we can determine the probability of the value of the controlled parameter in this interval:

$$p(a_i < x < \beta_i) = \int_{a_i}^{\beta_i} \varphi(X) dx \quad (11)$$

Determining the probabilities of the values of the parameter in all intervals of the partition, according to Shannon's formula (9), we can obtain an estimate of the entropy in this case.

1. The entropy of the source of information is maximum if all outgoing messages (outputs of the source) are different.
2. Entropy decreases if there is a relationship between outputs.

The entropy of the system $H(X, Y, \ldots)$, consisting of several subsystems having entropies $H(X), H(Y), \ldots$, is equal to the sum of entropies, if the messages of the subsystems do not depend on each other. If there is a dependence, the total entropy is less than the sum of the entropies of the subsystems:

$$H(X, Y, \ldots) \leq H(X) + H(Y) + \cdots \quad (12)$$

1. Information redundancy is manifested in the fact that the information content of messages is less than the resources that allow the transmission of these messages.
2. Information redundancy may be due to the following factors.
3. An excessive number of elements of discrete signals compared to those required for the presentation of data messages. For example, 8-bit binary code is used to transmit text. The number of different characters used in the text – 53: 33 letters, 10 decimal numbers, and 10 auxiliary characters (punctuation marks, parentheses, quotation marks). 6 bits of code (2^6 = 64) are enough to encode all characters, 2 bits are superfluous. They form redundancy.
4. The inequality of the appearance of individual messages. According to the first property of entropy, it decreases. If the source gives 4 different messages and they are different, the entropy according to the Hartley formula will be 2 bits. With different probabilities of messages, for example, 1/2, 1/4, 1/8, 1/8, entropy will be 1¾ bit.
5. The presence of interrelationship between messages. This statement, according to the second property of entropy, also reduces the entropy of messages.

Information redundancy is assessed by the expression:

$$R = \frac{(I_{max} - I)}{I_{max}} = 1 - \frac{I}{I_{max}} \quad (13)$$

I_{max} – the maximum possible entropy value for the selected messaging technology;
I – the true value of entropy.

Information flow is the average amount of information issued by a source per unit of time:

$$\Phi = \frac{I}{T} = \frac{H}{t_1} \quad (14)$$

H – source entropy;
t_1 – time of issuance by the source of one message.

Then the bandwidth of the information channel (communication line, measuring device, including sensor and information display means) is the maximum speed at which the channel can transmit information:

$$C = \left(\frac{I}{T}\right)_{max} = \frac{I_{max}}{T} \quad (15)$$

If at time T the channel can transmit m messages, and the transmission of each message occurs at time t_1, the formula (15) can be represented as:

$$C = m\frac{H_{max}}{m \cdot t_1} = \frac{H_{max}}{t_1} \quad (16)$$

H_{max} – maximum entropy that messaging resources can have (determined by Hartley's formula).

When sending messages in binary code, you can write:

$$C = \frac{H_{max}}{\alpha \cdot \tau} = \frac{n}{n \cdot \tau} = \frac{1}{\tau} \quad (17)$$

n – the number of bits of the code combination; τ – the time of transmission of one bit of code; H_{max}– code entropy (equal to the number of bits in the code combination).

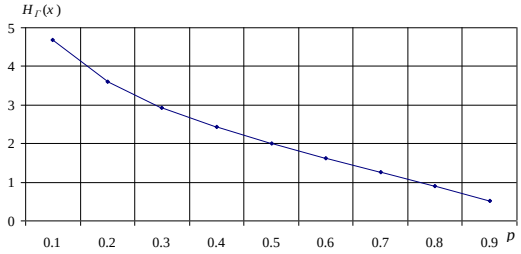

Fig. 3. Dependence of entropy of geometric distribution on probability of success of transfer p

The dependence of the entropy of the geometric separation on the probability of successful data transmission of one of the network nodes was calculated (Fig. 3). It has been seen that with a higher probability of success, the entropy of the distribution decreases, therefore, the required resource for data exchange decreases.

However, this has been achieved only by reducing the likelihood of network congestion. This can be achieved, for example, by limiting such a key performance indicator as to the maximum duration of packets transmitted [6, 8].

For comparison, the dependence of the differential entropy on the standard deviation of the transmission interval from the maximum allowable is calculated (Fig. 4). There is a monotonic increase in entropy, hence the growth of the required resource of data exchange.

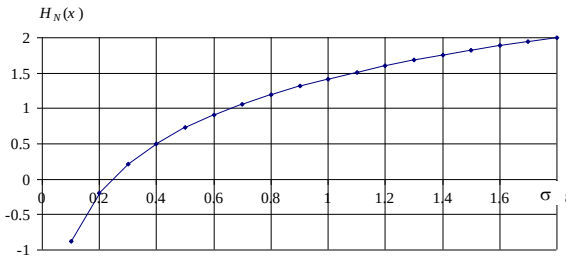

Fig. 4. Dependence of entropy of Gaussian (normal) distribution on standard deviation σ

Note that when calculating entropy measures, you can use different parameters of model distributions. At the same time, comparative estimates based on entropy will be quite universal and clear.

4. Conclusions

The optimal parameters for assessing the quality of service provision in the joint use of second and third-generation networks are selected.

The method of long-term measurement of the bit rate of information transmission through wireless communication channels is offered.

Mathematical modeling of Internet traffic consumption using the proposed measurement method is performed, and it is shown that the proposed method does not lead to excessive creation of service traffic.

Entropy estimates of the bandwidth of the information channel are given.

References

[1] Bakhovsky P., Yevsyuk M.: Some aspects of mobile telecommunication development. Adv. Technol. Dev. 13, 2018, 25–32.
[2] Bakhovskyi P. F., Amirkhanov E. D., Toroshanko Y. I., Khmara K. V.: Analysis of the economic feasibilities of introduction of technologies of VTF in the networks of SAE/EPS. Scientific Notes of the Ukrainian Research Institute of Communication 1(41), 2016.
[3] Bakhovskyy P. et al.: Stages of the Virtual Technical Functions Concept Networks Development. Cagáˇnová D. et al. (eds.): Advances in Industrial Internet of Things, Engineering and Management. EAI. Springer Innovations in Communication and Computing, 2021, 119–135 [http://doi.org/10.1007/978-3-030-69705-1_7].
[4] Bawa M., Cagáňová D.: Selecting network protocols for internet of things based upon innovation and knowledge management. J. Telecommun. Syst. Manag. 7(2), 2018, 1–4 [http://doi.org/10.4172/2167-0919].
[5] Bollini D. B., Naidu M. M., Nuka M. R.: Measurement of Mobile Switching Centres Throughput in GSM Network Integrating Sliding Window Algorithm with a Single Server Finite Queuing Model. Journal of Computer Networks and Communications 2016, Article ID 2061347, [http://doi.org/10.1155/2016/2061347].
[6] Cagáňová D. et al.: Internet of Things and Smart City, 1st ed. University of Zielona Góra, Zielona Góra 2017.
[7] Cagáňová D., Bawa M., Šujanová J., Saniuk A.: Innovation in Industrial Enterprises and Intercultural Management, 1st ed. University of Zielona Góra, Zielona Góra 2015.
[8] Chen C., Liu B., Wan S., Qiao P., Pei Q.: An Edge Traffic Flow Detection Scheme Based on Deep Learning in an Intelligent Transportation System. IEEE Transactions on In-telligent Transportation Systems 22(3), 2021, 1840–1852 [http://doi.org/10.1109/TITS.2020.3025687].
[9] Moroz S., Tkachuk A., Khvyshchun M., Prystupa S., Yevsiuk M.: Methods for Ensuring Data Security in Mobile Standards. Informatyka, Automatyka, Pomiary w Gospodarce i Ochronie Środowiska 12(1), 2022, 4–9 [http://doi.org/10.35784/iapgos.2877].
[10] Saiko V., Naritnik T., Bakhovsky P.: Ultra-fast terahertz radio access channel for 4th and 5th generation mobile networks. Technical news. Sci. J. 1(47), 2(48), 2018, 48–50.
[11] Tkachuk A. et al.: Basic Stations Work Optimization in Cellular Communication Network. Cagáˇnová D. et al. (eds.): Advances in Industrial Internet of Things, Engineering and Management, EAI. Springer Innovations in Communication and Computing, 2021, 1–19 [http://doi.org/10.1007/978-3-030-69705-1_1].
[12] Toroshanko Y., Selepyna Y., Yakymchuk N., Cherevyk V.: Control of traffic streams with the multi-rate token bucket, in International Conference on Advanced Information and Communications Technologies AICT 2019, 2019, 352–355 [http://doi.org/10.1109/AIACT.2019.8847860].

Ph.D. Valentyn Zablotskyi
e-mail: v.zablotsky@lntu.edu.ua

Research interests: Technological support of wear resistance conjugate parts machines and devices working surfaces. Research physical quantities of sensors functional features. Features of the optical communication lines organization and operation.

http://orcid.org/0000-0002-2921-0031

Ph.D. Yosyp Selepyna
e-mail: y.selepyna@lntu.edu.ua

Research interests: Modeling of electronic devices and systems. Digital signal processing and coding in telecommunication systems and networks.

http://orcid.org/0000-0002-2421-1844

Ph.D. Viktor Lyshuk
e-mail: vlyshuk@gmai.com

Research interests: telecommunication networks, radio engineering devices, power supply systems of radio engineering devices and systems.

http://orcid.org/0000-0003-4049-8467

M.Sc. Natalia Yakymchuk
e-mail: n.yakymchuk@lntu.edu.ua

Research interests: diagnostics and control of the telecommunication networks state, end-to-end diagnostics, congestion management.

http://orcid.org/0000-0002-8173-449X

Ph.D. Anatolii Tkachuk
e-mail: a.tkachuk@lntu.edu.ua

Vice-dean for R&D Faculty of Computer and Information Technologies Lutsk National Technical University.
Member of European Alliance for Innovation (EAI), International Association for Technological Development & Innovations (IATDI).

http://orcid.org/0000-0001-9085-7777

http://doi.org/10.35784/iapgos.2950 *received: 08.05.2022 | revised: 10.06.2022 | accepted: 15.06.2022 | available online: 30.06.2022*

NEW METHOD OF ON-LINE SUCCESSIVE-APPROXIMATION ADC CALIBRATION

Serhii M. Zakharchenko[1], Tetiana I. Korobeinikova[2], Aigul Tungatarova[3], Bakhyt Yeraliyeva[3]
[1]Vinnytsia National Technical University, Faculty of Information Technologies and Computer Engineering, Vinnytsia, Ukraine, [2]Lviv Polytechnic National University, Institute of Computer Technologies, Automation and Metrology, Lviv, Ukraine, [3]M. Kh. Dulaty Taraz Regional University, Taraz, Kazakhstan

Abstract. *A new method of successive approximation ADC calibration without interruption of the main conversion process is proposed. The method is based on the use of information redundancy in the form of redundant positional number systems. The method is based on the selection and analysis of unused combinations in the redundant ADC conversion characteristic.*

Keywords: analog-to-digital converter (ADC), successive-approximation algorithm, self-calibration, redundant number systems, ADC transfer function

NOWA METODA KALIBRACJI ON-LINE PRZETWORNIKA AC METODĄ KOLEJNYCH APROKSYMACJI

Streszczenie. *Zaproponowano nową metodę kalibracji przetwornika AC z aproksymacją sukcesywną bez przerywania głównego procesu konwersji. Metoda opiera się na wykorzystaniu redundancji informacji w postaci redundantnych systemów liczb pozycyjnych. Metoda opiera się na selekcji i analizie niewykorzystanych kombinacji w charakterystyce redundantnej konwersji AC.*

Słowa kluczowe: *przetwornik analogowo-cyfrowy (AC), algorytm kolejnych aproksymacji, samokalibracja, redundantny system liczbowy, funkcja przetwarzania przetwornika AC*

Introduction

Successive approximation ADCs have found wide application in information-measuring, data collection and processing, voice and video processing systems. However, when the resolution of the ADC is more than 12 bits, the problem of ensuring the conversion accuracy appears. This is the result of ADC bits deviations under the influence of environmental factors (temperature, humidity, pressure). The ways to overcome this problem can be divided into technological and algorithmic. The technological methods are cost- and time-consuming, and provide the ability to improve the linearity by several bits. A more universal method of overcoming this problem is to use the procedure of ADC bits calibration [4, 5, 9]. The calibration procedure is performed after turning on the device and periodically is repeated during operation, and the ADC can operate either in the main conversion or calibration mode. The use of weight redundancy in the successive approximation ADC permits to make the calibration procedure exclusively in digital form without physical or electrical impact on the ADC digits [1]. Weight redundancy may be used for compensation the dynamic errors in the process of analog-to-digital conversion [6, 7]. However, the problem of on-line correction (without interrupting the main conversion process) of the ADC bits remains actual. One of the possible solutions is using split architecture [14], but it involves using of several identical ADCs. The work [13] shows the possibility of cyclic ADC on-line calibrating by analysing the transfer function. The principal opportunity of on-line calibration redundant ADC was proved in [12]. The single bit deviations determining process for redundant ADC was considered in [11].

1. Successive approximation ADC transfer function analysis

The successive approximation algorithm provides the sequential determination of the output code bits from most significant bit (MSB) to least significant (LSB). The results of the algorithm operation for any input signal are demonstrated by the ADC transfer function (TF). The mathematic representation of ADC TF shows the expression (1) [2, 3, 10]

$$A(K^s) = \sum_{i=0}^{n-1} a_i \cdot Q_i, \qquad (1)$$

where K – code combination, s – the number of code combination (decimal notation of binary combination), n – ADC resolution, $Q_i = \alpha^i(1+\delta_i)$ – bit value with number i, where α – radix, δ_i – i-bit deviation, $a_i \in \{0,1\}$ – bit values of K.

The graphical interpretation of (1) for n = 5 and different radixs is shown in Fig. 1

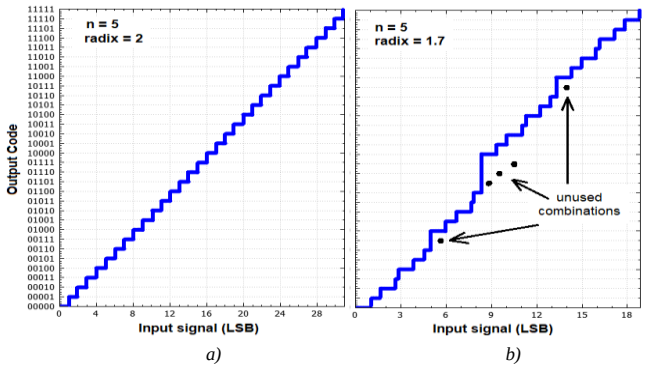

Fig. 1. Transfer function of n-bit successive approximation ADC for a) radix equal 2; b) radix equal 1.7

When using the binary number system, the TF has the form of a regular staircase (Fig. 1a), and all possible code combinations are used to form the output code. When using a number system with a radix less than 2, some code combinations fall out of the TF. For example, in Fig. 2 these are five combinations: 00111, from 01101 to 01111 and 10111. In [9] it is proposed to call them "unused" (UnC). Other combinations will be calling "used" (UC). The expression (2) determines if the combination belongs to unused category or not [8, 10]:

$$A(K_{UC}^{m-1}) < A(K_{UC}^{l})) \le A(K_{UnC}^{m}), \qquad (2)$$

where the input analog signal values correspond to the UC with the numbers m-1 and l, while the UnC with the number m and l > m.

In [11] it is shown that UnC form certain groups, called "unused combinations zones" (UnC zone). Each UnC zone has its own boundaries (from K_{UnC}^{m} to K_{UnC}^{l-1}) and is located in a certain place of the TF. In the central part of the TF there is a zone of the (n-1)-th level (in figure 1 these are three combinations from 01101 to 01111), in the same figure there is a zone of the (n-2)-th level, consisting of two subzones. The first subzone, which is located in the lower half of the TF, includes the combination 00111, the second subzone contains the combination 10111. The quantity of UnC in certain zone or subzone may be calculated as *l-m.*

The relationship between the number of UnC zone Nz, ADC radix and ADC resolution n is shown in Tab. 1

Table 1. The relationship between the number of UnC zone Nz, ADC radix resolution

α	1.618÷1.839	1.840÷1.928	1.929÷1.966	1.967÷1.984
Nz	n-3	n-4	n-5	n-6

2. The influence of ADC bit's deviations on TF

K_{UC}^{l} in (2) is a top border combination of certain zone (subzone). It's value is fixed and it is independent of ADC radix. For (n-1)-th level zone K_{UC}^{l} value equal 100…0 (10000 combination on Fig. 1b), for (n-2)-th level zone – 0100…0 (first subzone, 01000 combination on Fig. 1b) and 1100…0 (second subzone, 11000 combination on Fig. 1b). Therefor the location of the border combination on TF is defined only most significant bits (MSB) values. On the other hand the location of UnC is depends on least significant bits values (combinations 01111, 01110 and 01101 on Fig. 2b). If the MSB's value will be changed, the mutual location of border combinations and UnC will be changed too. As a result some UnC may transfer to used category and vice versa. The influence of -10% and +10% MSB deviation on TF is shown on Fig. 2.

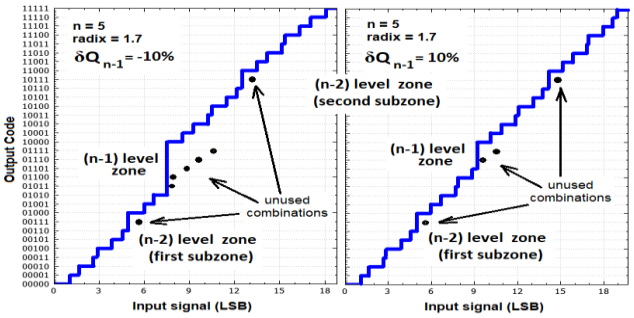

a) b)

Fig. 2. Transfer function of 5-bit successive approximation ADC for radix equal 1.7 with MSB deviation a) -10% ; b) +10%

Fig. 2 demonstrates, that MSB deviation affects only on UnC quantity in (n-1) th level zone, but has not effect on other level zones.

The relationship between MSB deviation and the UnC quantity may be calculated after substitution (1) to (2):

$$\frac{\sum_{0}^{n-2} a_i \alpha^i}{\alpha^{n-1}} - 1 < \delta_{n-1}^{p_{n-1}} \le \frac{\sum_{0}^{n-2} b_i \alpha^i}{\alpha^{n-1}} - 1, \tag{3}$$

where a_i and b_i are code combinations bits of K_{UC}^{m-1} and K_{UnC}^{m}, p_{n-1} is the UnC quantity in the (n-1)-level zone.

The generalized rule of relationship between k-bit deviation and UnC quantity in the j-level zone will be:

If j < k: the k-bit deviation does not influence on UnC quantity in the j-level zone;

$$\text{If j = k: } \frac{\sum_{0}^{j-1} a_i \alpha^i}{\alpha^k} - 1 < \delta_k^{p_j} \le \frac{\sum_{0}^{j-1} b_i \alpha^i}{\alpha^k} - 1, \tag{4}$$

$$\text{If j>k: } \frac{\alpha^j - \sum_{0}^{j-1} a_i \alpha^i}{\alpha^k} > \delta_k^{p_j} \ge \frac{\alpha^j - \sum_{0}^{j-1} b_i \alpha^i}{\alpha^k}. \tag{5}$$

Since different bit deviations have influence on different UnC zones, it is important to estimate the sensitiveness of the certain zone to different bit deviations.

Equation (6) demonstrates the ratio of $\delta_{n-1}^{p_{n-1}}$ influence to $\delta_{n-2}^{p_{n-1}}$:

$$\frac{\delta_{n-1}^{p_{n-1}}}{\delta_{n-2}^{p_{n-1}}} = \frac{\sum_{0}^{n-2} a_i \alpha^i}{\alpha^{n-1}} - 1 \Bigg/ \frac{\alpha^{n-1} - \sum_{0}^{n-2} a_i \alpha^i}{\alpha^{n-2}} = -\frac{1}{\alpha} \tag{6}$$

So the largest influence on j-level UnC zone has the j-bit deviation. The (j-1)-bit deviation has $-\alpha$ times less influence. Sine "-" indicates the different change direction: positive j-bit deviation results in reducing the UnC number in j-level zone, but results in increasing the UnC number in (j+1)-level zone.

3. The bit's weights calculation algorithm

In the case of simultaneous different bit's deviations the step by step calculation algorithm may be used.

Step 1. Define the number of least UnC level zone with UnC quantity change and assign it to variable j.

Step 2. Calculate the minimum and maximum values of j-bit deviations:

$$\delta_{j\min}^{p_j} = \frac{\sum_{0}^{j-1} a_i Q_i}{\alpha^j} - 1, \tag{7}$$

$$\delta_{j\max}^{p_j} = \frac{\sum_{0}^{j-1} b_i Q_i}{\alpha^j} - 1. \tag{8}$$

Step 3. Calculate the mean value of the of the j-bit deviation:

$$\delta_j^{p_j} = \frac{\delta_{j\min}^{p_j} + \delta_{j\max}^{p_j}}{2} \tag{9}$$

Step 4. Calculate the correct value of the j-bit:

$$Q_j = \alpha^i (1 + \delta_j^{p_j}) \tag{10}$$

Step 5. Recalculate j = j+1, if j < n go to Step2, j = n – calculation finished.

The results of algorithm realization for 6-bit ADC illustrated in Tab. 2

Table 2. The results of algorithm realization for 6-bit ADC

Bit number	0	1	2	3	4	5
Bit weight (LSB)	1	1.7	2.89	4.91	8.35	14.20
Bit weight real deviation (%)	0	0	0	5	-10	5
Bit weight estimated deviation (%)	0	0	0	3.6	-12.7	2.7
Estimation error (LSB)	0	0	0	-0.07	-0.22	-0.33

4. Method realization

For method realization the redundant successive approximation ADC structure [4] has been modified, so the new unit has been added (Fig. 3).

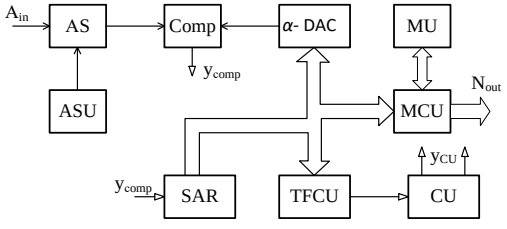

Fig. 3. Redundant successive approximation ADC with transfer function control unit

The main ADC units: AS – analog switch for input or auxiliary signal commutation on comparator input; ASU – auxiliary signal unit generates auxiliary signal for initial calibration; α-DAC – redundant DAC; MU, CU and MCU – memory unit, control unit and main computing unit are used for

algorithm realization. The transfer function control unit (TFCU) is a new block that used for unused combinations identification.

Simplified algorithm of redundant successive approximation ADC functioning with transfer function control illustrates on Fig. 4.

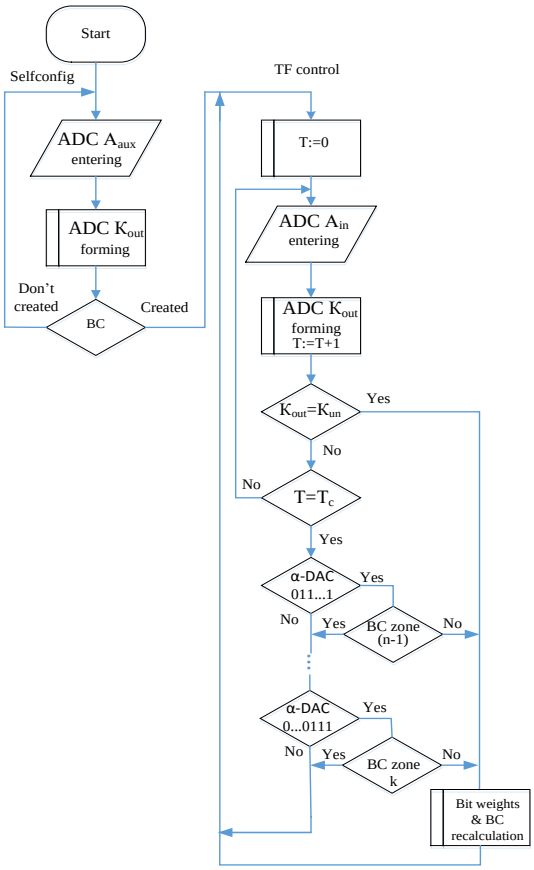

Fig.4. Redundant successive approximation ADC with transfer function control algorithm

Algorithm consists of two parts: self-configuration (Selfconfig) and main ADC conversion with transfer function control (TF control). Self-configuration is the first step after ADC turns on. The ASU generates linearly increasing signal which is converted by ADC. The aim of this phase is a border combination (BC) finding. The border combination is a last used combination before cortege of unused combinations (bottom BC), or first used combination after cortege of unused combinations (top BC). When all BCs pares are created the main ADC conversion phase with TF control begins.

During this phase the input signal converted to digital code TFCU instantly controls the transition of unused combinations in used category and vice versa. UnC to UC transition control is very simple because all BC pairs are created during Selfconfig phase. Every α-DAC code is checked if it belongs to unused combination zones ($K_{out} = K_{un}$). In the case of positive result the bit's weights calculation algorithm starts and new bit weights are calculated. BCs are renewed too.

The UC to UnC transition control is more complicated because it foresees the control of non-appearance of UC, when it must appear. The first applicants on UC to UnC transition are bottom border combinations. On the other side it is necessary the appearance of corresponding value of A_{in} on the ADC input. To control the transition of bottom border combinations to unused category, TFCU identifies the situations when top BC has appeared, but bottom BC has not appeared during control time interval T_c. It may be possible because

$$A(K_{tBC}) - A(K_{bBC})) \le 1LSB, \qquad (11)$$

where K_{tBC} and K_{bBC} are top and bottom border combinations for the same UnC zone.

5. Transfer function control unit realization

Transfer function control unit is a main specific unit on the Fig. 3. It must:

1) Ensure the fixation of the bottom border combination obtained in the process of self-configuration.
2) Select only combinations that are included or may be included in the proper zone of unused combinations.
3) Organize the comparison of the input combination, which was marked in item 2 with border combination fixed in item 1.
4) Ensure the formation of the control signal in case of transition of the unused combination to the category of used and vice versa.

TFCU consist of different subunits. Possible realization of control subunit for traversing UnC zones by the input signal illustrates on Fig. 5.

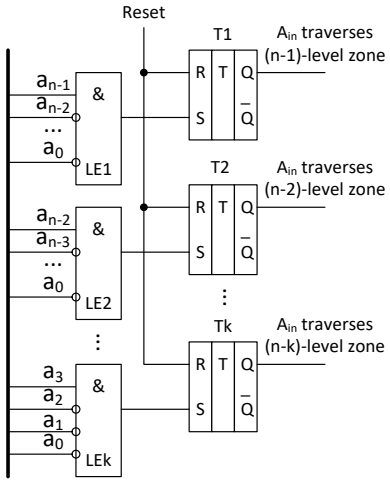

Fig. 5. Control subunit for traversing UnC zones by the input signal

Both: Logical element LEi and RS-trigger Ti – control the input signal traversing via the UnC (n-i)-level zone. The quantity of LE-T pairs corresponds to the number of UnC zones. It is important that LEi chooses all top border combinations from all subzones (n-i)-level zone.

Another TFCU subunit illustrates on Fig. 6.

Zone combinations filter is used for selection of combinations which situated or may be situated in the zone of unused combinations of appropriate level (in this sample (n-2)-level of 6-bit ADC). A common feature of all these combinations are fixed values of the (n-2)-nd and (n-3)-rd bits, they are "0" and "1" respectively. This combination allows the commutation of lower bits of these code combinations at the inputs A of the comparator. The other comparator inputs receive the values of least significant bits of actual bottom border combination. In fact "1" on the A>B comparator output indicates that combination transits from UnC category to UC category.

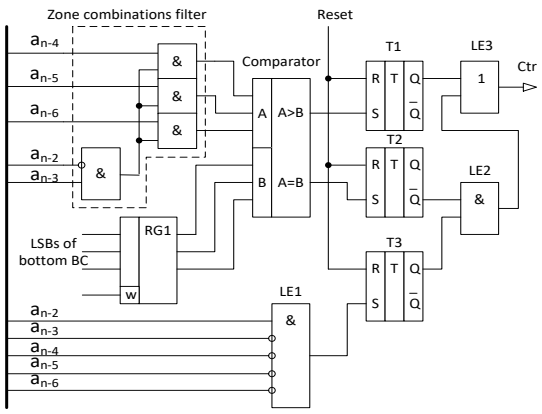

Fig. 6. Zone (n-2)-level control subunit for 6-bit redundant ADC

On the other hand if during some time the top border combination has formed on the SAR out ("1" on the LE1 out) but bottom border combination has not formed ("0" on the A = B comparator's output) it that combination transits from UC category to UnC. In both cases TFCU generates control signal for bit weights recalculation and the values of bottom BCc renewing.

6. Conclusions

It is shown that the use of weight redundancy in the form of redundant positional number systems creates fundamentally new opportunities for self-calibration analog to digital converter, the main feature of which is the execution of the calibration procedure exclusively into the digital form without the use of additional analog measures and components. Moreover the calibration may be performed on-line without interruption the main conversion process.

The structure of the ADC transfer function for successive approximation ADC with weight redundancy is analyzed, as a result the mathematical model of the ADC transfer function is improved by allocating zones of unused combinations.

Mathematical dependences between the different digits weights of ADC deviations and the list of unused combinations in the transfer function that allowed estimating weights digits deviations value without main conversion interruption are established.

A bits deviations estimating method of successive approximation ADC is proposed. It allows determining the deviations of converter individual bits without main conversion process interruption and thus reducing technological waste of time. Redundant successive approximation ADC with transfer function control algorithm is offered.

The practical implementation of bits weights deviations estimating method of the redundant successive approximation ADC by transfer function analysis is proposed. It allows implementing on-line calibration of SAR ADC with weight redundancy by adding the transfer function control unit. The technical realization solutions of transfer function control unit are offered.

References

[1] Azarov O. et al.: Charge accumulation self-calibrating ADC with redundant number system. Universum, Vinnytsia 2005.
[2] Azarov O. et al.: Method of correcting of the tracking ADC with weight redundancy conversion characteristic. Proc. SPIE 9816, 2015, 98161V.
[3] Azarov O. et al.: Method of glitch reduction in DAC with weight redundancy. Proc. SPIE 9816, 2015, 98161T.
[4] Lee H.S, Hodges D., Gray P.: A Self-calibrating 15-bit CMOS A/D Converter. IEEE J. Solid-State Circuits 19(6), 1984, 813–817.
[5] Lee H.S., Hodges D.: Self-calibration technique for A/D converters. IEEE Transactions on circuits and systems 30(3), 1983, 188–190.
[6] Ogawa T. et al.: SAR ADC Algorithm with Redundancy and Digital Error Correction. IEICE Trans. Fundamentals E93-A(2), 2010.
[7] Ogawa T. et al.: SAR ADC Algorithm with Redundancy. IEEE Asia Pacific Conference on Circuits and Systems, Macao, China, 2008, 268–271.
[8] Osadchuk V. S., Osadchuk A. V.: The magneticreactive effect in transistors for construction transducers of magnetic field. Electronics and Electrical Engineering. Technologija 3(109), 2011, 119–122.
[9] Tan K. S. et al.: Error correction techniques for high-performance differential A/D Converters. IEEE J. Solid-State Circuits 25(6), 1990, 1318–1327.
[10] Wójcik W. et al.: Method of evaluating the level of confidence based on metrological risks for determining the coverage factor in the concept of uncertainty. Proceedings of SPIE 10808, 2018, 108082C [http://doi.org/10.1117/12.2501576].
[11] Zakharchenko S. et al.: Bit error notification and estimation in redundant successive approximation ADC. Informatyka, Automatyka, Pomiary w Gospodarce i Ochronie Środowiska 10(4), 2020, 29–32.
[12] Zakharchenko S. et al.: The rapid detection method of deviations single digit weights for successive approximation ADC with weight redundancy. Information Technologies and Computer Engineering 32(1), 2015, 40–47.
[13] Zakharchenko S. et al.: The successive approximation ADC linearity operation control method. Visnyk Lviv Polytechnic National University: Heat energy. Environmental engineering. Automation 792, 2014, 21–28.
[14] Zakharchenko S., Troianovska T.: Method of cyclic ADC calibration by the conversion characteristics analysis. 2nd International Conference on Advanced Information and Communication Technologies, AICT 2017, 120–123.

Ph.D. Serhii Zakharchenko
e-mail: zahar@vntu.net

Serhii Zakharchenko is Associate Professor of the Department of Computer Engineering at the Vinnytsia National Technical University. His main scientific interests include analog to digital conversion, redundant number systems.

http://orcid.org/0000-0003-3977-2908

Ph.D. Tetiana Korobeinikova
e-mail: tetianakorobeinikova@gmail.com

Ph.D., Associate Professor of Department of Information Technology Security, Lviv Polytechnic National University. Research Interests: information technologies, computer networks, cybersecurity.

http://orcid.org/0000-0003-2487-8742

Ph.D. Aigul Tungatarova
e-mail: tungatarova70@gmail.com

Candidate of Pedagogical Sciences – Department of Information Systems, Taraz Regional University named after M.Kh.Dulaty, Kazakhstan.
Research area: information technology, information security.

http://orcid.org/0000-0001-7600-9608

M.Sc. Bakhyt Yeraliyeva
e-mail: yeraliyevabakhyt81@gmail.com

Senior lecturer of the Information Systems Department, Faculty of Information Technology, M. Kh. Dulaty Taraz Regional University, Taraz, Kazakhstan.
Research interests: Information technologies, fiber-optic technologies, microprocessor systems.

http://orcid.org/0000-0002-8680-7694

http://doi.org/10.35784/iapgos.2914 *received: 04.04.2022 | revised: 10.05.2022 | accepted: 15.06.2022 | available online: 30.06.2022*

DESIGN OF INNOVATIVE MEASUREMENT SYSTEMS IN ULTRASONIC TOMOGRAPHY

Michał Gołąbek[1], Tomasz Rymarczyk[1,2]
[1]Research and Development Center, Lublin Netrix S.A., Lublin, Poland, [2]University of Economics and Innovation, Lublin, Poland

Abstract. *The article describes the progress of construction and research works on ultrasound tomography. The devices allow for non-invasive measurements of various objects using ultrasonic low and high-frequency transducers. The first constructions were made in a dispersed system with active measurement probes using 40 kHz converters. The next constructions were centralized into one measurement system where the measurement probes were connected separately. As a result, the measuring range of the supported ultrasonic transducers with 300 kHz, 400 kHz and 1 MHz has been extended. Apart from transmission and reflection tomography, the latest designs allow for controlling the ultrasound beam (beamforming) and support transducers up to 5 MHz.*

Keywords: ultrasonic imaging, ultrasonic transducers, beamforming, ultrasonic time of flight

KONSTRUKCJA INNOWACYJNYCH SYSTEMÓW POMIAROWYCH W TOMOGRAFII ULTRADŹWIĘKOWEJ

Streszczenie. *Artykuł opisuje postępy prac konstrukcyjno-badawczych nad tomografią ultradźwiękową. Wykonane urządzenia pozwalają w sposób bezinwazyjny przeprowadzać pomiary różnych obiektów z użyciem ultradźwiękowych przetworników niskich i wysokich częstotliwości. Pierwsze konstrukcje wykonano w formie systemu rozproszonego z aktywnymi sondami pomiarowymi z użyciem przetworników 40kHz, kolejne konstrukcje scentralizowano w jeden system pomiarowy gdzie sondy pomiarowe były podłączane osobno. Rozszerzony został zakres pomiarowy obsługiwanych przetworników ultradźwiękowych o częstotliwości 300 kHz, 400 kHz oraz 1 MHz. Najnowsze konstrukcje oprócz tomografii transmisyjnej i odbiciowej pozwalają na sterowanie wiązką ultradźwiękową, tzw. beamforming i obsługują przetworniki do 5 MHz.*

Słowa kluczowe: obrazowanie ultradźwiękowe, przetworniki ultradźwiękowe, formowanie wiązki, czas przelotu fali ultradźwiękowej

Introduction

There are many techniques and numerical methods for examining objects on their edge [1–4, 10–29]. Ultrasound tomography has found wide application due to the possibility of imaging in a non-invasive way in medicine, automotive industry, construction industry, chemical industry, military, etc. [5–9]. Each of these applications was preceded by research. Measuring devices designed by Research and Development Center Netrix S.A. allow researchers to develop reconstruction algorithms and study various objects using various ultrasonic transducers.

1. First version of Ultrasound Tomograph

The 1.0 and improved version 1.1 of the ultrasound tomograph performs transmission measurements using active measuring probes operating at a frequency of 40 kHz (Fig.1 and 2). The probes were connected via the CAN bus with the control unit. The measurement time of the flight data matrix in the first version of the tomograph could be saved on the SD card and sent via USB1.0.

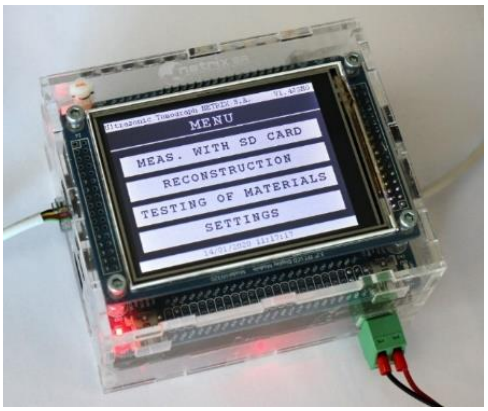

Fig. 1. Ultrasonic tomograph control unit 1.0

The next version of the control unit (1.1) allows saving data on USB flash drives and sending measurements via ETHERNET TCP/UDP and USB2.0. In the newer device, we also redesigned the user interface, and the appearance of the device housing and the speed of getting measurements were also increased.

Fig. 2. Ultrasonic tomograph control unit 1.1

The device was tested on a plastic tank, on the perimeter of which active measuring probes were mounted (Fig. 3). During the tests, the tomograph performed a series of transmission measurements calibrated in microseconds, where it measured the time of transmission of the transmitting wave from one transducer to the others and then from the next to the others until it made a full measurement matrix.

Fig. 3. Active 40 kHz probes mounted on the pipe and connected via CAN-bus

2. Second version of Ultrasound Tomograph

The second version of the ultrasound tomograph was designed to measure sound reflections using high-frequency transducers such as 1 MHz or higher (Fig. 4). The device has installed 64 multiplexed measurement channels, fast ADC 10MSPS, a square pulse generator with an excitation signal amplitude up to 144 Vp-p, a USB2.0 communication port for sending data, and a USB port to save data on the flash drive. In addition, the device performs analog measurements of the acoustic signal with the possibility of converting it to an envelope.

Fig. 4. Ultrasound tomograph 2.0

The device is made in the form of a reinforced suitcase. It makes it possible to transport the device conveniently and increases its resistance to mechanical shocks. The transmitters are connected using 8-channel industrial standard M12 sockets. In addition, the device has a touch-sensitive graphic interface for convenient operation. An additional advantage is the possibility of a remote operation via the USB port.

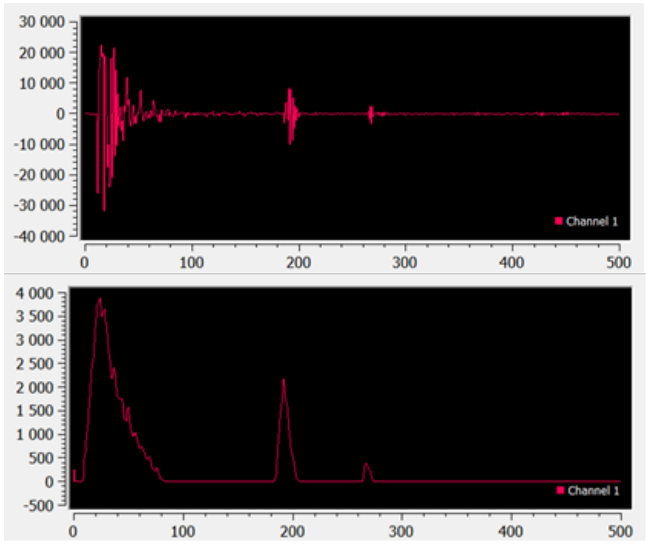

Fig. 5. Analog capture waveform via UST 2.0

The device has a defectoscope function that allows for direct imaging of the analog waveform of the reflected signal on the device screen. An analog signal or its envelope allows, using appropriate ultrasonic sensors, to investigate defects in various measurement objects (Fig. 5).

3. Third version of Ultrasound Tomograph

The third version of the ultrasound tomograph has all the advantages of the previous designs. It has 32 independent measurement channels. Each channel has its shielded measurement path, adjustable gain, three switchable analog filters for a wide range of transducers (40 kHz – 1 MHz), analog converter to the envelope with three conversion stages, 4MSPS ADC and its high voltage pulse adjustable from +/- 24V to +/- 72V (Fig. 6 and 7).

Fig. 6. Ultrasound 400 kHz transducers mounted on plexiglass tank

The tomograph can perform measurements in both transmission and reflection modes. As with previous scanners, data can be stored on USB drives or transferred via USB 2.0 to a computer. A new future in this device is the ability to send measurements to apache Kafka via ETHERNET or WiFi and the possibility of remote control from the server.

Fig. 7. Ultrasound tomograph 3.0

This enclosure, similar to the previous one, was made in the form of a reinforced suitcase, thanks to which the device can be easily transported.

The tomograph has a modern touch interface made in three languages (Fig. 8–11).

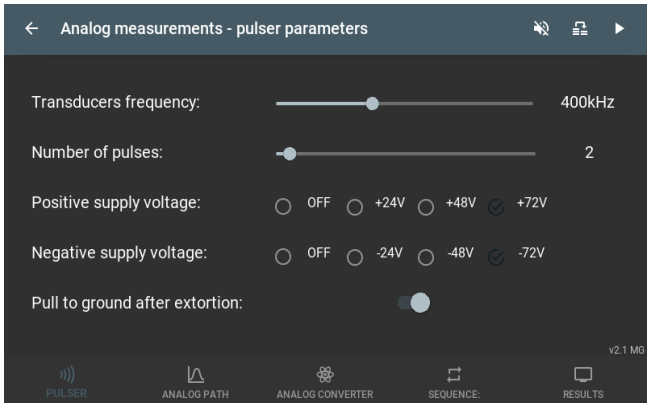

Fig. 8. UST 3.0 GUI: Pulser settings

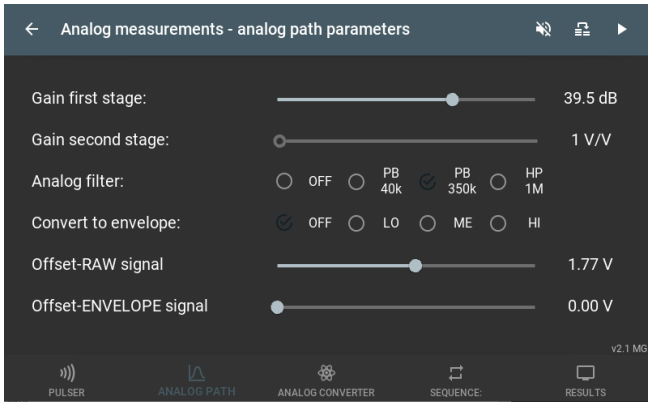

Fig. 9. UST 3.0 GUI: analog front end settings

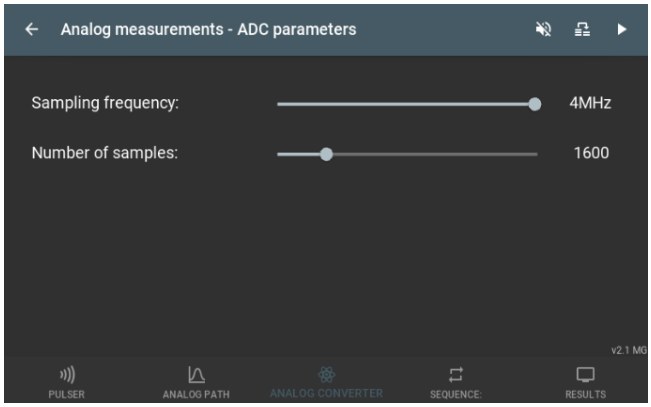

Fig. 10. UST 3.0 GUI: ADC settings

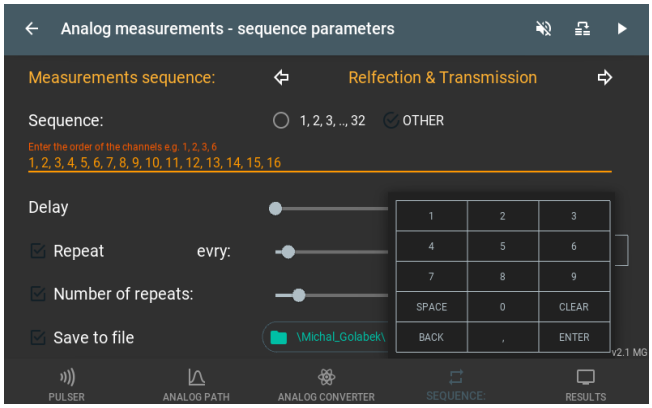

Fig. 11. UST 3.0 GUI: sequence order settings

The tomograph interface has an implemented defectoscope that allows for real-time analysis of acoustic waveforms. What can be used to detect defects in various types of materials (Fig. 12).

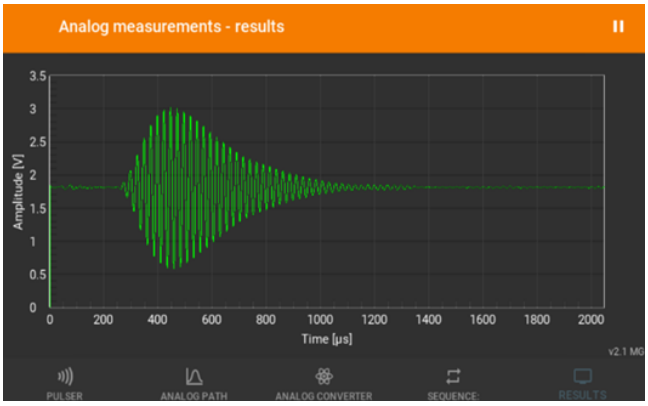

Fig. 12. UST 3.0 GUI: Captured analog signal from 40 kHz ultrasonic transducer

The system inside the reinforced suitcase consists of eight four-channel measurement cards connected via the FD CAN bus with the measurement module. The measuring module connects the microprocessor measuring system with a touch panel or an external control application. In addition, the measurement module supervises the measurement sequence, stores the parameters entered by the user, controls the high-voltage converter and switches the USB HS bus between the socket on the front panel and the touch panel (Fig. 13).

The touch panel was made using a RaspberryPi 4B 2GB RAM board and a 7-inch capacitive touch screen. The most important data buses have been led to the device's front panel.

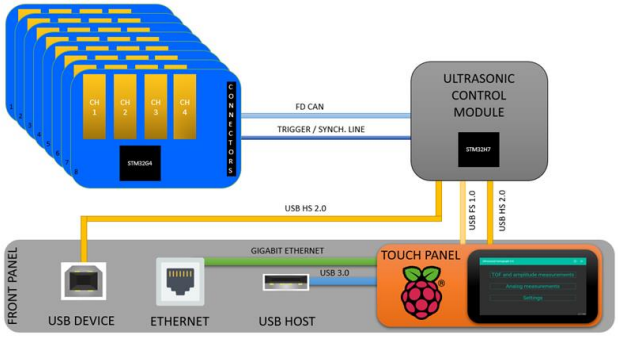

Fig. 13. Ultrasound tomograph 3.0 schematic block

Measurement card parameters (Fig. 14):

- Max sampling rate of one channel: 4 MBPS
- Each channel has a separate square wave generator with amplitude up to 144 Vp-p and current efficiency: 3 A (peak)
- A synchronous sampling of analog signal on all channels simultaneously.
- Built-in three eight-order filters on each of the channels for effective harmonic filtering, switched by analog keys:
  - A band-pass filter with 40 kHz center frequency and 50 kHz bandwidth for 40 kHz ultrasonic transducers.
  - A band-pass filter with 350 kHz center frequency and 200 kHz bandwidth for 300 kHz and 400 kHz ultrasonic transducers.
  - A high-pass filter with a 1 MHz cut-off frequency for 1 MHz ultrasonic transducers.
- Built-in envelope converter for converting an analog acoustic signal to the envelope with the possibility of switching its configuration for three frequency ranges adapted to 40 kHz, 300 kHz, 400 kHz and 1 MHz ultrasonic transducers
- Two-stage gain control on each of the channels:
  - Stage I: from + 7.5 dB to + 55.5 dB (AD8331)
  - Stage II: from + 6 dB to + 36 dB (6 presets – built-in PGA in stm32).
- Each channel is shielded, thanks to which the channels are very well isolated from each other.

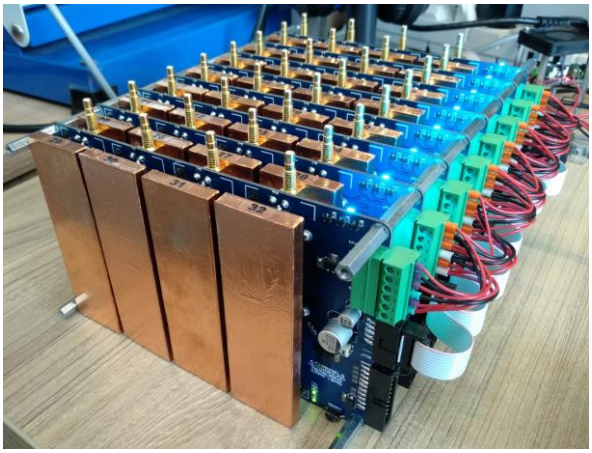

Fig. 14. Ultrasound tomograph 3.0 shielded measurements cards

4. Prototype of Ultrasound Beamforming Tomograph

Beamforming is a technology that allows focusing an ultrasonic wave beam at a specific angle or a specific point using an array of static ultrasonic transducers (Fig. 15).

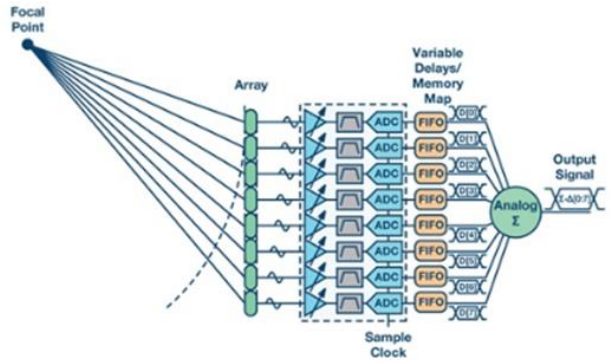

Fig. 15. Principle of ultrasound beamforming [30]

The main advantage of this technology is the ability to perform a large number of measurements using a small number of channels/transducers (and their number mainly results from the step with which the phase of the transmission signal will be shifted).

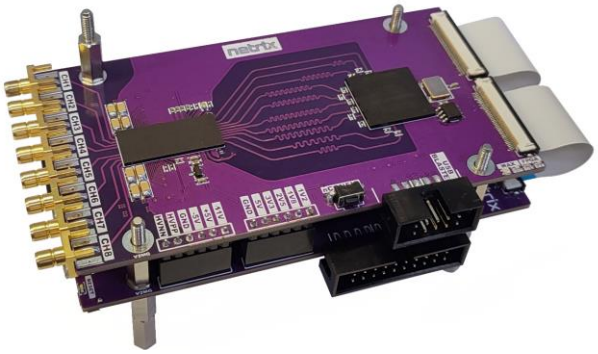

Fig. 16. Eight channels beamforming prototype board

The new prototype designed in Netrix SA opens up new possibilities in ultrasound tomography research. The construction has been reduced many times compared to the previous designs (Fig. 17).

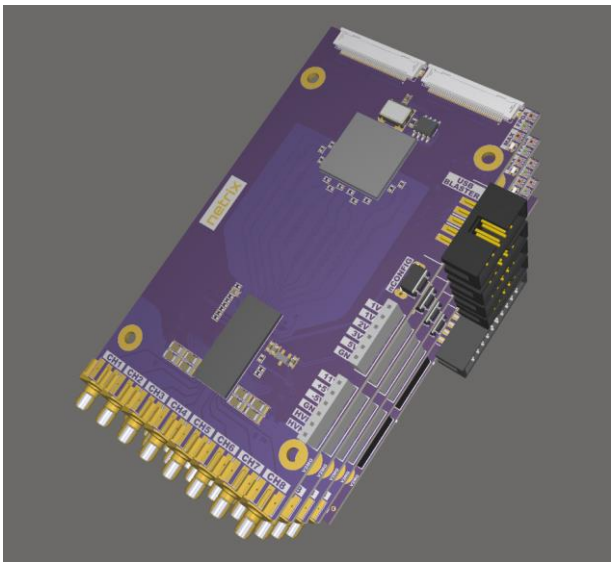

Fig. 17. 3D model of 32 channel beamforming prototype tomograph

The prototype beamforming prototype tomograph was made using the MAX2082 integrated circuit with eight independent measurement paths of ultrasonic signals. Each channel also has a 25 MSPS ADC converter with an LVDS output, a digitally controlled two high-pass filter, the ability to adjust the gain on each channel, and its 3-state +/- 72 V pulse generator. The MAX2082 chip is managed by the INTEL ALTERA CYCLONE IV FPGA chip. The collected measurement data is stored in the built-in FPGA RAM and then read via a parallel data bus by the FMC mechanism from the STM32H7 microcontroller level and then sent via USB2.0. The device has an additional USB port for control during the measurement. Delays on each of the channels can be changed using AT commands. Working multiple cards in parallel is possible thanks to the synchronization of measurement cards with a common clock, which allowed synchronizing the pulser outputs to 1 ns, with a control resolution of 5ns. The maximum speed of measurements with approximately 10,000 samples is approximately 13 ms. The device can be expanded by using additional cards up to 32 channels (Fig. 17–19).

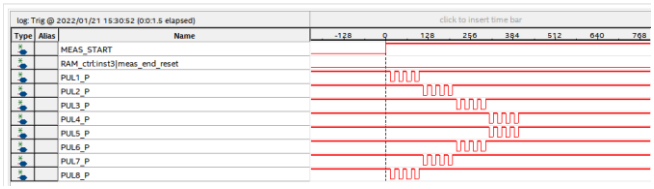

Fig. 18. Testing of beamforming eight-channel square high voltage pulser

Technical data:

- Maximum single-channel sampling rate: 25 MBPS;
- Each channel has a separate square wave generator with amplitude up to 144 Vp-p and instantaneous current efficiency: 2 A;
- The range of the transmitted ultrasonic signal: 1 MHz – 10 MHz;
- The maximum number of samples that the device can make: 16,000;
- Built-in two-row digital filter with active suppression;
- Beamforming resolution: 5 ns;
- The range of generated frequency of the excitation signal: 1 MHz – 5 MHz.

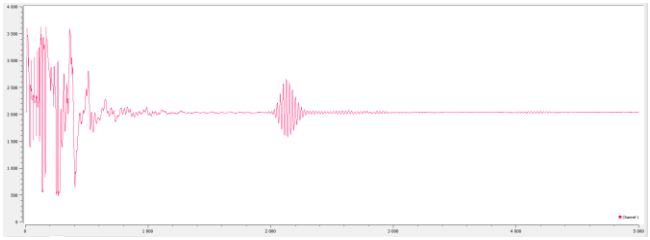

Fig. 19. Captured reflected signal from test object on 1 MHz transducer

5. Conclusion

The paper presents the author's construction of measurement devices for ultrasonic signals designed by the Research and Development Centre Netrix SA, using which it is possible to reconstruct images by solving the inverse problem. The presented solutions enable the examination of various objects using a wide range of ultrasonic transducers. Furthermore, the devices make it possible to perform non-invasive measurements of various objects using ultrasonic transducers of low and high frequencies.

References

[1] Babout L., Grudzień K., Wiącek J., Niedostatkiewicz M., Karpiński B., Szkodo M.: Selection of material for X-ray tomography analysis and DEM simulations: comparison between granular materials of biological and non-biological origins. Granul. Matter 20(3), 2018, 38.

[2] Chaniecki Z., Romanowski A., Nowakowski J., Niedostatkiewicz M.: Application of twin-plane ECT sensor for identification of the internal imperfections inside concrete beams Grudzien. IEEE Instrumentation and Measurement Technology Conference 2016, 7520512.

[3] Duda K., Adamkiewicz P., Rymarczyk T., Niderla K.: Nondestructive Method to Examine Brick Wall Dampness. International Interdisciplinary PhD Workshop, Brno, 2016, 68–71.

[4] Fiala P., Drexler P., Nešpor D., Szabó Z., Mikulka J., Polívka J.: The Evaluation of Noise Spectroscopy Tests. Entropy 18(12), 2016, 1–16.

[5] Gudra T., Opieliński K. J.: The multi–element probes for ultrasound transmission tomography. Journal de Physique 4(137), 2006, 79–86.

[6] Golabek M., Rymarczyk T., Adamkiewicz P.: Construction of ultrasonic reflection tomograph for analysis of technological processes, Applications of Electromagnetics in Modern Engineering and Medicine. XXIX Sympozjum PTZE 2019, 47–51.

[7] Herman G.T.: Image Reconstruction from Projections: The Fundamentals of Computerized Tomography. Academic Press, New York 1980.

[8] Jiang Y., Soleimani M., Wang B.: Contactless electrical impedance and ultrasonic tomography, correlation, comparison and complementary study. Measurement Science and Technology 30, 2019, 114001.

[9] Kaczmarz S.: Angenäherte Auflösung von Systemen Linearer Gleichungen. Bull. Acad. Polon. Sci. Lett. A, 6–8A, 1937, 355–357.

[10] Kak A. C., Slaney M.: Principles of Computerized Tomographic Imaging. IEEE Press, New York 1999.

[11] Kryszyn J., Wanta D. M., Smolik W. T.: Gain Adjustment for Signal-to-Noise Ratio Improvement in Electrical Capacitance Tomography System EVT4. IEEE Sens. J. 17(24), 2017, 8107–8116.

[12] Kryszyn J., Smolik W.: Toolbox for 3d modelling and image reconstruction in electrical capacitance tomography. Informatyka, Automatyka, Pomiary w Gospodarce i Ochronie Środowiska – IAPGOŚ 7(1), 2017, 137–145.

[13] Lopato P., Chady T., Sikora R., Ziolkowski M.: Full wave numerical modelling of terahertz systems for nondestructive evaluation of dielectric structures. COMPEL – The international journal for computation and mathematics in electrical and electronic engineering 32(3), 2013, 736–749.

[14] Majchrowicz M., Kapusta P., Jackowska-Strumiłło L., Sankowski D.: Optimization of Distributed Multi-node, Multi-GPU, Heterogeneous System for 3D Image Reconstruction in Electrical Capacitance Tomography. Image processing & communications 21(3), 2016, 81–90.

[15] Nowakowski J., Ostalczyk, P., Sankowski D.: Application of fractional calculus for modelling of two-phase gas/liquid flow system. Informatyka, Automatyka, Pomiary w Gospodarce i Ochronie Środowiska – IAPGOŚ 7(1), 2017, 42–45.

[16] Polakowski K., Sikora J.: Podstawy matematyczne obrazowania ultradźwiękowego. Politechnika Lubelska, Lublin 2016.

[17] Romanowski A., Łuczak P., Grudzień K.: X-ray Imaging Analysis of Silo Flow Parameters Based on Trace Particles Using Targeted Crowdsourcing. Sensors 19(15), 2019, 3317.

[18] Rymarczyk T., Kłosowski G.: Innovative methods of neural reconstruction for tomographic images in maintenance of tank industrial reactors. Eksploatacja i Niezawodność – Maintenance and Reliability 21(2), 2019, 261–267.

[19] Rymarczyk T., Filipowicz S. F., Sikora J.: Level Set Method for Inverse Problem Solution In Electrical Impedance Tomography. Journal Proceedings of the XII International Conference on Electrical Bioimpedance & V Electrical Impedance Tomography, 2004, 519–522.

[20] Rymarczyk T., Kozłowski E., Kłosowski G., Niderla K.: Logistic Regression for Machine Learning in Process Tomography. Sensors 19, 2019, 3400.

[21] Rymarczyk T., Szumowski K., Adamkiewicz P., Tchórzewski P., Sikora J.: Moisture Wall Inspection Using Electrical Tomography Measurements. Przegląd Elektrotechniczny 94, 2018, 97–100.

[22] Rymarczyk T., Nita P., Vejar A., Stefaniak B., Sikora J.: Electrical tomography system for Innovative Imaging and Signal Analysis. Przegląd Elektrotechniczny 95(6), 2019, 133–136.

[23] Soleimani M., Mitchell C. N., Banasiak R., Wajman R., Adler A.: Four-dimensional electrical capacitance tomography imaging using experimental data. Progress in Electromagnetics Research 90, 2009, 171–186.

[24] Szczęsny A., Korzeniewska E.: Selection of the method for the earthing resistance measurement. Przegląd Elektrotechniczny 94(12), 2018, 178–181.

[25] Vališ D., Hasilová K., Forbelská M., Vintr Z.: Reliability modelling and analysis of water distribution network based on backpropagation recursive processes with real field data. Measurement 149, 2020, 107026

[26] Wajman R., Fiderek P., Fidos H., Sankowski D., Banasiak R.: Metrological evaluation of a 3D electrical capacitance tomography measurement system for two-phase flow fraction determination. Measurement Science and Technology 24(6), 2013, 065302.

[27] Wang M.: Industrial Tomography: Systems and Applications. Elsevier 2015.

[28] Ye Z., Banasiak R., Soleimani M.: Planar array 3D electrical capacitance tomography. Insight: Non-Destructive Testing and Condition Monitoring 55(12), 2013, 675–680.

[29] Ziolkowski M., Gratkowski S., Zywica A. R.: Analytical and numerical models of the magnetoacoustic tomography with magnetic induction. COMPEL – The international journal for computation and mathematics in electrical and electronic engineering 37(2), 2018, 538–548.

[30] https://www.analog.com/en/technical-articles/an-interview-with-analog-devices-discussing-rf-electronics-for-phased-array-applications.html

D.Sc, Ph.D. Eng. Tomasz Rymarczyk
e-mail: tomasz@rymarczyk.com

He is the director in Research and Development Center in Netrix S.A. and the director of the Institute of Computer Science and Innovative Technologies in the University of Economics and Innovation, Lublin, Poland. He worked in many companies and institutes developing innovative projects and managing teams of employees. His research area focuses on the application of non-invasive imaging techniques, electrical tomography, image reconstruction, numerical modelling, image processing and analysis, process tomography, software engineering, knowledge engineering, artificial intelligence and computer measurement systems.

http://orcid.org/0000-0002-3524-9151

M.Sc. Eng. Michał Gołąbek
e-mail: michal.golabek@netrix.com.pl

Michał Gołąbek is graduated from Lublin University of Technology, Faculty of Electrical Engineering and Computer Science (Specialty: microprocessor drives in industrial automation).
At present he is constructor of tomographic equipment in NETRIX S.A. Research and Development Center.

http://orcid.org/0000-0002-2696-505X

http://doi.org/10.35784/iapgos.2921 received: 14.04.2022 | revised: 04.06.2022 | accepted: 15.06.2022 | available online: 30.06.2022

MATHEMATICAL SIMULATION OF A MICROELECTRONIC TRANSDUCER WITH FREQUENCY OUTPUT FOR MEASURING THE INDUCTION OF THE MAGNETIC FIELD

Alexander V. Osadchuk[1], Iaroslav A. Osadchuk[1], Volodymyr V. Martyniuk[1], Lyudmila V. Krylik[1], Maria V. Evseeva[2]

[1]Vinnytsia National Technical University, Vinnytsia, Ukraine, [2]National Pirogov Memorial Medical University, Vinnytsia, Ukraine

Abstract. *A new magnetically sensitive element based on the synthesized semiconductor material has been developed. A method for the synthesis of a complex compound has been developed tetrakis-μ_3-(methoxo) (methanol)-pentakis (acetylacetonate) (tricuprum (II), neodymium (III)) methanol (I). Conducted properties have been studied complex compound in compressed form in the temperature range 273 - 493 K. In the developed magnetoresistor when changing the induction of the magnetic field from 10^{-3} to 200 mT, the resistivity varies from $3.12 \cdot 10^{-5}$ Ohm to $1.25 \cdot 10^{-2}$ Ohm·m. On the basis of the developed magnetically sensitive resistive element the circuit solution of the frequency transducer of a magnetic field is offered. The frequency transducer of the magnetic field is a hybrid integrated circuit consisting of a bipolar transistor and a gate transistor. The frequency of generation of the developed transducer increases the most in the range from 10^{-3} T to 0.2 T, and at a supply voltage of 5.0 V varies from 250 kHz to 600 kHz, and in the whole range of changes in magnetic field induction varies from 250 kHz to 750 kHz. The sensitivity of the developed device with frequency output for measuring the induction of the magnetic field is from 400 Hz/mT to 800 Hz/mT.*

Keywords: microelectronic transducer, complex compound, magnetic field, conductivity, generation frequency, negative differential resistance

SYMULACJA MATEMATYCZNA PRZETWORNIKA MIKROELEKTRONICZNEGO Z WYJŚCIEM CZĘSTOTLIWOŚCIOWYM DO POMIARU INDUKCJI POLA MAGNETYCZNEGO

Abstrakt. *Opracowano nowy element czuły magnetycznie oparty na zsyntetyzowanym materiale półprzewodnikowym. Opracowano metodę syntezy związku złożonego tetrakis-μ3-(methoxo)(metanol)-pentakis(acetyloacetonian)(tricuprum (II), neodym (III)) metanol (I). Badano właściwości przewodzące związku złożonego w postaci sprasowanej, w zakresie temperatur 273–493 K. W opracowanym magnetooporniku przy zmianie indukcji pola magnetycznego od 10^{-3} do 200 mT rezystywność zmienia się od $3{,}12 \cdot 10^{-5}$ Ohm do $1{,}25 \cdot 10^{-2}$ Ohm·m. Na podstawie opracowanego magnetycznie czułego elementu rezystancyjnego zaproponowano rozwiązanie układu przetwornika pola magnetycznego na częstotliwość. Przetwornik ten jest hybrydowym układem scalonym składającym się z tranzystora bipolarnego i tranzystora bramkowego. Częstotliwość generacji opracowanego przetwornika wzrasta najbardziej w zakresie od 10-3 T do 0,2 T i przy napięciu zasilania 5,0 V zmienia się od 250 kHz do 600 kHz, zaś w całym zakresie zmian indukcji pola magnetycznego zmienia się od 250 kHz do 750 kHz. Czułość opracowanego urządzenia z wyjściem częstotliwościowym do pomiaru indukcji pola magnetycznego wynosi od 400 Hz/mT do 800 Hz/mT.*

Słowa kluczowe: przetwornik mikroelektroniczny, związek złożony, pole magnetyczne, przewodność, częstotliwość generacji, ujemna rezystancja różnicowa

Introduction

Leading specialists of the world are currently developing and creating primary transducers of physical quantities (humidity, temperature, pressure, magnetic field induction), because their measurement in a gas mixture (air) significantly affects both human well-being and the quality of technological processes in microelectronics technology and in various industries [3, 5, 20].

An important role in the development of new functional materials belongs to complex compounds in which β-diketone is a chelating and in some cases a bridging ligand. Nowadays, the field of practical use of functional materials containing β-diketonates of metals is constantly expanding. In particular, they are used in gas sensors, molecular thermometers, in the production of optical fiber and light-converting materials are the starting materials for materials with valuable electrical, optical, catalytic and other properties [2, 6–8, 19, 24]. Of particular interest among this class of complex compounds are heterometallic β-diketonates, which have semiconductor properties [12, 13, 21, 22].

A promising scientific direction in this field is the creation of frequency measuring devices for magnetic field induction based on semiconductor structures with negative resistance, in the development of the theory of which significant achievements have been made by domestic and foreign scientists. The use of the principle of "magnetic induction – frequency" based on transistor structures with negative resistance eliminates the use of analog-to-digital transducers in signal processing, which reduces the cost of control and management systems. In addition, microelectronic frequency magnetic transducers combine both simplicity and versatility, which are inherent in analog devices, as well as accuracy and noise immunity characteristic of transducers with code output, have high sensitivity to measurement parameters, low weight, size, information and design technology. microelectronic means of information processing. Which is their advantage over existing magnetic induction transducers [10, 11, 15]. Therefore, the development and practical application of such devices based on new nanocomposite materials is an urgent task.

1. Technological aspects

It is established that the technical level of sensory systems of physical quantities depends primarily on the technical development of the transducer, namely its sensitive elements, design solution, principle of operation and manufacturing technology [1, 9, 14, 17]. This motivates for the implementation of further research.

The purpose of the study is to develop devices with frequency output for measuring the induction of a magnetic field based on semiconductor structures with negative resistance (Fig. 1). The magnetically sensitive resistive element served as an experimental sample. This element was made from a complex compound – tetrakis-μ_3-(methoxo) (methanol)-pentakis (acetylacetonate) (tricuprum (II), neodymium (III)) methanol (I), of the following composition:

$$[Cu_3Nd(AA)_5(OCH_3)_4CH_3OH] \cdot CH_3OH$$

where HAA = $H_3C–C(O)–CH_2–C(O)–CH_3$.

This chemical structure was obtained by the following method: samples of salts 3.62 g (15 mmol) of copper (II) nitrate trihydrate and 2.19 g (5 mmol) of neodymium (III) nitrate hexahydrate were dissolved in 130 ml of absolute methyl alcohol containing 40 ml of orthomut ether, kept for 2 hours at room temperature in a hermetically sealed conical flask. Then 2.7 ml (25 mmol) of acetylacetone was added to the reaction mixture, the conical flask was closed with a reversible water cooler and placed on a heated magnetic stirrer. Then, with continuous stirring and heating (~ 50ºC), the piperidine was gradually introduced into the reaction mixture to pH = 8 and continued to heat and stir for one hour. After cooling, a homogeneous fine blue crystalline precipitate precipitated from the solution, which

was filtered on a glass filter, washed with a small amount of absolute methanol, diethyl ether and dried in a vacuum desiccator over silica gel. The practical yield is 4.07 g, which is 80% of theoretical. The isolated complex compound (I) is a fine crystalline powder, which is poorly soluble in dimethylformamide, preferably in dimethyl sulfoxide, practically insoluble in alcohols, chloroform, benzene, acetone, decomposes in water.

For the synthesized complex compound (I) in the dry powder state, elemental analysis was performed and it was found that it contains:

Cu – 18.65%; Nd – 14.25%; C – 36.68%; H – 5.24%

As can be seen from the above data, the ratio of metals in the compound(I) Cu:Nd = 1:3, and its composition corresponds to the following gross formula: $Cu_3NdO_{16}C_{31}H_{55}$. In addition, magnetochemical, IR spectroscopic and thermogravimetric studies were performed for the isolated heterometallic compound (I) [18]. A detailed analysis of the obtained experimental data of physicochemical research methods allows us to propose the following scheme of placement of chemical bonds for complex compound (I) (Fig. 1) [18]:

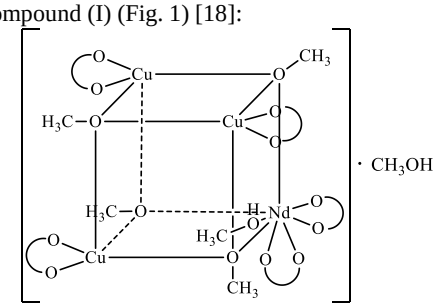

Fig. 1. Scheme of arrangement of chemical bonds in tetrakis-μ_3-(metokso) (methanol) pentakis (acetylacetonate) (tricuprum (II), neodymium (III)) methanol (I)

For the complex compound $[Cu_3Nd(AA)_5(OCH_3)_4CH_3OH]$ (I), a molar mass of 985.5 g/mol and the number of valence electrons in one molecule of 270 was calculated. The density of this material was also calculated as $\rho = 7.046 \cdot 10^3$ kg/m^3 and the band gap $\Delta E = 1.6125$ eV. The dependence of the conductivity of this material on temperature is shown in Fig. 2.

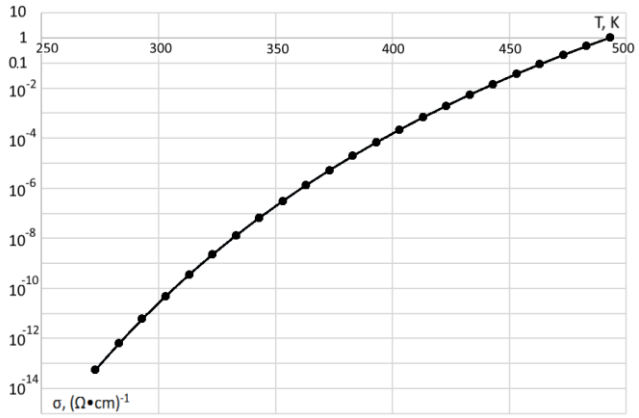

Fig. 2. Logarithmic dependence of the conductivity of heterometallic compound (I) on temperature

As can be seen from the graph, the conductivity varies from $5.67 \cdot 10^{-14}$ $(Ohm \cdot m)^{-1}$ at a temperature of 273 K to 1.06 $(Ohm \cdot m)^{-1}$ at a temperature of 493 K. The experiment showed that in the temperature range of 303–423 K, the specific resistance of the pressed sample of the studied material of compound (I) decreases from $2 \cdot 10^{10}$ Ohm·m to $5 \cdot 10^2$ Ohm·m, that is, the isolated compound is a semiconductor.

To use this complex compound (I) as a magnetically sensitive resistor, a device was created, by analogy with magnetoresistors of the MR-1, MR-2, MR-3 and CM1-1 types, the appearance of which is shown in Fig. 3., with the thickness of the active layer area $7 \cdot 10^{-4}$ m.

The dependence of the resistance of the magnetoresistor on temperature is shown in Fig. 4.

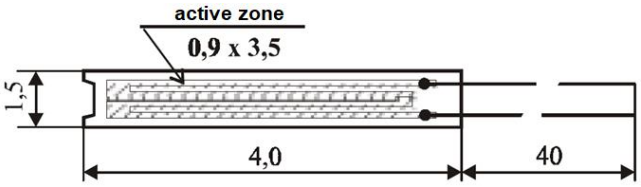

Fig. 3. Appearance and overall dimensions of the magnetically sensitive resistor

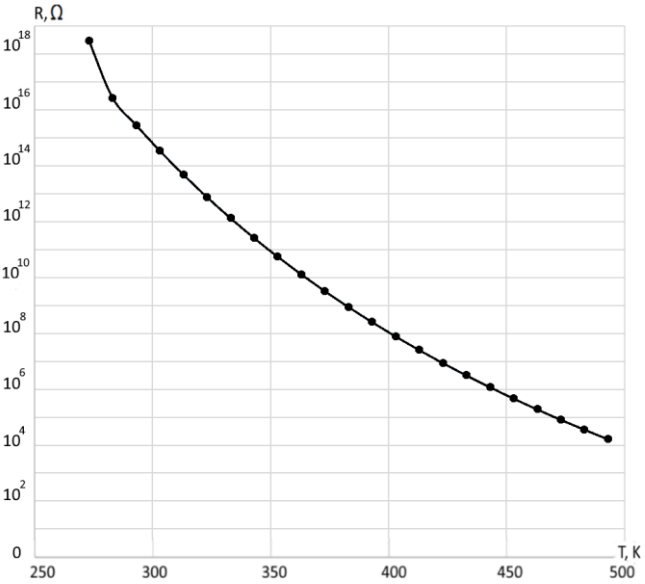

Fig. 4. Logarithmic dependence of the resistance of heterometallic compound (I) on temperature

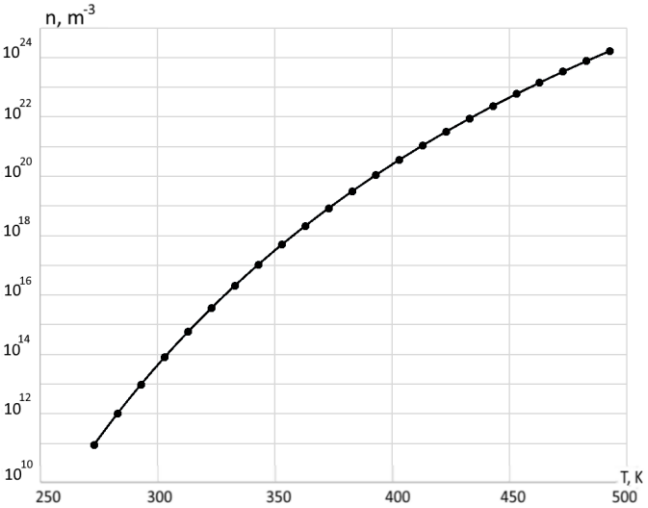

Fig. 5. Logarithmic dependence of charge carrier concentration on temperature

As can be seen from the graph, the concentration of charge carriers increases from $9.02 \cdot 10^{10}$ m^{-3} to $1.68 \cdot 10^{24}$ m^{-3}, in the temperature range from 273 K to 493 K.

The dependence of the change in resistivity of the magnetoresistor on the induction of the magnetic field at a temperature of 393 K is shown in Fig. 6.

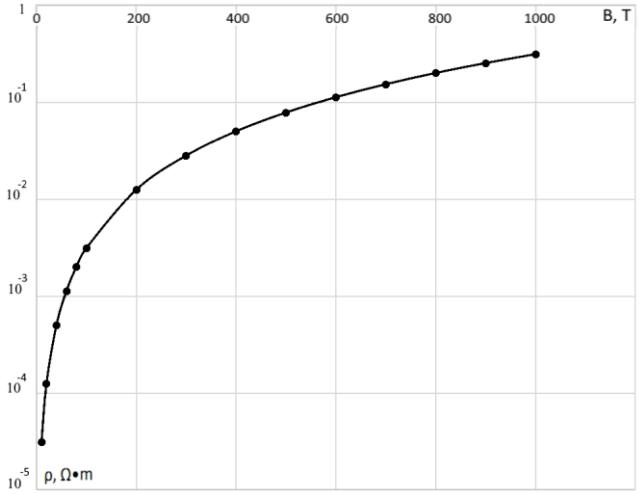

Fig. 6. Logarithmic dependence of the change in resistivity on the induction of the magnetic field

As can be seen from the graph, when changing the induction of the magnetic field from 10^{-3} to 200 mT, the resistivity varies from $3.12 \cdot 10^{-5}$ Ohm to m$1.25 \cdot 10^{-2}$ Ohm · m, and from 200 mT to 1 T, the resistivity varies from$1.25 \cdot 10^{-2}$ Ohm to 0.3 Ohm.

2. Mathematical modeling

The autogenerator transducer is designed as an integrated circuit based on a field-effect double-gate transistor VT1 and a bipolar transistor VT2. The negative differential resistance formed by the parallel connection of the impedance with the capacitive component on the emitter-collector electrodes of the bipolar transistor VT2 and the drain of the field-effect transistor VT1 and inductance L1 leads to the occurrence of electrical oscillations in the circuit. Two resistors R2 and R3 form a voltage divider to power the autogenerator transducer. The capacitor C1 and the resistance of the magnetically sensitive resistor R1 form a phase-shifting circuit [16]. To select the resonant frequency of the oscillatory circuit, capacitor C2 is connected in parallel to the equivalent capacitance of the transistor structure. The passage of alternating current through the DC voltage source is prevented by clamping capacitor C1. Under the action of a magnetic field on the magnetically sensitive resistive element R1, the capacitive component of the impedance on the electrodes of the transistor structure changes, which causes an effective change in the frequency of the oscillatory circuit. An experimental circuit of a microelectronic converter with a frequency output for measuring the magnetic field induction (Fig. 7) was assembled on a BC547 bipolar transistor and a BF998 field-effect double-gate transistor. The mode of transistors VT1 and VT2 for direct current was as follows: the current in the collector circuit of the transistor VT2 is 1.75 mA, and the voltage on the collector is 1.1 V. The circuit resistances have the following values R1 = 2.5 kOhm; R2 = 10 kOhm; R3 = 1.4 kOhm. The self-oscillator inductance is 100 μH. This regime at a magnetic field induction of 1 T corresponded to a generation frequency of 750.470 kHz. The described generator circuit allows you to get an output voltage of up to 1.6 V in a wide frequency range. The frequency instability is $1.17 \cdot 10^{-4}$ Hz.

Without knowing the parameters of the transducers, it is impossible to create, so the task was to develop a mathematical model, based on the solution of which the transformation function and sensitivity equations will be determined. Based on the electrical circuit of the device with a frequency output for measuring the magnetic field induction (Fig. 7), a converted nonlinear equivalent circuit of a microelectronic converter with a frequency output for measuring the magnetic field induction was developed (Fig. 8).

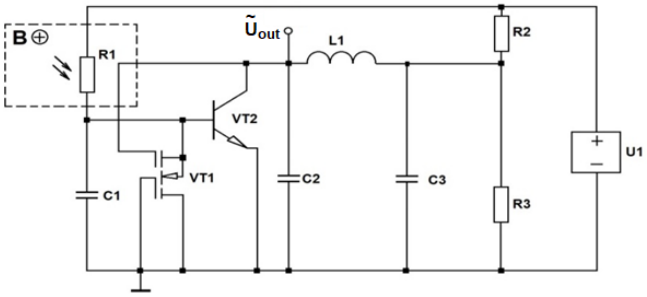

Fig. 7. Electrical circuit of a microelectronic transducer with frequency output for measuring the induction of a magnetic field

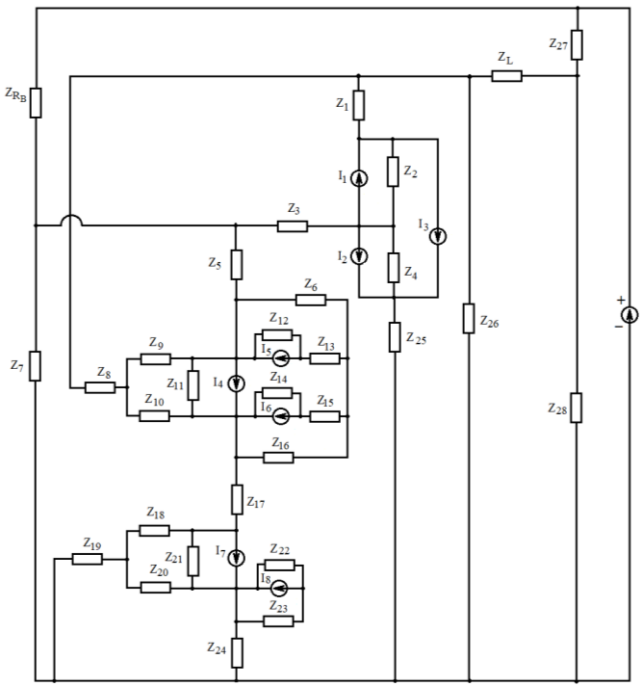

Fig. 8. Transformed equivalent circuit microelectronic transducer with frequency output for measuring magnetic field induction

Elements of the transformed equivalent circuit (Fig. 8) are described by the following values:

$$Z_{R_B} = R_1,\ Z_L = j\omega L,\ Z_1 = R_c + R_c' + j\omega L_c,\ Z_2 = \frac{1}{j\omega C_c},$$

$$Z_3 = R_{bb} + R_{bb}' + j\omega L_{bb},\ Z_4 = \frac{1}{j\omega C_e},$$

$$Z_5 = R_{s2} + R_{s2}' + j\omega L_{s2},$$

$$Z_6 = \frac{R_{b2}}{1+\omega^2 R_{b2}^2 C_{bs2}^2} - j\frac{R_{b2}^2 \omega C_{bs2}}{1+\omega^2 R_{b2}^2 C_{bs2}^2},\ Z_7 = \frac{1}{j\omega C_1},$$

$$Z_8 = R_{g2} + R_{g2}' + j\omega L_{g2},\ Z_9 = \frac{1}{j\omega C_{gs2}},\ Z_{10} = \frac{1}{j\omega C_{gd2}},$$

$$Z_{11} = R_{ds2},\ Z_{12} = \frac{1}{j\omega C_s},\ Z_{13} = R_{bs3},\ Z_{14} = \frac{1}{j\omega C_d'},$$

$$Z_{15} = R_{bd2},\ Z_{16} = \frac{1}{j\omega C_{bd2}},\ Z_{17} = R_{ds1},\ Z_{18} = \frac{1}{j\omega C_{gs1}},$$

$$Z_{19} = R_{g1} + R_{g1}' + j\omega L_{g1},\ Z_{20} = \frac{1}{j\omega C_{gd1}},\ Z_{21} = R_{ds1},$$

$$Z_{22} = \frac{1}{j\omega C_d},\ Z_{23} = R_{bd1} - j\frac{1}{\omega C_{bd1}},$$

$Z_{24} = R_{d1} + R'_{d1} + j\omega L_{d1}$, $Z_{25} = R_e + R'_e + j\omega L_e$,

$Z_{26} = \dfrac{1}{j\omega C_2}$, $Z_{27} = R_2$, $Z_{28} = R_3$.

where R_1 – magnetically sensitive resistor; L – inductance of the oscillating circuit; R_c – the resistance of the collector junction of the bipolar transistor; R'_c – ohmic resistance of the collector electrode of the bipolar transistor; L_c – collector electrode inductance; C_c – capacitance of the collector junction of the bipolar transistor; R_{bb} – base resistance; R'_{bb} – ohmic resistance of the base electrode; L_{bb} – inductance of the base electrode; C_e – emitter junction capacity; R_s – leakage resistance of the field-effect transistor; R'_s – ohmic leakage resistance; L_s – leakage electrode inductance; R_b – resistance of the substrate of the field-effect transistor; C_{bs} – capacitance substrate-leakage of the field-effect transistor; C_1, C_2 – capacitance capacitors C_1, C_2; R_g – resistance of the gate electrode; R'_g – ohmic resistance of the gate electrode of the field-effect transistor; L_g – inductance of the gate electrode; C_{gs} – shutter-leak capacity; C_{gd} – shutter-drain capacity; R_{ds} – drain-leakage resistance; C_s – leakage transition p-n capacitance; R_{bs3} – volumetric resistance p-n of the substrate-leakage transition; C_d, C'_d – capacity p-n runoff transition; R_{bd1}, R_{bd2} – three-dimensional supports p-n transition substrate-drain; C_{bd} – capacity substrate-drain; R_d – drain resistance; R'_d – ohmic drain resistance; L_d – inductance of the drain electrode; R_e – emitter transition resistance; R'_e – ohmic resistance of the emitter electrode; L_e – emitter electrode inductance; R_2, R_3 – divider supports; I_1 – collector-base current of transistor VT2; I_2 – emitter-base current of transistor VT2; I_3 – current emitter-collector of transistor VT2; I_4, I_7 – leakage currents of transistor VT1; I_5 – the substrate-source transition current of the transistor VT1; I_6 – substrate-drain-source transition current of transistor VT1; I_8 – the substrate-drain transition current of the transistor VT1.

The equation on the basis of which the analytical expression of the transformation function is obtained is determined from the circle of positive feedback of the nonlinear equivalent circuit (Fig. 8):

$$F_0 = \frac{2C_{ds}C_{bbe} \pm \sqrt{A_1 + A_2 + A_3 + A_4}}{2\pi(AA_1 + AA_2 + AA_3)} \tag{1}$$

where:

$$A_1 = C_{ds}^2 C_{bbe}^2 - 4R_B^2(B)C_{R_B}(B)C_{ds}C_{bbe}^2 - 4R_B^2(B)\times \times C_{R_B}(B)C_{ds}^2 C_{bbe}$$

$$A_2 = -4C_{bbe}^2 R_B^2(B)C_{R_B}(B)C_{cbb} - 8C_{bbe}R_B^2(B)C_{R_B}(B)\times \times C_{cbb}C_{ds} + 4C_{bbe}^2 LC_{cbb}$$

$$A_3 = 8C_{bbe}LC_{cbb}C_{ds} - 4C_{bbe}^2 R_B^2(B)C_{R_B}^2(B) - -8C_{bbe}R_B^2(B)C_{R_B}^2(B)C_{ds}$$

$$A_4 = -4C_{ds}^2 R_B^2(B)C_{R_B}(B)C_{cbb} + 4C_{ds}^2 LC_{cbb} - -4C_{ds}^2 R_B^2(B)C_{R_B}^2(B)$$

$$AA_1 = -4R_B^2(B)C_{R_B}(B)C_{ds}C_{bbe} - 4C_{bbe}R_B^2(B)C_{R_B}(B)C_{cbb}$$

$$AA_2 = 4C_{bbe}LC_{cbb} - 4C_{bbe}R_B^2(B)C_{R_B}^2(B) - -4C_{ds}R_B^2(B)C_{R_B}(B)C_{cbb}$$

$$AA_3 = 4C_{ds}LC_{cbb} - 4C_{ds}R_B^2(B)C_{R_B}^2(B)$$

Based on expression (1), the function of transforming a device with frequency output for measuring the induction of a magnetic field with a magnetically sensitive resistive element is theoretically calculated and experimentally investigated (Fig. 9).

Based on equation (1), the analytical expression of the sensitivity equation (2) of the developed device is determined:

$$S_B^{F_0} = -\frac{2C_{ds}C_{bbe} \pm 2\sqrt{A_1 + A_2 + A_3 + A_4}\cdot(D_1)}{2\pi(AA_1 + AA_2 + AA_3)} \pm \pm \frac{D_2}{\left(2\pi(AA_1 + AA_2 + AA_3)\sqrt{A_1 + A_2 + A_3 + A_4}\right)}, \tag{2}$$

where

$$D_1 = -8R_B(B)C_{R_B}(B)C_{ds}C_{bbe}\left(\frac{\partial R_B(B)}{\partial B}\right) - 4R_B^2(B)\times \times\left(\frac{\partial C_{R_B}(B)}{\partial B}\right)C_{ds}C_{bbe} - 8C_{bbe}R_B(B)C_{R_B}(B)C_{cbb}\times \times\left(\frac{\partial R_B(B)}{\partial B}\right) - 4C_{bbe}R_B^2(B)\left(\frac{\partial C_{R_B}(B)}{\partial B}\right)C_{cbb} - 8C_{bbe}\times \times R_B(B)C_{R_B}^2(B)\left(\frac{\partial R_B(B)}{\partial B}\right) - 8C_{bbe}R_B^2(B)C_{R_B}(B)\times \times\left(\frac{\partial C_{R_B}(B)}{\partial B}\right) - 8C_{ds}R_B(B)C_{R_B}(B)C_{cbb}\left(\frac{\partial R_B(B)}{\partial B}\right) - -4C_{ds}R_B^2(B)\left(\frac{\partial C_{R_B}(B)}{\partial B}\right)C_{cbb} - 8C_{ds}R_B(B)C_{R_B}^2(B)\times \times\left(\frac{\partial R_B(B)}{\partial B}\right) - 8C_{ds}R_B^2(B)C_{R_B}(B)\left(\frac{\partial C_{R_B}(B)}{\partial B}\right)$$

$$D_2 = -8R_B(B)C_{R_B}(B)C_{ds}C_{bbe}^2\left(\frac{\partial R_B(B)}{\partial B}\right) - 4R_B^2(B)\times \times\left(\frac{\partial C_{R_B}(B)}{\partial B}\right)C_{ds}C_{bbe}^2 - 8R_B(B)C_{R_B}(B)C_{ds}^2 C_{bbe}\times \times\left(\frac{\partial R_B(B)}{\partial B}\right) - 4R_B^2(B)\left(\frac{\partial C_{R_B}(B)}{\partial B}\right)C_{ds}^2 C_{bbe} - 8C_{bbe}^2\times \times R_B(B)C_{R_B}(B)C_{cbb}\left(\frac{\partial R_B(B)}{\partial B}\right) - 4C_{bbe}^2 R_B^2(B)\left(\frac{\partial C_{R_B}(B)}{\partial B}\right)\times \times C_{cbb} - 16C_{bbe}R_B(B)C_{R_B}(B)C_{cbb}C_{ds}\left(\frac{\partial R_B(B)}{\partial B}\right) - 8C_{bbe}\times \times R_B^2(B)\left(\frac{\partial C_{R_B}(B)}{\partial B}\right)C_{cbb}C_{ds} - 8C_{bbe}^2 R_B(B)C_{R_B}^2(B)\times \times\left(\frac{\partial R_B(B)}{\partial B}\right) - 8C_{bbe}^2 R_B^2(B)C_{R_B}(B)\left(\frac{\partial C_{R_B}(B)}{\partial B}\right) - 16C_{bbe}\times$$

$$\times R_B(B)C_{R_B}^2(B)C_{ds}\left(\frac{\partial R_B(B)}{\partial B}\right)-16C_{bbe}R_B^2(B)C_{R_B}(B)C_{ds}\times$$

$$\times\left(\frac{\partial C_{R_B}(B)}{\partial B}\right)-8C_{ds}^2R_B(B)C_{R_B}(B)C_{cbb}\left(\frac{\partial R_B(B)}{\partial B}\right)-4C_{ds}^2\times$$

$$\times R_B^2(B)\left(\frac{\partial C_{R_B}(B)}{\partial B}\right)C_{cbb}-8C_{ds}^2R_B(B)C_{R_B}^2(B)\left(\frac{\partial R_B(B)}{\partial B}\right)-$$

$$-8C_{ds}^2R_B^2(B)C_{R_B}(B)\left(\frac{\partial C_{R_B}(B)}{\partial B}\right)$$

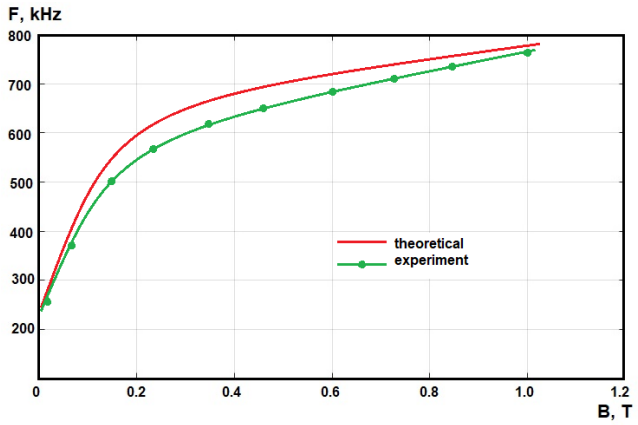

Fig. 9. Experimental and theoretical dependences of generation frequency on the influence of magnetic field induction

The experimental and theoretical dependences of the sensitivity on changes in the magnetic field induction of the developed device with a frequency output for measuring the magnetic field induction with a magnetically sensitive resistive element are shown in Fig. 10.

The sensitivity of the developed device with frequency output for measuring the induction of the magnetic field is from 400 Hz/mT to 800 Hz/mT.

3. Computer experiment

To confirm the existence of a section of negative resistance on the volt-ampere characteristic, an electric circuit microelectronic frequency transducer of the magnetic field with a magnetically sensitive resistive element and two power supplies (power supply and control source) was investigated in the circuit modeling environment LTSpice XVII [4] (Fig. 11).

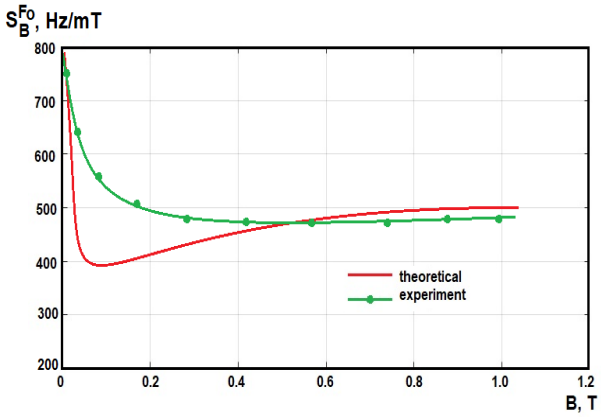

Fig. 10. Experimental and theoretical dependences of sensitivity on changes in magnetic field induction

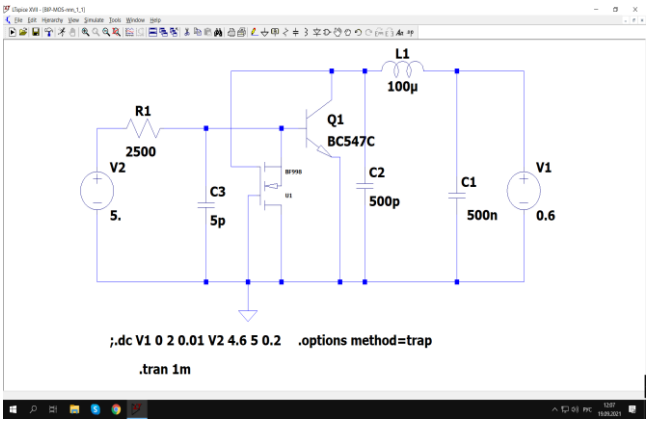

Fig. 11. Electrical circuit microelectronic transducer with frequency output for measuring magnetic field induction in the LTSpice environment

In Fig. 12 shows the volt-ampere characteristic a device with a frequency output for measuring the induction of the magnetic field obtained in the LTSpice environment [23]. From Fig. 12 shows that with increasing control voltage U_2 the area of negative resistance increases. Thus, at a current of 0.61 mA, the area of negative differential resistance U_1 lies from 0.05 to 0.4 V, at a current of 1.1 mA – from 0.07 to 0.6 V, at a current of 1.75 mA – from 1.1 to 0.8 V.

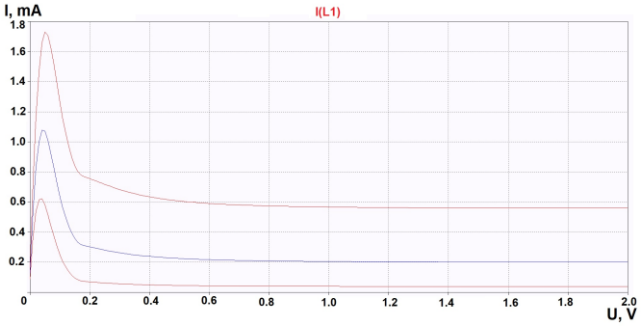

Fig. 12. Volt-ampere characteristic device with frequency output for measurement magnetic field induction

Figure 13 shows a diagram of a microelectronic transducer with frequency output for measuring the induction of a magnetic field with one power supply.

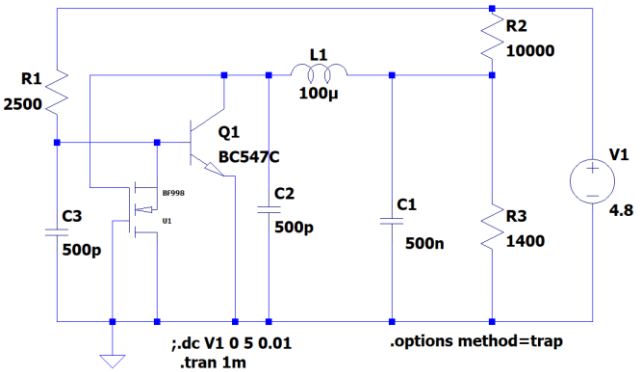

Fig. 13. Electrical circuit microelectronic transducer with frequency output for measuring magnetic field induction in the LTSpice environment with one power supply

The generation frequency of the developed microelectronic converter with a frequency output for measuring the magnetic field induction without the action of the magnetic field induction is 250 kHz. The generation frequency was tuned in the range

from 250 kHz to 750 kHz with a voltage change from 4.6 V to 5 V, which corresponds to a change in the magnetic field induction from 0 to 1 T. Figure 14 shows the changes in the output signal with time for different values of induction magnetic field: a) change in output voltage and current over time; b) change in the output voltage from time to time without the action of a magnetic field; c) change in the output voltage with time under the action of a magnetic field of 1 T.

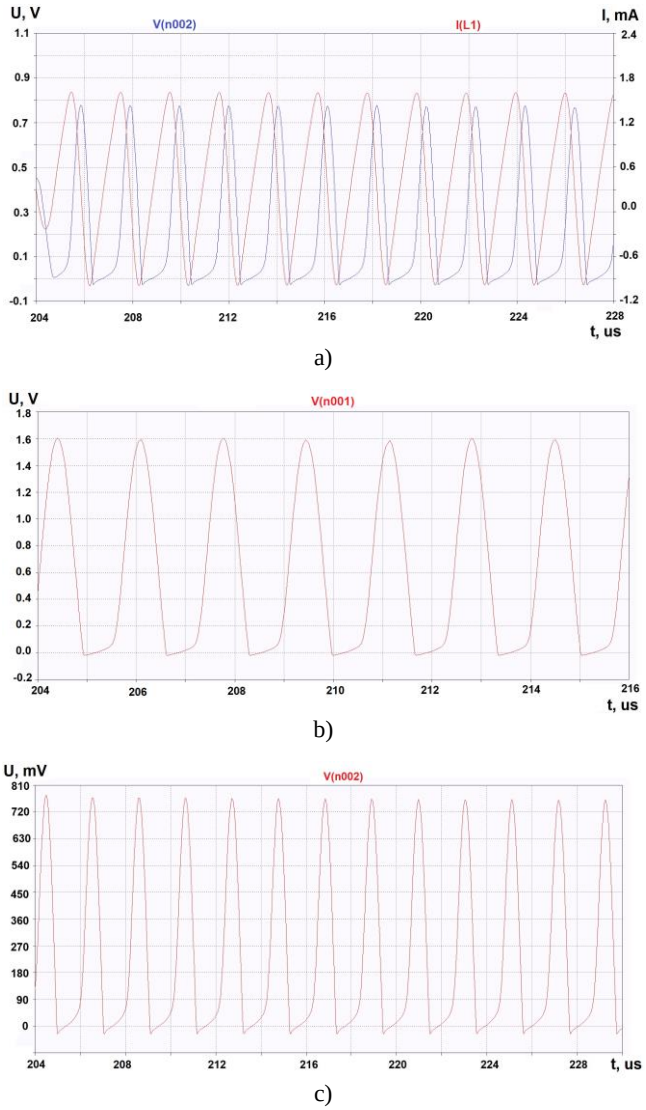

Fig. 14. Variation of the output signal with time for different values of the magnetic field induction

Based on the results of theoretical and experimental studies, it is easy to see that at the output of the microelectronic frequency transducer of the magnetic field, there will indeed be periodic oscillations, the frequency of which will increase with an increase in the value of the magnetic field induction. Comparing the obtained theoretical and experimental values of the output signal frequency, it was found that the relative error does not exceed 2.5%.

4. Conclusions

1) A new magnetically sensitive element based on the synthesized semiconductor material has been developed and investigated. A scheme for the placement of chemical bonds for this complex compound is proposed. Conducted studies of the electrically conductive properties of tetrakis-μ_3-(methoxo)(methanol)-pentakis (acetylacetonato) (tricuprum(II), neodymium(III)) methanol (I) in a compressed form in the temperature range 273–493 K showed that the conductivity changes $5.67 \cdot 10^{-14}$ $(\text{Ohm} \cdot \text{m})^{-1}$ to 1.06 $(\text{Ohm} \cdot \text{m})^{-1}$ when the temperature changes from 273 K to 493 K. In the developed magnetoresistor, when the magnetic field induction changes from 10^{-3} to 200 mT, the resistivity varies from $3.12 \cdot 10^{-5}$ Ohm·m to $1.25 \cdot 10^{-2}$ Ohm·m, and from 200 mT to 1 T, resistivity changes from $1.25 \cdot 10^{-2}$ Ohm·m to 0.3 Ohm·m.
2) On the basis of the developed magnetically sensitive resistive element, a circuit solution for a frequency converter of the magnetic field is proposed. The magnetic field frequency converter is a hybrid integrated circuit consisting of a bipolar transistor and a double-gate field-effect transistor, which creates the prerequisites for the creation of a self-oscillating device, the positive feedback circuit of which includes a magnetically sensitive resistor based on tetrakis-μ_3-(methoxo)(methanol)-pentakis(acetylacetonato) (tricuprum(II), neodymium(III)) methanol (I). Analytical expressions for the conversion function and sensitivity equations for a microelectronic transducer are obtained. The computer simulation of the developed converter was carried out in the LTSpice XVII circuit simulation environment. The generation frequency of the developed converter increases more in the range from 10^{-3} T to 0.2 T, and at a supply voltage of 5.0 V it changes from 250 kHz to 600 kHz, and over the entire range of magnetic field induction it changes from 250 kHz to 750 kHz. The sensitivity of the developed device with a frequency output for measuring the magnetic field induction is from 400 to 800 Hz/mT. The experimental studies carried out confirmed the theoretical calculations and showed that the values of the output signal frequency are described with a relative error not exceeding 2.5%.

References

[1] Azcona C. et al.: A frequency-output temperature sensor with supply voltage insensitivity for battery operated systems. 2015 IEEE International Conference on Industrial Technology (ICIT), 2015, 3330–3335.
[2] Escobar L. B. et al.: Synthesis, Crystal Structures, and EPR Studies of First Mn Ln Hetero -binuclear Complexes. Inorganic Chemistry 57(1), 2018, 326–334.
[3] Gotra Z. Yu.: Microelectronic sensors of physical quantities. Volume 2. Liga-Press, Lviv 2003.
[4] https://www.analog.com/ru/design-center/design-tools-and-calculators/ltspice-simulator.html
[5] Jackson R. G. The latest sensors. Technosphere, Moscow 2007.
[6] Krisyuk V. V. et al.: Structure and thermal properties of heterometallic complexes for gas-phase deposition of SU-PD films. Journal of Structural Chemistry 8, 2017, 1573–1580.
[7] Krisyuk V.V. et al.: Volatile Pd – Pb and Cu – Pb heterometallic complexes: structure, properties, and trans-to-cis isomerization under cocrystallization of Pd and Cu β-diketonates with Pb hexafluoroacetylacetonate. Journal of Coordination Chemistry 68(11), 2015, 1890–1902.
[8] Layfield R. A.: Organometallic Single-Molecule Magnets. Organometallics 33, 2014, 1084−1099.
[9] Osadchuk A. V. et al.: Radiomeasuring pressure transducer with sensitive MEMS Capacitor. Przegląd Elektrotechniczny 93(3), 2017, 113–116.
[10] Osadchuk A. V. et al.: Research on a magnetic field sensor with a frequency output signal based on a tunnel-resonance diode. Informatyka, Automatyka, Pomiary w Gospodarce i Ochronie Środowiska 4, 2020, 51–56.
[11] Osadchuk A. V. et al.: Theory of photoreactive effect in bipolar and MOSFET transistors. Proceedings SPIE 11176, 2019, 111761I.
[12] Osadchuk O. V. et al.: Investigation of the effect of temperature on the physical parameters of the semiconductor мего-methoxo (copper (II), bismuth (III)) acetylacetonate. Bulletin of Vinnytsia Polytechnic Institute 4(145), 2019, 80–86.
[13] Osadchuk O. V. et al.: Magnetically sensitive sensor based on heterometallic complex compound. Bulletin of the Khmelnytsky National University 3, 2019, 97–101.
[14] Osadchuk O. V. et al.: Physical parameters of the synthesized complex compound of cobalt (II) with N, N′-Bis (salicylidene) semicarbazide. Physics and Chemistry of Solid State, 21(4), 2020, 749–755.
[15] Osadchuk V. S. et al.: Microelectronic frequency transducers of magnetic field with Hall elements. Proceedings of SPIE 10808, 2018, 108086P.
[16] Osadchuk V. S. et al.: Reactive properties of transistors and transistor circuits. Universum-Vinnytsia, Vinnytsia 1999.
[17] Osadchuk V. S. et al.: The Pontial of Modern Science. Chapters. Microelectronic frequency transducers of the magnetic field based on semiconductor structures with negative differential resistance. Volume 3. Published by Science Publishing. Wenlock Road, London 2019, 212–237.

[18] Samus N. M. et al.: Heteronuclear μ-methoxo (copper, yttrium or lanthanide) acetylacetonate. Journal of General Chemistry 62(3), 1992, 510–515.
[19] Shabanova I. V. et al.: Heteronuclear complex compounds of iron (III) and neodymium (III) with hydroxy acids as starting materials for the synthesis of nanomaterials. Ecological Bulletin of the BSEC Scientific Centers 3, 2004, 91–94.
[20] Sharapov V. M., Polishchuk E. C.: Sensors: Reference manual. Technosphere, Moscow 2012.
[21] Slyusarchuk L. I. et al.: Synthesis of complex oxides from heteronuclear β-diketonate complexes of 3d-4f-metals. Abstracts of the XX Ukrainian Conference on Inorganic Chemistry. Dnipro 2018.
[22] Thurston J. H. et al.: Toward a General Strategy for the Synthesis of Heterobimetallic Coordination Complexes for Use as Precursors to Metal Oxide Materials: Synthesis, Characterization, and Thermal Decomposition of $Bi_2(Hsal)_6 \cdot M(Acac)_3$ (M = Al, Co, V, Fe, Cr). Inorg. Chem. 43(10), 2004, 3299–3505.
[23] Volodin V. Ya.: LTspice: computer simulation of electronic circuits. BHV-Petersburg, St. Petersburg 2010.
[24] Zolotareva N. V., Semenov V. V.: Diketonates and their derivatives in sol-gel processes. Uspekhi khimii 80(10), 2013, 964–987.

Prof. Alexander Osadchuk
e-mail: osadchuk.av69@gmail.com

Doctor of Technical Sciences, professor, Head of the Department of Information Radioelectronic Technologies and Systems of Vinnitsia National Technical University, Academician of the Academy Metrology Ukraine. Author of over 900 publications, including 34 monographs, 17 textbooks, 295 patents for inventions of Ukraine, more than 500 scientific articles in professional journals, of which 63 are in the scientometric databases Scopus and Web of Science.

http://orcid.org/0000-0001-6662-9141

Ph.D. Iaroslav Osadchuk
e-mail: osadchuk.j93@gmail.com

Candidate of Technical Sciences, associate professor of the Department Radio Engineering of Vinnytsia National Technical University. Author of more than 160 publications, including 6 monographs, 50 patents for inventions and more than 100 scientific articles in professional journals, of which 24 are in scientometric databases Scopus and Web of Science.

http://orcid.org/0000-0002-5472-0797

Ph.D. Volodymyr Martyniuk
e-mail: gyravl6@gmail.com

Candidate of Technical Sciences, associate professor of the Department General Physics of Vinnytsia National Technical University. Author of more than 100 publications, including, 20 patents for inventions and more than 30 scientific articles in professional journals, of which 4 are in scientometric databases Scopus and Web of Science.

http://orcid.org/0000-0001-5401-3980

Ph.D. Lyudmila Krylik
e-mail: lyudmila.krylik@gmail.com

Candidate of Technical Sciences, associate professor of the Department for Computer Science of Vinnytsia National Technical University. Author of more than 136 publications, including 2 monographs, 10 textbooks, 50 patents for inventions of Ukraine and more than 70 scientific articles in professional journals, of which 5 are in scientometric database Scopus.

http://orcid.org/0000-0001-6642-754X

Ph.D. Maria Evseeva
e-mail: eseevamv359@gmail.com

Candidate of Chemical Sciences, associate professor of the Department of Pharmaceutical Chemistry of National Pirogov Memorial Medical University, Vinnytsya. Author of more than 120 publications, including 3 monographs, 20 patents for inventions and more than 45 scientific articles in professional journals, of which 23 are in scientometric databases Scopus and Web of Science.

http://orcid.org/0000-0002-4570-2845

http://doi.org/10.35784/iapgos.2933 *received: 08.05.2022 | revised: 15.06.2022 | accepted: 15.06.2022 | available online: 30.06.2022*

STUDY OF THE ELECTROMAGNETIC IMPACT OF THE OVERHEAD TRANSMISSION LINES OF 330 KV ON ECOLOGICAL SYSTEMS

Veronika Cherkashina[1], Svitlana Litvinchuk[2], Vladyslav Lesko[3], Svetlana Kravets[4], Volodymyr Netrebskiy[3], Olena Sikorska[3], Orken Mamyrbayev[5], Baglan Imanbek[5]

[1]Kharkiv National Technical University "Kharkiv Polytechnic Institute", Kharkiv, Ukraine, [2]Mykolayiv National Agrarian University, Mykolayiv, Ukraine [3]Vinnytsia National Technical University, Vinnytsia, Ukraine, [4]Vinnytsia National Agrarian University, Vinnytsia, Ukraine, [5]Al Farabi Kazakh National University, Institute of Information and Computer Technologies, Almaty, Kazakhstan

Abstract. *The analysis of factors and approaches to the conditioning of the electromagnetic impact of 330 kV overhead transmission lines on ecological systems has been carried out. The analysis performed enabled to reveal that the world experience, recording the introduction of the transmission lines of the carrying capacity and reduced environmental impact, including the compact and controlled self-compensating lines, is expedient to take into consideration in the process of the object design, as compared with the transmission line of the conventional construction, operated in Ukraine. The technique of electromagnetic field of the 330 kV overhead transmission lines calculation is improved for the ecological systems and to clarify the width of the sanitary protection zone. Unlike other technique, the given one takes into account the line clearance and the sag of, also this technique is universal as it enables to calculate and analyze the variation of the electromagnetic field of the overhead transmission lines of different construction not only on the line route, but also at a distance from it.*

Keywords: overhead transmission line, construction, electromagnetic field, ecologic system, sanitary protection zone

BADANIE ODDZIAŁYWANIA ELEKTROMAGNETYCZNEGO NAPOWIETRZNYCH LINII PRZESYŁOWYCH 330 KV NA SYSTEMY EKOLOGICZNE

Streszczenie. *Przeprowadzono analizę czynników i podejść do uwarunkowań oddziaływania elektromagnetycznego napowietrznych linii przesyłowych 330 kV na systemy ekologiczne. Analiza pozwoliła stwierdzić, że doświadczenia światowe, odnotowujące wprowadzenie linii przesyłowych o większej nośności i mniejszym oddziaływaniu na środowisko, w tym linii kompaktowych i sterowanych samokompensujących, są celowe do uwzględnienia w procesie projektowania obiektu, w porównaniu z linią przesyłową o konstrukcji konwencjonalnej, eksploatowaną na Ukrainie. Technika obliczania pola elektromagnetycznego napowietrznych linii przesyłowych 330 kV została udoskonalona pod kątem systemów ekologicznych oraz w celu uściślenia szerokości strefy ochrony sanitarnej. W odróżnieniu od innych technik, ta uwzględnia prześwit i zwis linii, a także jest uniwersalna, gdyż umożliwia obliczanie i analizę zmienności pola elektromagnetycznego napowietrznych linii przesyłowych o różnej konstrukcji nie tylko na trasie linii, ale także w pewnej odległości od niej.*

Słowa kluczowe: napowietrzna linia przesyłowa, budowa, pole elektromagnetyczne, system ekologiczny, strefa ochrony sanitarnej

Introduction

Rates of commissioning of objects of electric power systems of Ukraine reached their peak values in the 60-70s of the last century. Nowadays with the same rate electric engineering objects overstep their 50-year limit. In the process of operation, the conditions of electric power systems changed, these changes are characterized by an increase of the transmitted power density both in normal modes and in emergency modes, necessity of the compact realization of the electric energy objects due to considerable rise in the value land, increased requirements concerning the reliability, controllability and automation, as well as a more rigid ecological policy.

Increase of the compactness and ecological safety of the electric energy objects in the requirement of the present day, the necessity to apply new approaches for the assessment of the priority decisions.

Right of ways under overhead transmission lines with the account of their considerable length can reach considerable size. For electrical – of 35 – 750 kV the area of the disposed territories as a result of the overhead transmission lines passage is 21,179.55 km [5].

This problem is extremely actual for the territories with the developing infrastructure, where the value of land increases exponentially. To reduce the disposal of territory under the overhead transmission lines and decrease the ecological impact so-called non-conventional line find wide application along with the overhead transmission lines of the conventional construction: compact overhead lines (COL); controllable self-compensated overhead lines (CSCOL); overhead lines with circuits of different voltage classes (combined overhead lines); overhead lines with insulated conductors (OLIC) [1].

1. Aim of the paper

Analyze factors and approaches, regulating electromagnetic impact of the overhead lines on the ecological systems. Improve the technique of the electromagnetic field strength – fir the determination of their impact on ecological systems and to – the width of the sanitary-protection zone, depending on the construction of the lines.

2. Main materials of the research

Analysis of factors and approaches to the normalization of the electromagnetic impact of the overhead transmission lines on the ecological systems. Relatively the impact of the AC overhead transmission lines on the ecological systems, the criteria of the harmful impact assessment are established, principles of regulation and protection measures. Numerous international organizations, such as the World Health Organization (WHO), the International Electrotechnical Commission (IEC), the European Committee for Electrotechnical Standardization (CENELEC), the Commission of the European Union (CEU), National Commissions, deal with problems of the normalization of electromagnetic field influencing the staff and population.

Main factor of the overhead transmission lines of 330 kV, determining the width of the sanitary-protection zone and influencing the ecological systems in electromagnetic field (EMF), characterized by the electromagnetic field strength. All the manifestations of the negative impact on the ecological systems may be divided into groups [1, 7, 10, 14]:

1. Impact of the electromagnetic field on the living organisms.
2. Impact of the harmonic noise on communication lines.
3. Interaction of overhead lines with engineering communications.
4. Acoustic impact of overhead lines on the environment.
5. Interaction of overhead lines with the natural landscape.

Normalization of the factors of AC overhead lines impact, their coordination with the results of numerous and sometimes contradictory medical research is extremely complex task, especially taking into simultaneous and interconnected impact of several factors. The importance of the consideration of EMF impact on the ecological systems all over the world is caused by the necessity of the objective assessment of the real danger for human health. Such an approach is determined also by the economic reasons as the observance of the sanitary norms and provision of the normalized width of the sanitary-protection zone for overhead lines (OHL) is connected with the considerable expenditures.

By its frequency characteristic electromagnetic field (EMF) of the overhead lines (OHL) is referred to the low-frequency range. As a rule, the staff maintaining the overhead installations is exposed by the short-term impact of the strong EMF. The population main remain in the zone of the weak fields of the industrial frequency, for instance, living near an overhead lines.

Nowadays the attention of the biophysicists and medical scientists is drawn not only to the study of the effects of short-term impact of the strong fields, but to the determination of the long-term consequences impact of weak low-frequency EMF, up to the super weak ones with the intensity of approximately 0.1 A/m (0.12 μTl), comparable with the intensity of low-frequency earth geomagnetic field.

It is known that the intensity of EMF near 330 kV overhead lines and higher may reach the boundary of the individual field susceptibility, when a person by indirect indication (hair stirring, pin sensation between the body and clothing) can determine the field. Approximately 5% of people feel the presence of EMF, starting from the intensity of 7 kV/m, and 60% do not feel the field with the intensity of up to 20 kV/m. Intensity of the EMF of 5 kV/m, acceptable by the standard, determined by biological impact be acceptable, taking into account the possible unfavorable. Action of the electrical charges in the process of the human contact with surrounding objects. By the results of the research the intensity of the EMF, when 80% of people do not feel pain sensations at the discharges, equals 5.2 kV/m [6, 8, 10, 11].

Negative impact of EMF of the industrial frequency was disclosed as a result of the examination of the staff, servicing energy objects, experiments on the laboratory animals and study volunteers, carried out since the 60s of the last century, further in the studies of numerous researchers. International recognition of the biological activity of EMF required the residence time regulation. As a result, in the USSR state standard GOST 12.1.002-84 was elaborated and approved. For the staff of the unrelated organizations and the local population the following norms were established: 20 kV/m for the in accessions location; 15 kV/m for unpopulated areas. Besides, admissible intensity 0.5 kV/m is normalized this allows the stay of a person in the electrical field for 24 hours a day.

International recommendations are based on the revealing of the negative impact on the organism, manifested directly at the moment or immediately after impact to EMF, and do not take into account possible long-term exposure to the impact of weak EMF [4, 7, 12, 13, 15].

As a result of numerous researches, carried out in recent decades the biological activity of weak low-frequency fields was revealed. This result turned but to be unexpected, because as a rule, the intensity of the bioeffects increases in proportionally the intensity of the acting factor. Swedish, Finnish, American, Canadian, French researchers identified carcinogenic effect up weak EMF.

Simultaneously, there appeared studies, denying these observations. Nowadays, approximately 30% of the studies prove that weak EMF of the industrial frequency can increase the number of a cancer related disease, 30% of studies claim the opposite and in 40% of cases scientists neither agree nor disagree, considering that epidemiological studies must be well-planned taking into account the variety of the factors of the environment and professional activity [4, 7, 15].

In 1996, World Health Organization (WHO) initiated the International EMF Project. The aim of the given project is to collection, analysis, generalization and coordination of the results of all the investigations, carried out in this field. In 2001 WHO issued information message, recommending to keep to the “precautionary principle” regarding the impact of low-intensity EMF and by all available means limiting the impact of EMF on human. In 1998, the International Committee ICNIRP, one of the participants in the WHO Project, released the document, regulating the permissible levels of EMF for the population.

All developed countries realize their programs to studying the impact of electromagnetic radiation on human and environment. For instance, Austria, Germany, Czech Republic, Australia, Spain, Italy and other counties, follow the recommendations suggested by ICNIRP, recording the regulation of EMF [4, 7, 12–15].

In general case, the parameter which determines the degree of EMF impact on a human is the density of the current induced in the body. In greater part of the International Standards non-dangerous for the organism density of current 10 mA/m^2 is considered as the initial value for establishing of the admissible levels of EMF parameters. Equivalent intensity of EMF, corresponding to this density, can then be decreased, applying the factor of margin for the conditions of the industrial impact and for the population. Reference level, obtained in such a way is fixed as normalized levels [7].

Such an approach to the normalization of the factors is often used abroad. In Ukraine and in some other countries, as the parameter, determining admissible levels of field intensity, maximum admissible current, flowing across the human body in case of the contact in the zone of EMF impact with the isolated machine or other large insulated object is considered. Environmental legislation functioning in Ukraine, defines principles, rules and ecological system. So-called sanitary regulation, regulating maximum permissible levels of the electric field intensity, formed by A.C. electric transmission installation of the industrial frequency [14].

Staying of the people, not electrical engineering staff, in the zone of EMF impact nowadays in Ukraine is regulated by the intensity of EMF, which is on the territory of the residential area –1 kV/m. But it should be noted that such level of EMF intensity is on the boundary of sanitary-protection zone of the overhead lines, limits of which on the both sides from the projection of the outer conductors on the earth are: 20 m – for 330 kV overhead lines and 40 m – for 750 kV overhead lines and for the overhead lines bellow 330 kV sanitary-protection zones are not established [10, 14].

As the organization of the boundaries of sanitary protection zone of the overhead lines is connected not only with considerable economic expenses, but also with the exclusion of land. This circumstance caused the necessity to perform the additional calculations of EMF impact factor in the points, remote from the conductors of the line and indicate the boundaries of the sanitary-protection zone. As in Ukraine conventional overhead lines are used, then all normative documents correspond to certain construction realization. Taking into consideration the world experience, regarding the introduction of the transmission lines of enhanced carrying capacity and decreased ecological impact, to which compact and controlled self-compensating overhead lines, are referred to, it is expedient to consider them and compare with the conventional overhead lines.

3. Method

Formation of the technique of EMF intensity calculation for the determination of 330 kV overhead lines impact on the ecological systems and adjustment of the width of sanitary-protection zone, depending on the construction of the lines.

From the point of view of determination of EMF impact on the ecological systems, that is determined by the value of EMF intensity, the problem is reduced to finding the potential of the conducting body placed in the field of the overhead line (Fig. 1).

For the determination the EMF intensity of 330 kV overhead lines of various construction (Fig. 1), the following initial data are used: U – the voltage of the overhead lines (OHL), kV; H – dimensions of the conductors of overhead lines, m; H_w – dimensions of the steel wires of the overhead lines, m; S_w – distance from the axis of the overhead line to the steel wire, m; S_z – distance between phase circuits, m; S_f – distance between phases, m; a – the distance between the conductors in a phase, m; n – the number of conductors in a phase; r_{cond} – radius of the overhead line wire, m; r_w – radius of the steel wire, m; L – horizontal distance from the axis of the outer conductor of the overhead line to the calculated point, m (towards the middle phase with the sing "-"); h – coordinates of the preset point, m; Δh – differentiation step, m.

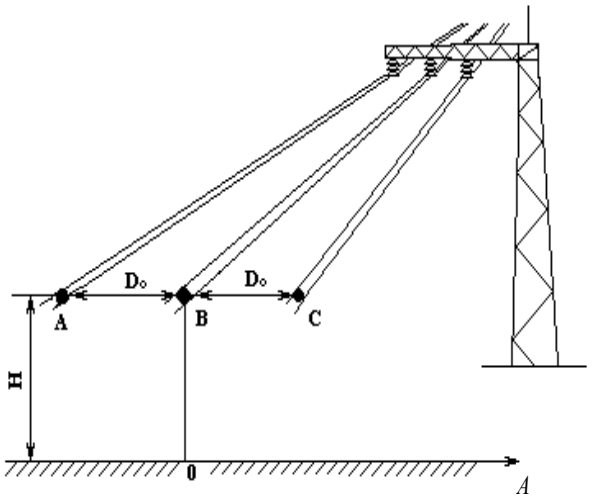

Fig. 1. Schematic representation of the overhead line for the determination of EMF intensity

Calculation of the field parameters is possible to perform using Maxwell equation for the system "conductors – steel wires – earth" [2, 3, 9]:

$$U_{ij} = \sum_{n=1}^{n} \alpha_{ij} \cdot q_{ij} \tag{1}$$

where U – phase voltage of the overhead line conductors; α_{ij} – are potential coefficients; q_{ij} – are charges of conductors per unit length.

Potential coefficients α_{ij} are determined from the following relations:

Proper potential coefficients $i = j$

$$\alpha_{ii} = \frac{1}{2\pi\varepsilon} \ln \frac{H_{ii}}{r_{ii}} \tag{2}$$

where H_{ii} – is the distance between the i^{th} conductor and its mirror reflection; r_{ii} – is equivalent radius of the conduction or steel wire.

Mutual potential coefficients $i \neq j$

$$\alpha_{ij} = \frac{1}{2\pi\varepsilon} \ln \frac{H_{ij}}{r_{ij}} \tag{3}$$

where H_{ij} – is the distance between i^{th} conductor and mirror reflection of the j^{th} conductor; r_{ij} – is the distance between i^{th} and j^{th} conductors.

Using the system of equations (1) the potential coefficients of the impact object α_{jA} are identified

$$\alpha_{jA} = \frac{1}{2\pi\varepsilon} \ln \frac{H_{jA}}{r_{ji}} + L \tag{4}$$

where H_{jA} – is the distance between the j^{th} conductor and object; r_{ij} – is the distance between i^{th} and j^{th} conductors; L – is the distance to the object.

Using the second group of Maxwell equations for the determination of the charges on the conductor's capacitive coefficients β are formed:

$$q_{ij} = \sum_{n=1}^{n} \beta_{ij} \cdot U_{ij} \tag{5}$$

However, it should be noted that the given technique does not require the calculation of the charge on the conductors and the system of equations (4) is used only for the formation of the capacitance coefficients β, which are determined by the formula:

$$\beta_{ij} = (-1)^{i+j} \Delta_{ij} / \Delta \tag{6}$$

where Δ – is the matrix determinant, composed of the coefficients α of the Maxwell equations system (1); Δ_{ij} – is the algebraic complement of the i^{th} and j^{th} elements.

In the process of improvement of the given model the symmetry of the three-phase system of voltages $\dot{U}_1, \dot{U}_2, \dot{U}_3$ was taken into account:

$$\begin{aligned} \dot{U}_1 &= U \\ \dot{U}_2 &= U \cdot a \\ \dot{U}_3 &= U \cdot a^2 \end{aligned} \tag{7}$$

where a and a^2 are complex operators of voltage vector rotation,

$a = -0.5 + j0.86$; $a^2 = -0.5 - j0.86$

Potential $\dot{U}_A$ in the present point is determined using (1 – 7):

$$\begin{aligned} \dot{U}_A = U \sum [\beta_{ij} - 0.5\left(\beta_{ij} + \beta_{ij}\right)\alpha_{jA}] + \\ + U \sum j0.86[\left(\beta_{ij} - \beta_{ij}\right)\alpha_{jA}] \end{aligned} \tag{8}$$

Having denoted the active and reactive parts of $\dot{U}_A$ by $\dot{U}_{Aa}$ and $\dot{U}_{Ap}$ correspondingly for the module $\dot{U}_A$ we will write down the equation:

$$U_A = \sqrt{U_{Aa}^2 + U_{Ap}^2} \tag{9}$$

While determining the field strength at point A, we will change its vertical component. Having determined the potential at point U_A in point A at height h and $\dot{U}_A{}'$ in the point A′ at the $h - \Delta h$ the field strength is determined by expression:

$$E_A = \frac{U_A - U_A{}'}{\Delta h} \tag{10}$$

The obtained value E_A corresponds to the vertical component of the average strength of the electric field in the region of the human head of a person of 1.8 m of height.

4. Results and discussion

Improved technique of calculation unlike other techniques, takes into account the dimension of the line and the sag of the conductor as well it is universal because it enables to calculate and analyze the change of EMF of 330 kV overhead lines of different constructions.

Application of modern technical facilities enables to solve the given task with extreme accuracy. The developed technique was used to compose the block-diagram for automatic calculation of the zone of electromagnetic impact of 330 kV overhead lines on the ecological systems (Fig. 2).

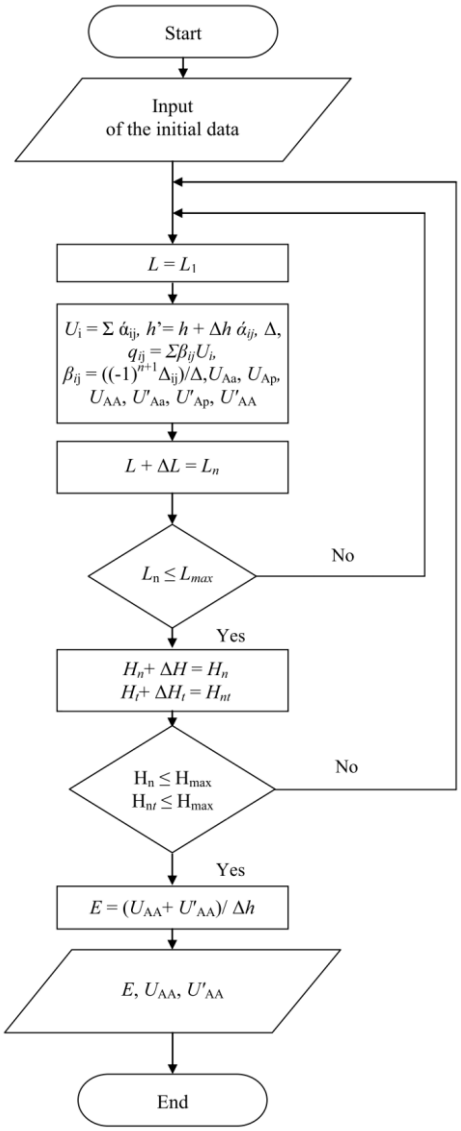

Fig. 2. Block-diagram for automated calculation of the zone of electromagnetic impact of the overhead transmission lines on the ecological systems

Modification of the EMF strength of the overhead lines of 330 kV depends on the dimension and construction of the lines, this is proved by the results of the calculations, performed according to the improved technique (1–10), using block-diagram (Fig. 2) by means of the programming platform the PowerCalc (Copyright Inprise Corporation) and presented in tables 1–3, and figure 3–5.

Fig. 6 presents the generalized graphical representation of the span of the 330 kV overhead transmission line.

Proceeding from the above-mentioned, it follows that the improvement of the construction of 330 kV overhead transmission lines not only increases their carrying capacity, but also limits the strength of EMF near the overhead transmission line, that leads to the decrease of the eliminated areas for overhead transmission lines. Thus, in the process of overhead transmission lines design, routes of which pass near the residential areas or other places where people remain for a long time (play grounds, gardens) it is expedient to include in the pre-project assessment of the variants the analysis of electromagnetic situation near the route of the overhead transmission line, in particular, consider the strength value of EMF not only on the route of the line, but also at a distance of more than 20 m from the projection of the outer conductor, because with the distance from the overhead transmission line, the strength decreases slower, than at small distances, that is why, the given fact requires more accurate calculation [16, 17].

Table 1. Modification of the EMF strength for 330 kV overhead transmission lines of the conventional construction

Dimension H, m	Distance, m	E, kV/m	Distance, m	E, kV/m	Distance, m	E, kV/m
10	20	0.997	20	0.997	28	0.466
12	20	1.21	23	0.922	32	0.445
14	20	1.41	25	0.936	34	0.486
16	20	1.58	27	0.941	36	0.493
20	20	1.78	30	0.976	44	0.462
24	20	1.84	33	0.962	48	0.485
26	20	1.83	34	0.965	50	0.489

Table 2. Modification of the EMF strength compact for 330 kV overhead transmission lines

Dimension H, m	Distance, m	E, kV/m	Distance, m	E, kV/m	Distance, m	E, kV/m
10	20	1.13	22	0.938	30	0.468
12	20	1.34	22	0.938	33	0.467
14	20	1.51	26	0.926	35	0.491
16	20	1.65	27	0.982	38	0.482
20	20	1.81	30	0.983	43	0.483
24	20	1.83	32	0.996	47	0.472
26	20	1.81	33	0.988	49	0.491

Table 3. Modification of EMF strength value for the controlled self-compensating 330 kV overhead transmission lines

Dimension H, m	Distance, m	E, kV/m	Distance, m	E, kV/m	Distance, m	E, kV/m
10	20	0.549	16	0.846	22	0.450
12	20	0.644	16	0.957	24	0.494
14	20	0.725	18	0.864	26	0.445
16	20	0.892	18	0.927	28	0.439
20	20	0.868	18	0.984	30	0.471
26	20	0.870	18	0.952	32	0.496

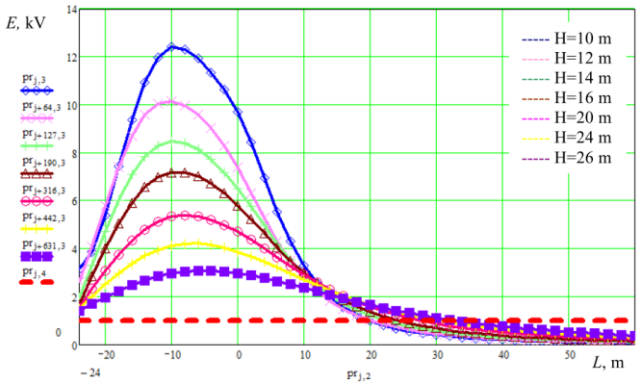

Fig. 3. Dependence of EMF strength modification on the dimension of 330 kV overhead transmission line of the conventional construction

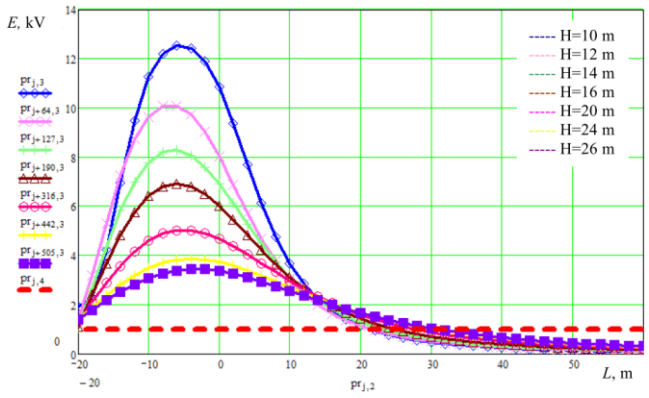

Fig. 4. Dependence of EMF strength modification of the dimension of compact 330 kV overhead transmission line

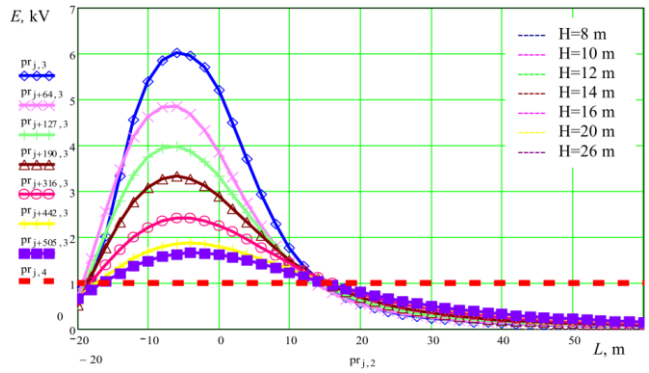

Fig. 5. Dependence of EMF strength modification on the dimension of CSOTL 330 kV

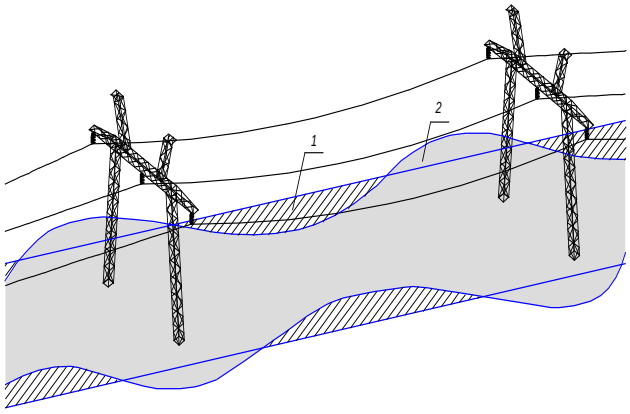

Fig. 6. Generalized graphical presentation of the span of 330 kV overhead transmission line: 1 – territory, normalized for the overhead transmission line, with the account of sanitary-protection zone; 2 – the territory, calculated for the overhead transmission line, with the account of sanitary protection-zone

For the realization of these tasks the following engineering solutions can be used:

- decrease of the interphase distances at a result of carrying out measures, aimed at reduction of the calculated overvoltage ratio;
- transition from the conventional to compact and self-compensating transmission lines of the increased carrying capacity and reduced ecological impact;
- usage of the vegetation arrays to provide the ecological safety of the lines.

5. Conclusions

1. Analysis of the factors and approaches of the normalization of the electromagnetic impact of the overhead transmission lines of 330 kV on ecological systems enables to determine that the world experience regarding the implementation of the overhead transmission lines of the increased carrying capacity and decreased ecological impact, which compact and controlled self-compensating overhead lines are referred, it is expedient to take into account in the process of the object design as compared with the lines of the conventional construction, operated in Ukraine.

2. Technique of the 330 kV the electromagnetic field strength for the determination of their impact on the ecological systems and specification of the sanitary-protection zone width is improved. Unlike other techniques, the given technique takes into account the dimension of the line and sag of the conductor, it is universal because it enables to calculate and analyze of the electromagnetic field of the 330 kV overhead transmission lines of different constructions. Realization of the given technique in the package of programs APM of the designer of the overhead transmission lines will enable determine with greater efficient the main direction in the process of the object design, taking into account electromagnetic situation not only on the route of the line, but also at the distance from it.

References

[1] Cherkashina V. V., Cheremisin M. M.: Establishment of a priority projecting line in the minds of the day. Proceedings of Controlled power transmission lines 2007–2017, 9, 2017, 50–91.
[2] Cherkashina V. V., Cheremisin M. M.: In accordance with the method of assessing the tension of electric fields of power transmission lines. Proc. 5th Inter. Sc. and Pract. Conf. Problems and prospects for the development of energy, electrical technology and automation in the agro-industrial complex, 2019, 31–32.
[3] D'yakov A. F. (ed.): Super- and Ultrahigh Voltage Electrical Networks of the Russian Unified Energy System. Theoretical and Practical Base. STC Energoprogress, Moscow 2012.
[4] Directive 2013/35/EU. Electromagnetic fields: Social innovation "EaSI" (2014–2020).
[5] Energy strategy of Ukraine for the period up to 2035 r. "Safety, energy efficiency, competitiveness". Ordering from September 18, 2017. No. 605-r. http://www.ukrenergo.energy.gov.ua
[6] Hatibovic A.: Advanced Application of the Catenary and the Parabola for Mathematical Modeling of the Conductor and Sag Curves in the Span of an Overhead Line (doctoral thesis). Óbuda University, Budapest 2019.
[7] International Commission on Non-Ionizing Radiation Protection (ICNIRP): Guidelines for limiting exposure to electromagnetic fields (100 kHz to 300 GHz). Health Physics 118(5), 2020, 483–524.
[8] Ivanov I. E.:Assessment of the influence of various factors on the values of resistances and conductivities of a high-voltage overhead power line. Bulletin of ISUE 3, 2017, 30–39.
[9] Morozov Yu. A., Yakobson B. G.: A simplified method for calculating the electric field strength under the wires of high-voltage power lines. Sci. slave. Institute of Labor Protection All-Union Central Council of Trade Unions 103, 1976, 21–23.
[10] Rules for the regulation of electrical installations. Industry, Kharkiv 2017.
[11] Singhal A: Volt/var control with high solar PV penetration in distribution systems and its impact on the transmission grid (Theses and Dissertations). Iowa State University, Ames 2019.
[12] Stam R.: Comparison of international policies on electromagnetic fields. National Institute for Public Health and the Environment, Bilthoven 2018.
[13] Stam R.: National precautionary policies on magnetic fields from power lines in Belgium, France, Germany, the Netherlands and the United Kingdom. National Institute for Public Health and the Environment, Bilthoven 2018.
[14] State sanitary norms and rules of protection of the population from the effects of electromagnetic radiation with changes were registered by the Ministry of Justice of Ukraine on May 16, 625/30493, 2017.
[15] Statement and further consultation: Proposed measures to require compliance with international guidelines for limiting exposure to electromagnetic fields (EMF). Ofcom, 2020.
[16] Vasilevskyi O. M., Kulakov P. I., Dudatiev I. A. et al.: Vibration diagnostic system for evaluation of state interconnected electrical motors mechanical parameters. Proc. of SPIE 10445, 2017, 104456C.
[17] Vasilevskyi O., Didych V., Kravchenko A. et al.: Method of evaluating the level of confidence based on metrological risks for determining the coverage factor in the concept of uncertainty. Proc. of SPIE 10808, 2018, 108082C.

D.Sc. Eng. Veronika Cherkashina
e-mail: veronika2473@gmail.com

Doctor of Science (Engineering), associate professor, Department of Electric Power Transmission, Kharkiv National Technical University "Kharkiv Polytechnic Institute", Kyrpychova str., 2, 61002, Kharkiv, Ukraine.

http://orcid.org/0000-0002-5639-9722

Ph.D. Volodymyr Netrebskiy
e-mail: netrebskiy@ukr.net

Ph.D., associate professor, Department of Power Plants and Systems, Vinnytsia National Technical University, Khmelnytsky highway, 95, 21000, Vinnytsia, Ukraine

http://orcid.org/0000-0003-2855-1253

Ph.D. Svitlana Litvinchuk
e-mail: svitlanalitvinchk@ukr.net

Ph.D. in pedagogy, associate professor of the Department of Methodology of Vocational Training, Faculty of Engineering and Energy, Mykolaiv National Agrarian University. Author of more than 50 publications, including five textbooks and more than 30 scientific articles in professional journals, 7 of them in scientometric databases Web of Science, Google Scholar, Index Copernicus International.

http://orcid.org/0000-0002-9885-7234

Ph.D. Olena Sikorska
e-mail: olenasikorska@ukr.net

Ph.D., Department of Power Plants and Systems, Vinnytsia National Technical University, Khmelnytsky highway, 95, 21000, Vinnytsia, Ukraine

http://orcid.org/0000-0001-7341-9724

Ph.D. Vladyslav Lesko
e-mail: leskovlad@ukr.net

Ph.D., associate professor, Department of Power Plants and Systems, Vinnytsia National Technical University, Khmelnytsky highway, 95, 21000, Vinnytsia, Ukraine.

http://orcid.org/0000-0002-5477-7080

Ph.D. Orken Mamyrbayev
e-mail: morkenj@mail.ru

Deputy Deputy General Director in science and head of the Laboratory of computer engineering of intelligent systems at the Institute of Information and Computational Technologies of the Kazakh National Technical University named after K. I. Satbayev and associate professor in 2019 at the Institute of Information and Computational Technologies.
Main research field: machine learning, deep learning, and speech technologies.
http://orcid.org/0000-0001-8318-3794

M.Sc. Svetlana Kravets
e-mail: swkravec2017@gmail.com

M.Sc., research assistant, Department of Technological Processes and Equipment for Processing and Food Industries, Vinnytsia National Agrarian University.

http://orcid.org/0000-0001-8628-8479

Ph.D. Baglan Imanbek
e-mail: imanbek.baglan18.06@gmail.com

Ph.D., associate professor, Department of AI&BigData, Al Farabi Kazakh National University, Almaty, Kazakhstan.

http://orcid.org/0000-0001-7249-380X

http://doi.org/10.35784/iapgos.2948 *received: 08.05.2022 | revised: 10.06.2022 | accepted: 15.06.2022 | available online: 30.06.2022*

DETERMINATION OF THE OPTIMAL FREQUENCY OF THE PRIMARY MEASURING TRANSDUCER OF THE THICKNESS OF DIELECTRIC COATINGS OF METAL SURFACES

Kostyantyn V. Ovchynnykov[1], Oleksandr M. Vasilevskyi[1], Volodymyr M. Sevastianov[1], Yurii A. Polievoda[2], Aliya Kalizhanova[3], Bakhyt Yeraliyeva[3]

[1]Vinnytsia National Technical University, Faculty of Intelligent Information Technology and Automation, Vinnytsia, Ukraine, [2]Vinnytsia National Agrarian University, Department of technological processes and equipment for processing and food production, Vinnytsia, Ukraine, [3]M. Kh. Dulaty Taraz Regional University, Taraz, Kazakhstan

Abstract. *The article provides an analysis of the physical processes underlying the operation of the measuring transducer, with a time based information presentation. A mathematical model is developed that describes the process of free oscillation attenuation excited in the LC-contour of primary measuring transducer, and analyzes and evaluates the influence of external factors that influence the measurement results. The ways of elimination of their influence on the results of measuring control are offered.*

Keywords: measuring, transducer, thickness, dielectric coating, metal surface, oscillation

WYZNACZANIE OPTYMALNEJ CZĘSTOTLIWOŚCI PIERWOTNYCH PRZETWORNIKÓW POMIAROWYCH DO POMIARU GRUBOŚCI POWŁOK DIELEKTRYCZNYCH NA POWIERZCHNIACH METALOWYCH

Streszczenie. *Artykuł zawiera analizę procesów fizycznych leżących u podstaw pracy przetwornika pomiarowego wraz z prezentacją informacji w czasie. Opracowano model matematyczny opisujący proces tłumienia drgań swobodnych wzbudzanych w obwodzie LC głównego przetwornika pomiarowego, analizujący i oceniający wpływ czynników zewnętrznych na wyniki pomiarów. Proponowane są sposoby wyeliminowania ich wpływu na wyniki kontroli pomiarów*.

Słowa kluczowe: pomiar, przetwornik, grubość, powłoka dielektryczna, powierzchnia metalu, oscylacja

Introduction

The basic principles of construction of measuring transducers, based on the excitation method in the electrically conductive basis of the measuring object of vortex currents, are described in [4, 5, 24]. The process of energy transfer in a oscillatory circuit can be of a different nature. Depending on the ratio of the active and characteristic (wave) contour resistance, the periodic (oscillatory) process can turn into aperiodic. But regardless of the nature of the transient process in the circuit, the time constant remains unchanged for certain parameters [14].

Since in a real oscillatory circuit, due to losses of accumulated energy for heating, free oscillations will always be attenuating; the main characteristic of the oscillatory circuit is the damping decrement, which is directly proportional to the active contour resistance and inversely proportional to the contour circuit's wavelength and its Q factor. The greater the active resistance of the contour, the smaller the time of attenuation of excited free fluctuations in it. The main energy losses in the circuit occur mainly in the active resistance of the coil, so the decay of the attenuation and the quality of the circuit will be determined by the quality factor of the coil of inductance [23, 26].

The equivalent circuit of the measuring transducer is shown in Fig. 1.

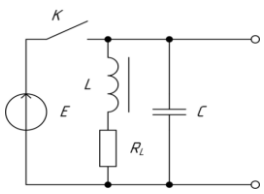

Fig 1. Equivalent circuit of the measuring transducer

1. Formulation of the problem

The change in the duration of the transition process in the circuit when applying the active component of the resistance in the form of a metal base of the object to be measured will depend on many factors. To increase the accuracy of measurement of such a time interval, it is necessary to ensure the maximum amplitude of the change in the damping time of free oscillations of the isolated circuit and the circuit that interacts with the object of measurement. One of the parameters that can be changed in a wide range without changing the hardware properties of the measuring transducer is the frequency of oscillations in the circuit. Therefore, the task of determining the optimal value of the oscillation circuit frequency is relevant, at which the maximum accuracy of measuring the attenuation time of free oscillations in the circuit can be achieved

2. Theoretical research

The total resistance of the inductor Z_{lss} coil will be determined as [25]:

$$Z_{lss} = Z_0 + Z_{md} = Z_0 + 2\pi f M \Psi(\beta,\gamma), \quad (1)$$

where Z_{lss} – the resistance of the coil; Z_0 – complete resistance in the absence of electromagnetic field conductive material; Z_{md} – additional resistance (introduced), which occurs when the coil of the conductive material appears; M – coefficient of co-induction (interaction) of a coil of inductance and conductive material; $\Psi(\beta,\gamma)$ – a function of flow coupling for a coil located normal to a flat conduct or plate with certain dimensions, conductivity and other parameters of the conductive material; β, γ – generalized parameters that characterize the geometrical and physical properties of the metal base of the control object.

The co-induction coefficient M is a functional dependence of the distance ℓ between the end of the core of the coil and the surface of the conductive material [6], which is described by the expression:

$$M = M_0 e^{-\frac{6l}{d_e}} \quad (2)$$

where M_0 – the coefficient of co-induction between the coil inductance and its mirror image at zero gap between the ends of their rods; d_e – equivalent diameter of the coil of inductance. For the convenience of calculations, the equivalent diameter value is taken to be equal to the average diameter of the coil. The value of the coefficient M_0 is determined from the ratio:

$$M_0 = \frac{e_1}{\frac{\Delta i_2}{\Delta t}} \quad (3)$$

where e_1 – the electromotive force of interinvitation, which arises in the first circuit with a uniform change in current at 1 amperes per second in the second circuit; i_2 – the current flowing along the second contour, with the first and second contours being inductively connected.

The value of the co-induction coefficient M_0 is determined experimentally under the following conditions: two coils of inductance L and L' having identical electrical, physical and geometric parameters, connecting the cores one of them is connected to the generator of the sinusoidal voltage through the resistor $R1$ (Fig. 2), which satisfies the condition:

$$R1 >> \sqrt{R_L^2 + (L \cdot \omega)^2} \tag{4}$$

where R_L – the active resistance of the inductance coil, L – the inductance of the input coil, ω – the angular frequency of the sinusoidal voltage. Another coil is connected to a voltmeter. The resistor $R2$ with a nominal resistance of about 10^3 Ohm for the load of the inductor L' is connected.

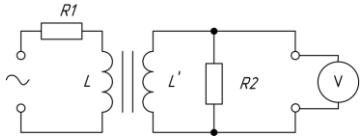

Fig. 2. Schematic diagram of the installation to determine the coefficient of co-induction between the coil and its mirror image

Using the scheme (Fig. 2), the expression for determining the coefficient of interinduction (3) can be rewritten as follows

$$M_0 = \frac{e_2 R1}{2\pi f U_0} \tag{5}$$

where e_2 – the electromotive force occurring in the second coil; $R1$ – the resistance, which specifies the current in the coil of the inductance; f – the frequency of the generator signal; U_0 – the amplitude value of the sinusoidal voltage of the generator. During the change of current Δt in the first circuit, the period of sinusoidal voltage e_1 was taken.

For a non-ferromagnetic plane conductor plate, the flow-coupling function $\Psi(\beta,\gamma)$ has the form

$$\Psi(\beta,\gamma) = -j\frac{2\beta^2 + th\frac{\gamma}{4}\sqrt{9+j4\beta^2}}{3\sqrt{9+j4\beta^2} + (9+j2\beta^2)th\frac{\gamma}{4}\sqrt{9+j4\beta^2}} \tag{6}$$

where $\beta = \frac{d_e}{2}\sqrt{2\pi f\mu\sigma}$; $\gamma = \frac{4h}{d_e}$; μ – the magnetic permeability of the plate; σ – specific electrical conductivity of the material of the plate; h – the thickness of the plate.

Substituting the equation (1), (3) and (6) in expression (1), we obtain the dependence for the complete resistance of the oscillatory circuit

$$Z_{вт} = Z_0 - j2\pi f M_0 e^{-\frac{6l}{d_e}} \frac{2\beta^2 + th(\frac{\gamma}{4}\sqrt{9+j4\beta^2})}{\sqrt[3]{9+j4\beta^2} + (9+j2\beta^2)th(\frac{\gamma}{4}\sqrt{9+j4\beta^2})} \tag{7}$$

To ensure the maximum sensitivity of the measuring transducer, it is necessary that the conductive object of a certain size, when approaching the inductance coil, contributes the maximum value of the full resistance to the contour. Since the circuit works in a resonant mode, the reactive component of the introduced resistance can be neglected [1, 27].

The expression for determining the time constant of free-fluctuation attenuation in the contour is written as follows [14]

$$\tau_k = \frac{2L}{Z_0 + Z_{вн}} = \frac{2L}{R_L + R_{вн}} \tag{8}$$

Performing the substitution in expression (8) of the above relations, we obtain an equation that describes the dependence of the time of attenuation of free oscillations excited in the LC-contour from the distance of the end of the core of the inductance coil to the conductive material of the control object's basis [2, 13].

$$\tau_k = \left[-2L\frac{K}{R_L}\left(9+54P+81P^2+4\beta^4P^2\right)\right] \times \left(-9K-54KP-81KP^2-4K\beta^4P^2+4Y\beta^2P^2\frac{K}{R_L}+6Y\beta^2\sqrt{\frac{2K}{R_L}-18}+4Y\beta^4P\sqrt{\frac{2K}{R_L}+18}+18\beta^2P\sqrt{\frac{2K}{R_L}-18}\right)^{-1} \tag{9}$$

where $K = R_L\sqrt{81+16\beta^4}$; $P = th\left(\frac{1}{4}\gamma\right)$; $Y = \pi f M_0 e^{-\frac{6l}{d_e}}$.

3. Experimental research

The analysis of equation (9) shows that the dependence of the decay time of free oscillations excited in the circuit from the distance l of the end of the inductor coil to the conductive basis of the control object has a nonlinear character. At the same time, the transformation function (9) has a plot with an approximate linear character, and if using elements of the oscillatory circuit with optimal parameters it is possible to create a measuring transformer with a transformation function that is close to linear in a definite range of variation of the distance from the end of the coil to electrical conductive basis of the object of control.

To conduct research, we will address the following characteristics of the object of measurement control [13, 15, 20]:

- thickness of dielectric coating ℓ, μm: 10 – 200;
- metal base material: steel grades 040A10, 1449-1HR, 1HR, 2HR, DC01, DD13;
- specific electrical conductivity of the base material σ, Sm/m: 6.8×10^6;

The following parameters of inductance coils of the primary measuring transducer (L1, L2, L3) are used for the analysis:

- coil inductance is $122\cdot10^{-3}$ mH, $520\cdot10^{-3}$ mH, $1000\cdot10^{-3}$ mH;
- active resistance of coils 2.0 Ohm, 3.7 Ohm, 4.6 Ohm;
- the equivalent diameter of the coils is 7 mm, 8 mm, 9 mm.

For each coil, the value of the coefficient of interinduction M_0 was determined experimentally. To do this, an experimental installation was used, the principal scheme of which is shown in Fig. 2. The research was carried out in the frequency range of the generator of sinusoidal voltage from 5 kHz to 50 kHz. The averaged values of the experimental results for coils with different parameters in the form of the dependence of the coefficient of co-induction of the coil and its mirror image of the frequency of the supply voltage are given in Fig. 3. Significant change in the coefficient of interinduction is observed when the frequency of the supply voltage varies from 5 kHz to 50 kHz, so the theoretical study determined the average value of the M_0 coefficient from the specified frequency range of the supply voltage.

To determine the M_0 coefficient, the amplitude value of the voltage in the second circuit was determined from the results of the experiment (Fig. 2). The results are shown in Table 1.

Table 1. Amplitude values of the voltage in the second circuit when changing the frequency of the supply voltage from 5 kHz to 50 kHz

f, kHz	5	10	15	20	25
$e_2(L1)$, mV	25.0	25.0	30	32.5	35.0
e_2 ($L2$), mV	22.5	22.7	25.9	27.5	30.0
e_2 ($L3$), mV	21.3	22.1	24.8	27.0	29.0
f, kHz	30	35	40	45	50
$e_2(L1)$, mV	40.0	40.5	41.1	41.4	41.7
e_2 ($L2$), mV	35.0	35.2	35.8	36.1	36.3
e_2 ($L3$), mV	32.0	32.2	32.7	32.9	33.1

The graph of the change of the coefficient of interconnection M_0 from the frequency of the supply voltage is presented in Fig. 3.

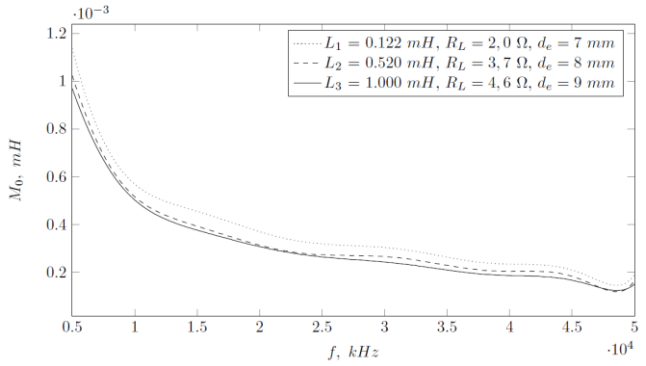

Fig. 3. Dependence of the co-induction coefficient of the coil and its mirror image on the frequency of the supply voltage

For theoretical studies, the mean value was chosen for the value of the co-induction coefficient. According to the results of the experiment, the following values of the coefficients of interinvitation were obtained [15, 22]:

- for L1, the coefficient of interinvection M_0 = 0.40 mH;
- for L2, the coefficient of interinvection M_0 = 0.36 mH;
- for L3, the coefficient of interinvection M_0 = 0.34 mH.

The choice of the optimum frequency of the measuring transducer was carried out provided that the primary sensitivity of the primary measuring transducer was maximized in the range of the change in the thickness of the dielectric coating from 0 μm to 200 μm. To ensure maximum sensitivity in the absence of external perturbing factors, it is necessary to ensure the maximum value of the introduced resistance when changing the thickness of the coating by 1%, and accordingly the maximum value of the increase in the time of attenuation of excited free oscillations. To determine the optimal frequency value, we obtain the following dependence [10, 21]

$$\delta(\mathrm{f}) = \tau_{\mathrm{k}}(\mathrm{f},\mathrm{l}) - \tau_{\mathrm{k}}(\mathrm{f},(\mathrm{l}\cdot 1.01)) \tag{10}$$

and a definite argument of the function at which it acquires the maximum value [11, 16].

Theoretically, the values of the optimal frequency were determined for different thicknesses of the basis of the control object h (0.18 mm, 0.22 mm, 0.36 mm) [8] at various values of the parameters of the inductance coils of the measuring transducer [3, 9, 12, 17–19]:

- inductance of coils L1 – $122\cdot10^{-3}$ mH, L2 – $520\cdot10^{-3}$ mH, L3 – $1000\cdot10^{-3}$ mH;
- active resistance of coils R1 – 2.0 Ohm, R2 – 3.7 Ohm, R3 – 4.6 Ohm;
- the equivalent diameter of the coils $d1_e$ – 7 mm, $d2_e$ – 8 mm, $d3_e$ – 9 mm.

For conducting theoretical investigations, the magnetic permeability of the base material (steel grade 040A10, 1449-1HR, 1HR, 2HR, DC01, DD13[20]) was taken into account as 600 objects by known practical studies [7, 23], which determine the physical and chemical properties of steel for annealing temperature in the range of 0–200°C set the initial and maximum permeability respectively μ_i = 400 and μ_m = 650. Specific electrical conductivity of the material of the basis of the object of control was determined on the basis of the known value of the specific resistance ρ of the 08КП alloy at a temperature of 20°C $\rho = 147\times10^{-9}$ Ω·m and assumed to be equal to 6.8×10^6 cm/m.

4. Conclusions

The given data of theoretical studies testify that the optimum frequency of the oscillatory circuit of the measuring transducer depends on the parameters of the inductance coil of the measuring transducer. So, for an inductor of a primary converter of $122\cdot10^{-3}$ mH, the frequency from the range 170 - 400 kHz can be considered optimal. As the inductance increases to $1000\cdot10^{-3}$ mH, the optimal frequency will increase, and the optimal value will be within the range of 340–750 kHz. At the same time, the absolute value of the gain of the decay time of oscillations also depends on the parameters of the inductance of the oscillatory circuit and increases with increasing its inductance. So, when using the inductance L1 = $122\cdot10^{-3}$ mH, with an equivalent diameter of the coil of 7 mm, the absolute value of the gain of the oscillation decay time is 260 μs. With an increase in inductance to L3 = $1000\cdot10^{-3}$ mH, this gain will be 720 μs.

Obviously, for the control of objects with different thickness of the metal base, it is advisable to use one type of inductance at different frequency values, since the change in the increase in the oscillation decay time for the range of change in the thickness of the base 0.18–0.36 mm for one inductance will be: for L1 $122\cdot10^{-3}$ mH – 4%; for L2 $520\cdot10^{-3}$ mH – 3%; for L2 $1000\cdot10^{-3}$ mH – 3%. At the same time, the difference in the attenuation time for different inductances at the same frequency (350 kHz) at best would be 55% for L1 and L2, in the worst case for L1 and L3 at the same frequency would be 68%.

References

[1] Azarov O. D., Dudnyk O. V., Kaduk O. V., Smolarz A., Burlibay A.: Method of correcting of the tracking ADC with weight redundancy conversion characteristic. Proc. of SPIE 9816, 2015, 98161V.
[2] Azarov O. D., Murashchenko O. G., Chernyak O. I., Smolarz A., Kashaganova G.: Method of glitch reduction in DAC with weight redundancy. Proc. of SPIE 9816, 2015, 98161T.
[3] Bereziuk O. V., Lemeshev M. S., Bogachuk V. V., Duk M.: Means for measuring relative humidity of municipal solid wastes based on the microcontroller Arduino UNO R3. Proc. of SPIE 10808, 2018, 108083G [http://doi.org/10.1117/12.2501557].
[4] Cathey J.: Electric Machines. McGraw-Hill, 2001.
[5] Fitzgerald A. E., Kingsley C. Jr., Umans S. D.: Electric Machinery. McGraw-Hill, 2005.
[6] Grover F. W.: Inductance Calculations. Dover Publications, 2009.
[7] Hechler O., Axmann G., Donnay B.: The right choice of steel. Sections.arcelormittal.com (11.01.2019).
[8] ISO 6892-1:2016 Metallic materials - Tensile testing - Part 1: Method of test at room temperature, 2016.
[9] Kozlov L. G., Bogachuk V. V., Bilichenko V. V. et al.: Determining of the optimal parameters for a mechatronic hydraulic drive. Proc. of SPIE 10808, 2018, 1080861 [http://doi.org/10.1117/12.2501528].
[10] Kvyetnyy R. N., Sofina O. Yu., Lozun A. V. et al.: Modification of fractal coding algorithm by a combination of modern technologies and parallel computations. Proc. of SPIE 9816, 2015, 98161R.
[11] Obertyukh R. R., Slabkyi A. V., Marushchak M. V. et al.: Dynamic and mathematical models of the hydraulic-pulse device for deformation strengthening of materials. Proc. of SPIE 10808, 2018, 108084Y [http://doi.org/10.1117/12.2501519].
[12] Ogorodnikov V. A., Zyska T., Sundetov S.S.: The physical model of motor vehicle destruction under shock loading for analysis of road traffic accident. Proc. of SPIE 10808, 2018, 108086C [http://doi.org/10.1117/12.2501621].
[13] Osadchuk V. S., Osadchuk A. V.: The magneticreactive effect in transistors for construction transducers of magnetic field. Electronics and Electrical Engineering 3(109), 2011, 119-122.
[14] Pain H. J.: The physics of vibrations and waves. John Wiley & Sons, 2005.
[15] Pavlov S. V., Kozhemiako V. P., Kolesnik P. F. et al.: Physical principles of biomedical optics: monograph. VNTU, Vinnytsya 2010.
[16] Polishchuk L. K., Kozlov L. G., Piontkevych O. V. et al.: Study of the dynamic stability of the conveyor belt adaptive drive. Proc. of SPIE 10808, 2018, 1080862 [http://doi.org/10.1117/12.2501535].
[17] Semenov A., Osadchuk O., Semenova O., Bisikalo O., Vasilevskyi O., Voznyak O.: Signal Statistic and Informational Parameters of Deterministic Chaos Transistor Oscillators for Infocommunication Systems. International Scientific-Practical Conference Problems of Infocommunications – Science and Technology (PIC S&T), 2018.

[18] Trishch R., Nechuiviter O., Dyadyura K., Vasilevskyi O., Tsykhanovska I., Yakovlev M.: Qualimetric method of assessing risks of low quality products. MM Science Journal 2021(4), 2021, 4769–4774.
[19] Vasilevskyi O. M., Kulakov P. I., Dudatiev I. A. et al.: Vibration diagnostic system for evaluation of state interconnected electrical motors mechanical parameters. Proc. of SPIE 10445, 2017, 104456C [http://doi.org/10.1117/12.2280993].
[20] Vasilevskyi O. M.: Calibration method to assess the accuracy of measurement devices using the theory of uncertainty. International Journal of Metrology and Quality Engineering 5, 2014, 403.
[21] Vasilevskyi O., Kulakov P., Kompanets D. et al.: A new approach to assessing the dynamic uncertainty of measuring devices. Proc. of SPIE 10808, 2018, 108082E [http://doi.org/10.1117/12.2501578].
[22] Vassilenko S. V., Teixeira J.P., Pavlov S.: Energy harvesting: an interesting topic for education programs in engineering specialities. Proc. of Internet, Education, Science IES-2016, 2016, 149-156.
[23] Vedmitskyi Y. G., Kukharchuk V. V., Hraniak V. F.: New non-system physical quantities for vibration monitoring of transient processes at hydropower facilities, integral vibratory accelerations. Przeglad Elektrotechniczny 93(3), 69-72, 2017.
[24] Webster J. G., Eren H.: Measurements, instrumentation and sensors handbook: Spatial, mechanical, thermal and radiation measurement. CRC press, 2014.
[25] Wojcik W., Kisala P.: The method for the recovery of the apodization function of the fiber Bragg gratings on the basis of its spectra. Przeglad Elektrotechniczny 86(10), 2010, 127-130.
[26] Wojcik W.: Application of fibre-optic flame monitoring systems to diagnostics of combustion process in power boilers. Bulletin of the Polish Academy of Sciences-Technical Sciences 56 (2), 2008, 177-195.
[27] Wójcik W., Vasilevskyi O., Didych V. et al.: Method of evaluating the level of confidence based on metrological risks for determining the coverage factor in the concept of uncertainty. Proc. of SPIE 10808, 2018, 108082C [http://doi.org/10.1117/12.2501576].

Ph.D. Kostyantyn Ovchynnykov
e-mail: ovkos1980@gmail.com

Ph.D., associate professor of Department of Automation and Intelligent Information Technologies, Vinnytsia National Technical University. Research Interests: measurement of geometrical sizes of dielectric coatings on conducting bases with the use of conversion
of measuring information in tin intervals, software of measuring equipment.

http://orcid.org/0000-0003-4685-1137

Prof. Oleksandr Vasilevskyi
e-mail: o.vasilevskyi@gmail.com

Doctor of Technical Sciences, professor, Professor of the Department of Metrology and Industrial Automatcs, as well as Professor of the Department of Computer Science of the Vinnitsa National Technical University. Academician of the Academy of Metrology of Ukraine, an official representative from Ukraine in the IMEKO. Author of more than 200 publications, including 3 monographs, 3 collective monographs, 16 textbooks, 5 patents for inventions of Ukraine, more than 100 scientific articles in peer-reviewed journals, 24 of them in the Scopus scientometric databases and Web of Science.

http://orcid.org/0000-0002-8618-0377

Ph.D. Volodymyr Sevastianov
e-mail: sevastiyanov.vladimir@vntu.edu.ua

Ph.D., associate professor of Department of Automation and Intelligent Information Technologies, Acting Dean of the Faculty of Intelligent Information Technology and Automation Vinnytsia National Technical University. Research Interests: information-measurement and control systems, software engineering, computer science & education, Industry 4.0, Internet of Things.

http://orcid.org/0000-0001-8385-7146

Ph.D. Yurii Polievoda
e-mail: vinyura36@gmail.com

Candidate of Technical Sciences, associate professor of the Department of technological processes and equipment for processing and food production, Vinnytsia National Agrarian University. Author of more than 86 publications, including 3 textbooks, 33 patents for inventions and more than 51 scientific articles in professional journals, of which 9 are in scientometric databases Scopus and Web of Science.

http://orcid.org/0000-0002-2485-0611

Ph.D. Aliya Kalizhanova
e-mail: kalizhanova_aliya@mail.ru

Candidate of physical and mathematical sciences, professor, University of Power Engineering and Telecommunications, the chief researcher of the Institute of Information and Computational Technologies of the Ministry of Education and Science CS of the Republic of Kazakhstan. Scientific interests of the leader: mathematical modeling of systems, models of transport systems network analysis, optimization methods, technologies for developing sensor systems for signals receive-transmit, mathematical modeling of Bragg fiber gratings.

http://orcid.org/0000-0002-5979-9756

M.Sc. Bakhyt Yeraliyeva
e-mail: yeraliyevabakhyt81@gmail.com

Senior lecturer of the Information Systems Department, Faculty of Information Technology, M. Kh. Dulaty Taraz Regional University, Taraz, Kazakhstan.
Research interests: Information technologies, fiber-optic technologies, microprocessor systems.

http://orcid.org/0000-0002-8680-7694

http://doi.org/10.35784/iapgos.2949 *received: 08.05.2022 | revised: 08.06.2022 | accepted: 15.06.2022 | available online: 30.06.2022*

DYNAMICS OF THE CONVEYOR SPEED STABILIZATION SYSTEM AT VARIABLE LOADS

Leonid K. Polishchuk[1], Oleh V. Khmara[1], Oleh V. Piontkevych[1], Oksana O. Adler[1], Aigul Tungatarova[2], Ainur Kozbakova[3]

[1]Vinnytsia National Technical University, Vinnytsia, Ukraine, [2]Taraz Regional University named after M.Kh.Dulaty, Taraz, Kazakhstan, [3]Almaty Technological University, Institute of Institute of Information and Computational Technologies of the Ministry of Education and Science CS of the Republic of Kazakhstan, Almaty, Kazakhstan

Abstract. *The dynamic processes of the system of stabilization of the speed of the conveyor belt with a built-in hydraulic drive on the basis of an improved mathematical model, which takes into account the physical phenomena occurring in the hydraulic system during the action of alternating load. The influence of the main parameters of the hydraulic system and the magnitude of the load on the course of dynamic processes is analyzed and recommendations for their selection are formulated. The proposed scheme of the built-in hydraulic drive of a conveyor belt with system of stabilization of speed of movement automatically provides its uninterrupted work. The use of an additional hydraulic pump allowed to stabilize the speed of the conveyor belt to 7.8%, provided that the load on the working link is 2.3 times.*

Keywords: dynamics, belt conveyor, built-in hydraulic drive, speed stabilization system, variable load

DYNAMIKA SYSTEMU STABILIZACJI PRĘDKOŚCI PRZENOŚNIKA PRZY ZMIENNYCH OBCIĄŻENIACH

Streszczenie. *Rozważono procesy dynamiczne układu stabilizacji prędkości taśmy przenośnika z wbudowanym napędem hydraulicznym w oparciu o udoskonalony model matematyczny uwzględniający zjawiska fizyczne zachodzące w układzie hydraulicznym podczas działania obciążenia zmiennego. Przeanalizowano wpływ głównych parametrów układu hydraulicznego i wielkości obciążenia na przebieg procesów dynamicznych oraz sformułowano zalecenia dotyczące ich doboru. Zaproponowany schemat wbudowanego napędu hydraulicznego przenośnika taśmowego z systemem stabilizacji prędkości ruchu automatycznie zapewnia jego nieprzerwaną pracę. Zastosowanie dodatkowej pompy hydraulicznej pozwoliło ustabilizować prędkość taśmy przenośnika na poziomie 7,8% przy założeniu, że obciążenie ogniwa roboczego jest 2,3 razy większe.*

Słowa kluczowe: dynamika, przenośnik taśmowy, wbudowany napęd hydrauliczny, system stabilizacji prędkości, zmienne obciążenie

Introduction

The belt conveyors are the important components of current production technologies in various industries and the national economy. To a large extent, the efficiency of their use is determined by the technical characteristics of the drive device, the technical and economic indicators of which must provide the operating conditions of transport machines and their modes of operation [1, 4, 16].

Receipt and distribution of cargo moving on the conveyor belt, as a rule, can occur according to various laws.

Therefore, belt conveyors are mainly used in conditions of variable loads, the maximum excess of which in comparison with the nominal can become significant. When operating belt conveyor drives, conditions arise under which, due to the large load increase, the drive needs to be stopped immediately to prevent breakage of the drive. This reduces the productivity of the conveyor [3, 6, 14].

To increase the productivity of conveyors operated in the above conditions, it is proposed to use built-in hydraulic actuators with a control system for switching on an additional hydraulic motor. This will ensure uninterrupted operation, as well as greatly simplify the kinematic scheme according to the work [9, 13, 18]. Such drives work in the mode of constant supply of working liquid therefore the hydraulic system does not allow to provide stability of speed of movement of a belt of the conveyor [8,10]. When the additional hydraulic motor is switched on, the fluid flow is reduced by the value of the characteristic volume of this hydraulic motor and the speed of cargo transportation is reduced. The instability of the speed of movement of the conveyor belt leads to a decrease in productivity and reduces the efficiency of the control system with hydraulic automation [15, 19, 20].

1. Statement of the research problem

The purpose is to study the dynamic processes in the hydraulic drive conveyor speed stabilization system (SSS) of the belt and recommend the choice of parameters of the drive system.

To achieve this goal, the following tasks were solved in the work:

- for the developed hydraulic system of the belt conveyor, what operates in the modes of variable cargo flows, in which the means of hydro- and electroautomatics ensure the stability of the speed of the belt movement [11];
- the analysis of the influence of the main parameters of the hydraulic system and the magnitude of the load on the course of dynamic processes in the built-in hydraulic drive with the SSS was carried out.

2. Research and modeling method

Theoretical studies of the dynamic processes of the SSS of the conveyor for the action of variable loads were carried out by methods of physical and mathematical modeling. The solution of the improved mathematical model was performed using the software package MATLAB Simulink, which was used in previous studies of the hydraulic system [2, 12, 13]. 0.1% modeling accuracy and the 2nd order Rosenbrock research method have proven to be a qualitative way to calculate such systems.

To construct an improved mathematical model of the dynamics of the SSS of the conveyor, which operates under variable loads, a cyclogram of the operation of the hydraulic drive with the specified control system has been developed. For each phase of the cyclogram, differential equations were added, which took into account the physical processes characteristic of the corresponding time interval.

Fig. 1 shows a calculation scheme of the hydraulic system of the conveyor drive, operating in the mode of alternating cargo flows, for theoretical studies of dynamic processes.

The moving parts of the conveyor are represented by two discrete masses (12 and 14). The masses of rotating parts of drive devices with the moment of inertia I_3 are reduced to the first mass, to the second – moving links of the transporting part of the conveyor with the moment of inertia I_4. The moment of resistance of the useful forces M_0 acting on the conveyor is applied to the tail drum. The tensile forces of the tape F_1, F_2, F_3, F_4 are applied to the discrete masses 12 and 14. The conveyor belt is presented by Voigt's rheological model with elastic-dissipative connections.

SSS contains main 1 and additional 2 hydraulic pumps with characteristic volumes q_{n1} and q_{n2}, respectively. The maximum pressure created by them is determined by adjusting the safety valve 3. The executive units of the SSS hydraulic drive of the conveyor are the main 9 and additional 10 hydraulic motors with the corresponding characteristic volumes q_{m1} and q_{m2}. The flow of working fluid from the pumping station is supplied to the hydraulic motors with the corresponding supply. The executive link is a plunger 8 with a corresponding mass m_3 of friction clutch 7, which turns on the transmission mechanism of the additional hydraulic motor 10. The plunger 8 is loaded with a spring with a stiffness k_3. The working cavities of the hydraulic motors and the pressure plunger are connected to the corresponding cavities of the main component of the SSS by short hydraulic lines. The control device (CD) of the valve type performs the function of a distributor [5, 7, 17].

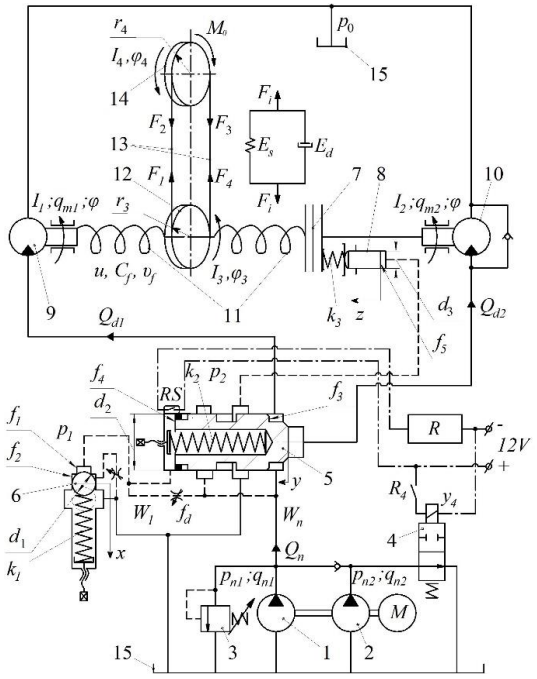

Fig. 1. Calculation scheme of the built-in hydraulic drive with system of stabilization of speed of movement of a belt of the conveyor

The main components of the CD are the valve of the first stage 6 (sensor), the ball shut-off element of which mass m_1 is loaded by a spring with stiffness k_1. The valve of the second stage 5 in the form of a shut-off and distribution element (SDE) with a mass of m_2 is loaded with a control spring of stiffness k_2. A control throttle with a cross-sectional area f_{d2} is installed between the intermediate and drain cavities of the sensor. In the hydraulic line between the cavities of the shut-off and distribution element is a control throttle with a cross section of area f_d. The shank of the shut-off and distribution element is equipped with a magnetic ring. On the side surface of the case there is a sensor type reed switch RS. Friction clutch 7 is activated when the set value of the pressure in the hydraulic system, which corresponds to the increased load. After that, the second transmission mechanism is activated by the additional hydraulic motor 10.

To compensate for the losses of the working fluid entering the main hydraulic motor 9 when the additional hydraulic motor 10 is connected to the hydraulic system, it is necessary to make up for the losses of the working fluid from the pumping station in the hydraulic system. This is ensured by switching on an additional hydraulic pump 2. Automation of this process is carried out due to operation of the sensor of the reed switch RS type at the beginning of movement of the shut-off and distributing device. According to the specified cyclogram with a small delay in time, it connects an additional hydraulic motor 10, and then triggers the friction clutch 7 of the drive gear of its transmission. The reed switch RS supplies an electrical signal to the switch R_4 to turn on the power supply of the hydraulic lock 4, which turns on the supply of an additional hydraulic motor 10 to the hydraulic system. Due to the replenishment of the flow of working fluid in the hydraulic system, the speed of rotation of the shafts remains unchanged, as in the nominal load on the conveyor. The speed of the conveyor belt remains unchanged

The improved mathematical model of SSS is built on the basis of the calculation scheme (Fig. 1). D'Alembert's principle is applied to the forces acting on the moving elements of the mechanical system and the balance of the working fluid flow [13]. In the differential equations of change of the moment of forces of useful resistance, action of forces of viscous friction on rotating elements of hydraulic motors, change of directions of movement of working liquid in the course of work of CD, energy dissipation during movement of moving elements of system are considered.

The given mathematical model is an improved model of the adaptive hydraulic drive of the belt conveyor, the hydraulic system of which works in the mode of constant liquid consumption [13, 14].

Equation of equilibrium of moments on the shafts of the main 9 and additional 10 hydraulic motors during CD operation ($y > 0$; $F_a > F_{tr}$):

$$M + M_0 = q_{m1} \cdot p_n + q_{m2} \cdot p_n - \beta_m \frac{d\varphi}{dt} \quad (1)$$

The opening of the locking element of the sensor 6 occurs under the condition of increasing the pressure in the hydraulic drive to the value

$$p_1 \geq (k_1 \cdot x)/f_1 \quad (2)$$

The movement of the ball locking element after opening the sensor, provided that the pressure in the drain cavity $p_0 \approx 0$, is written by the equation:

$$f_2 \cdot p_1 = m_1 \frac{d^2x}{dt^2} + k_1(x_0 + x) + b_1 \frac{dx}{dt} + F_{g1} \quad (3)$$

where F_{g1} – hydrodynamic force in the sensor to be determined

$$F_{g1} = F'_{g1} - F''_{g2} = \rho Q \upsilon_w \cdot \cos\beta_0 - \rho Q \upsilon_c = \rho Q(\upsilon_w \cdot \cos\beta_0 - \upsilon_c) \quad (4)$$

If $0 \leq x \leq h_c$, $h_c = h_{cd} + h_{cb}$ flow rate through the sensor

$$Q = \mu \cdot \pi \cdot d_1 \cdot x \sqrt{2|p_1|/\rho} \cdot \mathrm{sgn}(p_1) \quad (5)$$

The displacement of the shut-off element 5 for $0 \leq y \leq h_b$ is written by the equation:

$$p_n f_3 = p_1 f_4 + k_2 y_0, \text{ if } y = 0 \quad (6)$$

$$p_n f_3 = m_2 \frac{d^2y}{dt^2} + k_2(y_0 + y) + b_2 \frac{dy}{dt} + p_1 f_4 + F_{g2}, \text{ if } y > 0 \quad (7)$$

where F_{g2} – hydrodynamic force in the SDE to be determined

$$F_{g2} = \psi_g p_n f_3 \quad (8)$$

Equation of working fluid flow balance in a pressure hydraulic line:

$$Q_{n1} = Q_{m1} + Q_{fd} + \beta W_n \frac{dp_n}{dt}, \quad \text{if } y = 0 \quad (9)$$

$$Q_{n1} + Q_{n2} = Q_{m1} + Q_{m2} + Q_{fd} + \beta W_n \frac{dp_n}{dt} \quad \text{if } 0 < y < h$$

$$Q_{n1} + Q_{n2} = Q_{m1} + Q_{m2} + Q_{fd} + Q_k + \beta W_n \frac{dp_n}{dt}, \text{ if } y \geq h_d \quad (11)$$

there is an opening of the cavity of the plunger of SDE, where:

$$Q_{fd} = \mu \cdot f_d \sqrt{2|p_n - p_1|/\rho} \cdot \mathrm{sgn}(p_n - p_1) \quad (12)$$

$$Q_k = \mu \cdot \pi \cdot d_2 \cdot (y - (h_b + h_d)) \sqrt{2|p_n - p_2|/\rho} \cdot \mathrm{sgn}(p_n - p_2) \quad (13)$$

The flow rate of the working fluid Q_{fd} after the choke with a cross section f_d and the shut-off and distribution element in the cavity of the plunger 8 Q_k are determined by the expressions:

$$Q_{fd} = Q + \beta W_1 \frac{dp_1}{dt} \quad (14)$$

$$f_5 \cdot \frac{dz}{dt} + \mu \cdot \pi \cdot d_2 \cdot (h_b - y) \sqrt{2|p_2|/\rho} \cdot \mathrm{sgn}(p_2) + \beta W_2 \frac{dp_2}{dt} = 0 \quad (15)$$

if $y = 0 \ldots h_b$ – there is a drain of the working fluid from the cavity of the plunger 8.

$$f_5 \cdot \frac{dz}{dt} + \beta W_2 \frac{dp_2}{dt} = 0, \text{ if } y = h_b \ldots h_d \quad (16)$$

$$Q_k = f_5 \cdot \frac{dz}{dt} + \beta W_2 \frac{dp_2}{dt}, \text{ if } y = h_d \ldots h \quad (17)$$

it is the working fluid is injected into the cavity of the plunger 8.

The equation of motion of the plunger 8 of the friction clutch:

$$p_2 f_5 = m_3 \frac{d^2 z}{dt^2} + k_3 (z_0 + z) + b_3 \frac{dz}{dt} + F_a \quad (18)$$

The force F_a begins to act at the moment of contact of the plunger with the coupling.

Closing of the ball locking element of the sensor occurs under the condition of reducing the pressure to the value [2]

$$p'_1 \le p_1 \cdot f_1 / f_2 + (k_1 \cdot x) / f_2 \quad (19)$$

The following notations are used in equations (1-19): M – torque on the shafts of hydraulic motors; p_n – pressure in the hydraulic system at rated load on the working link; p_1 and p'_1 – pressure "opening" and "closing" of the ball locking element corresponding to the calculated maximum load on the working link; p_2 – pressure in the cavity of the plunger of the pressure mechanism; x, y, z – coordinates of movement of the corresponding masses; x_0, y_0, z_0 – initial deformation of compression springs; β_m – coefficient of viscous friction in the hydraulic motor; β – coefficient of pliability taking into account the compressibility of the working fluid; μ – coefficient of supply; ρ – the density of the working fluid; $S = f_1/f_2$ – the ratio of the area of contact of the shut-off element with the valve seat to the area of the cylindrical part of the valve; f_3, f_4, f_5 – respectively, the surface area of the ends of the shut-off and distribution element and the plunger 8; h_c, h, h_m – respectively the course of the ball locking element 6, shut-off and distribution element 5 and the friction clutch discs; W_n, W_1, W_2 – the volume of the pressure line, the cavity of the sensor 6 and the cavity of the plunger 8, respectively; d_1, d_2, d_3 – diameter of ball locking element 6, shut-off and distribution element 5 and friction clutch disks, respectively; b_1, b_2, b_3 – viscous damping factor; β_0 – the angle of inclination of the jet of working fluid; v_w, v_c – the speed of the fluid in the slit and the saddle, respectively; ψ_g – force factor; Q_{fd}, Q_k – fluid flow rate for the throttle with a cross-sectional area fd, in the cavity of the plunger 8, respectively; F_{g1}, F_{g2} – hydrodynamic forces acting on the ball valve 6 and shut-off and distribution element 5; F_a – coupling reaction of couplings; F_{tr} – friction force between the clutch discs.

3. Results and discussions

Consider the case when the disturbance for the hydraulic system is a change in load torque of 2.3 times compared to the nominal. In Fig. 2 shows the dependence of the load torque M and the angular velocity $d\varphi/dt$ of rotation of the drive drum of the conveyor from time t without the use of an additional hydraulic pump. The overload mode occurs when the moment of force of resistance M increases from 4500 to 10500 N·m. The mechanical system in this case perceives a decrease in the speed of rotation of the drive drum by 27.7%. When the additional hydraulic motor 10 is switched on, the angular velocity $d\varphi/dt$ is exceeded by 13% relative to the nominal one. After the overload disappears and the additional hydraulic motor 10 is switched off, the value of exceeding the angular velocity $d\varphi/dt$ is 18.1%, which is negatively reflected in the dynamics of the conveyor.

In Fig. 4 shows the influence of the characteristic volume of the additional hydraulic pump 2 and the characteristic volume of the additional hydraulic motor 10 of the conveyor hydraulic drive on the accuracy of the speed stabilization δ, the value of σ_{on} the excess of the angular speed $d\varphi/dt$ relative to the nominal one when the additional hydraulic motor 10 is turned on and the value of σ_{off} – during its shutdown at a constant overload value. On the abscissa axis, point 1 corresponds to the specified characteristics of the conveyor hydraulic drive at a ratio of 25% of the characteristic volume of the additional hydraulic motor 10 to the characteristic volume of the main hydraulic motor 9 and in the absence of an additional hydraulic pump 2.

When using the additional hydraulic pump 2 in the hydraulic system, the dynamic and static characteristics of the conveyor drive are significantly improved (Fig. 3). Consider the case of using in the hydraulic system of the additional hydraulic pump 2 with a characteristic volume of 25% of the main hydraulic pump 1, and the same ratio of the characteristic volumes of the additional 9 and the main 10 hydraulic motors

It is established that the accuracy of speed stabilization δ improves to 7.8%, and the dynamics of the drive drum improves when turning off the additional hydraulic motor 10. The value of exceeding the angular velocity $d\varphi/dt$ relative to the nominal is 8.4%, which is 2.2 times less than when working with one hydraulic pump and reduced belt speed of the conveyor.

It is established that the accuracy of speed stabilization δ improves to 7.8%, and the dynamics of the drive drum improves when turning off the additional hydraulic motor 10. The value of exceeding the angular velocity $d\varphi/dt$ relative to the nominal is 8.4%, which is 2.2 times less than when working with one hydraulic pump and reduced belt speed of the conveyor.

Point 2 – corresponds to the characteristics of the hydraulic system, the design diagram of which is shown in Fig. 1, with a ratio of 25% of the characteristic volume of the additional hydraulic motor 10 to the characteristic volume of the main hydraulic motor 9, and the same ratio of the characteristic volumes of the additional 2 and main 1 hydraulic pump in the overload mode. Point 3 – corresponds to the above ratio, which is 37.5%, and point 4 – 50%.

The analysis of the obtained characteristics showed that with the increase of the ratios of the characteristic volumes of hydraulic motors and hydraulic pumps from 25% to 50%, the accuracy of stabilization of the speed δ of the conveyor increases from 7.8% to 4.4%. However, there is a deterioration in the quality of dynamic characteristics: the value of σ_{on} exceeding the angular velocity $d\varphi/dt$ relative to the nominal when turning on the additional hydraulic motor 10 varies from 20.7% to 51.9%, and the value of σ_{off} when turning off the additional hydraulic motor 10 – from 8.4% to 26.5%.

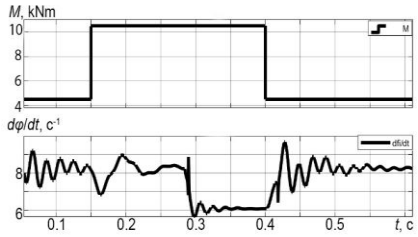

Fig. 2. Dependence of loading moment M and angular speed of rotation of a driving drum dφ/dt on time t without the auxiliary hydraulic pump

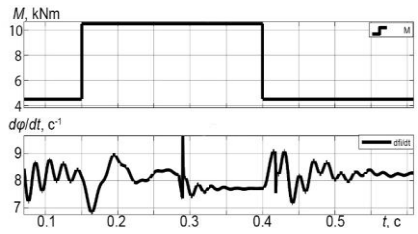

Fig. 3. Dependence of loading moment M and angular speed of rotation of a driving drum dφ/dt on time t with the auxiliary hydraulic pump

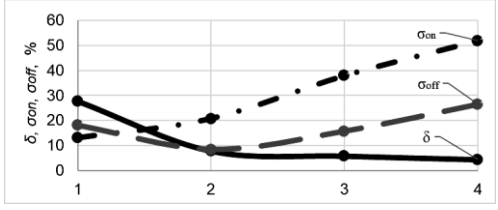

Fig. 4. Static and dynamic characteristics of the hydraulic drive of the conveyor with control systems at different ratios of characteristic volumes of hydraulic motors 9 and 10, and also hydraulic pumps 1 and 2

4. Conclusions

1. The proposed scheme of the built-in hydraulic drive of a conveyor belt with system of stabilization of speed of movement automatically provides its uninterrupted work. The use of an additional hydraulic pump allowed to stabilize the speed of the conveyor belt to 7.8%, provided that the load on the working link is 2.3 times.
2. Analysis of the transients of the dynamic characteristics of the mechanical system of the conveyor for an advanced mathematical model of the pressure pn in the pressure line of the hydraulic drive showed a slight effect of increasing the flow of working fluid when connected to the hydraulic system of an additional hydraulic pump 2.
3. The most appropriate for this increase in the load on the working link of the conveyor is the use of an additional hydraulic motor 10 and hydraulic pump 2 with a ratio of characteristic volumes of 25% to the main.

References

[1] Forental V., Forental M., Nazarov F.: Investigation of Dynamic Characteristics of the Hydraulic Drive with Proportional Control. Procedia Engineering 129, 2015, 695–701.
[2] Gubarev A. P., Hanpantsurova O. S., Belikov K. A. et al.: Logic correctness of control algorithms for mechatronic discrete systems with parallel processes. Proc. of SPIE 11176, 2019, 1117660.
[3] Gubarev A., Yakhno O., Ganpantsurova O.: Control Algorithms in Mechatronic Systems with Parallel Processes. Solid State Phenomena 164, 2010, 105–110 [http://doi.org/10.4028/www.scientific.net/SSP.164.105].
[4] He D., Liu X., Zhong B.: Sustainable belt conveyor operation by active speed control. Measurement 154, 2020, 107458.
[5] Khmara L. A., Shatov S. V., Polishchuk L. K. et al.: Algorithm to calculate work tools of machines for performance in extreme working conditions. Wójcik W., Pavlov S., Kalimoldayev M. (ed.): Mechatronic Systems I. Applications in Transport, Logistics, Diagnostics and Control. Taylor & Francis Group – CRC Press, London, New York 2021, 29–38.
[6] Kozlov L. G., Polishchuk L. K., Piontkevych O. V. et al.: Experimental research characteristics of counterbalance valve for hydraulic drive control system of mobile machine. Przeglad Elektrotechniczny 95(4), 2019, 104–109.
[7] Kozlov L., Polishchuk L., Piontkevych O. et al.: Optimization of design parameters of a counterbalance valve for a hydraulic drive invariant to reversal loads. Wójcik W., Pavlov S., Kalimoldayev M. (ed.): Mechatronic Systems I. Applications in Transport, Logistics, Diagnostics and Control. Taylor & Francis Group – CRC Press, London, New York 2021, 137–148.
[8] Kukharchuk V. V., Bogachuk V. V., Hraniak V. F. et al.: Method of magneto-elastic control of mechanic rigidity in assemblies of hydropower units. Proc. of SPIE 10445, 2017, 104456A.
[9] Kukharchuk V. V., Kazyv S. S., Bykovsky S. A. et al.: Discrete wavelet transformation in spectral analysis of vibration processes at hydropower units. Przeglad Elektrotechniczny 93(3), 2017, 65–68.
[10] Kushwaha P., Dasgupta K., Ghoshal S. K.: A comparative analysis of the pump controlled, valve controlled and prime mover controlled hydromotor drive to attain constant speed for varying load. ISA transactions 120, 2022, 305–317 [http://doi.org/10.1016/j.isatra.2021.03.020].
[11] Nykyforov V. V., Salamatin D. M., Digtiar S. V. et al.: Toxicity by Digestate of Methanogenic Processing of Biomass Wójcik W., Pawłowska M. (ed.): Biomass as Raw Material for the Production of Biofuels and Chemicals. Taylor & Francis Group – CRC Press, London 2021, 155–170.
[12] Obertyukh R., Slabkyi A., Polishchuk L. K. et al.: Method of project calculation of hydroimpulsive device for vibroturning with an incorporated cycle spring pressure pulse generator. Wójcik W., Pavlov S., Kalimoldayev M. (ed.): Mechatronic Systems I. Applications in Transport, Logistics, Diagnostics and Control. Taylor & Francis Group – CRC Press, London, New York 2021, 1–16.
[13] Polishchuk L. K., Kozlov L. G., Piontkevych O. V., Gromaszek K., Mussabekova A.: Study of the dynamic stability of the conveyor belt adaptive drive. Proc. of SPIE 10808, 10808, 2018, 1–10.
[14] Polishchuk L., Kharchenko Ye., Piontkevych O., Koval O.: The research of the dynamic processes of control system of hydraulic drive of belt conveyors with variable cargo flows. Eastern Eur. J. Enterp. Technol. 2(8(80)), 2016, 22–29.
[15] Polishchuk L., Mamyrbayev O., Gromaszek K.: Mechatronic Systems II. Applications in Material Handling Processes and Robotics. Taylor & Francis Group – CRC Press, Boca Raton, London, New York, Leiden 2021 [http://doi.org/10.1201/9781003225447].
[16] Semrád K., Draganová K., Koščák P., Čerňan J.: Statistical prediction models of impact damage of airport conveyor belts. Transportation research procedia 51, 2020, 11–19 [http://doi.org/10.1016/j.trpro.2020.11.003].
[17] Shatokhin V., Granko B., Sobol V. et al.: Vibration diagnostic of wear for cylinder-piston couples of pumps of a radial piston hydromachine. Wójcik W., Pavlov S., Kalimoldayev M. (ed.): Mechatronic Systems I. Applications in Transport, Logistics, Diagnostics and Control. Taylor & Francis Group – CRC Press, London, New York 2021, 39–52.
[18] Vedmitskyi Y. G., Kukharchuk V. V., Hraniak V. F.: New non-system physical quantities for vibration monitoring of transient processes at hydropower facilities, integral vibratory accelerations. Przeglad Elektrotechniczny 93(3), 2017, 69–72.
[19] Wójcik W., Pavlov S., Kalimoldayev M.: Mechatronic Systems I. Applications in Transport, Logistics, Diagnostics and Control. Taylor & Francis Group – CRC Press, London, New York 2021 [http://doi.org/10.1201/9781003224136].
[20] Yelizarov M. O., Pasenko A. V., Zhurav V. V. et al.: Fallen Leaves and Other Seasonal Biomass as Raw Material for Producing Biogas and Fertilizers. Wójcik W., Pawłowska M. (ed.): Biomass as Raw Material for the Production of Biofuels and Chemicals. Taylor & Francis Group – CRC Press, London 2021, 145–154.

Prof. Leonid K. Polishchuk
e-mail: leo.polishchuk@gmail.com

Doctor of Technical Sciences, professor, academician at the Ukraine Academy of Hoisting-and-Transport Sciences. Vinnytsia National Technical University. Head of the Department of Industrial Engineering at Vinnitsia National Technical University.
The scientific focus is the dynamics of drive systems with devices and control systems with variable operating modes and diagnostics of metal structures of hoisting-and-transport and technological machines.

http://orcid.org/0000-0002-5916-2413

M.Sc. Oleh V. Khmara
e-mail: khmara211@ukr.net

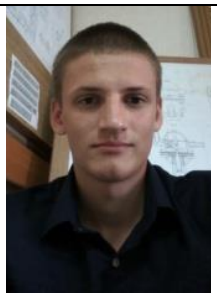

Postgraduate student at Vinnytsia National Technical University.
Scientific direction – improving the efficiency of operation of mobile complexes of machines through the use of hydraulic drives in their working units with improved technical parameters. He has 5 scientific publications.

http://orcid.org/0000-0002-3849-6879

PhD. Oleh V. Piontkevych
e-mail: piontkevych@vntu.edu.ua

PhD. Techn. Sc., Oleh V. Piontkevych, Vinnytsia National Technical University.
The scientific focus is the dynamics of drive systems with devices and control systems with variable operating modes and diagnostics of metal structures of hoisting-and-transport and technological machines. He has more than 50 scientific publications of which 7 are of scientific nature in publications such as Scopus and WoS.

http://orcid.org/0000-0002-3460-8060

Ph.D. Oksana O. Adler
e-mail: oksana_adler1983@ukr.net

Associate Professor of department of Enterprise Economics and Production Management, Vinnytsia National Technical University.
Research interests: advanced methods of diagnosis and increasing the competitiveness of modern enterprises in a market economy.

http://orcid.org/0000-0002-4673-366X

Ph.D. Aigul Tungatarova
e-mail: tungatarova70@gmail.com

Candidate of Pedagogical Sciences - Department of Information Systems, Taraz Regional University named after M.Kh.Dulaty, Kazakhstan.
Research area: information technology, information security.

http://orcid.org/0000-0001-7600-9608

Ph.D. Ainur Kozbakova
e-mail: ainur79@mail.ru

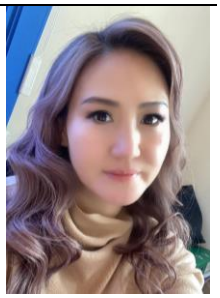

Ph.D, Associate Professor Almaty Technological University, the Institute of Institute of Information and Computational Technologies of the Ministry of Education and Science CS of the Republic of Kazakhstan. Research interests: mathematical modeling of discrete systems, evacuation tasks, operations research, technology design of complex systems.

http://orcid.org/0000-0002-5213-4882

http://doi.org/10.35784/iapgos.2966 *received: 12.05.2022 | revised: 10.06.2022 | accepted: 15.06.2022 | available online: 30.06.2022*

ON PRECISION ACOUSTIC WAVE CALCULATION IN A FREQUENCY DOMAIN

Tomasz Rymarczyk[1,2], Jan Sikora[1,2]
[1]Research & Development Centre Netrix S.A., Lublin, Poland, [2]University of Economics and Innovation in Lublin, Faculty of Transport and Informatics, Lublin, Poland

Abstract. *The accuracy of the calculation of acoustic problems formulated in the frequency domain is presented in this work. The issues of the acoustic point sources modelling were discussed and the influence of frequency as well as the impact of the geometry of the analysed area on the accuracy of calculations were indicated. Speaking about the influence of geometry, we mean not only discretization but also the configuration of the considered area, such as for example point sources localization close to the outer edge.*

Keywords: acoustics wave propagation, computational modeling, source simulation, BEM simulation

O PRECYZYJNYM OBLICZANIU FAL AKUSTYCZNYCH W DZIEDZINIE CZĘSTOTLIWOŚCI

Streszczenie. *Dokładności obliczeń zagadnień akustycznych sformułowanych w dziedzinie częstotliwości została przedstawiona w tej pracy. Omówiono problemy modelowania źródeł punktowych oraz wskazano na wpływ częstotliwości a także wpływ geometrii analizowanego obszaru na dokładność obliczeń. Mówiąc o wpływie geometrii mamy na myśli nie tylko dyskretyzacje, ale także konfigurację rozpatrywanego obszaru jak na przykład punktowe źródła energii położone blisko zewnętrznego brzegu.*

Słowa kluczowe: propagacja fal akustycznych, modelowanie obliczeniowe, symulacja źródeł, symulacja metodą elementów brzegowych (MEB)

Introduction

According to [7, 8] four different computational methods engage in acoustic analysis and solutions of the inverse problems: ray tracing, FEM, BEM, and DG-FEM (Discontinuous Galerkin – Finite Element Method). The key problem of each inverse problem is the forward problem, and this paper is devoted accuracy and effectiveness of the calculation of the forward problem for acoustic.

We now briefly introduce several types of problems which frequently occur in practical applications. Problems of wave propagation phenomena are usually classified as interior or exterior, depending on whether one is interested in the sound field in bounded or unbounded regions in space. In some cases, also could be defined the third type of the acoustic problem when the domain of interest is not a simply connected one (see for example Fig. 1c).

Three different types of problem could be formulated for acoustics [2]. Those are:
1) interior problem,
2) exterior problem,
3) hybrid interior-exterior problem.

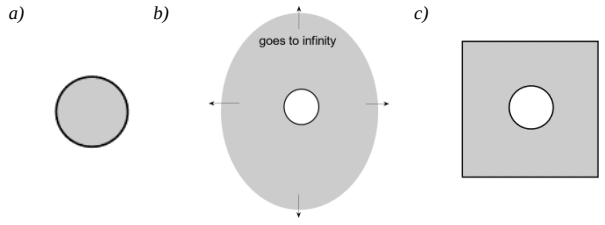

Fig. 1. Sketch of the area for: a) interior problem, b) exterior problem, c) hybrid interior-exterior problem. The greyish area represents the calculation domain

In this paper we would like to focus readers attention on the BEM for interior problem (Fig. 1a) formulated for the frequency domain.

Dedicated iterative methods make it possible to formulate the inverse problems and solve the tomography tasks for acoustic. The advantages of acoustic or ultrasound approach for imaging is obvious and do not demand further explanations.

Ultrasound tomography models are different from the mathematical models formulated for X-ray tomography models [3]. Unlike X-rays, ultrasound waves do not travel in a simple straight line, it undergoes multiple deflections too. The ultrasound wave propagation speed is low, such that delay in propagation times can also be measured. Various methods have been suggested to deal with these refractive problems.

1. Governing equations for the forward internal acoustic problem

The acoustic field is assumed to be present in the domain of a homogeneous isotropic fluid and it is modelled by the linear wave equation [3]:

$$\nabla^2\psi(\mathbf{p},t) = \frac{1}{c^2}\frac{\partial^2}{\partial t^2}\psi(\mathbf{p},t) \tag{1}$$

where $\psi(\mathbf{p},t)$ [m^2/s] is the scalar time-dependent velocity potential related to the time-dependent particle velocity $\mathbf{v}(\mathbf{p},t) = \nabla\psi(\mathbf{p},t)$ [m/s] and c [m/s] is the propagation velocity ($\mathbf{p}$ and t are the spatial and time variables in meters and seconds respectively). The time-dependent sound pressure is equal $p(\mathbf{p},t) = -\rho\frac{\partial}{\partial t}\psi(\mathbf{p},t)$ where ρ [kg/m^3] is the density of the acoustic medium.

Transferring from the time domain to the frequency domain the velocity potential ψ can be expressed as follows:

$$\Psi(\mathbf{p},t) = \mathrm{Re}\{\varphi(\mathbf{p})\mathrm{e}^{-\mathrm{i}\omega t}\}, \tag{2}$$

where: $\omega = 2\pi f$ [1/s] and $\varphi(\mathbf{p})$ is the velocity potential amplitude. The substitution of the above expression into the wave equation reduces it to the Helmholtz equation of the form [3]:

$$\nabla^2\varphi(\mathbf{p}) + k^2\varphi(\mathbf{p}) = Q, \tag{3}$$

where $k^2 = \frac{\omega^2}{c^2}$ and is the wave number and the wavelength is equal to [m]. The right-hand side Q stands for the acoustic source. The complex-valued function $\varphi(\mathbf{p})$ possess the magnitude and phase shift.

Acoustic source term from Eq. (3) very often is treated as the Monopole Source which models a point source that radiates sound isotropically. An example of the acoustic source in 2D space might be a cross section of a cylinder with a small radius which alternately expands and contracts [4].

Such approach could be modelled by the Dirichlet boundary conditions of the internal boundary circle which represent the cross section of the source. But if we make use of the monopole source term Q in Eq. (3) may be written as Q=Q_0 $\delta(\boldsymbol{p}_s)$. The $\delta(\boldsymbol{p}_s)$ means the Delta Dirac function located in the point $\boldsymbol{p}_s$. Such a mathematical model is particularly convenient in integral formulation of the Partial Differential Equations (PDE). It will be shown in the next section of this paper.

2. Mathematical model of the acoustic source based on hybrid interior-exterior problem

Let us consider hybrid interior-exterior acoustic problem as it is presented in the Fig. 1c. Using this idea, we would like to build the mathematical model for the acoustic source placed in the centre of the square region. The internal boundary should be as small as possible in order to simulate the point source inside the region as it is shown in Fig. 2. Mathematical model based on the Helmholtz equation in the frequency domain [5] in the integral form is described by the following equation.

$$c(\boldsymbol{r})\varphi(\boldsymbol{r}) + \int_{\Gamma} \frac{\partial G(|\boldsymbol{r}-\boldsymbol{r}'|)}{\partial n}\varphi(\boldsymbol{r}')d\boldsymbol{\Gamma} = \\ = \int_{\Gamma} G(|\boldsymbol{r}-\boldsymbol{r}'|)\frac{\partial\varphi(\boldsymbol{r}')}{\partial n}d\boldsymbol{\Gamma} \tag{4}$$

Internal boundary (Fig. 2b) of the circular shape with Dirichlet boundary conditions simulates the point source located as it is shown in Fig. 2a.

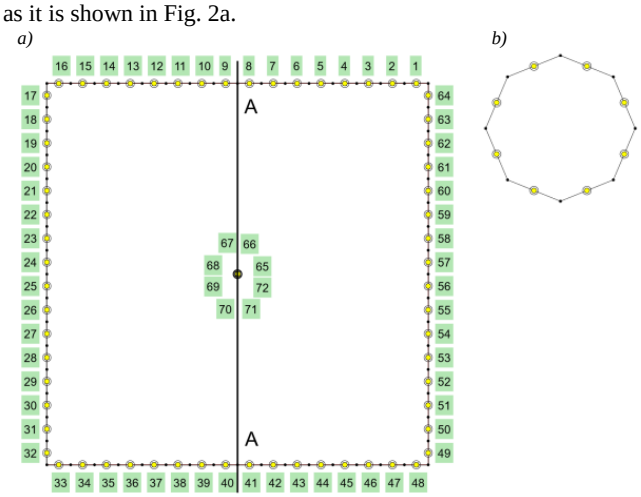

Fig. 2. Discretization of the region under consideration (a) and enlarged internal boundary as a model of the point source (b)

This problem could be treated as an acoustic benchmark for numerical simulation because of its geometrical simplicity. The point sources for the acoustic tomographic problems simulate the multi excitation set so they are especially important. We have to know BEM software behaviour particularly in case of high frequencies like for example ultrasound frequency range.

For one reason the hybrid problem is significant. The unite normal vector have to be directed outside the analysed region. So, for the external boundary the normal derivative would be directed to infinity but for internal boundary to the empty subregion (see for example Fig. 2b).

The following figures shows the solution of the problem with centred point source modelled by hybrid interior – exterior problem. The left-hand side column a) belongs to analytical solution based on Eq. (5), but the right-hand side figures represent the numerical solution. In Eq. (5) the Q_0 is the point source strength but in the BEM model it is replaced by Dirichlet boundary conditions.

Due to singularity of the solution the hybrid model of the problem makes only possible qualitative comparison between analytical and numerical calculations. The singularity point in numerical model is excluded and replaced by Dirichlet boundary conditions imposed on the internal boundary circumfluent the real point source position (see Fig. 3 and Fig. 4).

In the Fig. 3 and Fig. 4 acoustic field is presented for two frequencies: 20 Hz the lowest audible frequency (top row) and 680 Hz frequency (bottom row) [1]. At the external boundary homogeneous Dirichlet boundary conditions were imposed (Sound Soft BC).

It is clear that such approach could be applied to model acoustic point sources particularly useful in acoustic tomography.

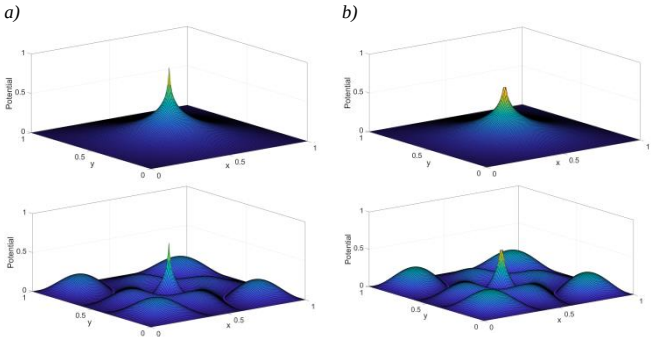

Fig. 3. Relief plot of absolute value of complex potential distribution for the analytical solution - column a) and for BEM numerical solution – column b)

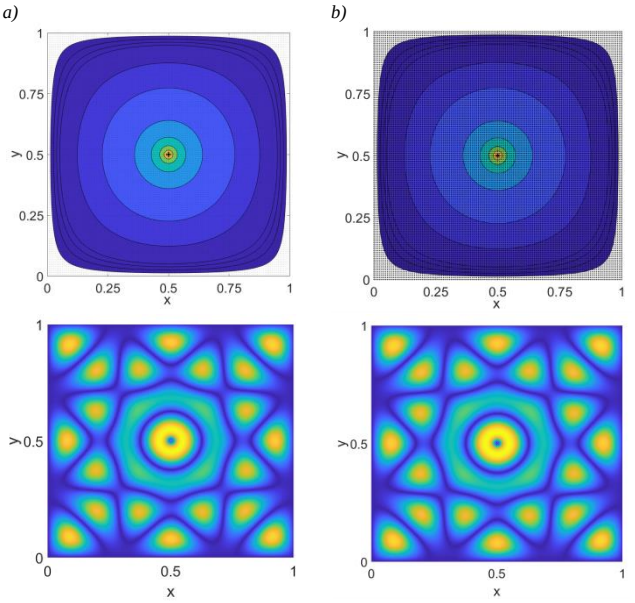

Fig. 4. Qualitative comparison between analytical (left, column a) and BEM (right, column b) solutions for the Helmholtz equation for a source located in the centre of the square region

3. Acoustic source modelled by Delta Dirac function

Similar task but this time with the point source modelled by the Delta Dirac function were considered. In order to make the Quantitative comparison following [1] let us consider the analytical solution of the acoustic problem formulated in previous paragraph:

$$\varphi(\boldsymbol{x},\boldsymbol{y}) = \frac{4Q_0}{ab}\sum_{n=1}^{\infty}\sum_{m=1}^{\infty}\left[\frac{sin\left(\frac{n\pi x}{a}\right)sin\left(\frac{m\pi y}{b}\right)sin\left(\frac{n\pi\eta_0}{a}\right)sin\left(\frac{m\pi\xi_0}{b}\right)}{\pi^2\left(\frac{n^2}{a^2}+\frac{m^2}{b^2}\right)-k^2}\right] \tag{5}$$

where Q_0 is the point source strength, $a = b$ dimensions of the square region.

Equation (5) describes the outgoing wave of wavenumber k, produced by a point source of strength Q_0, located at point (η_0, ξ_0), observed at (x, y) subject to homogeneous Dirichlet boundary conditions ($\varphi = 0$) on the external boundary of the unite square.

Having the analytical solution such a problem could be treated as a benchmark problem. The issue of precision of the Boundary Element solution with respect to the excitation frequency as well as the spatial discretization would be considered.

The Helmholtz equation should be modified by an integral over the whole region Ω (see the last term of Eq. (6)).

$$c(\boldsymbol{r})\varphi(\boldsymbol{r}) + \int_{\Gamma} \frac{\partial G(|\boldsymbol{r}-\boldsymbol{r}'|)}{\partial n}\varphi(\boldsymbol{r}')d\boldsymbol{\Gamma} = \\ = \int_{\Gamma} G(|\boldsymbol{r}-\boldsymbol{r}'|)\frac{\partial\varphi(\boldsymbol{r}')}{\partial n}d\boldsymbol{\Gamma} - \int_{\Omega} G(|\boldsymbol{r}_s-\boldsymbol{r}'|)\,Q_0\delta_s d\Omega \tag{6}$$

where Q_0 is the magnitude of the source and δ_s is a Dirac delta function which integral is equal to one at the point $\boldsymbol{r}_s = \boldsymbol{p}_s$

and zero elsewhere. Taking above into account and assuming that only one point source exists, after some integration Eq. (6) could take the following form:

$$c(\boldsymbol{r})\varphi(\boldsymbol{r}) + \int_{\Gamma} \frac{\partial G(|\boldsymbol{r}-\boldsymbol{r}'|)}{\partial n}\varphi(\boldsymbol{r}')d\boldsymbol{\Gamma} = \\ = \int_{\Gamma} G(|\boldsymbol{r}-\boldsymbol{r}'|)\frac{\partial \varphi(\boldsymbol{r}')}{\partial n}d\boldsymbol{\Gamma} - G(|\boldsymbol{r}_s-\boldsymbol{r}'|)Q_s \qquad (7)$$

where for internal points of the region Ω coefficient $c(\boldsymbol{r})$=1.

The results of calculations are presented below. The left-hand column of the Fig. 5a contain the analytical solution and the right-hand side column the BEM solution. Because the solution was achieved in the frequency domain in the figures only the modulus of the complex amplitude is presented.

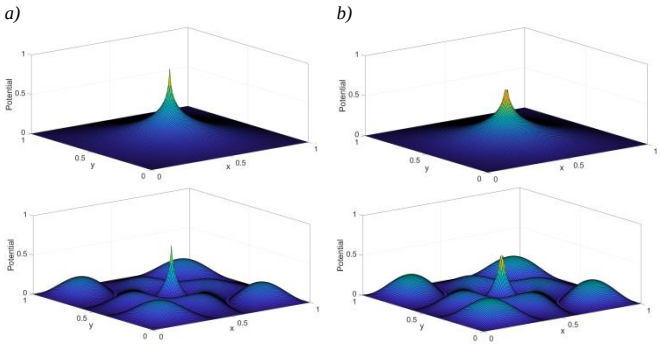

Fig. 5. Relief plot of absolute value of complex potential distribution for the analytical solution – column a) and for BEM numerical solution – column b)

The image of the acoustic field is presented in the Fig. 6 for two frequencies 20 Hz and 680 Hz. Using those figures only qualitative comparison to the benchmark is possible.

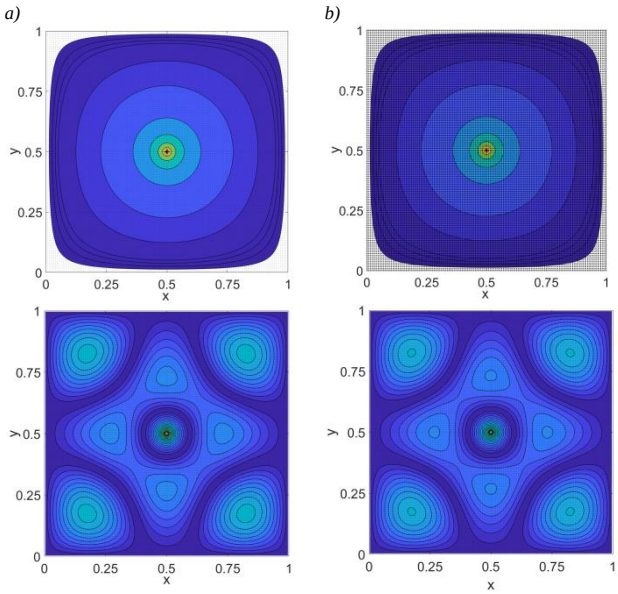

Fig. 6. Qualitative comparison between analytical (left, column a) and BEM (right, column b) solutions for the Helmholtz equation for the point source located in the centre of the square region

If the line A-A in Fig. 2a would be considered than the quantitative comparison between the analytic solution (treated as a benchmark) and the numerical solution became possible.

The boundary element discretization was modest because only sixty-four boundary elements were used. In case of the frequency 20 Hz agreement was excellent but when the frequency become higher the discrepancy become bigger. Therefore, it is necessary to increase the number of boundary elements. We can observe the reduction of a relative error in case of frequency 680 Hz comparing the Fig. 7b and Fig. 9b.

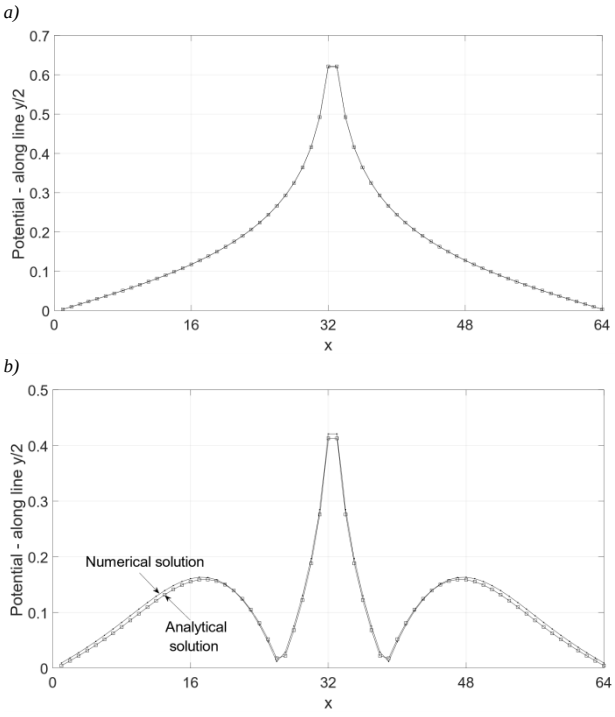

Fig. 7. Potential (acoustic pressure) comparison along the A-A line (see Fig. 2a) for 20 Hz (above) and 680 Hz (below)

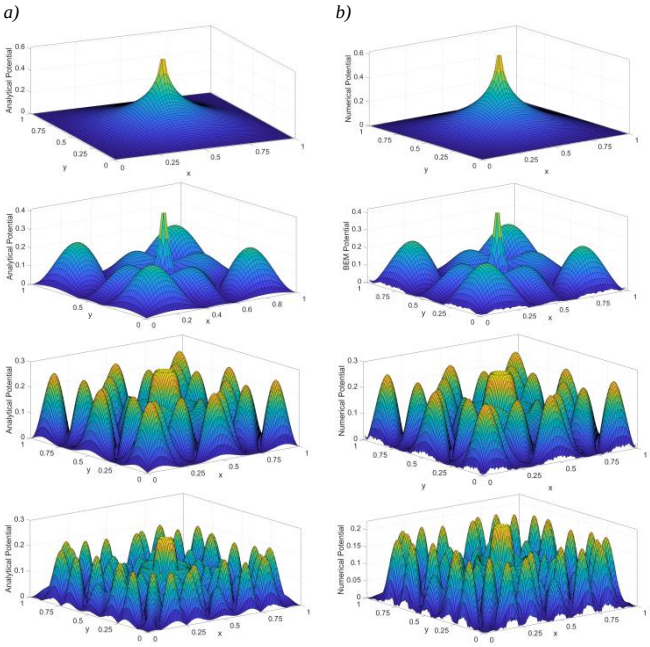

Fig. 8. Qualitative comparison between analytical (left, column a) and BEM (right, column b) solutions of the Helmholtz equation for the point source located in the centre of the square region for the frequencies: 20 Hz, 680 Hz, 1340 Hz and 2000 Hz

Along the A-A line (see Fig. 2a) comparison between analytic and numerical solution is presented below. The highest source frequency the bigger relative error one may observe. The error reduction is possible by increasing the number of boundary elements.

Inspecting those figures one conclusion is clear, that acoustic problem could effectively be solved for a wide range of acoustic parameters of the environment and excitation (frequency for example). The maximal relative error does not exceed 10% and easily could be reduced by applying dense discretization.

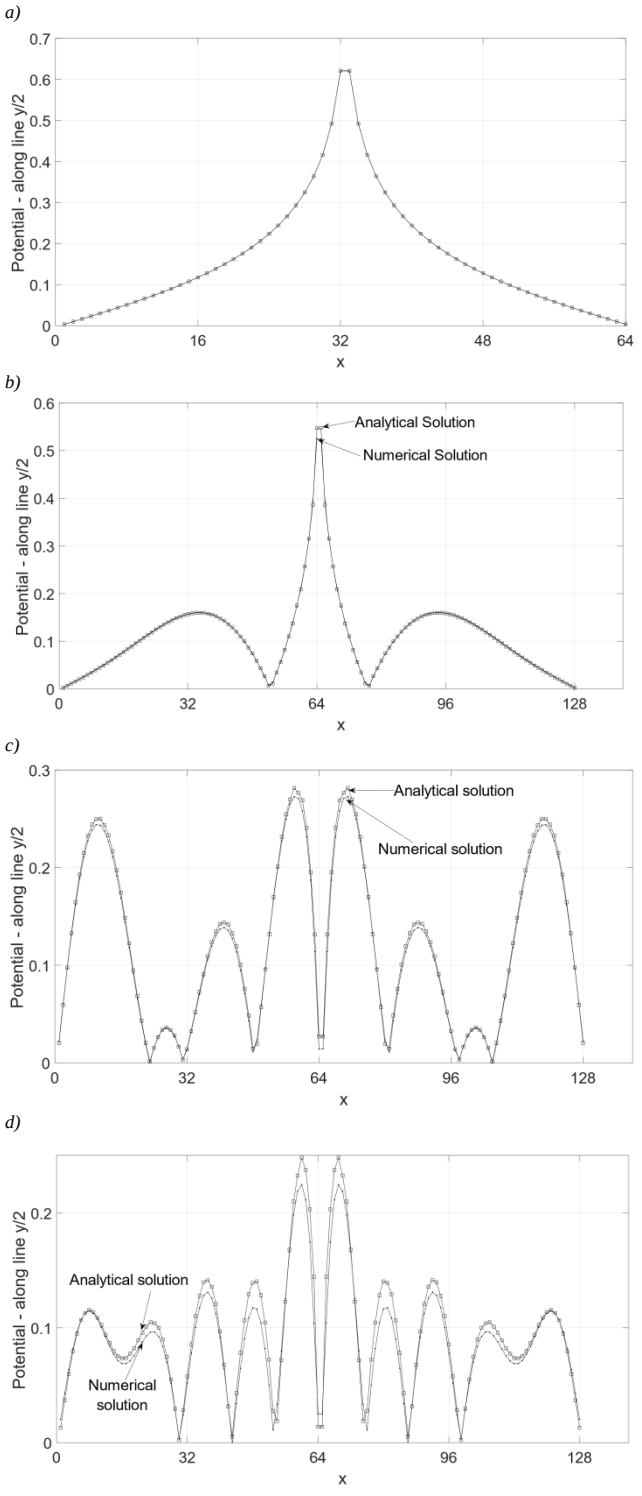

Fig. 9. Potential (acoustic pressure) comparison along the A-A line (see Fig. 2a) for 20 Hz (above) and subsequently 680 Hz, 1340 Hz and finally 2000 Hz

Table 1. Basic data for acoustic benchmark calculation

f [Hz]	20	680	1340	2000
δ%	0	-2.02	3.19	9.48
k [1/m]	0.37	12.42	24.48	36.53
λ [m]	17.20	0.51	0.26	0.17
element length [m]	0.1250	0.0625	0.0625	0.0625
arg. of Henkel function	0.058	1.977	3.895	5.814
no of BE per λ	138	8	4	3

From tomography point of view the most important is a grid providing a minimum number of points per wavelength to resolve acoustic problem even for the highest frequencies. As our goal is the ultrasound tomography, we have to consider frequency above 20000 Hz. For such frequencies, the wavelength became noticeably short even less than 0.017 m.

From tomography point of view satisfactory target would be such a number of boundary elements which allows to achieve a relative error of less than 10%. Furthermore, this selection adheres to the eight point per wavelength rule suggested by [1] for the approximation of acoustic waves. Only frequencies 20 Hz and 680 Hz fulfil this condition. But it does not mean that the remains cases are nor useful for the tomography cases. The relative error remains low even thou the number of elements is about three per wavelength.

However, to calculate acoustic problem of the ultrasound frequency and preserve this condition the region of interest should be much smaller. It means that the acoustic wavelength must be much greater than the length scale of the geometry. So, instead the unite square region the size was reduced by ten up to 0.1 m.

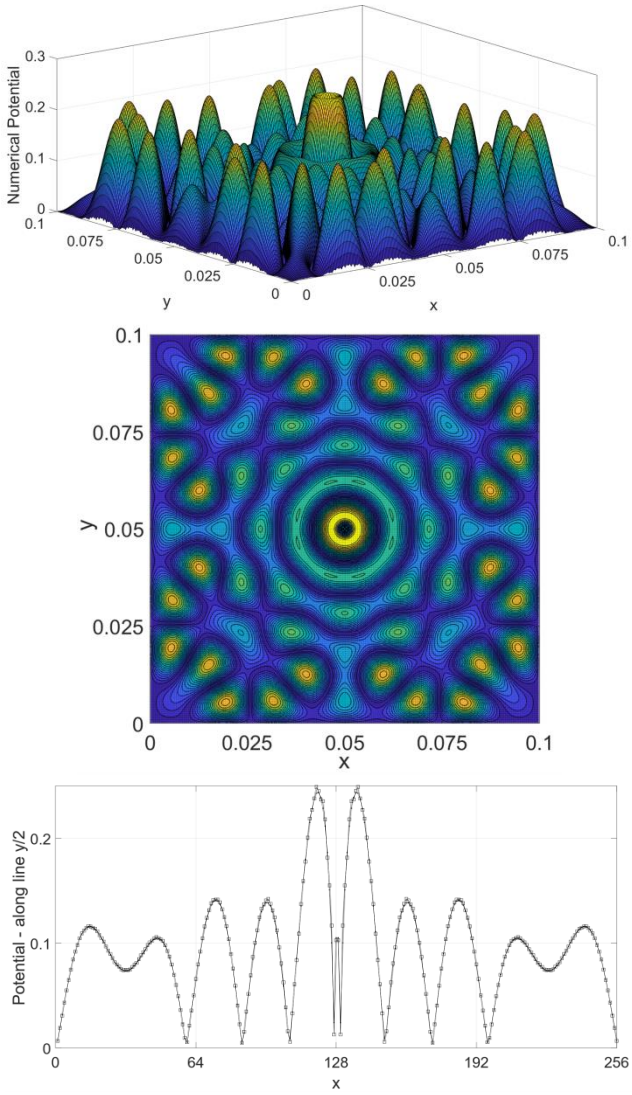

Fig. 10. Ultrasound modelling of the Helmholtz problem with soft boundary conditions

The results are quite satisfactory and the maximal error (with the exception of singularity point in the centre of region) is less than 2.45%.

4. Near-Boundary Source

For tomography problems it is necessary to fix the sensor on the boundary or inside the region but remarkably close to the boundary. It is interesting to investigate numerical solution behaviour in such cases. Let us consider a situation with one point source located near boundary and on the external boundary of unite square the homogeneous Dirichlet boundary conditions were imposed (sound soft boundary conditions).

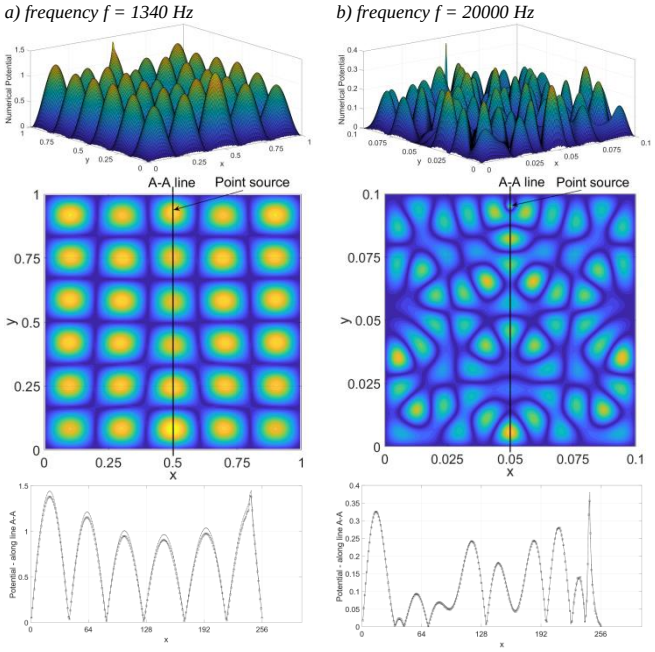

Fig. 11. Ultrasound modelling of the Helmholtz problem with a near-boundary point source and sound soft boundary conditions: column a) for excitation with frequency 1340 Hz, column b) with excitation of 20000 Hz

It is easily to notice that the precision of calculations depends not only on the frequency but also depends on the formulation of the acoustic problem itself. Regarding frequency, the higher frequency the more rigoristic demands of the problem. Particularly it concerns the ultrasound frequencies. Precision might be kept on low level but the ratio of wavelength to the length of boundary element should be not less than eight.

That demand fine discretization what means high time consumption. But tomographic problems which are solved by iteration process have to be as fast in each iteration step as possible. In some particular cases (see table 1) the number of boundary elements per wavelength could be reduce up to 3 or 4 and the maximal relative error would not exceed 10%. It might provide satisfactory results for the tomography imagining.

5. Conclusions

Very often in tomography problems, we have to deal with many sensors emitting and receiving signals which are closely located to the external boundary. As an example, a Diffuse Optical Tomography or Radio Tomography could be mentioned [5, 6].

In this paper two different mathematical models of the acoustic point sources were investigated. For the purposes of the forward tomography problem formulated in the integral form the second mathematical model of the acoustic point source is more convenient.

In all modalities of the tomography only external boundary is accessible so the integral form and the Boundary Element Method possess obvious advantages over the Finite Element Method [5, 6]. The second approach to the acoustic point source involves less boundary elements so it is more convenient to the tomography. Even applying constant boundary elements results of the Helmholtz equation in a broad range of frequency is able to provide results with a maximal relative error less than 10%. In the literature [1–3] is stressed that the acoustic wavelength should be much greater than the length scale of the region under consideration. That simply means that the ratio of the wavelength to the length of the boundary element should be at least equal to eight. Then the precision of calculation would be secured. We can see that in the table 1.

However, in tomography sometimes might be difficult to fulfil such rigorous demands. For example, for the ultrasound frequency band the length of the boundary elements should be extremely small if the level of the error should be kept on the low level. From the point of view of the Inverse Problem efficiency calculation such decision would be difficult to justify. Some compromise between the accuracy and the execution time has to be preserved. We can see that in the case of ultrasound frequency when only three boundary elements within the length of the wave provide results of the forward solution with a maximal error less than 10% inside the region. But on the boundary this error could be even less. In the authors opinion such coarse discretization might be sufficient.

References

[1] Harwood A. R. G.: Numerical Evaluation of Acoustic Green's Functions. PhD School of Mechanical, Aerospace & Civil Engineering, University of Manchester, Manchester 2014.
[2] Henríquez V. C., Juhl P. M.: OpenBEM – An open source Boundary Element Method software in Acoustics. Conference Internoise 2010, Lisbon 2010.
[3] Kirkup S.: The Boundary Element Method in Acoustics: A Survey. Applied Sciences 9(8), 2019, 1642 [https://doi.org/10.3390/app9081642].
[4] Opieliński K. J., Pruchnicki P., Gudra T.: Ultrasonic Mammography with Circular Transducer Array. Archives of Acoustics 39(4), 2014, 559–568 [http://doi.org/10.2478/aoa-2014-0060].
[5] Rymarczyk T.: Tomographic Imaging in Environmental, Industrial and Medical Applications. Innovatio Press Publishing Hause, Lublin 2019.
[6] Sikora J.: Boundary Element Method for Impedance and Optical Tomography. Warsaw University of Technology Publishing Hause, Warsaw 2007.
[7] https://www.comsol.com/acoustics-module
[8] https://reference.wolfram.com/language/PDEModels/tutorial/Acoustics/AcousticsFrequencyDomain.html

D.Sc., Ph.D. Eng. Tomasz Rymarczyk
e-mail: tomasz@rymarczyk.com

He is the director in Research and Development Centre in Netrix S.A. and the director of the Institute of Computer Science and Innovative Technologies in the University of Economics and Innovation, Lublin, Poland. He worked in many companies and institutes developing innovative projects and managing teams of employees. His research area focuses on the application of non-invasive imaging techniques, electrical tomography, image reconstruction, numerical modelling, image processing and analysis, process tomography, software engineering, knowledge engineering, artificial intelligence, and computer measurement systems.

http://orcid.org/0000-0002-3524-9151

Prof., D.Sc., Ph.D. Eng. Jan Sikora
e-mail: sik59@wp.pl

Prof. Jan Sikora (PhD. DSc. Eng.) graduated from Warsaw University of Technology Faculty of Electrical Engineering. During 44 years of professional work, he has obtained all grades, including the position of full professor at his alma mater. Since 1998 he has also worked for the Institute of Electrical Engineering in Warsaw. In 2008, he has joined Electrical Engineering and Computer Science Faculty in Lublin University of Technology. During 2001–2004 he has worked as a Senior Research Fellow at University College London in the prof. S. Arridge's Group of Optical Tomography. His research interests are focused on numerical analysis application in the field theory. He is an author of eight books and more than 180 papers published in the international journals and conferences.

http://orcid.org/0000-0002-9492-5818

http://doi.org/10.35784/iapgos.2951 received: 08.05.2022 | revised: 17.06.2022 | accepted: 17.06.2022 | available online: 30.06.2022

METHODS FOR DETECTING AND SELECTING AREAS ON TEXTURE BIOMEDICAL IMAGES OF BREAST CANCER

Ainur Orazayeva[1], Jamalbek Tussupov[1], Waldemar Wójcik[2], Sergii Pavlov[3], Gulzira Abdikerimova[1], Liudmyla Savytska[3]

[1]L.N. Gumilyov Eurasian National University, Nur-Sultan, Kazakhstan, [2]Lublin University of Technology, Lublin, Poland, [3]Vinnytsia National Technical University, Vinnytsia, Ukraine

Abstract. *This paper is devoted to topical issues - the development of methods for analyzing texture images of breast cancer. The main problem that is resolved in the article is that the requirements for the results of pre-processing are increasing. As a result of the task, images of magnetic resonance imaging of the breast are considered for image processing using texture image analysis methods. The main goal of the research is the development and implementation of algorithms that allow detecting and isolating a tumor in the breast in women in an image. To solve the problem, textural features, clustering, orthogonal transformations are used. The methods of analysis of texture images of breast cancer, carried out in the article, namely: Hadamard transform, oblique transform, discrete cosine transform, Daubechies transform, Legendre transform, the results of their software implementation on the example of biomedical images of oncological pathologies on the example of breast cancer, it is shown that The most informative for image segmentation is the method based on the Hadamard transform and the method based on the Haar transform. The article presents recommendations for using the results in practice, namely, it is shown that clinically important indicators that make a significant contribution to assessing the degree of pathology and the likelihood of developing diseases, there are other information parameters: diameter, curvature, etc. Therefore, increased requirements for the reliability, accuracy, speed of processing biomedical images.*

Keywords: biomedical image processing, textural features, clustering, orthogonal transformations

METODY WYKRYWANIA I WYRÓŻNIANIA OBSZARÓW W TEKSTUROWANYCH OBRAZACH BIOMEDYCZNYCH RAKA PIERSI

Streszczenie*. Niniejszy artykuł jest poświęcony aktualnemu tematowi - opracowaniu metod analizy obrazów tekstury raka piersi. Główny problem, który został rozwiązany w artykule, polega na tym, że wymagania wobec wyników przetwarzania wstępnego są coraz większe. W wyniku realizacji zadania rozpatrzono obrazy rezonansu magnetycznego piersi przeznaczone do przetwarzania metodami teksturowej analizy obrazu. Głównym celem badań jest opracowanie i wdrożenie algorytmów wykrywania i odróżniania na obrazie guza w piersi u kobiet. Do rozwiązania tego problemu wykorzystuje się cechy tekstury, grupowanie i transformacje ortogonalne. W artykule przedstawiono metody analizy obrazów teksturowych raka piersi, tj. transformatę Adamarda, transformatę skośną, transformatę dyskretno-cosinusową, transformatę Dobeshiego, transformatę Lejandre'a, oraz wyniki ich implementacji programowej na przykładzie obrazów biomedycznych patologii onkologicznej w przypadku raka piersi. Metoda oparta na transformacie Adamarda oraz metoda oparta na transformacie Haara są najbardziej przydatne do segmentacji obrazów. W artykule przedstawiono zalecenia dotyczące wykorzystania wyników w praktyce, a mianowicie wykazano, że inne parametry informacyjne, takie jak średnica, krzywizna itp. są ważnymi klinicznie wskaźnikami, które w istotny sposób przyczyniają się do oceny stopnia patologii i prawdopodobieństwa rozwoju choroby. W związku z tym wzrastają wymagania dotyczące niezawodności, dokładności i szybkości przetwarzania obrazów biomedycznych w urządzeniach diagnostycznych*.

Słowa kluczowe: przetwarzanie obrazów biomedycznych, cechy tekstury, klasteryzacja, transformacje ortogonalne

Introduction

Despite the ubiquitous presence of textures in images, there is no single and formal approach to the description of texture and its strict definition at the moment. Texture analysis methods are usually developed for each individual case.

Recently, there have been many works devoted to the analysis of dynamic textures and color images. Analyzing the textures of color images, additional designations are introduced for their characteristics, based on measuring the intensity levels of each color and distributing them over the image field. When analyzing dynamic structures that change in time, space-time is introduced, which is the third dimension, which is connected to two spatial coordinates [7, 18, 19].

Spectral analysis is a powerful tool for analyzing signals and images, because it has long been noted that the spectrum is very sensitive to various changes in the structure of signals and images.

To perform spectral analysis, it is necessary to first decompose the signal or image into frequencies. For this, different sets of basis functions are used. The corresponding algorithms are called transforms: cosine, Hadamard, Haar, oblique, etc. Note that the Haar and Daubechies, Mueller-matrix polarimetry (MMP) [13, 14] for the transforms are the simplest wavelet transforms. These methods, according to the theory of signal processing, can be applied to stationary random processes, but often we do not have this. However, it is possible to select for analysis areas that are considered conditionally stationary (in other words, quasi-stationary) and whose size is sufficient to obtain statistically correct results [14, 15].

1. Method

The program is implemented in the Matlab environment and allows performing spectral transformations of six types: 1) cosine, 2) Hadamard of order 2^n, 3) Hadamard of order $n = p + 1$, $p = 3 (\mathrm{mod} 4)$ is a prime number, i.e. based on the Legendre symbol, 4) Haar, 5) oblique, 6) Daubechies-4, 7) MMP.

To normalize the Haar function, the following formula is used:

$$\alpha_{mk}(\theta) = \begin{cases} \sqrt{2^m}, & \theta \in \left[\frac{k}{2^m}, \frac{k+1/2}{2^m}\right) \\ -\sqrt{2^m}, & \theta \in \left[\frac{k+1/2}{2^m}, \frac{k+1}{2^m}\right). \\ 0, & \theta \in \left[\frac{k}{2^m}, \frac{k+1}{2^m}\right) \end{cases} \quad (1)$$

The Daubechies-4 transform is given [6, 7] by the following matrix

$$M = \sqrt{2}\begin{bmatrix} h_0 & h_1 & h_2 & h_3 & & & & \\ & & h_0 & h_1 & h_2 & h_3 & & \\ & & & & h_0 & h_1 & h_2 & h_3 \\ h_2 & h_3 & & & & & h_0 & h_1 \\ h_3 & -h_2 & h_1 & -h_0 & & & & \\ & & h_3 & -h_2 & h_1 & -h_0 & & \\ & & & & h_3 & -h_2 & h_1 & -h_0 \\ h_1 & -h_0 & & & & & h_3 & -h_2 \end{bmatrix} \quad (2)$$

Matrix elements are calculated using the formulas below:

$$h_0 = (1+\sqrt{3})/8, \quad h_1 = (3+\sqrt{3})/8, \quad h_2 = (3-\sqrt{3})/8, \quad h_3 = (1-\sqrt{3})/8. \quad (3)$$

In most cases, iterative algorithms are used to select areas in grayscale images. For example, the k-mean algorithm [16, 17] is mainly used in the space of pixel brightness and divides images into regions according to a given number. The main feature of this algorithm is its simplicity and speed of execution [15–17].

This method is implemented in the MatLab environment and is used for image analysis. The image is divided by software into separate parts. When studying textures, you can use various non-standard approaches that use orthogonal transformation. For example, the original image is divided into square windows that do not intersect. Experiments have shown that it is better to take a large window size for its intended purpose: 32 × 32, 64 × 64, etc. We carry out an integral transformation of each window. In the two-dimensional case, the frequency spectra have the form of a matrix. We place the elements of the matrix in the form of vectors. For example, we can arrange the rows of a matrix sequentially at the end of each other. As a result, we carry out the procedure of clustering these vectors [1, 2, 4].

2. Experimental results

During the experiment, 30 X-ray images of the mammary glands were taken as initial images. Each of the images has dimensions of 1024 × 1024.

The images were first classified by an expert physician into three classes:

- Images of the mammary gland without pathology were taken as sample No 1 (Fig. 1a).
- Images of the breast on the right side with different stages of pathologies were considered as sample No 2 (Fig. 1b).
- Images of the breast on the left side with different stages of pathologies were considered as sample No 3 (Fig. 1c).

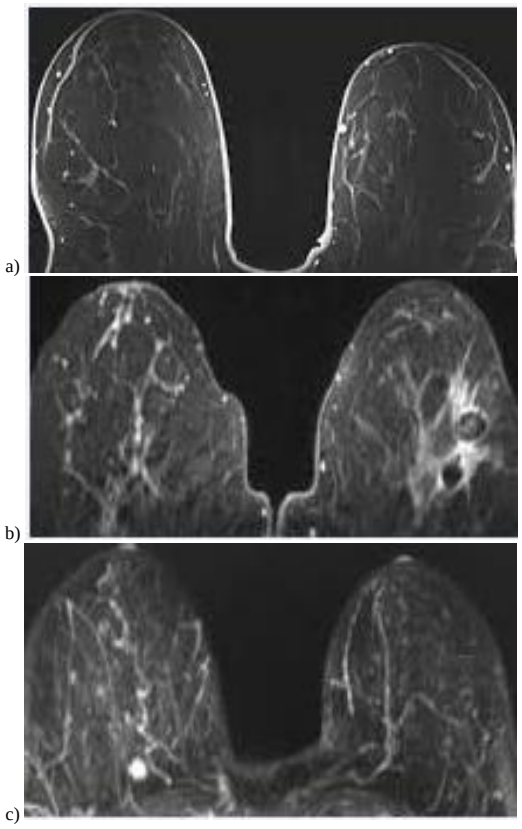

Fig. 1. Sample No 1 of the image of the mammary gland without pathology (a); sample No 2 of the image of the breast on the right side with different stages of pathologies (b); sample No 3 the image of the breast on the left side with different stages of pathologies (c)

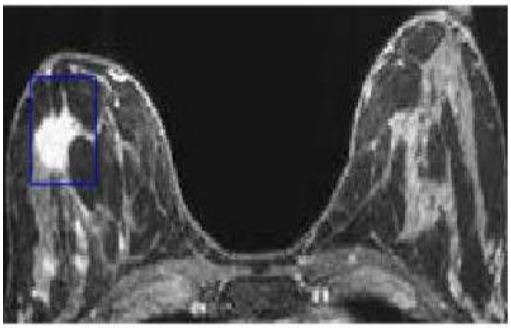

Fig. 2. Selection of a fragment for calculating the orthogonal transformation

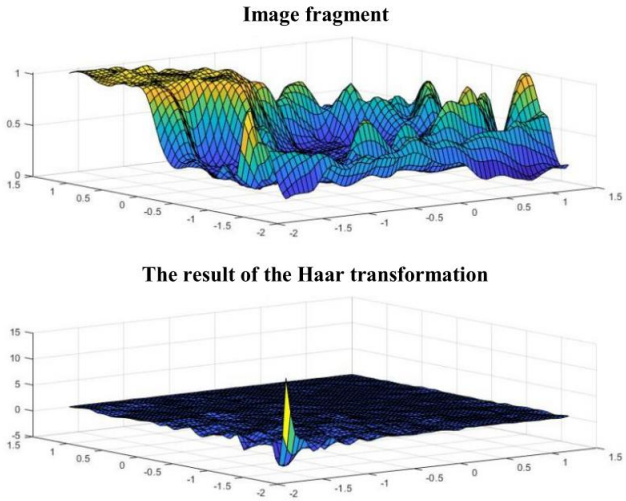

Fig. 3. Graph of the original brightness function in the window and the result of the Haar transformation

The entire code of the main program can be manually inserted into the Matlab workspace, and the results will immediately appear – graphics and 7 text files. Graphs of the results of transformations will be presented each in a separate window, and all at the same time in one window. Matlab allows graphs to be rotated and viewed from different angles. Text files store the original data and the results of the six transformations listed above. All text files are automatically saved in the work directory, inside the Matlab system [3, 10, 12].

It can be concluded that orthogonal transformations are effective for mammographic images; all images were clustered. As an example, after applying an orthogonal transformation to figure 4, as shown in the result of figure 5, 4% of women were found to have a tumor on the left side of the breast [5 9, 11].

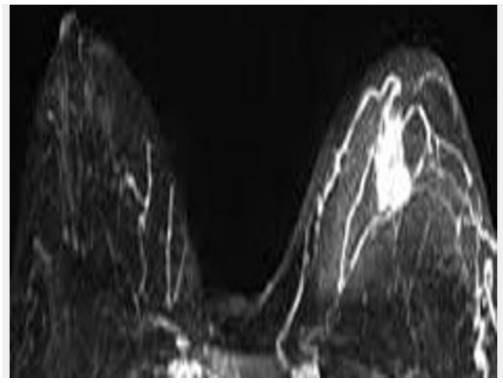

Fig. 4. Original image

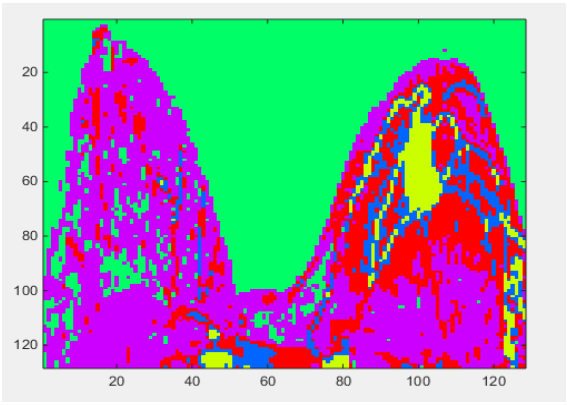

a)

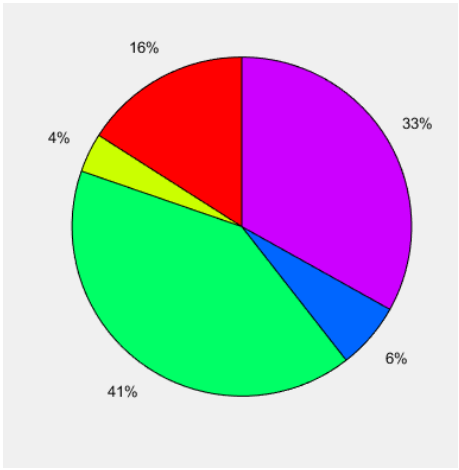

b)

Fig. 5. The result of clustering by the Daubechies method, the window size is 8×8 (a); percentage result of Daubechies clustering result (b)

The percentages of the presence of breast tumors according to the considered figures are presented in the table below (table 1).

Table 1. Percentage of biomedical image processing by 6 methods of orthogonal transformations

Methods	Images													
	1	2	3	4	5	6	7	8	9	10	11	12	13	14
haara	4	2	2	3	8	3	3	6	2	3	5	3	5	4
dobeshi	5	2	2	4	8	3	3	4	2	2	5	3	5	4
discrete	4	2	2	4	8	3	3	5	1	3	5	3	5	4
naklon	4	2	2	4	8	3	3	6	3	2	5	3	5	4
legandr	4	2	2	4	8	3	3	5	2	3	5	3	5	4
hadamard	4	2	2	4	8	3	3	5	1	3	5	3	5	4

Methods	Images													
	15	16	17	18	19	20	21	22	23	24	25	26	27	28
haara	6	10	4	5	3	6	5	5	8	7	3	9	4	9
dobeshi	2	11	3	4	2	1	2	4	8	7	3	6	4	8
discrete	4	11	3	5	2	3	5	4	8	7	3	6	4	9
naklon	4	11	4	5	3	4	5	5	8	7	3	6	4	9
legandr	2	11	4	5	2	4	5	5	8	7	3	6	4	8
hadamard	2	11	3	5	4	4	5	3	8	7	3	6	4	9

From the considered methods, a graphical representation of the Haar method is shown in the following diagram (figure 6).

Of the considered methods, a graphical representation of the Haar method is shown in the following diagram (figure 6).

Checking the results of cluster solutions. To check the correct distribution over clusters, the following formula (4) is used. Percentage of correct class definitions:

$$P = \frac{w(1)' * 100}{w(1)} \tag{4}$$

where

- $w(1)'$ is the number of correct objects in the cluster;
- $w(1)$ number of all considered images.

The selected methods determine the pathology of breast cancer in images by an average of 98% (table 2).

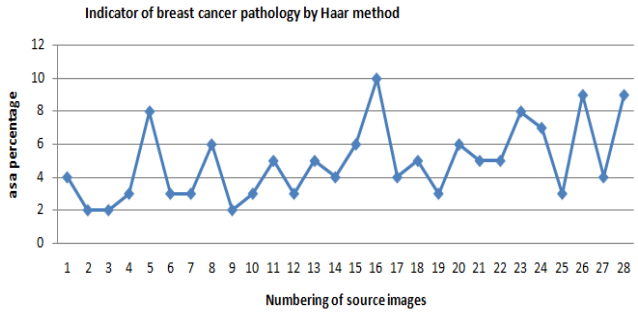

Fig. 6. Indicator of the pathology of breast cancer by the Haar method

Table 2. Clustering result

Methods used	The result of determining the pathology in percent (*P*)	
	Without pathology	With pathology
Haara	97%	97%
Dobeshi	98%	97%
Discrete	98%	97%
Naklon	98%	97%
Legandr	98%	97%
Hadamard	98%	97%
Mueller-matrix polarimetry	98%	97%

3. Conclusions

This investigation is devoted to the study of texture images. The source is mammography images. The main result is the creation of software tools and experiments on image processing. The program is implemented in the Matlab environment, which allows performing spectral transformations of six types: 1) cosine, 2) Hadamard of order 2^n, 3) Hadamard of order n = p + 1, p = 3(mod4) is a prime number, i.e. based on the Legendre symbol, 4) Haar, 5) oblique, 6) Daubechies-4, 7) Mueller-matrix polarimetry.

The algorithms that were considered in this paper allowed us to effectively isolate areas on the analyzed images that are characterized by different stages of breast cancer. More precisely, doctors are interested in early diagnosis of breast pathology in women.

The images used in this article were taken from the Department of Computed Tomography of the Republican Diagnostic Center, 28 images were taken from there, including 26 images with pathology, 2 images without pathology. Based on these data, an experiment was conducted on image processing, and when using spectral transformations of six types, the program shows a 2% error [8, 20].

Looking at figure 6 we can say that when processing images with 6 methods of orthogonal transformations, the percentage of clustering result of 2% and below is 98% of images without pathology, and above 2% – images with pathology. This corresponds to the result of determining the pathology by 98%.

In our further studies, the parameters of indicators can be associated with different stages of breast cancer and other characteristics. The software system can be trained by examples using algorithms based on brain-computer or other approaches commonly used in machine learning. After training, the system will be able to predict the values of the parameters.

References

[1] Abdikerimova G. B. et al.: Algorithms and software for the analysis of disordering the structure of cellular walls. Bulletin of the Novosibirsk Computing Center – Series „Computer science" 40, 2016, 1–14.

[2] Abdikerimova G. B. et al.: Software tools for cell walls segmentation in microphotography. Journal of Theoretical and Applied Information Technology 96, 2018, 4783–4793.

[3] Ablyazov T., Baizakov N.: Theory and Practice of Territories Spatial Development Based on the Smart City Concept. In: Rudskoi A., Akaev A., Devezas T. (eds): Digital Transformation and the World Economy. Studies on Entrepreneurship, Structural Change and Industrial Dynamics. Springer, Cham 2022 [http://doi.org/10.1007/978-3-030-89832-8_9].

[4] Arazayeva A. R. et al.: Efficiency of Biomedical Breast Cancer Image Processing Using Filters. The National Academy of Sciences of the Republic of Kazakhstan ¬– Physics and Information Technology Series 1(341), 2022, 69–76 [http://doi.org/10.32014/2022.2518-1726.118].
[5] Bayzakov S., Forrest J. Y.-L., Baizakov N. A.: Modeling the management of the economies of developing countries. Advances in Systems Science and Applications 19 (2), 2019, 101–119 [http://doi.org/10.25728/assa.2019.19.2.673].
[6] Fu K. S., Mu J. K.: A survey on image segmentation. Pattern Recognition 13(1), 1981, 3–16.
[7] Grady L.: Random walks for image segmentation. IEEE Transactions on Pattern Analysis and Machine Intelligence 28(11), 2006, 1768–1783.
[8] Karpinski M., Ziubina R., Azatov A., Shaikhanova A., Teliushchenko V., Falat P.,: Information Security Software Using Quality and Reliability Criteria. IEEE 5th International Symposium on Smart and Wireless Systems within the Conferences on Intelligent Data Acquisition and Advanced Computing Systems (IDAACS-SWS), 2020, 1–5 [http://doi.org/10.1109/IDAACS-SWS50031.2020.9297069].
[9] Pavlov S. et al.: System of three-dimensional human face images formation for plastic and reconstructive medicine. In: Arras P., Luengo D. (Eds.): Teaching and subjects on bio-medical engineering Approaches and experiences from the BIOART-project. Acco cv, Leuven 2021, 187–203.
[10] Rani R.: Performance analysis of different orthogonal transform for image processing application. International Journal of Applied Research 1(12), 2015, 844–847.
[11] Serik M. , Yerlanova G., Karelkhan N. , Temirbekov N.: The Use of the High-Performance Computing in the Learning Process. International Journal of Emerging Technologies in Learning (iJET) 16(17), 2021, 240–254 [http://doi.org/10.3991/ijet.v16i17.22889].
[12] Sidorova V. S.: Hierarchical Cluster Algorithm for Remote Sensing Data of Earth. Pattern Recognition and Image Analysis 22(2), 2012, 373–379.
[13] Stashkevich A. T. et al.: Differential Mueller-matrix tomography of the polycrystalline structure of biological tissues with different damage durations. Proceedings of SPIE 12040, 2021, 120400G.
[14] Stashkevich A. T. et al.: Multiparameter polarization-phase microscopy of optically anisotropic networks of biological crystals. Proceedings of SPIE 12040, 2021, 120400F.
[15] Stashkevich A. T. et al.: Spectral polarimetry of laser images of biological fluid layers in the differentiation of necrotic conditions. Proceedings of SPIE 12040, 2021, 120400C.
[16] Wang J. Z., Du Y.: Scalable integrated region-based image retrieval using IRM and statistical clustering. Proceedings of the 1st ACM/IEEE-CS joint conference on Digital libraries 2001, 268–277.
[17] Wang J. Z., Li J., Wiederhold G.: SIMPLIcity: Semantics-Sensitive Integrated Matching for Picture Libraries. IEEE Transactions on Pattern Analysis and Machine Intelligence 23(9), 2001, 947–963.
[18] Wójcik W., Pavlov S., Kalimoldayev M.:. Information Technology in Medical Diagnostics II. Taylor & Francis Group, CRC Press, Balkema book, London 2019 [http://doi.org/10.1201/ 9780429057618].
[19] Wójcik W., Smolarz A. (ed.): Information Technology in Medical Diagnostics. CRC Press 2017.
[20] Zhao F., Nagarathnam M.: 5418 Parallel Computer Architecture and Programming Project Report: Implementation and Comparison of Parallel LZ77 and LZ78 Algorithms. 2021.

M.Sc. Ainur Orazayeva
e-mail: oaris.83@gmail.com

Master, doctoral student of Department of Information Systems, L.N. Gumilyov Eurasian National University, Nur-Sultan, Kazakhstan.
Scientific direction: biomedical information technologies for the diagnosis of oncological diseases. Deals with the development of biomedical diagnostic systems and methods.

http://orcid.org/0000-0002-2899-9886

D.Sc. Jamalbek Tussupov
e-mail: tussupov@mail.ru

Doctor of Physical and Mathematical Sciences, professor Department of Information Systems, L.N. Gumilyov Eurasian National University, Nur-Sultan, Kazakhstan.
Scientific direction: mathematics, discrete mathematics, mathematical logic, theory of algorithms, computable algebraic structures, number theory, algebra, graph theory, group theory, computer science (computer science), abstract data types, graphs and algorithms, models of computation, analysis and complexity of algorithms, sequential and parallel algorithms.

http://orcid.org/0000-0002-9179-0428

Prof. Waldemar Wójcik
e-mail: waldemar.wojcik@pollub.pl

He was Director of the Department of Electronics and Information Technology, former long-time dean of the Faculty of Electrical Engineering and Computer Science at Lublin University of Technology. Doctor Honoris Causa of universities in Ukraine and Kazakhstan. He is also a member of European Academy of Science and Arts, International Academy of Applied Radioelectronics, The International Informatization Academy of Kazakhstan and many other scientific organisations of Poland as well as Europe and Asia.
In his research he mainly deals with process control, optoelectronics, digital data analysis and also heat processes or solid state physics.

http://orcid.org/0000-0002-6473-9627

D.Sc. Sergii Pavlov
e-mail: psv@vntu.edu.ua

Academician of International Applied Radioelectronic Science Academy, Professor of Biomedical Engineering and Optic-Electronic Systems Department Vinnitsia National Technical University
Scientific direction: biomedical information optoelectronic and laser technologies for diagnostics and physiotherapy influence.
Deals with issues of improving the distribution of optical radiation theory in biological objects, particularly through the use of electro-optical systems, and the development of intelligent biomedical optoelectronic diagnostic systems and standardized methods for reliably determining the main hemodynamic cardiovascular system of comprehensive into account scattering effects.

http://orcid.org/0000-0002-0051-5560

Ph.D. Gulzira Abdikerimova
e-mail: gulzira1981@mail.ru

Ph.D., Associate professor of Department of Information Systems, L.N. Gumilyov Eurasian National University, Nur-Sultan, Kazakhstan.
Scientific direction: image and signal processing, textural feature analysis, machine learning.

http://orcid.org/0000-0002-4953-0737

Ph.D. Liudmyla Savytska
e-mail: lyudik0304@gmail.com

Docent of Software Department Vinnitsia National Technical University She graduated from VNTU with a degree in "Intelligent Information Processing and Decision Making" with honors and qualified as a software engineer. She successfully defended her dissertation on "Methods of adaptive data compression based on the linear Fibonacci form".
Scientific direction: image and signal processing, machine learning.

http://orcid.org/0000-0003-1130-2621

http://doi.org/10.35784/iapgos.2974 received: 23.05.2022 | revised: 13.06.2022 | accepted: 15.06.2022 | available online: 30.06.2022

NUMERICAL SIMULATIONS OF A FLAT PHANTOM IN THE NEAR-FIELD OF SYMMETRIC DIPOLE ANTENNA

Monika Styła[1,2], Sebastian Styła[2]
[1]Medical University of Lublin, Faculty of Medicine, Chair and Department of Biophysics, Lublin, Poland, [2]Lublin University of Technology, Faculty of Electrical Engineering and Computer Science, Department of Electrical Engineering and Electrotechnologies, Lublin, Poland

Abstract. *The paper presents a numerical electromagnetic simulations of SAR limited to human tissues based on FDTD algorithm using Sim4Life platform. Flat-bottomed dielectric vessel (flat phantom) and half-wave symmetric dipole antenna were modeled. Simulations were done for the frequencies 0.9 GHz and 0.6 GHz. The analysis were performed according to the IEEE/IEC62704-1 standard and include distributions of electric and magnetic fields around the phantom and antenna. Finally, SAR distributions in the phantom and near the antenna.*

Keywords: specific absorption rate, numerical simulation, Sim4Life

SYMULACJE NUMERYCZNE PŁASKIEGO FANTOMU W BLISKIM POLU SYMETRYCZNEJ ANTENY DIPOLOWEJ

Streszczenie. *W pracy przedstawiono numeryczne symulacje elektromagnetyczne SAR dla tkanek ludzkich w oparciu o algorytm FDTD z wykorzystaniem platformy Sim4Life. Zamodelowano płaskodenny dielektryk (fantom płaski) oraz półfalową symetryczną antenę dipolową. Symulacje wykonano dla częstotliwości 0.9 GHz i 0.6 GHz. Analizy zostały wykonane zgodnie ze standardem IEEE/IEC62704-1 i obejmują rozkłady pól elektrycznych i magnetycznych wokół fantomu i anteny. Na koniec zaprezentowano rozkłady SAR w fantomie i pobliżu anteny.*

Słowa kluczowe: współczynnik absorpcji swoistej, symulacje numeryczne, Sim4Life

Introduction

Starting from the 90s [3, 8, 9, 12, 17] many researchers have made a lot of numerical simulations for the accurate dosimetric evaluation of human tissues models, which are exposed to radiated antennas (e.g. mobile phones) or other wireless communication devices. The electromagnetic interaction between biological tissues and antennas are constantly proven and most of these numerical and experimental results are available in the literature [1, 4–6, 14, 18].

Electric fields are associated with the presence of electric charge but magnetic fields are the result of the physical movement of this electric charge (electric current).

The plane-wave model is a good approximation of the electromagnetic field propagation in the far-field region. In this case, the minima and maxima of magnetic and electric fields arise at the same points along the direction of propagation [7].

In the near-field region the situation is more complicated. The EM field structure might be highly inhomogeneous. In this case, the electric and magnetic fields must be determined.

In addition to the electric and magnetic fields distribution the Specific Absorption Rate (SAR) is one of the most widely used parameters for the evaluation of radiation exposure in the near-field. It is a measure of the rate at which energy is absorbed per unit mass by a human body when exposed to a radio frequency electromagnetic field [19]. It is frequently used to measured power absorbed during magnetic resonance imaging procedures and from mobile phone technologies.

Low SAR can reduces electromagnetic exposure. Now it is possible to modelling SAR distribution by using standardized models of the human body that are filled with liquids that simulate the RF absorption parameters of different human tissues [2, 19].

In this paper we presents simulated SAR distribution in a flat phantom filled with a liquid (HSL, head simulating liquid) with human tissue properties and distribution of electric and magnetic fields around the phantom and dipole antenna.

1. Materials and methods

Geometry models, simulations and analysis are made using Sim4Life platform (www.zmt.swiss). Sim4Life allows an intuitive approach to the analysis of biomedical phenomena, near-field as well.

The setup of simulation consists of symmetric dipole antenna for tuning over a wide range of frequencies (900 MHz bandwidth in this case), the flat-bottom dielectric phantom, filled with tissue simulating liquid, and the source (a line between dipoles that will be used as a source exciting the antenna). In this case the antenna consist of two conductors (dipoles) of equal length oriented end-to-end with the feedline connected between them [13]. The dipole is the simpliest type of the antennas.

1.1. Building a model

The first step of the modelling the setup was creating a geometry of phantom and geometry of dipole antenna (Fig. 1). For simplicity, the phantom was designed as a rectangular box (cube) filled with a mixture with properties such as brain tissue (HLS), described in the next section.

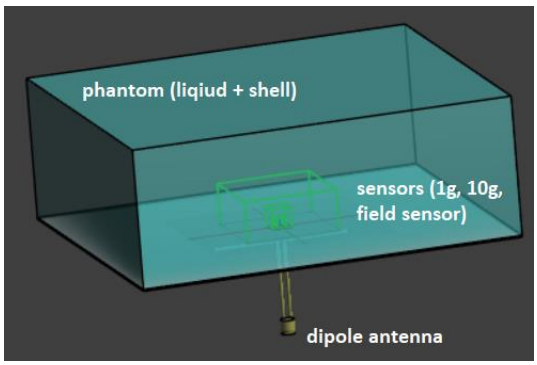

Fig. 1. Symmetric dipole antenna with the phantom (3D view)

Figure 2 illustrates a distance between the shell of the phantom and the antenna. The dipole antenna has been placed under the phantom so that the distance between them could be varied, but the paper presents the only one case that a gap between antenna and phantom is 15 mm. The shell thickness is 2 mm.

Inside the phantom three light green boxes are placed. The biggest box (the field sensor in this case) has dimension 100 mm × 100 mm × 45 mm, in X, Y and Z axis, respectively. The box in the middle is 10g sensor with dimension 21.5 mm in the three planes. The smallest box (1g sensor) has a dimension 10mm in three planes. 1 g and 10 g sensors are required for average SAR distribution pattern.

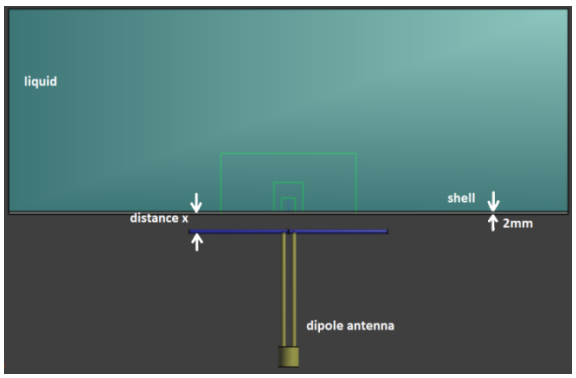

Fig. 2. Schematic diagram showing antenna with the phantom (front view)

1.2. Adjusting simulation settings

A methodology of the simulation is to preparing the environment by choosing a type of the simulation and determine properties of the materials. For a near-field issues a FDTD (Finite-difference time-domain method) is recommended. FDTD method uses Maxwell's differential equations to determine electromagnetic field [15, 16]. Additionally, the IEEE/IEC62704-1 standard defines the application of the FDTD technique when used for determining SAR in the human body [7].

PEC is a type of material assigned to all of the parts of dipole antenna. Shell of the phantom has a dielectric properties (relative permittivity ε_r is 3.1 and mass density is 1000 kg/m^3). The same value of mass density assigned to a tissue-simulation liquid of the phantom. Electrical properties of the liquid: electric conductivity σ is 0.97 S/m and relative permittivity ε_r is 41.5.

Type of signal used to excite a source is Gaussian. Edge source settings were: 0.9 GHz as a center frequency in the first case, amplitude 1 V and resistance 50 Ω. The second simulation was performed to 0.6 GHz frequency.

Moreover 3 different separated sensors were determined 1 g, 10 g and a field sensor.

A coarse grid with over 824k cells was used in the first simulation. To improve the quality of the simulation results a more precise mesh (fine grid with over 15M cells) was used later. Additionally, Kernel software was used to make a simulation much faster.

2. Results

In general, exposure to an electromagnetic field causes in a highly non-uniform deposition and distribution of energy within the body, which must be assessed by dosimetric measurement and calculation.

In the near-field there are strong capacitive and inductive effects from the currents and charges in the antenna. They cause electromagnetic components that do not behave like far-field radiation, therefore it was worth starting with the simulation of the electric and magnetic fields distributions.

2.1. Electromagnetic simulations

According to the principle of the interaction of electromagnetic fields with each other, the sources placed inside the object produces a total electromagnetic field simulating the field excited outside the object, whereas the sources placed outside the object produces a total electromagnetic field simulating the field excited inside the object [11].

Figure 3 shows a total near-field distribution of the electric field strength around the antenna for the frequency 0.9 GHz. The maximum electric field strength covers extreme parts of the dipoles and the value is 5.87×10^{-7} V/m. Equally large value is located in between two stubs. The electromagnetic field strength decreases with the distance from the antenna and practically do not include the phantom. It can be assumed that increasing the distance between the phantom and the antenna may cause that the electric field inside the phantom will be negligible.

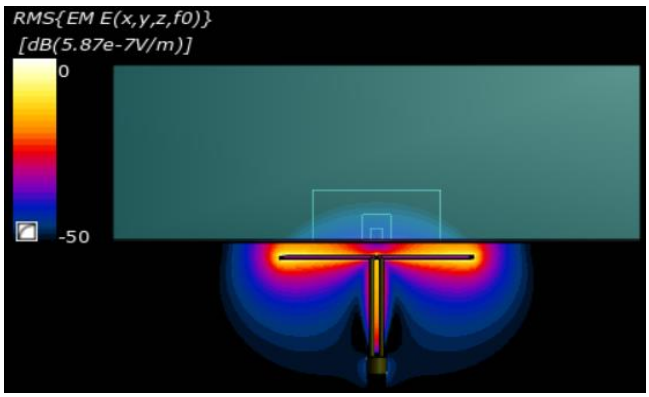

Fig. 3. Distribution of the electric field strength for 0.9 GHz. In the xz plane. The maximum value is 5.87×10^{-7} V/m

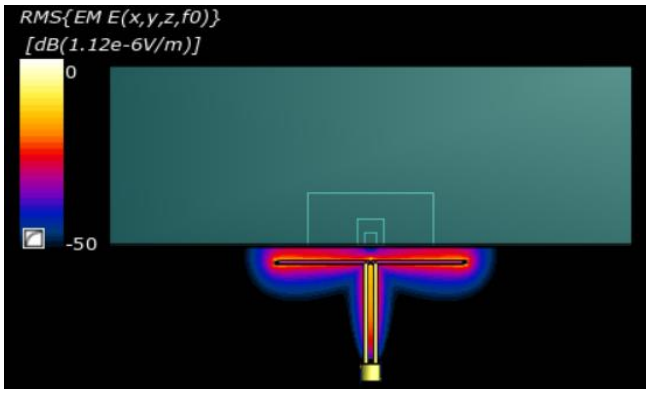

Fig. 4. Distribution of the electric field strength for 0.6 GHz. In the xz plane. The maximum value is 1.12×10^{-6} V/m

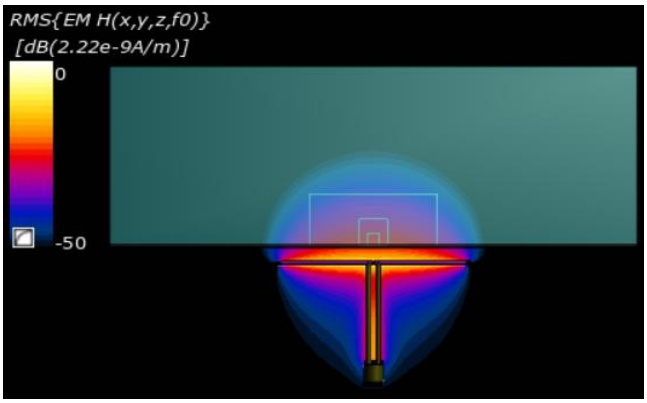

Fig. 5. Distribution of the magnetic field strength for 0.9 GHz in the xz plane. The maximum value is 2.22×10^{-9} A/m

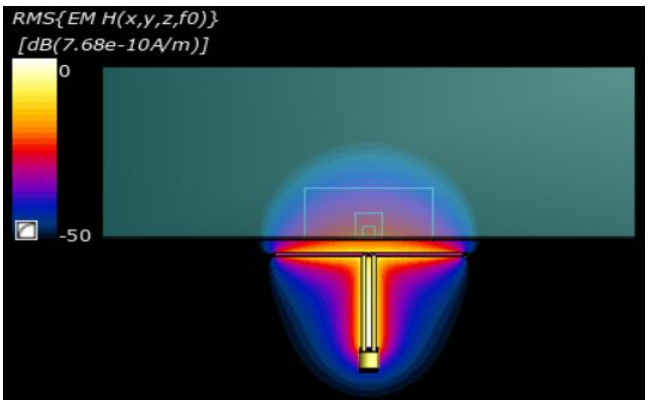

Fig. 6. Distribution of the magnetic field strength for 0.6 GHz in the xz plane. The maximum value is 7.68×10^{-10} A/m

In the near-field, both the electric (Fig. 3 and 4) and the magnetic (Fig. 5 and 6) field structures are crearly visible. Interestingly, the electric field strength for the frequency 0.6 GHz does not include the phantom at all. The maximum magnetic field strength for both values of the frequencies places along the whole antenna. Additionally, the spectrum of the magnetic field includes phantoms identically for both frequencies. Figures 5 and 6 show the *xy* planes where the lines of the magnetic field for the frequency 0.9 GHz and 0.6 GHz are centered and arranged circularly.

The input port voltage reflection coefficient is a complex quantity, whose absolute value is an indicator for the reflection. |S11| = 0 means that the circuit is perfectly matched and that none of the incident power wave is reflected [10]. The magnitude of the S11 value is determined by the resistance value (50 Ω) of the antenna.

Reflection coefficient less than -10 dB means the condition where 90% of the signals are successfully transmitted while only 10% is reflected back.

Figure 7 presents the return loss of the dipole antenna and the value is -50dB for the frequency 0.9 GHz. Resonance curve for the frequency 0.6 GHz looks similar and it is negligible in this paper.

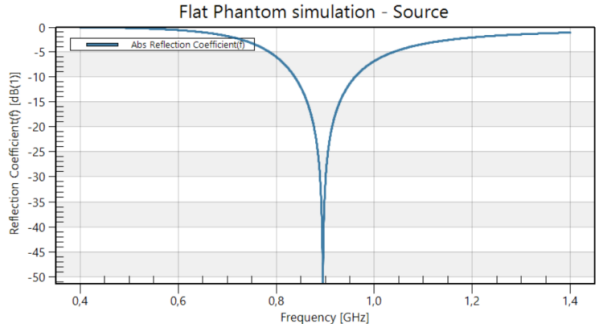

Fig. 7. A plot with the resonance curve of the dipole antenna. The return loss of the dipole antenna in dB

2.2. Power balance

Sim4Life platform enables to calculate a power balance value. Ideally, the balance ratio should be 1. The balance ratio is determined as the ratio of total dissipated and input power and for a coarse grid od designed simulation is 0.95. The balance ratio value can be improved by using a better (finer) grid while extending a simulation time. For a fine grid the value is close to 1, as Fig. 8 demonstrated.

Power Balance

Show 25 entries Filter:

Frequency 9.000e+08 Hz	coarse grid	fine grid
Input Power	3.92465e-21 W	3.9124e-21 W
Lumped Elements Loss	0 W	0 W
Dielectric Loss	3.21236e-21 W	3.36385e-21 W
Radiated Power	5.03578e-22 W	5.18762e-22 W
Balance Ratio (Total Dissipated/Input Power)	0.94682	0.992386

Fig. 8. The result of power balance for coarse grid and fine grid

2.3. SAR distributions

For phantom that are equivalent homogeneous tissue, the SAR can be calculated by the formula

$$SAR = \frac{\sigma}{2\rho} E^2 \quad (1)$$

where: σ is the conductivity [S/m], ρ is the density [kg/m^3], and E is electric field [V/m].

Specific absorption rate is usually averaged either over the whole body, or over a small sample volume (typically 1 g or 10 g of tissue). The value of SAR is the maximum level measured in the body part studied over the stated volume or mass. In this paper SAR of the whole phantom was calculated for 0.9 GHz and 0.6 GHz. The results are shown in the figures 9 and 10. The maximum 1 g peak spatial-average SAR is 10.6 W/kg and 9.72 W/kg, respectively.

When measuring the SAR due to a RF exposure, dipole antenna is placed against a representation of a flat phantom. The SAR value is then measured at the place that has the highest absorption rate in the entire phantom, which is usually as close to the dipole antenna as possible.

Figures 9 and 10 illustrate a spatial-averages of SAR for 0.9 GHz and 0.6 GHz, respectively, with moving constant-mass cubes as recommended in IEEE/IEC62704-1 Standard. The SAR is not evenly distributed within the phantom. The maxima of the SAR are clearly concentrated around the central part of the phantom in front of the antenna for both cases. These simulations do not include an area around the antenna.

The maxima SAR values in the xy planes for both frequencies are placed in a center bottom surface of the phantom, the nearest surface to the antenna. Figure 11 presents SAR statistics including maximum and minimum SAR position in *xyz*.

According to the IEEE/IEC62704-1 standard [7], the safe SAR limits is 2 W/kg averaged over the 10 g of tissue absorbing the most signal. 3.2 W/kg is the limit of the SAR value for human head tissues.

In case described in this paper, the highest SAR value is in front of the dipole antenna and it greatly exceeds safe limits. Increasing the distance from the antenna may decrease the SAR value.

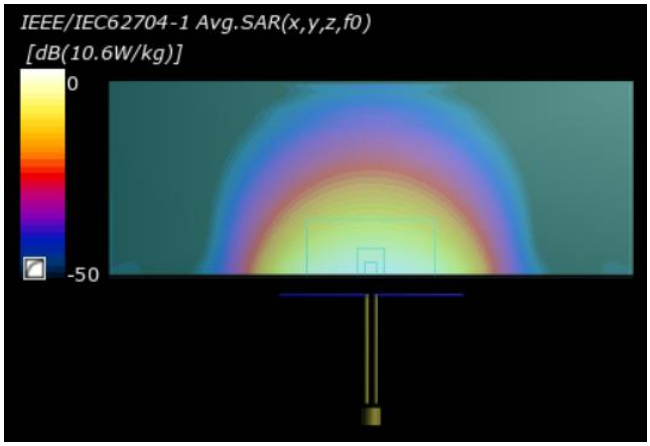

Fig. 9. Peak average SAR for 0.9 GHz in the xz plane. The maximum 1 g peak spatial-average SAR is 10.6 W/kg

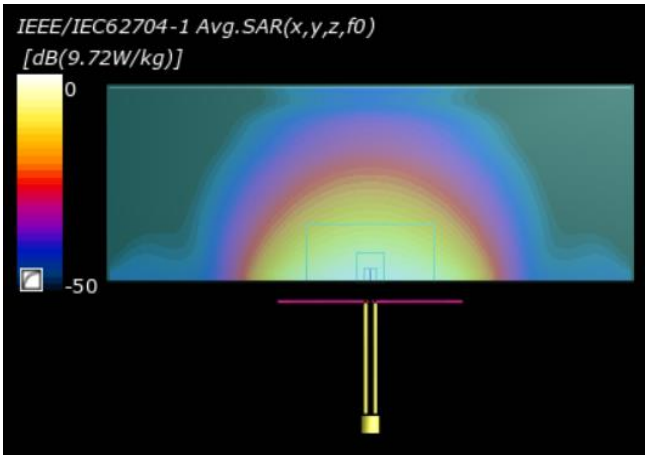

Fig. 10. Peak average SAR for 0.6 GHz in the xz plane. The maximum 1 g peak spatial-average SAR is 9.72 W/kg

SAR Statistics

	9.000e+08 Hz	6.000e+08 Hz
Min	0 W/kg	0 W/kg
Min Index	(0, 0, 0)	(0, 0, 0)
Min Center	(-0.293213, -0.279713, -0.202351) m	(-0.293213, -0.279713, -0.202351) m
Max	14.8687 W/kg	13.3978 W/kg
Max Index	(57, 48, 38)	(57, 48, 38)
Max Center	(-0.00025, 0.00045, 0.00125) m	(-0.00025, 0.00045, 0.00125) m
Average	0.00523836 W/kg	0.00554689 W/kg
Integral	0.000818508 W/kg	0.000866717 W/kg

Fig. 11. SAR statistics for 0.9 GHz and 0.6 GHz

3. Conclusions

The design of a dipole antenna and a flat phantom presented in this paper was performed using the Sim4Life platform with FDTD solver.

The simulations, including return loss of the dipole antenna and specific absorption rate distribution were made for the bandwidth with two different center frequencies. Total near-field distribution of electromagnetic field around the antenna and inside the phantom shows that the electric field is mainly concentrated around the dipoles and the stubs of the antenna, whereas the magnetic field concentrates in the middle of antenna and is arranged circularly. The maximum value of the electric field strength is larger for the lower frequency (0.6 GHz) but the maximum value of the magnetic field strength is larger for the higher frequency (0.9 GHz).

SAR distributions inside the whole phantom were simulated based on recommendation in IEEE/IEC62704-1 standard. The results are specified as maximum 1g SAR and normalized to 1 W radiated power. The maximum SAR values are greatly exceed the permitted limits for the entire sensors placed in the phantom because of a small distance between the antenna and the phantom. The higher value of SAR occurs for the higher frequency of the antenna.

According to the presented results and the remarks discussed above, it can be assumed the local and the average SAR induced due to the radiation from a dipole antenna inside a flat phantom depends on the resonant frequency of the antenna and the distance between the antenna and the phantom. Placing the antenna too close to the phantom causes a very high SAR value.

References

[1] Alekseev S. I., Radzievsky A. A., Szabo I., Ziskin M. C.: Local heating of human skin by millimeter waves: Effect of blood flow. Bioelectromagnetics 26(6), 2005, 489–501 [http://doi.org/10.1002/bem.20118].
[2] Andrenko A., Shimizu Y., Wake K.: SAR Measurements of UHF RFID Reader Antenna Operating in Close Proximity to a Flat Phantom. IEEE International Conference on RFID Technology and Applications (RFID-TA), 2019 [http://doi.org/10.1109/RFID-TA.2019.8892054].
[3] Balzano Q., Garay O., Jr T. J.: Electromagnetic Energy Exposure of the Users of Portable Cellular Telephones. Vehicular Technology, IEEE Transactions, 44, 1995, 390–403 [http://doi.org/10.1109/25.406605].
[4] Bonato M., Dossi L., Gallucci S., Benini M., Tognola G., Parazzini M.: Assessment of Human Exposure Levels Due to Mobile Phone Antennas in 5G Networks. International Journal of Environmental Research and Public Health 19(3), 2022, 1546 [http://doi.org/10.3390/ijerph19031546].
[5] Colombi D., Thors B., TöRnevik C., Balzano Q.: RF Energy Absorption by Biological Tissues in Close Proximity to Millimeter-Wave 5G Wireless Equipment. IEEE Access 6, 2018, 4974–4981, [http://doi.org/10.1109/ACCESS.2018.2790038].
[6] Hirata A.: Human exposure to radiofrequency energy above 6 GHz: review of computational dosimetry studies. Physics in Medicine and Biology 66, 2021, 08TR01 [http://doi.org/10.1088/1361-6560/abf1b7].
[7] ICNIRP guidelines for limiting exposure to time-varying electric, magnetic and electromagnetic fields (up to 300 GHz). Health Physics 74(4), 1998, 494–522.
[8] Kuster N., Balzano Q.: Energy absorption mechanism by biological bodies in the near field of dipole antennas above 300 MHz. Vehicular Technology, IEEE Transactions 41, 1992, 17–23 [http://doi.org/10.1109/25.120141].
[9] Kuster N., Kastle R,, Schmid T.: Dosimetric Evaluation of Handheld Mobile Communications Equipment with Known Precision. EICE Transactions on Communications E80-B(5), 1997, 645–652.
[10] Papakanellos P. J., Nanou E. D., Sakka N. I., Tsiafakis V. S. G.: Near field interaction between a brain tissue equivalent phantom and a dipole antenna. 2nd International Workshop on Biological Effects of Electromagnetic Fields, 2001, 888–897.
[11] Riu P. J., Foster K.: Heating of tissue by near-field exposure to a dipole: A model analysis. IEEE transactions on biomedical engineering 46, 1999, 911–917 [http://doi.org/10.1109/10.775400].
[12] Schmid T., Egger O., Kuster N.: Automated E-field scanning system for dosimetric assessments. IEEE Transactions on Microwave Theory and Techniques 44(1), 1996, 105–113 [http://doi.org/10.1109/22.481392].
[13] Stutzman W. L., Thiele G. A.: Antenna Theory and Design. Wiley, 2012.
[14] Thors B., Colombi D, Ying Z., Bolin T., Törnevik C.: Exposure to RF EMF From Array Antennas in 5G Mobile Communication Equipment. IEEE Access 4, 2016, 7469–7478 [http://doi.org/10.1109/ACCESS.2016.2601145].
[15] Umashankar K., Taflove A.: A Novel Method to Analyze Electromagnetic Scattering of Complex Objects. IEEE Transactions on Electromagnetic Compatibility 4, 1982, 397–405 [http://doi.org/10.1109/TEMC.1982.304054].
[16] Yee K,: Numerical solution of initial boundary value problems involving maxwell's equations in isotropic media. IEEE Transactions on Antennas and Propagation 14, 1966, 302–307 [http://doi.org/10.1109/TAP.1966.1138693].
[17] Yu Q., Gandhi O.P., Aronsson M., Wu D.: An automated SAR measurement system for compliance testing of personal wireless devices. IEEE Transactions on Electromagnetic Compatibility 41, 1999, 234 [http://doi.org/10.1109/15.784158].
[18] Ziskin M., Alekseev S., Foster K., Balzano Q.: Tissue models for RF exposure evaluation at frequencies above 6 GHz. Bioelectromagnetics – Wiley Online Library 39, 2018, 17389 [http://doi.org/10.1002/bem.22110].
[19] fcc.gov/consumers/guides/specific-absorption-rate-sar-cell-phones-what-it-means-you (13.05.2022).

M.Sc. Eng. Monika Styła
e-mail: monika.styla@umlub.pl

Monika Styła graduated from Lublin University of Technology, biomedical engineering. She currently works as assistant in Chair and Department of Biophysics at Medical University of Lublin. Author of 20 scientific papers.
Her research is related to RF coils design and electromagnetic simulations in biomedical applications.

http://orcid.org/0000-0001-6310-3582

D.Sc. Eng. Sebastian Styła
e-mail: s.styla@pollub.pl

Sebastian Styła currently works as assistance professor in Department of Electrical Engineering and Electrotechnologies at Lublin University of Technology. He defended his PhD dissertation in Electrical Engineering in 2015. Author of over 50 scientific papers, including 1 patent.
His research is related to the new milling technologies using EM field and diagnosics of electric and electronic automotive equipment.

http://orcid.org/0000-0002-3239-4433

http://doi.org/10.35784/iapgos.2968 *received:16.05.2022 | revised: 27.05.2022 | accepted: 15.06.2022 | available online: 30.06.2022*

USING BAYESIAN METHODS IN THE TASK OF MODELING THE PATIENTS' PHARMACORESISTANCE DEVELOPMENT

Mariia A. Voronenko[1], Ulzhalgas M. Zhunissova[2], Saule S. Smailova[3], Luidmila N. Lytvynenko[4], Nataliia B. Savina[5], Pavlo P. Mulesa[6], Volodymyr I. Lytvynenko[1]

[1]Kherson National Technical University, Kherson, Ukraine, [2]Astana Medical University, Astana, Kazakhstan, [3]D.Serikbayev East Kazakhstan State Technical University, Ust-Kamenogorsk, Kazakhstan, [4]Kherson City Psychoneurological Clinic, Kherson, Ukraine, [5]National University of Water and Environmental Engineering, Rivne, Ukraine, [6]Uzhhorod National University, Uzhhorod, Ukraine

Abstract. *In this paper, we propose a methodology for using static Bayesian networks (BN) in modeling the development of pharmacoresistance in patients with a diagnosis of epilepsy. Methods for constructing the structure of a static BN, their parametric training, validation, sensitivity analysis and "What-if" scenario analysis are considered. The model was designed in collaboration with expert doctors, as well as expert pharmacologists in the selection and quantification of input and output variables.*

Keywords: epileptology, pharmacoresistance, Bayesian networks, structural learning, parametric learning, sensitivity analysis, validation

ZASTOSOWANIE METOD BAYESOWSKICH DO MODELOWANIA ROZWOJU FARMAKOOPORNOŚCI U PACJENTÓW

Streszczenie. *W niniejszej pracy zaproponowano metodologię wykorzystania statycznych sieci bayesowskich (BN) w modelowaniu rozwoju farmakooporności u pacjentów z rozpoznaniem padaczki. Rozważane są metody konstruowania struktury statycznej BN, jej parametrycznego treningu, walidacji, analizy wrażliwości i analizy scenariuszy "co-jeśli". Model został zaprojektowany we współpracy z ekspertami – lekarzami, a także ekspertami – farmakologami w zakresie doboru i kwantyfikacji zmiennych wejściowych i wyjściowych.*

Słowa kluczowe: epileptologia, farmakooporność, sieci bayesowskie, uczenie strukturalne, uczenie parametryczne, analiza wrażliwości, walidacja

Introduction

Research in the field of expert systems focused on the development and implementation of those systems and models that are able to mimic areas of human activity that require thinking, a high level of skill and experience. One such application is medicine. The study is devoted to the creation of a system to achieve the effectiveness of drug therapy in epilepsy.

In accordance with the requirements of ILAE: "Pharmacoresistance is the inability to achieve control of the disease during therapy with two drugs in the form of monotherapy and/or combination therapy" [11].

Despite the development of the anticonvulsant drugs (PSP) number and the increase in the effectiveness of surgical treatment, the establishment of the most informative predictors and their combination as factors in the development of pharmacological resistance in a particular patient is one of the primary tasks of modern epileptology.

The work aims to develop a static Bayesian model in the problem of pharmacoresistance in patients with a diagnosis of "epilepsy".

1. Problem statement

Based on the study of the disease dynamics in patients with pharmacoresistant form of epilepsy, the following predictors of pharmacoresistance were identified:

- the presence of relatives with the diagnosis of "epilepsy",
- a history of febrile convulsions,
- the traumatic brain damage,
- the frequency of attacks more than 10 before the start of treatment,
- the lack of response to the first CAP,
- a break in treatment,
- the mental comorbidity (the patient has at least two disorders, each of which can be considered independent and diagnosed independently of each other).

The occurrence of pharmacoresistance in the future was also indicated by some electroencephalographic indicators:

- the diffuse changes on the electroencephalogram (EEG),
- a high index of epileptiform activity in the background EEG recording,
- the focal epileptiform activity,
- the polymorphism of epileptiform changes,
- the presence of several foci [6].

An important role in the development of pharmacological resistance is also played by genetic factors. They determine the development of both epilepsy itself, as well as receptor polymorphism and PSP transporter [7].

2. Review of the literature

The earliest medical decision support systems for CDS in medicine were flowcharts of problem tasks developed by doctors and coded for use by a computer [14].

While later systems are based on logistic regression models, artificial neural networks, support vector machines, and others. Although the possible use of computers in making medical decisions was mentioned 50 years ago, CDS systems have not yet been widely used and are not accepted in clinical practice [1, 13].

The potential to make them more acceptable for clinical practice has been proposed by several authors [8, 15, 16].

[15] identified four functions that are critical for CDS systems:

(i) the system should be provided to clinicians automatically, without interfering with the workflow,
(ii) provide decision support at the time and place of decision making,
(iii) provide recommendation and
(iv) should be implemented on the computer.

As the formalism is declarative in nature, any (often conditional) probabilistic statement can be computed from a given BN, where the statement may concern both individual and combinations of variables.

This allows asking questions such as "What is likely to be the result for the patient if I decide to request this test, to prescribe this treatment and so on".

Another attractive feature of the formalism is that it is closely related to causal models, which explains why some researchers refer to it as the causal probabilistic network (CPN) formalism.

In this article, BNs are discussed from the point of view of their use in making medical decisions, in particular, to simulate the development of pharmacological resistance in patients when solving the problem of choosing a treatment regimen for epilepsy.

3. Materials and methods

Bayesian network (BN) – this is a pair <G, B>, in which the first component of G is a directed acyclic graph corresponding to random variables [3, 12]. A graph is written as a set of conditions of independence: each variable is independent of its parents in G. The second component of the pair, B, is a set of parameters defining the network. It contains the parameters $Q_{x^i|pa(X^i)} = P(x^i \mid pa(X^i))$ for each possible value of x^i from X^i and $pa(X^i)$ from $Pa(X^i)$, where $Pa(X^i)$ denotes the set of parents of the variable X^i in G. Each variable X^i in the graph G is represented as a vertex. If we consider more than one graph, then we use the notation $Pa^G(X^i)$ to identify the parents X^i in the graph G [4].

The total joint BN's probability B is calculated by the formula $P_B(X^1,...,X^N) = \prod_{i=1}^{N} P_B(X^i \mid Pa(X^i))$. From a mathematical point of view, BN is a model for representing probabilistic dependencies, as well as the absence of these dependencies. At the same time, the A → B relationship is causal, when event A causes B to occur, that is, when there is a mechanism whereby the value adopted by A affects the value adopted by B. BN is called causal (causal) when all its connections are causal.

The goal of parametric learning is to find the most likely θ variables that explain the data. Let $D=\{D_1, D_2, \ldots, D_N\}$ be learning data, where $D_1=\{x_1[l], x_2[l], \ldots, x_n[l]\}$ consists of instances of Bayesian network nodes. The learning parameter is quantified by a log-likelihood function, denoted as $L_D(\theta)$.

The sensitivity analysis of the Bayesian network allows you to set for each of the network parameters a function expressing the output probability from the point of view of the parameter being studied [2, 5, 10].

To derive the probability, we will consider the posterior marginal probability of the form $y=p(a|e)$, where a is the value of the variable A and e means available evidence. Each of the network parameters has the form $x = p(b_i \mid \pi)$, where b_i is the value of the variable B and π is an arbitrary combination of the values of the set of parents $\Pi=pa(B)$ of B.

Denote $p(a|e)(x)$ as a function expressing the a posteriori marginal probability $p(a|e)$ in terms of the parameter x. In the future, we will assume that in a sensitivity analysis, as the parameter $x = p(b_i \mid \pi)$ changes, each of the probabilities $p(b_j \mid \pi)$ changes accordingly. The function $y(x)$, obtained as a result of sensitivity analysis, is a quotient of two linear functions in x [9].

The sensitivity analysis in the GeNie software environment is performed using influence diagrams (Fig. 1). The influence diagram shows the most sensitive parameters for the selected state of the target node Y, sorted from the most sensitive to the least sensitive.

4. Experiments and results

Observation of patients with a diagnosis of "epilepsy" lasted one year – this is the time during which you can titrate two caps to the maximum possible therapeutic doses. 310 people were examined, the experience of the disease in each patient was at least 1 year. The average age of patients is 29 +/- 2 years. All patients underwent the following examinations:

- clinical examination,
- defined neurological and mental status,
- performed magnetic resonance imaging (MRI) of the brain,
- conducted a routine electroencephalogram (EEG) and video EEG.

A survey was conducted to establish a history.

If necessary, some patients have been adjusted drug treatment in accordance with accepted standards. The purpose of the simulation is to select curable (treatable) and resistant (resistant to treatment) from the studied group of patients. We identified the following indicators, which, in our opinion, could serve as criteria (baseline) for determining the prognosis of epilepsy in a particular patient.

Table 1. The initial data for the study

Observational data (history)	
X1	An epileptic status in history
X2	Presence /absence of epilepsy in relatives
X3	Febrile seizures in history
X4	Mental disorders in history
X5	Craniocerebral trauma with changes in MRI
X6	More than 10 attacks before treatment
X7	The response to the drug after the first epileptic seizure
X8	Transferred a stroke
X9	Effective treatment for relatives with epilepsy
Xl0	A positive result on the EEG after the first Epileptic Seizure
Laboratory tests	
Z1	Diffuse changes in the EEG
Z2	High index of epileptic activity
Z3	Focal epileptic activity with the generator
Z4	Polymorphism of epileptic changes
Z5	High slow-wave EEG
Z6	Many epileptic foci on the EEG
Z7	Presence / absence of epilepsy on the EEG
Z8	No / there are changes in MRI
Z9	Genetic analysis of glycoproteins P-gp1, P-gp2, SCN1A
Z10	Total Blood Pressure Monitoring

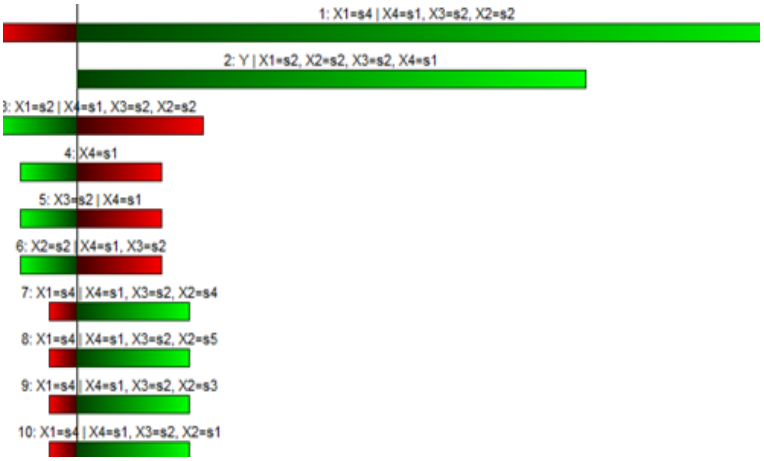

Fig. 1. The sample of influence chart

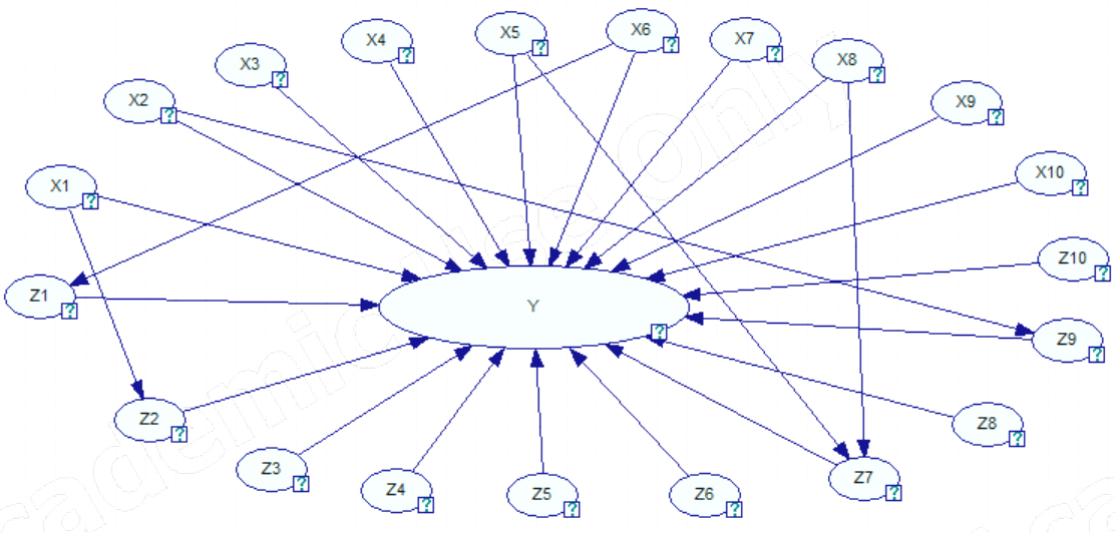

Fig. 2. Structural model of static BN in determining patient pharmacological resistance

Figure 2 shows the structural model of the static BN being developed. According to the presented model, a variety of different concepts that characterize it (both historical data and laboratory results) can be associated with pharmacological resistance. At the same time, the proposed model does not limit the rigid unidirectionality of actions but can be used both to detect causal characteristics and to predict the consequences.

The above-described properties of the model in figure 2 are illustrated by arrows showing the movement of information between the selected blocks. All indicators X and all indicators Z are directly related to Y (presence/absence), there is also a correlation of some studies with historical data: X1→Z3, X6→Z2, X5→Z8, X8→Z8, X2→Z9.

It should be noted that, due to the specifics of the work of Bayesian networks, all conclusions of this model, with respect to the information sought, are of a probabilistic nature and are presented in the form of a ranked list (according to the values of probability of fidelity of one or another conclusion).

The final decision on the confirmation of pharmacoresistant/curability and prescription of treatment to the patient is made by the doctor.

The solution to the problem of building a Bayesian network was made using the GeNIe 2.3 Academic software environment. At the same time, we carry out parameterization, sensitivity analysis of the model and validation. The node determining the presence/absence of pharmacoresistance was taken as the target node.

Let the nodes X1-X10 represent observational data (history). Nodes Z1-Z10 – laboratory tests and the results of the analyzes. Y – the presence/absence of pharmacoresistance in a particular patient.

All nodes have two states:
state s1 – means the absence of this feature;
state s2 – means the presence of this sign in the clinical picture.

We have clinical observations of the symptoms of 310 patients, supported by the analyses performed. We took a sample of data from 16 patients and analyzed each specific clinical case. The results of the analysis are shown in table 2.

The static Bayesian network model, focused on solving the problem of determining pharmacoresistance in an individual patient, is presented in figures 3–6. Consider a clinical case 1. As can be seen from table 2 with a probability of 75% the patient is curatable, which means he will respond well to the standard scheme of drug treatment (Fig. 3).

Table 2. The results of clinical observations analysis of the patients' symptoms and laboratory studies

Clinical Case:	Clinical observations and anamnesis										Conducted research										The probability of the presence/absence of pharmacoresistance
No	X1	X2	X3	X4	X5	X6	X7	X8	X9	X10	Z1	Z2	Z3	Z4	Z5	Z6	Z7	Z8	Z9	Z10	Y
1 fig. 2	0	1	0	1	0	0	1	1	1	1	1	1	1	0	1	1	0	1	1	1	Yes–25% No–75%
2	1	0	0	1	0	1	1	1	0	0	0	1	0	1	1	0	0	0	1	1	Yes–25% No–75%
3	1	1	1	0	0	1	0	1	0	0	1	0	1	0	1	0	1	0	1	0	Yes–75% No–25%
4	1	1	0	1	1	0	1	1	0	1	1	0	1	0	0	1	0	0	0	1	Yes–25% No–75%
5	0	0	0	1	0	0	0	1	1	0	0	0	1	1	0	0	1	0	1	0	Yes–25% No–75%
6 fig. 3	0	1	0	1	1	1	0	0	1	1	0	0	0	0	1	0	1	1	0	0	Yes–50% No–50%
7	1	0	1	1	1	0	1	1	1	1	1	1	1	1	1	0	0	0	1	1	Yes–25% No–75%
8	1	1	0	1	0	1	1	0	1	1	1	1	0	1	0	0	1	1	0	1	Yes–25% No–75%
9 fig. 4	1	1	0	0	1	0	0	0	1	0	1	1	1	0	1	0	0	1	1	1	Yes–75% No–25%

Table 2 (cont.). The results of clinical observations analysis of the patients' symptoms and laboratory studies

Clinical Case:	Clinical observations and anamnesis										Conducted research										The probability of the presence/absence of pharmacoresistance
10	0	1	0	1	0	0	1	0	1	0	1	1	0	0	1	0	0	0	0	1	Yes–25% No–75%
11	1	1	0	1	1	0	1	0	1	0	1	0	1	1	0	0	0	1	1	1	Yes–75% No–25%
12	0	0	0	1	1	1	0	0	0	0	0	0	0	1	1	1	1	1	1	0	Yes–75% No–25%
13	1	1	1	1	1	1	0	0	1	0	1	0	1	0	1	0	0	0	0	1	Yes–25% No–75%
14	1	1	1	0	0	1	0	1	1	1	1	1	0	0	0	1	1	0	0	0	Yes–75% No–25%
15	1	0	0	0	0	0	1	1	0	0	1	1	0	0	1	0	1	1	0	1	Yes–25% No–75%
16	0	0	0	1	0	0	0	0	1	1	0	1	1	0	1	0	1	0	0	0	Yes–25% No–75%

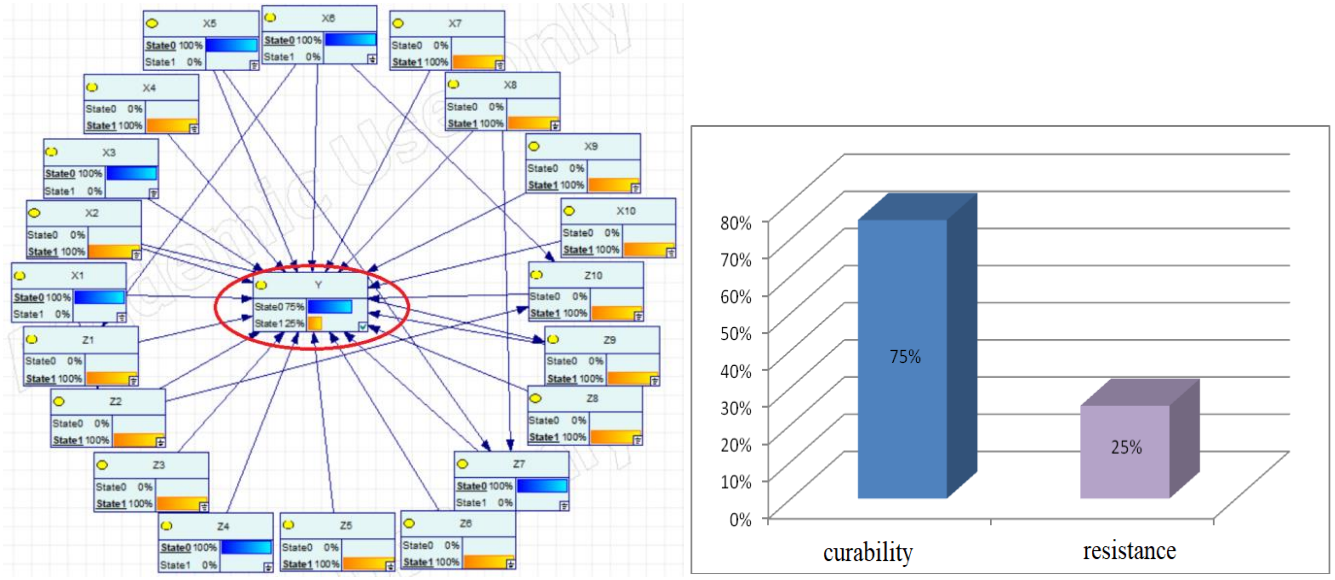

Fig. 3. Clinical Case Simulation Results 1

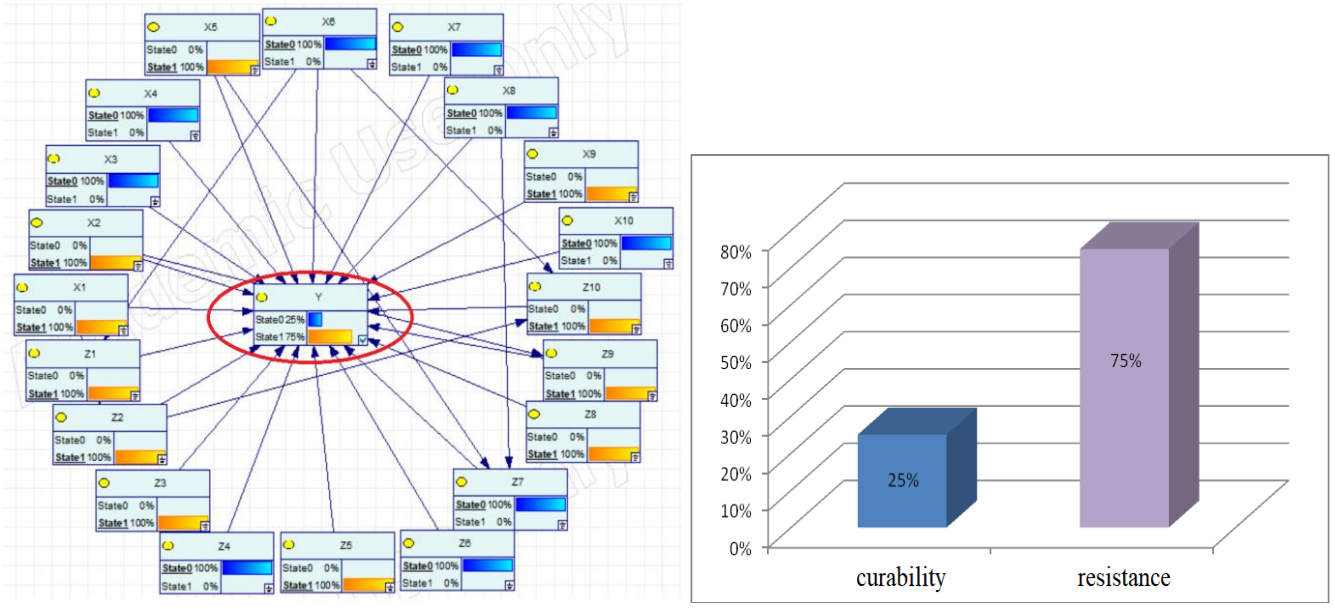

Fig. 4. Clinical Case Simulation Results 9

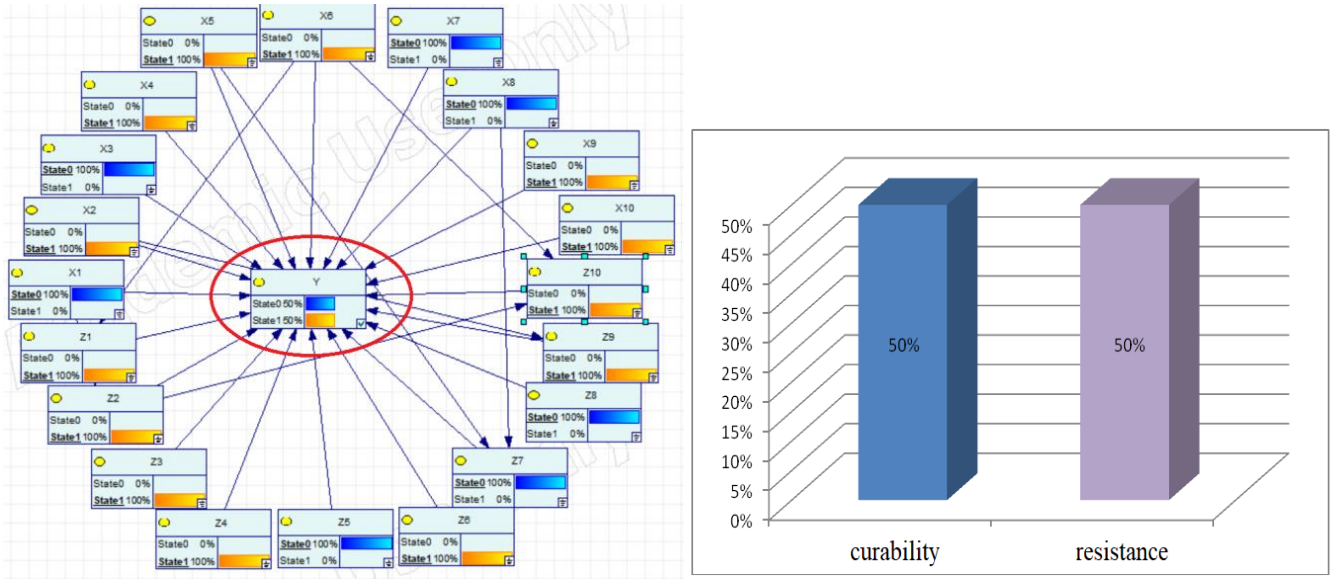

Fig. 5. Clinical Case Simulation Results 6

Consider a clinical case 9. As can be seen from table 2, a patient is 75% likely to be pharmacoresistant, that is, they need alternative methods for treating epilepsy, such as: pharmacogenetics, electrophysiology, and also surgery for epilepsy when it is possible (Fig. 4).

Consider a clinical case 6. As can be seen from table 2, the patient has a controversial result. This result requires additional analyzes and research, as usually in such a situation the doctor will further clarify the clinical picture (Fig. 5).

As can be seen from table 2, in 6 cases, their 16 presence of pharmacological resistance was confirmed with a probability of 75% (red), in 9 cases out of 16 – we are talking more about the absence of pharmacological resistance (green). In the only case with patient No. 9, the probability of the presence/absence of drug resistance is 50% to 50%.

5. Discussion

BNs are interesting for representing knowledge because they allow both top-down and bottom-up, they easily capture the opinions of experts and can be trained on data, updated and personalized.

Pharmacoresistance is:

- high-amplitude slow-wave bilateral activity on the background EEG;
- lack of response to the first drug intake;
- diffuse changes on EEG;
- symptomatic epilepsy;
- the presence of several foci on the EEG;
- more than 10 attacks before treatment.

The results of the analysis of clinical observations of the symptoms of patients and laboratory studies are shown in Fig. 6.

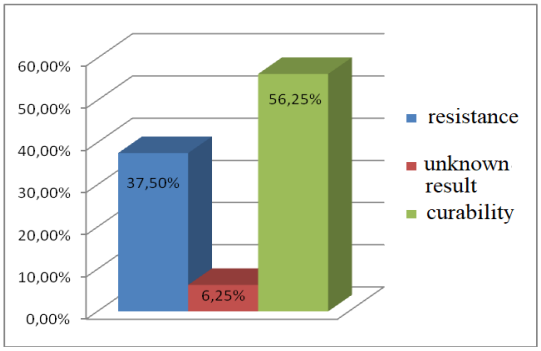

Fig. 6. The results of the analysis of clinical observations of the symptoms of patients

6. Conclusions

The paper proposes a model of a static Bayesian network for solving the problem of predicting the effectiveness of drug therapy for such diseases as epilepsy. The simulation results showed that 56.25% of patients are amenable to standard treatment, 6.25% have a controversial result and in this case need additional examination, but 37.5% of patients need alternative methods of treatment of epilepsy, such as: pharmacogenetics, electrophysiology , as well as surgery for epilepsy when possible.

In our future research, we apply the proposed model to the diagnosis of other diseases.

References

[1] Bates D. W., Kuperman G. J., Wang S., Gandhi T., Kittler A.: Ten commandments for effective clinical decision support: Making the practice of evidence-based medicine a reality. Journal of the American Medical Informatics Association 10, 2003, 523–530.

[2] Castillo E. F., Guti´errez J. M., Hadi A. S.: Sensitivity analysis in discrete Bayesian networks. IEEE Transactions on Systems, Man, and Cybernetics – Part A: Systems and Humans 27(4), 1997, 412–423.

[3] Cheeseman P., Kelly M., Taylor W., Freema D., Stutz J.: Bayesian classification. Proceedings of AAAI, St. Paul 1988, 607–611.

[4] Cooper G. F.: Current research directions in the development of expert systems based on belief networks. Applied Stochastic Models and Data Analysis 5, 1989, 39–52.

[5] Darwiche A.: A differential approach to inference in Bayesian networks. Proceedings of Uncertainty in Artificial Intelligence 2000, 123–132.

[6] Hiritis N.: Predictors of pharmacoresistant epilepsy. Epilepsy research 75(2-3), 2007, 192–196.

[7] Kahane Ph., Berg A., Loscher W.: Current knowledge on basic mechanism of drug resistance. Drug resistant epilepsy, UK John Libbey Eurotext, 2008, 47–57.

[8] Kawamoto K., Houlihan C. A., Balas E. A., Lobach D. F.: Improving clinical practice using clinical decision support systems: a systematic review of trials to identify features critical to success. British Medical Journa 330, 2005, 765–773.

[9] Kipersztok O., Wang H.: Another look at sensitivity of Bayesian networks to imprecise probabilities. Proceedings of the Eighth International Workshop on Artificial Intelligence and Statistics 2001, 226–232.

[10] Kjærulff U., van der Gaag L. C.: Making sensitivity analysis computationally efficient. Proceedings of Uncertainty in Artificial Intelligence 2000, 317–325.

[11] Kwan P., Arzimanoglou A., Berg A. T., Brodie M. J.: Definition of drug resistant epilepsy: Consensus proposal by the ad hoc Task Force of the ILAE Commission on Therapeutic Strategies. Epilepsia 51(6), 2010, 1069–1077.

[12] Lucas P. J. F., Boot H., Taal B. G.: Decision-theoretic network approach to treatment management and prognosis. Knowledge-based Systems 11, 1998, 321–330.

[13] Miller R.: Medical diagnostic decision support systems-past, present and future. Journal of the American Medical Informatics Association 1, 1994, 8–27.

[14] Musen M. A., Shahar Y., Shortliffe E. H.: Biomedial Informatics: computer applications in health care and biomedicine. Springer, New York 2006, 698–736.

[15] Osheroff J. A.: Improving medication use and outcomes with clinical decision support: a step-by-step guide. Healthcare Information and Management Systems Society, Chicago 2009.

[16] Percell G. P.: What makes a good clinical decision support system. British Medical Journal 330, 2005, 740–741.

Ph.D. Mariia A. Voronenko
e-mail: mary.voronenko@gmail.com

Docent of the Department of Informatics and Computer Science, Kherson National Technical University, Kherson, Ukraine.
Area of scientific interests: combined iterative algorithms, Group method of data handling, Inductive modeling of complex systems, computer intelligence systems, Bayesian networks

http://orcid.org/0000-0002-5392-5125

M.Sc. Ulzhalgas M. Zhunissova
e-mail: ulzhalgas@list.ru

Master of Science, Senior teacher of the Department of Biostatistics, Bioinformatics and Information Technologies, Astana Medical University, Kazakhstan.
Science interests: data processing, medical data, machine learning methods, neural networks, Bayesian networks, evolutionary algorithms, clustering, information technology.

http://orcid.org/0000-0001-5255-9314

Ph.D. Saule Smailova
e-mail: Saule_Smailova@mail.ru

Saule Smailova is currently a lecturer at the Department of Information Technology. She is a co-author over 60 papers in journals, book chapters, and conference proceedings. Member of Expert Group in the Computer Science specialization of IQAA. Her professional interests are teaching, artificial intelligence, software engineering, data processing.

http://orcid.org/0000-0002-8411-3584

Luidmyla Lytvynenko
e-mail: llytvynenko58@gmail.com

Psychiatrist, Kherson City Psychiatric Center. Research interests: medical information systems, diagnosis and treatment of psychiatric diseases, epileptology, pharmacoresistance.

http://orcid.org/0000-0001-8445-5704

Prof. Nataliia Savina
e-mail: n.b.savina@nuwm.edu.ua

Conduct scientific, technical and innovative activities of the university, including the implementation of research results. Promotes the development of scientific relations with other universities, scientific institutions, centers and other enterprises, institutions and organizations. Organizes scientific relations with International centers, funds, programs, other foreign institutions.He has awards from the university, city and regional authorities, the Ministry of Education and Science of Ukraine, departmental awards.
Science interests: opinion and forecasting of investment efficiency in logistics projects, logistic and economic systems, and human capital.

http://orcid.org/0000-0001-8339-1219

Ph.D. Pavlo P. Mulesa
e-mail: pavlo.mulesa@uzhnu.edu.ua

Head of the Department of Cybernetics and Applied Mathematics, Uzhgorod National University, Uzhgorod, Ukraine.
Area of scientific interests: decision making systems and methods, data mining, data visualization, neural networks and artificial intelligence.

http://orcid.org/0000-0002-3437-8082

Prof. Volodymyr Lytvynenko
e-mail: immun56@gmail.com

Doctor of Science, Head of the Department of Informatics and Computer Scienc, Professor, Kherson National Technical University.
Science interests: Modeling of complex systems in economics, biology, medicine, machine learning methods, neural networks, Bayesian networks, evolutionary algorithms.

http://orcid.org/0000-0002-1536-5542